HIGH-ORDER HARMONIC GENERATION IN GRAPHENE AND CARBON NANOTUBES

Óscar Zurrón Cifuentes

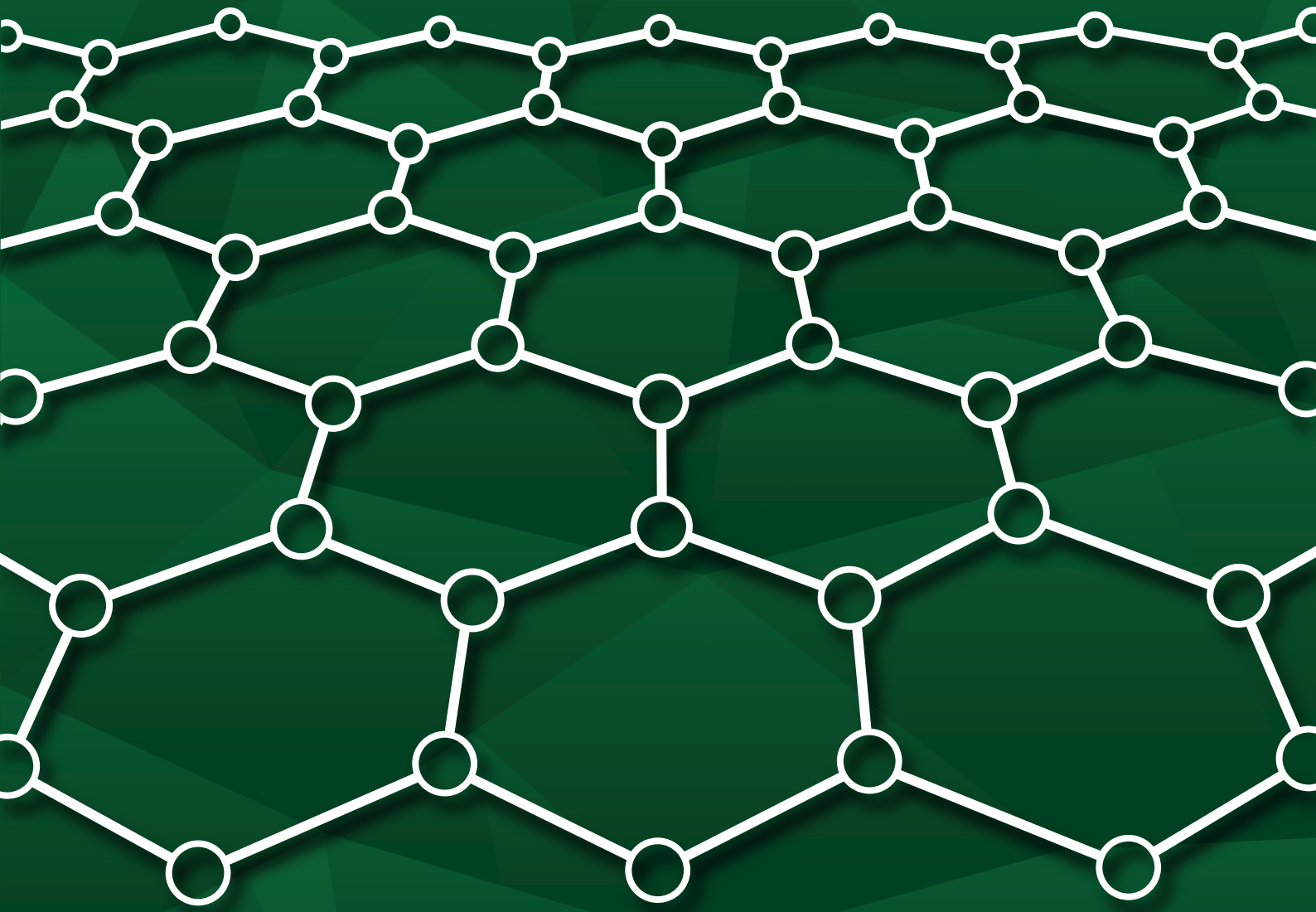

Tesis doctoral

Marzo 2021

VNiVERSiDAD D SALAMANCA
CAMPUS DE EXCELENCIA INTERNACIONAL

ÓSCAR ZURRÓN CIFUENTES

HIGH-ORDER HARMONIC GENERATION IN GRAPHENE AND CARBON NANOTUBES

HIGH-ORDER HARMONIC GENERATION IN GRAPHENE AND CARBON NANOTUBES

ÓSCAR ZURRÓN CIFUENTES

VNiVERSiDAD D SALAMANCA

CAMPUS DE EXCELENCIA INTERNACIONAL

Departamento de Física Aplicada. Área de Óptica.

Grupo de Investigación en Aplicaciones de los Láseres y Fotónica (ALF)

A thesis submitted for the degree of

Doctor in Physics at Universidad de Salamanca

Supervised by Prof. Dr. Luis Plaja Rustein

March 2021

Óscar Zurrón Cifuentes: *High-order harmonic generation in graphene and carbon nanotubes.* A thesis submitted for the degree of Doctor in Physics at Universidad de Salamanca. © March 2021.

Esta tesis doctoral es un compendio de las siguientes publicaciones:

1. Zurrón, Ó., Picón, A. & Plaja, L. Theory of high-order harmonic generation for gapless graphene. *New Journal of Physics* **20,** 053033 (2018).
2. Óscar Zurrón-Cifuentes, Boyero-García, R., Hernández-García, C., Picón, A. & Plaja, L. Optical anisotropy of non-perturbative high-order harmonic generation in gapless graphene. *Opt. Express* **27,** 7776–7786 (2019).
3. Óscar Zurrón-Cifuentes, Boyero-García, R., Hernández-García, C. & Plaja, L. High harmonic generation in armchair carbon nanotubes. *Opt. Express* **28,** 19760–19771 (2020).

VNiVERSiDAD D SALAMANCA
CAMPUS DE EXCELENCIA INTERNACIONAL

DEPARTAMENTO DE FÍSICA APLICADA
ÁREA DE ÓPTICA

D. LUIS PLAJA RUSTEIN, Catedrático de Óptica del Departamento de Física Aplicada de la Universidad de Salamanca, **CERTIFICA:**

Que la presente memoria, **"High-order harmonic generation in graphene and carbon nanotubes" / "Generación de armónicos de orden elevado en grafeno y nanotubos de carbono"** ha sido realizada por **D. ÓSCAR ZURRÓN CIFUENTES,** bajo su dirección en el Área de Óptica del Departamento de Física Aplicada de la Universidad de Salamanca y que constituye su Tesis Doctoral para optar al grado de Doctor en Física por la Universidad de Salamanca.

En Salamanca, a 19 de marzo de 2021

Fdo.: Luis Plaja Rustein

Ohana means family.
Family means nobody gets left behind, or forgotten.

— Lilo & Stitch

Dedicated to
Beatriz, María and Pablo,
my beloved family.

ABSTRACT

This thesis presents a comprehensive theoretical study of the process of high-order harmonic generation (HHG) induced by intense few-cycle infrared laser pulses in two different types of low dimensional carbon allotropes: 2D single layer graphene (SLG) and 1D single-wall carbon nanotubes (SWNTs). Our results show the emergence of a non-perturbative spectral plateau at large intensities but, unlike other more common systems, such as atoms, molecules or bulk solids, there is no simple law governing the scaling of the cut-off frequency. Interpreting this particular behavior allows to unveil the fundamental mechanism for HHG in those low dimensional carbon allotropic structures. Using a model for the emission dipole based on the saddle-point approximation, we show that the first step for HHG in these carbon compounds is radically different from the tunneling ionization/excitation process found in gas systems and finite gap solids, and that is closely related to the singular geometry of their band structure. In this sense, we demonstrate the crucial role that Dirac points in graphene and van Hove singularities in SWNTs play in the creation of electron-hole pairs. We also show that the high-order harmonic response in SLG is highly anisotropic, making it possible to emit elliptically polarized harmonics from linear-polarized drivers, and linearly polarized harmonics from elliptically-polarized pulses.

RESUMEN

Esta tesis presenta un estudio teórico exhaustivo del proceso de generación de armónicos de orden alto (HHG) inducidos por pulsos láser infrarrojos, ultracortos e intensos, en dos tipos diferentes de alótropos de carbono de baja dimensión: grafeno monocapa 2D (SLG) y nanotubos de carbono de pared simple 1D (SWNTs). Los resultados obtenidos muestran la aparición de una meseta espectral no perturbativa cuando la intensidad del láser es lo suficientemente elevada, aunque a diferencia de otros sistemas más conocidos, como átomos, moléculas o sólidos semiconductores, no parece existir una ley simple que gobierne el escalado de la frecuencia de corte espectral con la intensidad del pulso. La interpretación de este comportamiento particular nos permite revelar el mecanismo fundamental para la HHG en esas estructuras alotrópicas. Usando un modelo para la emisión dipolar basado en la aproximación del punto de silla, mostramos que el primer paso para la HHG en estos materiales es radicalmente diferente del proceso de ionización/excitación por efecto túnel que se observa en sistemas gaseosos y en sólidos semiconductores, y que está

estrechamente relacionado con la geometría singular de su estructura de bandas. En este sentido, demostramos el papel crucial que los puntos de Dirac en el grafeno y las singularidades de van Hove en los SWNTs juegan en la creación de pares electrón-hueco. También mostramos que la respuesta armónica de orden alto en SLG es altamente anisotrópica, lo que hace posible la emisión de armónicos polarizados elípticamente a partir de pulsos láser con polarización lineal, y de armónicos polarizados linealmente a partir de pulsos polarizados elípticamente.

PUBLICATIONS

The results included in this report have been published in the following research articles and conference contributions:

RESEARCH ARTICLES

1. Zurrón, Ó., Picón, A. & Plaja, L. Theory of high-order harmonic generation for gapless graphene. *New Journal of Physics* **20,** 053033 (2018).
2. Óscar Zurrón-Cifuentes, Boyero-García, R., Hernández-García, C., Picón, A. & Plaja, L. Optical anisotropy of non-perturbative high-order harmonic generation in gapless graphene. *Opt. Express* **27,** 7776–7786 (2019).
3. Óscar Zurrón-Cifuentes, Boyero-García, R., Hernández-García, C. & Plaja, L. High harmonic generation in armchair carbon nanotubes. *Opt. Express* **28,** 19760–19771 (2020).

CONFERENCE CONTRIBUTIONS

1. Zurrón, O., Iglesias, J. M., Rengel, R., Martín, M. J. & Plaja, L. *High order harmonic generation in graphene* in *Conference on Lasers and Electro-Optics CLEO Europe 2017* (Munich, Germany, 2017).
2. Zurrón, O., Iglesias, J. M., Martín, M. J., Rengel, R. & Plaja., L. *Non perturbative high harmonic generation in graphene* in *X Spanish Optoelectronics Meeting OPTOEL 2017* (Santiago de Compostela, Spain, 2017).
3. Zurrón, Ó., Iglesias, J. M., Rengel, R., Martín, M. J. & Plaja, L. *High harmonic generation in graphene: Temporal and spectral properties* in *SPIE Photonics West 2017* (San Francisco, CA, USA, 2017).
4. Zurrón, Ó., Picón, A. & Plaja, L. *Non perturbative high harmonic generation in graphene (Poster)* in *2nd Ultrafast Science and Technology Spain USTS 2017* (Salamanca, Spain, 2017).
5. Zurrón, Ó., Picón, A., Hernández-García, C. & Plaja, L. *Underlying mechanism for High Harmonic Generation in Graphene* in *XII Reunión Nacional de Óptica* (Castellón, Spain, 2018).
6. Zurrón, O., Picón, A., Hernández-García, C. & Plaja, L. *Fundamental mechanisms for the non-perturbative high harmonic generation in graphene* in *XXIst International Conference on Ultrafast Phenomena UP2018* (Hamburg, Germany, 2018).

7. Boyero-García, R., Zurrón-Cifuentes, Ó., Hernández-García, C., Picón, A. & Plaja, L. *Polarization control of high-harmonic pulses generated in gapless graphene* in *The European Conference on Lasers and Electro-Optics OSA 2019* (Munich, Germany, 2019).
8. Zurrón-Cifuentes, Ó., Boyero-García, R., Hernández-García, C., Picón, A. & Plaja, L. *Polarization control of non-perturbative high-order harmonics in gapless graphene* in *XXXVII Reunión Bienal de la Real Sociedada Española de Física* (Zaragoza, Spain, 2019).
9. Zurrón-Cifuentes, Ó., Boyero-García, R., Hernández-García, C., Picón, A. & Plaja, L. *Mechanism for high-order harmonic generation in graphene and carbon nanotubes* in *Joint Conference of the Condensed Matter Divisions of RSEF and EPS CMD2020GEFES* (Madrid, Spain, 2020).

Other work carried during the predoctoral period and not included in this report

1. Boyero-García, R., Zurrón-Cifuentes, O., Plaja, L. & Hernández-García, C. Transverse phase matching of high-order harmonic generation in single-layer graphene. *Opt. Express* **29,** 2488–2500 (2021).

"Science, my lad, is made up
of mistakes, but they are mistakes which it is
useful to make, because they lead little by little to the truth."

— Jules Verne, *A journey to the center of the Earth.*

ACKNOWLEDGMENTS

Dear Reader:

There are certain moments when life presents us with the opportunity to step back from the daily hustle and reflect on how we have come to be where we are. On occasion, those moments arise in a completely unexpected way and force us to put our everyday tasks on hold, even when we consider ourselves so essential that we fear everything is going fall apart simply for doing so. My personal experience has taught me that we must try to seize these opportunities to the fullest, because they seldom appear and tend to pass by us so quickly that we barely notice them. In my personal case, one such rare occasion presented itself after a surgical intervention forced me to completely suspend my professional activities. During the weeks of recovery, I had the opportunity to talk with my dear friend Pablo Moreno, who suggested that I contact Luis Plaja to begin the project that culminates with this thesis. My first thanks go to them, as they are the ones principally responsible for my having been able to achieve a goal that I set out to accomplish many years ago, and that life circumstances forced me to delay until now.

Although I have known Luis Plaja practically since he arrived in Salamanca, and knew of his accomplished scientific career, these years as a doctoral student have allowed me to appreciate his tremendous personal qualities. Because, in addition to being an excellent scientist, Luis is an extraordinary professor and, above all, a great person. His enthusiasm for science, immense creativity, and continual dedication, to his students in general and to me in particular, have been fundamental aspects of what allowed this project to come to successful fruition. My most sincere appreciation, Luis.

Apart from being a great professional and scientist, Pablo Moreno is that friend who always has been, is, and will be close by. Together we studied Physics at the University of Salamanca, sharing friends, times of leisure, many joys, and some sorrows, and together we watched our respective families grow. Although our professional careers took different paths from the first moment, we were both always-present witnesses of the successes that the other was achieving, and we always lent each other mutual support when it was needed. Thank you for always being there, Pablo.

My next acknowledgement is directed to José María Cerveró, for being the person who awakened my interest in science a long time ago. The circumstances of life led my professional career down a course distinct from academics, but the seed that José María planted bore fruit, and ever since then, my curiosity to continue learning has remained intact, and has also in great measure helped me to get here. Many thanks for that, José María.

At the same time, this thesis could not have been written without the work of the co-authors of the articles that are summarized here. I therefore wish to express my appreciation to Antonio Picón, Carlos Hernández and Roberto Boyero for their contributions to these, and for the interesting discussions that we had in the process of their preparation. Many thanks to all three.

I would also like to thank Julio San Román, Enrique Conejero, Javier Rodríguez, Iñigo Sola, Benjamín Alonso, Laura Rego, Aurora Crego, and the rest of the members of the Research Group on Laser and Photonics Applications (ALF-USAL) for their warm welcome into a group that is of indubitable human and professional quality. In addition, I wish to acknowledge María Jesús Martín, Raúl Rengel and José Manuel Iglesias for the interdisciplinary collaboration that we maintained at the beginning of the project, and Miguel Rico for the design of the covers.

Finally, I want to dedicate a mention of special thanks to my entire family. To my parents, for their enduring example and for having educated me as they did, giving me the opportunity to be the person I am. To my siblings, who I know are as thrilled about the completion of this project as I am. But above all, to Beatriz, for making me so happy by sharing her life with me, and to our children, Pablo and Maria, of whom I feel proud as a father, but particularly for their having chosen to pursue the same university degree as myself. The three of them have suffered first-hand the absences caused by my dedication to this project. This work is dedicated to them.

"La ciencia, muchacho,
está hecha de errores, pero de errores
útiles de cometer, pues poco a poco, conducen a la verdad."

— Julio Verne, *Viaje al centro de la Tierra.*

AGRADECIMIENTOS

Estimado lector:

Hay ciertos momentos en los que la vida nos brinda la oportunidad de alejarnos del ajetreo diario y reflexionar sobre cómo llegamos hasta donde estamos. En ocasiones, esos momentos surgen de forma totalmente inesperada y nos obligan a detener abruptamente nuestras tareas cotidianas, aún cuando nos consideremos tan imprescindibles como para pensar que todo se va a desmoronar por el mero hecho de hacerlo. Mi experiencia personal me ha enseñado que hay que tratar de aprovechar esas oportunidades al máximo, porque aparecen muy de vez en cuando y suelen pasar ante nosotros tan deprisa que apenas nos damos cuenta. En mi caso personal, una de esas raras ocasiones se presentó tras una intervención quirúrgica que me obligó a suspender por completo mi actividad profesional. Durante las semanas de convalecencia tuve la oportunidad de conversar con mi gran amigo Pablo Moreno, que fue quien sugirió la idea de contactar con Luis Plaja para iniciar el proyecto que culmina con esta tesis. A ellos dos van dirigidos mis primeros agradecimientos, ya que son los principales responsables de que haya podido alcanzar un objetivo que me propuse lograr hace muchos años, y que las circunstancias de la vida obligaron a retrasar hasta ahora.

Aunque conozco a Luis Plaja prácticamente desde su llegada a Salamanca y sabía de su trayectoria científica, estos años como doctorando me han permitido apreciar su enorme calidad personal. Porque además de ser un excelente científico, Luis es un profesor extraordinario y sobre todo, una gran persona. Su entusiasmo por la ciencia, enorme creatividad y continua dedicación, a sus alumnos en general y a mí en particular, han sido piezas fundamentales para que este proyecto llegara a buen término. Mi más sincero agradecimiento, Luis.

Aparte de ser un grandísimo profesional y científico, Pablo Moreno es ese amigo que siempre ha estado, está, y estará cerca. Juntos cursamos los estudios de Física en la Universidad de Salamanca, compartiendo amigos, momentos de ocio, muchas alegrías y algunas tristezas, y juntos vimos crecer a nuestras respectivas familias. A pesar de que nuestras trayectorias profesionales tomaron caminos diferentes desde el primer momento, ambos fuimos testigos permanentes de los éxitos que cada uno iba alcanzando, y nos prestamos apoyo mutuo

siempre que la situación lo requirió. Gracias por estar siempre ahí, Pablo.

Mi siguiente mención va dirigida a José María Cerveró, por ser quien despertó mi interés por la ciencia, hace ya bastante tiempo. Las circunstancias de la vida hicieron después que mi carrera discurriera por un ámbito distinto al académico, pero la semilla que José María sembró dio su fruto, y desde entonces siempre he mantenido intacta la curiosidad por seguir aprendiendo, lo que en buena medida me ha permitido también llegar hasta aquí. Muchas gracias por ello, José María.

Por otra parte, esta tesis no habría llegado a ser escrita sin el trabajo de los coautores de los artículos que aquí se compendian. Por ello, deseo expresar mi agradecimiento a Antonio Picón, Carlos Hernández y Roberto Boyero por su contribución a los mismos, y las interesantes discusiones que mantuvimos durante su elaboración. Muchas gracias a los tres.

Me gustaría también agradecer a Julio San Román, Enrique Conejero, Javier Rodríguez, Iñigo Sola, Benjamín Alonso, Laura Rego, Aurora Crego y al resto de componentes del Grupo de Investigación en Aplicaciones del Láser y Fotónica (ALF-USAL) su cálida acogida en un grupo de indudable calidad humana y profesional. Deseo citar además a María Jesús Martín, Raúl Rengel y José Manuel Iglesias por la colaboración interdisciplinar que mantuvimos en los inicios del proyecto, y a Miguel Rico por el diseño de las portadas.

Finalmente, quiero dedicar una mención especial de agradecimiento a toda mi familia. A mis padres, por su ejemplo permanente y haberme educado como lo hicieron, dándome la oportunidad de ser la persona que soy. A mis hermanos, a los que sé que llegar a culminar este proyecto les hace tanta ilusión como a mí. Pero sobre todo, a Beatriz por hacerme tan feliz compartiendo su vida conmigo, y a nuestros hijos, Pablo y María, de los que me siento orgulloso como padre, pero particularmente por haber elegido los mismos estudios universitarios que yo cursé. Ellos tres han sufrido de primera mano las ausencias provocadas por mi dedicación a este proyecto. A ellos está dedicado este trabajo.

CONTENTS

LIST OF FIGURES

ACRONYMS

BZ Brillouin zone

CNT Carbon nanotube

DOS Density of states

FWHM Full width at half maximum

HHG High-order harmonic generation

IR	Infrared
MWNT	Multi-wall carbon nanotube
SPAM	Saddle-point approximation model
SLG	Single layer graphene
SOC	Spin-orbit coupling
SWNT	Single-wall carbon nanotube
TDSE	Time-dependent Schrödinger equation
TFA	Time-frequency analysis
TMD	Transition metal dichalcogenide
XUV	Extreme ultraviolet

CONSTANTS

Quantity	**Symbol**	**Value**
Carbon-to-carbon distance in graphene	a_{cc}	1.42 Å
Lattice constant of graphene	a	2.46 Å
Velocity of light in vacuum	c	$2.997\,92 \times 10^{8}$ m·s^{-1}
Average energy of the $2p_z$ orbital of carbon in graphene	ε_{2p}	0.28 eV
Average interaction energy in graphene	γ_0	−2.97 eV
Plank's constant	$\hbar$	$6.626\,18 \times 10^{-34}$ J·s
Electron mass	m_e	$9.109\,53 \times 10^{-31}$ kg
Electron charge	q_e	$-1.602\,19 \times 10^{-19}$ C
Overlapping integral of graphene	s_0	0.073
Group velocity at the Fermi level in graphene	v_F	9.601×10^{5} m·s^{-1}

$\mathbf{a}$	Acceleration
$\mathbf{a}_{\leftrightarrow}$	Acceleration, intraband component
$\mathcal{A}$	Armchair nanotube
$\mathbf{A}$	Vector potential
a_0	Translational period, nanotubes
$\mathbf{a}_1$, $\mathbf{a}_2$	Primitive lattice vectors of graphene
$\mathbf{b}_1$, $\mathbf{b}_2$	Reciprocal lattice vectors of graphene
$\mathcal{C}$	Chiral nanotube
$\mathbf{C}_h$	Chiral vector
$C_\pm$	Amplitude probability coefficients of the conduction (+) and valence (-) bands
C^M, C^P	Off-diagonal amplitude probability coefficients
d_t	Nanotube diameter
$\mathbf{d}$	Dipole moment
$\tilde{\mathbf{d}}_\updownarrow$	Complex part of the interband component of the emission dipole
$\mathbf{D}$	Transition matrix element
D_m	Transition matrix element of band m (nanotubes)
$\mathcal{D}_0$	Ansatz for the magnitude of the impulse in the SPAM
$\mathcal{D}_0^m$	Ansatz for the magnitude of the impulse in band m in the SPAM (nanotubes)
$\delta(\mathbf{k})$, $\delta(t)$	Dirac delta function
ΔU	Corrections to H_{at} due to interactions with the lattice
$E_\pm$	Energy of the conduction (+) and valence (-) bands
$E_m^\pm$	Energy of the conduction (+) and valence (-) bands with angular momentum m (nanotubes)
ε	Ellipticity
$\varphi_z(\mathbf{r})$	Eigenfunction of the $2p_z$ orbital of carbon in graphene
$\varphi_{\mathbf{k}}$	Phase of $f(\mathbf{k})$
$f(\mathbf{k})$	Complex form factor
$f_m(k)$	Complex form factor in band m (nanotubes)
F_o	Amplitude of the driving electric field
$\mathbf{F}$	Driving electric field

$\phi_A(\mathbf{r})$, $\phi_B(\mathbf{r})$	Wave functions of the Bloch electrons in sublattices A and B
$\Phi^{\pm}_{\mathbf{k}}$	Eigenfunctions of H_o
$\Phi^{\pm}_{k,m}$	Eigenfunctions of H_o (nanotubes)
$\Phi^{(H)}_{\pm,\mathbf{k}}$	Houston function
Γ	Center of the BZ of graphene
H_{at}	Carbon atomic hamiltonian
H_o	Tight-binding hamiltonian of graphene
I	Intensity
I_p	Ionization potential
k	Axial quasi-momentum quantum numer (nanotubes)
$k^m_{\perp}$	Wave vector along the circumferential direction (nanotubes)
$\mathbf{k}$	Wave vector
$\mathbf{k}_D$	Coordinate of the wave vector at the Dirac Point K
K, K′	Dirac points
$\boldsymbol{\kappa}_t$	Kinetic quasi-momentum
m	Angular momentum quantum numer (nanotubes)
m_F	Angular momentum quantum number at the Fermi level
M	Midpoint of the line K-K′
$\mathcal{N}_{CB}$	Occupation density (conduction band)
n	Greatest common divisor of n_1, n_2
n_1, n_2	Chiral indices
$\psi_{\mathbf{k}}$	Wave function of the electron at wave vector $\mathbf{k}$
$\psi_{k,m}$	Wave function of the electron with quasi-momentum k in band m (nanotubes)
Ψ	Electronic wave function (real space)
q	Harmonic order, also Order of the isogonal point group (nanotubes)
$\mathbf{r}$	Position vector
$\mathbf{R}$	Lattice vector
$S_{\pm}(\mathbf{k}, t, t_o)$	Action integral between times t and t_o
$\mathcal{S}_0, \mathcal{S}_1, \mathcal{S}_2, \mathcal{S}_3$	Stokes parameters
σ_h	Horizontal mirror plane
σ_v	Vertical mirror plane
$t_{D,\mathbf{k}}$	Time of creation of the electron-hole pair at the Dirac point
t_H	Time of creation of the electron-hole pair at the first van Hove singularity
$\mathbf{T}$	Translational vector

$u^{\mathbf{k}}_{\mathrm{A}}(\mathbf{r}), u^{\mathbf{k}}_{\mathrm{B}}(\mathbf{r})$	Periodic amplitudes of the Bloch states in sublattices A and B
U	Two-fold symmetry axis
U_{p}	Ponderomotive energy
$\mathrm{V_C}$	Crystal potential
$\mathbf{v}_{\pm}$	Velocity of the electron in the conduction (+) and valence (-) bands
$v_m^{\pm}$	Velocity of the electron in the conduction (+) and valence (-) bands with angular momentum m (nanotubes)
V_{int}	Interaction Hamiltonian
ω	Frequency
ω_o	Frequency of the driving electromagnetic field
Ξ_m^k, Θ_m^k	Arguments of the trigonometric functions appearing in the definition of D_m in zigzag nanotubes
θ	Tilt angle, also Chiral angle (nanotubes)
$\mathcal{Z}$	Zigzag nanotube

1 INTRODUCTION

The science of carbon-based materials has rapidly evolved during the last 30 years boosted by the discovery of new low-dimensional allotropic forms, which exhibit remarkable chemical and physical properties. As shown in Fig. 1.1, carbon nanomaterials show a rich polymorphism in all possible effective dimensions: C_{60} Buckminsterfullerene (0D), nanotubes (1D), graphene (2D) or nano-diamonds (3D) are selected examples of such nanostructures [1]. The theoretical understanding of graphene is doubtless the cornerstone of the scientific and technological developments on this field [2]. Monolayer graphite, single layer graphene (SLG) or simply, graphene, are the names given to an infinite one-atom-thick planar arrangement of sp^2-bonded carbon atoms packed in a honeycomb lattice. Though in 1962 graphene was already observed on metal surfaces through electron microscopy [3], it was presumed not to exist as a stand-alone structure, since it was considered to be unstable towards the formation of curved allotropes, such as fullerenes or nanotubes. Nevertheless, graphene was isolated and characterized in 2004 by Geim and Novoselov [4], who were awarded in 2010 with the Nobel prize in Physics. The material was proved to be easily isolated either by mechanical exfoliation (known as the "scotch-tape" method) [4, 5] or by epitaxial growth through thermal decomposition of SiC [6]. These capabilities renewed the interest of the scientific community in graphene, which has been the subject of numerous theoretical and experimental studies since then.

Graphene displays remarkable electronic properties arising from its structural symmetries and the confinement of electrons in two dimensions. SLG is a zero-gap semiconductor with the valence and conduction bands contacting at the Dirac points in the first Brillouin zone (BZ), where the band dispersion is almost linear. As a result, electrons and holes propagate in the vicinity of the Dirac points as massless fermions with group velocity $\sim 10^6$ m/s, holding a new degree of freedom, called pseudospin, which appears as a consequence of the inherent symmetries. Equally, graphene shows large charge mobility at room temperature $\sim 10^5$ $cm^2 \cdot V^{-1} \cdot s^{-1}$ and a minimum zero-point conductivity close to $4e^2/h$ [7]. In addition, graphene is demonstrated to exhibit anomalous half-integer quantum Hall effect [8], as a consequence of the coupling between pseudospin and orbital motion, which gives rise to a geometrical phase (Berry's phase) of π accumulated along cyclotron trajectories around the Dirac points [7].

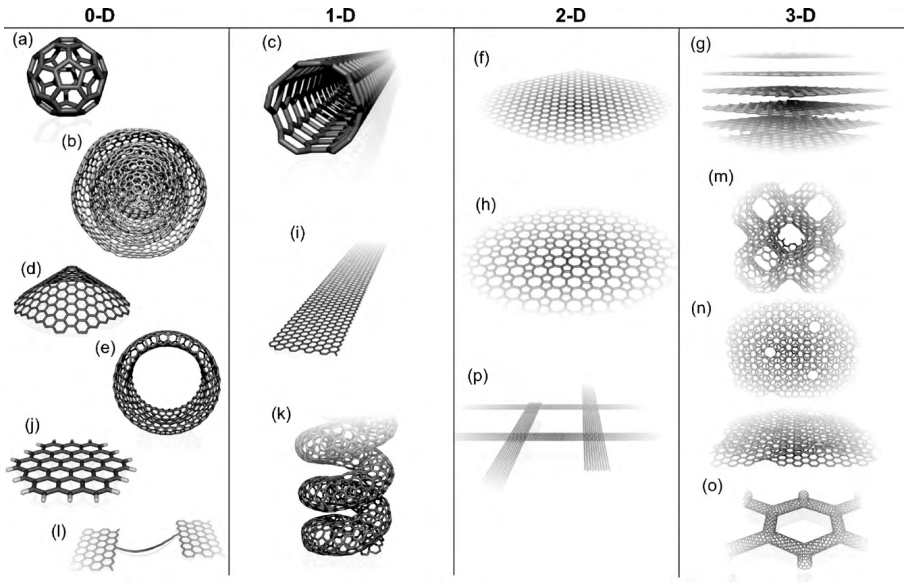

Figure 1.1: Examples of carbon nanostructures exhibiting different dimensionalities, 0D, 1D, 2D and 3D: (a) C_{60}: Buckminsterfullerene; (b) nested giant fullerenes or graphitic onions; (c) carbon nanotube; (d) nanocones or nanohorns; (e) nanotoroids; (f) graphene surface; (g) 3D graphite crystal; (h) Haeckelite surface; (i) graphene nanoribbons; (j) graphene clusters; (k) helicoidal carbon nanotube; (l) short carbon chains; (m) 3D Schwarzite crystals; (n) carbon nanofoams (interconnected graphene surfaces with channels); (o) 3D nanotube networks, and (p) nanoribbons 2D networks. Figure extracted from Terrones *et al.* [1].

The gapless band structure of SLG allows also for optical resonant excitations at all frequencies, up to the vacuum ultraviolet. This broad resonance endorses graphene with particular optical properties, as a strong broadband linear response with a comparatively large optical absorption of visible light ($> 2\%$) [9], and a strong non-linear response for THz radiation [10, 11]. While the generation of the second harmonic is forbidden in the dipole approximation, due to the centrosymmetric structure of ideal SLG, it can be observed in stacked samples [12]. Third-order nonlinearities are found to be also remarkably strong in SLG, with nonlinear susceptibilities several orders of magnitude higher than those of transparent materials, and of the same order as in other resonant materials, such as metal nanoparticles. The third harmonic has been observed in few-layer graphene for transitions occurring near the K and M points of the Brillouin zone [13–15]. High-order harmonic generation (HHG) in gapless graphene has not been reported until recently [16, 17], with the observation of up to the ninth harmonic of a mid-infrared driving laser. These pioneering studies demonstrate the experimental feasibility of producing HHG in monolayer graphene.

Besides these outstanding electronic and optical properties, graphene displays also other remarkable physical properties. The thermal conductivity of suspended graphene has been measured to be approximately 5000 $W \cdot m^{-1} \cdot K^{-1}$ [18], ten times larger than that of copper and more than double than in pyrolytic graphite. Graphene is very light (0.77 mg/cm^2) and, at the same time, an extremely hard and stiff material. Indeed, it is the strongest material ever tested, with a Young's modulus close to 1 TPa and a tensile strenght of 130 GPa, which corresponds to a breaking strength of 42 N/m [19, 20], 100 times higher than that of the strongest steel. The 2010 Nobel Prize announcement highlighted these properties by stating that it should be possible to make a nearly invisible 1 m^2 hammock out of graphene that could hold a 4 kg cat without breaking, weighing less than 1 mg, just as much as one of the cat's whiskers. These discoveries paved the way to a number of technological applications in great variety of fields, including solar cells, touch screens and bondable electronics for smartphones, capacitors and batteries, solid-state gas sensors for single molecules, DNA sequencing or fabrication of composite materials such as paints, coatings and lubricants. In summary, the outstanding properties of graphene make it a very appealing material, suitable for a wide range of technological applications and also, for bringing further insight into the underlying physics behind them.

Carbon nanotubes (CNTs) are another enthralling example of carbon based nanostructures. CNTs are allotropic forms of carbon featuring a hollow cylinder with a length-to-diameter ratio that may reach up to 10^8 [21], notably larger than other one-dimensional materials. The cylinder walls are formed by one-atom-thick sheets of carbon rolled up at specific chiral angles. The interest for the study of CNTs rocketed after the work by Ijima in 1991 [22], although some works had already reported the observation of such structures before [23–25]. Using high-resolution transmission electron microscopy, Ijima characterized "graphite microtubules", made of concentric shells of carbon atoms with diameters ranging from a few to several hundred nanometers, which constitute what we now call multi-wall carbon nanotubes (MWNTs). A couple of years later, carbon nanotubes made of a single graphene layer rolled into a hollow cylinder were synthesized by arc discharge methods with transition metal catalysts [26, 27]. These structures, called single wall carbon nanotubes (SWNTs), had diameters about one nanometer and an extraordinarily perfect crystalline structure. SWNTs may behave as metals or semiconductors depending on their geometry [28]. Metallic nanotubes can hold an axial current density of 4×10^9 A/cm^2, more than 1000 times greater than cooper [29]. There is experimental evidence that the high order harmonic emission spectra of SWNTs can be controlled either by tuning their electronic structure, or by carrier injection using electrolyte gating approaches, with up to the 11th harmonic being observed in

semiconductor tubes of relative large band gap ~ 1.26 eV [30]. All nanotubes are very good thermal conductors along the axial direction, with measured conductivity of about 3500 $W \cdot m^{-1} \cdot K^{-1}$ [31], but good thermal insulators in the radial direction, showing thermal conductivity values at room-temperature as low as soil (1.52 $W \cdot m^{-1} \cdot K^{-1}$) [32]. As a consequence of the covalent sp^2 bonds between carbon atoms, CNTs are very strong and stiff under stretching forces in the axial direction (their tensile strength may reach up to 100 GPa [33]), but are not as strong under compression, tending to undergo buckling when subjected to compressive, torsional or bending stress because of their hollow structure and high aspect ratio [34]. On the other hand, they are rather soft in the radial direction, showing Young's modulus of the order of several GPa [35], with experimental evidences suggesting that even van der Waals forces can deform two adjacent nanotubes [36]. All these properties are extremely valuable for technological applications in nanotechnology, electronics, mechanics, optics and other fields of materials science, such us composite materials [37].

The remarkable optical properties of graphene and carbon nanotubes have attracted our interest to further study their non-linear response after irradiation by strong laser fields. Despite the considerable theoretical advances made in this field, we observe that certain fundamental aspects have not been completely addressed in the current models that describe such non-linear dynamics. This is the leitmotiv of the present work, which is dedicated to investigate the process of high-order harmonic generation in the aforementioned low-dimensional systems.

HHG is an extreme non-linear process in which a target irradiated by an intense laser pulse emits radiation in the form of high-frequency harmonics of the driving beam, see Fig. 1.2. This remarkable process has paved the way to extend coherent radiation to the extreme regions of the electromagnetic spectrum, which is one of the major challenges since the invention of the laser in 1960 [38]. The non-perturbative character of HHG has a distinguishable signature in the harmonic spectrum: the emergence of a *plateau* structure followed by an abrupt *cut-off* [39]. The plateau is characterized by a dependence of the spectral intensity with the harmonic order q much less pronounced than that predicted by the perturbation theory (q-th power). Furthermore, the plateau structure may extend the harmonic emission up to thousands of harmonic orders, leading to a wide range of applications, from imaging and spectroscopy with sub-femtosecond resolution, to sources of coherent radiation in the extreme ultraviolet (XUV) or even, in the X-ray regime [40, 41]. The first experimental evidence of harmonic generation was demonstrated by Franken *et al.* in 1961 [42], who observed the second harmonic of a ruby laser with wavelength 694 nm in a quartz crystal. Nevertheless, it was not until the late 1980s when the availability of laser sources of high intensity

made it possible to observe non-perturbative harmonics [43, 44]. The most relevant aspects of HHG were established during the 1990s, following intense theoretical and experimental activity which boosted the development of the field. In 1993, L'Huillier and Balcou observed up to the 135th harmonic in Ne using pulses 1 ps long and intensities as large as 10^{15} W/cm^2 [45], and Mackling *et al.* reported the observation of harmonics greater than the 109th for incident wavelengths in the near infrared range using the same target [46]. Also in 1993, Schafer *et al.* presented the renowned *three step model* to explain HHG on a semiclassical basis [47] and almost simultaneously, Corkum published his work with similar ideas [48]. Shortly after (1994), Lewenstein *et al.* presented a fully quantum theory that revealed the physics underlying HHG and produced quantitative predictions [49]. Since then, different groups have reported the observation of harmonics of progressive higher order in gas systems [50, 51].

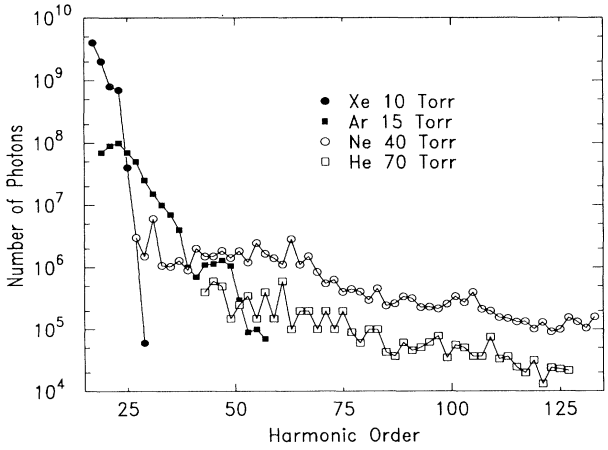

Figure 1.2: Experimental data of the high-harmonic yield from Xe, Ar, Ne and He driven by a 1 ps, 1053 nm, Nd-laser pulse at 10^{15} W/cm^2 peak intensity. Figure extracted from L'Huillier and Balcou (1993) [45].

Currently, targets for high order harmonic emission include not only atomic or molecular systems, but also solids and plasmas. In particular, HHG from solid targets has burgeoned a great interest, mainly motivated by the quadratic scaling of the harmonic conversion efficiency with the density of the target, as a result of the coherent nature of the process [52–59]. In the case of plasmas, HHG is based on the response of the system to relativistic field strengths [60]. For atomic or molecular gases and semiconductor solids, high-order harmonics appear below the relativistic limit. In all these systems, HHG shares some basic principles [59]. In particular, harmonics are generated by electrons that are initially bound and promote to slightly bonded (or unbound) states by tunneling. Once promoted, the electrons are accelerated by the electric field until they release the acquired kinetic

energy in the form of high-frequency radiation. Despite these similarities, the first experiment on HHG in solid state systems revealed substantial differences in the laws governing the spectral plateau and cut-off frequency compared to the case of atomic or molecular systems [52]. In the latter, the cut-off frequency scales with the product of the laser intensity times the square of the wavelength. In contrast, it is known that for semiconductors the cut-off frequency scales linearly with the amplitude of the field [52]. This behavior could remind the HHG process of two-level systems, where the cut-off frequency is associated with the maximum Stark effect [61, 62]. However, the behavior of two-level systems is not sufficient to explain the complex dynamics introduced by intraband contributions. Several theoretical models have been used to explain this non-linear response [63–68]. Since the tunnel effect is known to play a fundamental role as the first step of the HHG process in systems that exhibit an energy gap, the singular structure of the energy bands of graphene and carbon nanotubes opens a new scenario.

Objectives and outline of the work

The main purpose of this PhD thesis report is to deepen into the study of the non-linear optical response of the low-dimensional carbon allotropes described above, upon irradiation by intense laser fields. In particular, our interest is focused on studying the process of HHG. Although some experimental work has been already done [16, 17, 30], to the best of our knowledge there is not much literature in relation to the particular mechanism that causes the generation of high-order harmonics. Given the unique geometrical features of the electronic structure of these materials, it is reasonable to think that there may be substantial differences with respect to other crystalline solids. In this context, we have focused in the following objectives:

- To establish the equations that rule the electron dynamics in the periodic potential of graphene during the interaction with intense electromagnetic fields. The strategy for integrating such equations must be carefully addressed in order to tackle the subtle physical processes arising from the unsual geometry of the graphene band structure. Once accomplished, this objective will allow to compute the optical emission dipole and thus, the high-order harmonic spectra.
- To develop a simulation tool that includes the most relevant aspects of HHG in graphene as identified in the previous objective. The results obtained with the tool must be confronted with the literature in order to correctly fulfill the forthcoming objectives.
- To investigate the modification of high-order harmonic spectra under varying conditions of the field, by tuning the wavelength,

or modifying the intensity and polarization of the driver. Special attention must be paid to the scaling of the cut-off frequency with the intensity, as it is well-know that this parameter gives insight into the HHG mechanism for atoms, molecules and finite gap solids. Possible ultrafast polarization changes in the spectra must be also taken into account.

- To draw conclusions on the mechanism for high-order harmonic generation in graphene and compare it with that of other physical systems.
- To extend the above referred methodology to carbon nanotubes of different sizes and chirality, in order to study the spectral yield and draw conclusions on the HHG mechanism in these 1D structures.

For such purposes, this report is organized as follows. In chapter 2 we introduce the fundamental concepts. This chapter includes a full description of the electronic properties of graphene and carbon nanotubes, and the derivation of the hamiltonian that accounts for the interaction between light and matter. The most relevant aspects of high-order harmonic generation in gases and finite gas solids are also addressed. Chapter 3 explores HHG in graphene. We first derive and integrate the equations that account for the population dynamics in the conduction and valence bands during the interaction with intense laser pulses. Then, we calculate the emission dipole and compute the spectral yield for varying parameters of the driver pulse. Specific features of the high-order harmonic spectra, like the harmonic plateau, cut-off scaling, harmonic ellipticity and some subtle ultrafast changes are also studied in detail. Using a saddle-point analysis, we develop a model for HHG in graphene, which gives new insight into the mechanism for high-order harmonic emission in this 2D material, putting at the foreground the unique geometric features of its electronic band structure. Next, chapter 4 is devoted to the study of HHG in carbon nanotubes. Based on the methods previously developed for graphene, we study the spectral yield from these 1D structures, demonstrating that HHG is strongly dependent on the geometry of the electronic bands and thus, that it can be tuned by the proper control of their structural parameters. Finally, chapter 5 summarizes the main findings and prospects for future work in this field.

INTRODUCCIÓN

La ciencia de los materiales en base al carbono ha evolucionado rápidamente durante los últimos 30 años impulsada por el descubrimiento de formas alotrópicas de baja dimensión, que exhiben propiedades químicas y físicas notables. Como se muestra en la Fig. 1.1, los nanomateriales de carbono muestran un rico polimorfismo en todas las posibles dimensiones efectivas: el buckminsterfullereno C_{60} (0D), los nanotubos (1D), el grafeno (2D) o los nano-diamantes (3D) son algunos ejemplos de tales nanoestructuras [1]. La comprensión teórica del grafeno es sin duda la piedra angular de los avances científicos y tecnológicos que se han ido sucediendo en este campo [2]. Grafito monocapa, grafeno monocapa (SLG) o simplemente grafeno, son los nombres por los que se conoce a una estrucutura plana e infinita de átomos de carbono unidos mediante enlaces covalentes, que se generan a partir de la superposición de orbitales híbridos sp^2 empaquetados con disposición hexagonal. Aunque en 1962 ya se observó grafeno en superficies metálicas mediante microscopía electrónica [3], se suponía que éste no podía existir como estructura independiente, ya que se consideraba inestable frente a la formación de alótropos curvos, tales como los fullerenos o los nanotubos. Sin embargo, el grafeno fue aislado y caracterizado en 2004 por Geim y Novoselov [4], quienes fueron galardonados en 2010 con el premio Nobel de Física. Se demostró entonces que el material se podía aislar fácilmente mediante exfoliación mecánica (método conocido como de "cinta adhesiva") [4, 5] o mediante crecimiento epitaxial a través de la descomposición térmica del SiC [6]. Estas capacidades renovaron el interés de la comunidad científica por el grafeno, que ha sido objeto de numerosos estudios teóricos y experimentales desde entonces.

El grafeno muestra notables propiedades electrónicas como consecuencia de sus simetrías estructurales y del confinamiento de los electrones en dos dimensiones. SLG es un semimetal, con las bandas de valencia y conducción degeneradas en los puntos de Dirac, donde la dispersión es casi lineal. Como resultado, los electrones y los huecos se propagan en la vecindad de los puntos de Dirac como fermiones sin masa con velocidad de grupo $\sim 10^6$ m/s, y con un nuevo grado de libertad, llamado pseudopin, que aparece como consecuencia de las simetrías inherentes. Además, el grafeno muestra una gran movilidad de carga a temperatura ambiente $\sim 10^5$ $cm^2 \cdot V^{-1} \cdot s^{-1}$ y una conductividad mínima cercana a $4e^2/h$ [7]. También se ha demostrado que el grafeno exhibe efecto Hall cuántico fraccionario [8], como consecuencia del acoplamiento entre el pseudoespín y el movimiento orbital, lo que a su vez da lugar a una fase geométrica (fase de Berry) igual a π acumulada a lo largo de trayectorias de ciclotrón alrededor de los puntos de Dirac [7].

La estructura de bandas degeneradas del SLG permite excitaciones ópticas resonantes en cualquier frecuencia hasta el ultravioleta de vacío. Esta amplia resonancia dota al grafeno de propiedades ópticas particulares, tales como una intensa respuesta lineal de banda ancha, con una absorción óptica de la luz visible comparativamente grande ($> 2\%$) [9], y una intensa respuesta no lineal para la radiación en el rango del THz [10, 11]. Si bien la generación del segundo armónico está prohibida en la aproximación dipolar, debido a la estructura centrosimétrica del SLG, puede observarse en muestras apiladas [12]. Las no linealidades de tercer orden también son notablemente fuertes en SLG, con susceptibilidades no lineales varios órdenes de magnitud superiores a las de los materiales transparentes, y del mismo orden que en otros materiales resonantes, como las nanopartículas metálicas. El tercer armónico se ha observado en grafeno de pocas capas para transiciones en el entorno de los puntos K y M de la zona de Brillouin [13–15]. Sin embargo, la generación de armónicos de orden elevado (HHG) en grafeno no se había reportado hasta tiempos recientes [16, 17], con la observación de hasta el noveno armónico de un láser incidente de longitud de onda en el infrarrojo medio. Estos estudios pioneros demuestran la viabilidad experimental de producir HHG en grafeno monocapa.

Además de estas excepcionales propiedades electrónicas y ópticas, el grafeno muestra otras propiedades físicas notables. Se ha calculado que la conductividad térmica del grafeno en suspensión es aproximadamente de 5000 $W{\cdot}m^{-1}{\cdot}K^{-1}$ [18], diez veces mayor que la del cobre, y más del doble que la del grafito pirolítico. El grafeno es muy ligero ($0,77$ mg/cm^2) y, al mismo tiempo, se trata de un material extremadamente duro y rígido. De hecho, es el material más resistente jamás ensayado, con un módulo de Young cercano a 1 TPa y una resistencia a la tracción de 130 GPa, correspondiente a una resistencia a la rotura de 42 N/m [19, 20], 100 veces mayor que la del acero más resistente. El anuncio del Premio Nobel de 2010 destacó estas propiedades afirmando que sería posible hacer una hamaca casi invisible de grafeno de 1 m^2 capaz de sostener el peso de un gato de 4 kg sin romperse, cuya masa sería de menos de 1 mg, tanto como uno de los bigotes del gato. Estos descubrimientos allanaron el camino para el desarrollo de aplicaciones tecnológicas en una gran variedad de campos, incluyendo células solares, pantallas táctiles y electrónica flexible para teléfonos inteligentes, condensadores y baterías, sensores de gas de estado sólido para moléculas individuales, secuenciación de ADN o fabricación de materiales compuestos como como pinturas, revestimientos y lubricantes. Todas estas propiedades hacen del grafeno un material extraordinariamente atractivo, no sólo por ser adecuado para una amplia gama de aplicaciones tecnológicas, si no también porque su estudio teórico permite aportar mayor comprensión sobre los fenómenos físicos subyacentes tras de ellas.

Los nanotubos de carbono (CNTs) son otro fascinante ejemplo de nanoestructuras basadas en el carbono. Los CNTs son formas alotrópicas en forma de cilindro hueco con una relación de longitud–diámetro que puede alcanzar hasta 10^8 [21], notablemente superior a la de otros materiales unidimensionales. Las paredes del cilindro están formadas por láminas de un átomo de espesor enrolladas según ángulos quirales específicos. El interés por el estudio de los CNTs se disparó a partir del trabajo de Ijima en 1991 [22], aunque algunos autores ya habían reportado la observación de tales estructuras con anterioridad [23–25]. Utilizando microscopía electrónica de transmisión de alta resolución, Ijima caracterizó los "microtúbulos de grafito", hechos de capas concéntricas de átomos de carbono con diámetros que iban desde unos pocos a varios cientos de nanómetros, y que constituyen lo que ahora llamamos nanotubos de pared múltiple (MWNTs). Un par de años más tarde, nanotubos formados por una sola capa de grafeno enrollada se sintetizaron mediante métodos de descarga de arco con catalizadores de metales de transición [26, 27]. Estas estructuras, llamadas nanotubos de pared simple (SWNTs), tienen diámetros del orden del nanómetro y una estructura cristalina extraordinariamente perfecta. Los SWNTs puede comportarse como metales o semiconductores dependiendo de su geometría [28]. Los nanotubos metálicos pueden contener una densidad de corriente axial de 4×10^9 A/cm^2, más de 1000 veces mayor que la de cobre [29]. Existe evidencia experimental de que los espectros de emisión de armónicos de orden elevado de los SWNTs pueden controlarse ajustando su estructura electrónica o mediante métodos de inyección de portadores a través de compuertas electrolíticas, habiéndose observado hasta el decimoprimer armónico en tubos semiconductores de gap relativamente grande ($\sim$ 1.26 eV) [30]. Todos los nanotubos son muy buenos conductores térmicos en la dirección axial, con una conductividad de aproximadamente 3500 W$\cdot$m$^{-1}\cdot$K^{-1} [31], pero buenos aislantes térmicos en la dirección radial, con valores de conductividad térmica a temperatura ambiente tan bajos como la de la tierra (1.52 W$\cdot$m$^{-1}\cdot$K^{-1}) [32]. Como consecuencia de los enlaces covalentes sp^2 entre los átomos de carbono, los CNTs son muy duros y rígidos bajo fuerzas de estiramiento en la dirección axial (su resistencia a la tracción puede alcanzar hasta 100 GPa [33]), pero no son tan rigidos bajo compresión, y tienden a sufrir pandeo cuando se someten a esfuerzos de compresión, torsión o flexión debido a su estructura hueca y elevada relación de aspecto [34]. Por otro lado, son poco rígidos en la dirección radial, mostrando un módulo de Young del orden de varios GPa [35], existiendo evidencias experimentales que sugieren que incluso las fuerzas de van der Waals pueden deformar dos nanotubos adyacentes [36]. Todas estas propiedades son extremadamente valiosas para aplicaciones tecnológicas en nanotecnología, electrónica, mecánica, óptica y otros campos de la ciencia de los materiales [37].

Las notables propiedades ópticas del grafeno y de los nanotubos de carbono que se citan en los párrafos precedentes motivaron nuestro interés para profundizar en el estudio de su respuesta no lineal durante la irradiación con campos láser intensos. A pesar de los considerables avances teóricos realizados en este campo, observamos que ciertos aspectos fundamentales no han sido completamente abordados en los modelos actuales que describen esta dinámica no lineal. Este es el leitmotiv del presente trabajo, que se centra en la investigación del proceso de generación de armónicos de orden elevado en los sistemas de baja dimensión antes mencionados.

La HHG es un proceso no lineal extremo en el que un blanco irradiado por un pulso láser intenso emite radiación en forma de armónicos de alta frecuencia del haz incidente, ver Fig. 1.2. El descubrimiento de este notable proceso ha allanado el camino para extender la radiación coherente a las regiones extremas del espectro electromagnético, que es uno de los mayores desafíos desde la invención del láser en 1960 [38]. El carácter no perturbativo de HHG tiene una firma distinguible en el espectro de armónicos: la aparición de una estructura de meseta o *plateau* seguida de un corte abrupto [39]. El *plateau* se caracteriza por una dependencia de la intensidad espectral con el orden armónico q mucho menos pronunciada que la predicha por la teoría de perturbaciones (q-ésima potencia). Además, la estructura de *plateau* puede extender la emisión armónica hasta miles de órdenes armónicos, lo que lleva a una amplia gama de aplicaciones, desde generación de imágenes y espectroscopía con resolución de subfemtosegundos, hasta fuentes de radiación coherente en el ultravioleta extremo (XUV) o incluso, en el régimen de los rayos X [40, 41]. Aunque la primera evidencia experimental de generación armónica fue demostrada por Franken *et al.* en 1961 [42], quien observó el segundo armónico en un cristal de cuarzo, no fue hasta finales de la década de 1980 cuando la disponibilidad de fuentes láser de alta intensidad permitió observar armónicos no perturbativos [43, 44]. Los aspectos más relevantes de la HHG se establecieron durante la década de 1990, tras una intensa actividad teórica y experimental que impulsó el desarrollo de este campo de investigación. En 1993, L'Huillier y Balcou observaron hasta el 135-ésimo armónico en Ne usando pulsos de 1 ps de duración e intensidades del orden de $10^{15}\mathrm{W/cm^2}$ [45], y Mackling *et al.* reportaron la observación de armónicos superiores al 109-ésimo para longitudes de onda incidentes en el rango del infrarrojo cercano usando el mismo blanco [46]. También en 1993, Schafer *et al.* presentaron el famoso *modelo de tres pasos* para explicar la HHG sobre una base semiclásica [47] y casi simultáneamente, Corkum publicó un trabajo con ideas similares [48]. Poco después (1994), Lewenstein *et al.* presentaron una teoría completamente cuántica que reveló la física subyacente a la HHG y permitió realizar predicciones cuantitativas [49]. Desde entonces, diferentes grupos han reportado la observación

de armónicos de orden cada vez más elevado en sistemas gaseosos [50, 51].

Actualmente, los blancos que se utilizan para la generación de armónicos de orden elevado incluyen no sólo sistemas atómicos o moleculares, sino también sólidos y plasmas. En particular, la HHG de blancos sólidos ha despertado un gran interés, motivado principalmente por el escalado cuadrático de la eficiencia de conversión armónica con la densidad del blanco, como consecuencia de la naturaleza coherente del proceso [52–59]. En el caso de los plasmas, la HHG se basa en la respuesta del sistema a intensidades de campo relativistas [60]. Para gases atómicos o moleculares y sólidos semiconductores, los armónicos de orden elevado aparecen por debajo del límite relativista. En todos estos sistemas, la HHG comparte algunos principios básicos [59]. En particular, los armónicos son generados por electrones que inicialmente están ligados y que se promocionan a estados excitados, débilmente ligados (o no ligados), por efecto túnel. El campo eléctrico acelera entonces los electrones promocionados hasta que éstos liberan la energía cinética adquirida en forma de radiación de alta frecuencia. A pesar de estas similitudes, el primer experimento de HHG en sistemas de estado sólido reveló diferencias sustanciales en las leyes que gobiernan el *plateau* espectral y la frecuencia de corte en comparación con los sistemas atómicos o moleculares [52]. En este último caso, la frecuencia de corte escala con el producto de la intensidad del láser por el cuadrado de la longitud de onda, mientras que en los materiales semiconductores, la frecuencia de corte escala linealmente con la amplitud del campo [52]. Este comportamiento podría recordar el proceso de HHG en sistemas de dos niveles, donde la frecuencia de corte está asociada con el efecto Stark máximo [61, 62]. Sin embargo, el comportamiento de los sistemas de dos niveles no es suficiente para explicar la compleja dinámica introducida por las contribuciones intrabanda. Varios modelos teóricos has sido propuestos para explicar esta respuesta no lineal [63–68]. Sin embargo y dado que se sabe que el efecto túnel juega un papel fundamental como primera etapa del proceso de HHG en sistemas que exhiben *gap* finito, la estructura singular de las bandas de energía del grafeno y de los nanotubos de carbono abre un nuevo escenario.

Objetivos y estructura del trabajo

El objetivo principal de esta tesis doctoral es profundizar en el estudio de la respuesta óptica no lineal de los alótropos de carbono de baja dimensión descritos anteriormente frente a la irradiación por campos láser intensos. En particular, nuestro interés se focaliza en estudiar el proceso de HHG. Aunque hay algunos trabajos experimentales en este campo [16, 17, 30], por lo que sabemos, no existe mucha literatura en relación con el mecanismo particular que causa la generación de

armónicos de orden elevado. Dadas las características geométricas únicas de la estructura electrónica de estos materiales, es razonable pensar que puede haber diferencias sustanciales con respecto a otros sólidos cristalinos. En este contexto, nos hemos centrado en alcanzar los siguientes objetivos:

- Establecer las ecuaciones que rigen la dinámica de los electrones en el potencial periódico del grafeno durante la interacción con campos electromagnéticos intensos. La estrategia para integrar tales ecuaciones debe abordarse con cuidado a fin de considerar los sutiles procesos físicos que surgen de la inusual geometría de la estructura de bandas del grafeno. Una vez cumplido, este objetivo permitirá calcular el dipolo de emisión óptica y los espectros de armónicos de orden elevado.

- Desarrollar una herramienta de simulación que incluya los aspectos más relevantes de la HHG en el grafeno identificados en el objetivo anterior. Los resultados obtenidos con esta herramienta deben validarse con la literatura para abordar correctamente con los siguientes objetivos.

- Investigar los cambios en los espectros de armónicos de orden elevado bajo condiciones variables del campo, ajustando la longitud de onda o modificando la intensidad y polarización del haz incidente. Se debe prestar especial atención al escalado de la frecuencia de corte con la intensidad, ya que es bien sabido que este parámetro da idea del mecanismo de HHG para átomos, moléculas y sólidos de *gap* finito. También deben tenerse en cuenta los posibles cambios ultrarrápidos de la polarización de los armónicos.

- Establecer conclusiones sobre el mecanismo de generación de armónicos de orden elevado en el grafeno y compararlo con el de otros sistemas físicos.

- Ampliar la metodología mencionada anteriormente a nanotubos de carbono de diferente tamaño y quiralidad, con el fin de estudiar el rendimiento espectral y sacar conclusiones sobre el mecanismo de HHG en estas estructuras 1D.

Para tales efectos, este informe se organiza de la siguiente manera. En el capítulo 2 presentamos los conceptos fundamentales. Este capítulo incluye una descripción completa de las propiedades electrónicas del grafeno y de los nanotubos de carbono, y la derivación del hamiltoniano que describe la interacción entre la luz y la materia. También se abordan los aspectos más relevantes de la generación de armónicos de orden elevado en gases y sólidos de *gap* finito. El capítulo 3 explora la HHG en el grafeno. Primero derivamos e integramos las ecuaciones que rigen la dinámica de la población en las bandas

de conducción y valencia durante la interacción con pulsos láser intensos. Después calculamos el dipolo de emisión y el rendimiento espectral para diversos parámetros del pulso incidente. Además, estudiamos detalladamemte las características específicas de los espectros, tales como el *plateau* de armónicos, el escalado de la frecuencia de corte, la elipticidad de los armónicos y algunos cambios ultrarrápidos de su estado de polarización. Mediante un análisis de punto de silla, desarrollamos un modelo para la HHG en el grafeno, que brinda una nueva perspectiva para el mecanismo de emisión de armónicos de orden elevado en este material 2D, poniendo en primer plano las características geométricas únicas de su estructura electrónica de bandas. A continuación, el capítulo 4 está dedicado al estudio de la HHG en nanotubos de carbono. Basándonos en los métodos desarrollados previamente para el grafeno, estudiamos el rendimiento espectral de estas estructuras 1D, demostrando que la HHG depende en gran medida de la geometría de las bandas electrónicas y que, por tanto, puede ajustarse mediante el control de sus parámetros estructurales. Finalmente, el capítulo 5 resume los principales hallazgos y perspectivas de trabajo futuro en este campo de investigación.

2

FUNDAMENTALS

This chapter is aimed to provide a thorough description of the fundamentals of the present work. As we discussed earlier in chapter 1, high order harmonic generation is a non-linear process resulting from the interaction of intense electromagnetic fields with matter. The optical response of any physical system depends strongly on its electronic band structure. Therefore, the accurate characterization of such band structure is of paramount importance to any further development. For this reason, we first devote sections 2.1 and 2.2 to describe the remarkable electronic structure of graphene and carbon nanotubes, respectively. Using the well-known tight-binding approximation, we derive the unperturbed Hamiltonian that governs the dynamics of the Bloch electrons in such low dimensional carbon allotropes. Next, in section 2.3, we derive the Hamiltonian that accounts for the interaction of matter with intense laser fields. Finally, in section 2.4 we include some introductory material on HHG in gases and finite gap solids, needed as a benchmark for the results of our study. These contents, although presented in brief and general fashion, are required foundations to understand the achievements of this PhD thesis.

2.1 ELECTRONIC PROPERTIES OF GRAPHENE

Carbon is one of the most abundant elements in the universe and is present in all known forms of life. Its extraordinary hability to create compounds with a wide variety of atoms, using different types of bonds, makes it a very appealing subject of scientific and technological study. Carbon can present itself in form of allotropes whose physical properties vary widely, depending on the geometrical arrangement of the atoms and the type of bonds amongst them. For example, while graphite is opaque and soft enough as to be used in pencils, diamond is highly transparent and the hardest mineral ever found in Nature.

The electronic configuration of the carbon atom in its ground state is $1s^2 2s^2 2p^2$. It has two core electrons $1s$, which are not available for chemical bonding, and four valence electrons $2s$ and $2p$. Although carbon should normally form two bonds in its ground state from the two unpaired $2p$ electrons, it tends to maximize the number of bonds through a process called *hybridization*, since chemical bonding induces an effective decrease of the system energy. Thus, a $2s$ electron partially occupies an empty $2p$ orbital, leading to the formation of hybrid orbitals which are able to form up to four bonds.

One possible hybridization scheme consists in mixing the four valence orbitals, creating four sp^3 orbitals, each filled with one electron, as in diamond or methane (CH_4), see Fig. 2.1(a). These four hybrid orbitals optimize their position in space, minimizing repulsion, with a tetrahedral arrangement of σ bonds at angles of 109.5°. In another possible hybridization scheme, three valence orbitals are mixed (one 2*s* orbital + two 2*p* orbitals), forming three sp^2 orbitals. The sp^2 hybrid orbitals will then arrange themselves, creating a trigonal planar geometry of σ bonds separated by angles of 120°. The remaining *p*-type orbital will not mix and will remain perpendicular to this plane, creating π bonds with the neighboring carbon atoms. Ethylene (C_2H_4), shown in Fig. 2.1(b), as well as aromatic molecules like benzene (C_6H_6), or three-dimensional crystals like graphite are typical examples of sp^2 hybridization. Yet there is another possible hybridization scheme, that consists in mixing two atomic orbitals among the four (one 2*s* orbital + one 2*p* orbital), leading to the formation of two *sp* hybrid orbitals. The geometry which results is linear with an angle between the *sp* orbitals of 180°, as for example in acetylene, see Fig. 2.1(c). The two remaining *p*-type orbitals which are not mixed are perpendicular to each other. In such a configuration, the two *sp* hybrid orbitals will form σ bonds with the two nearest neighbors and the overlap of the two unmixed pure *p* orbitals will form π bonds between the carbon atoms, accounting for a carbon–carbon triple bond.

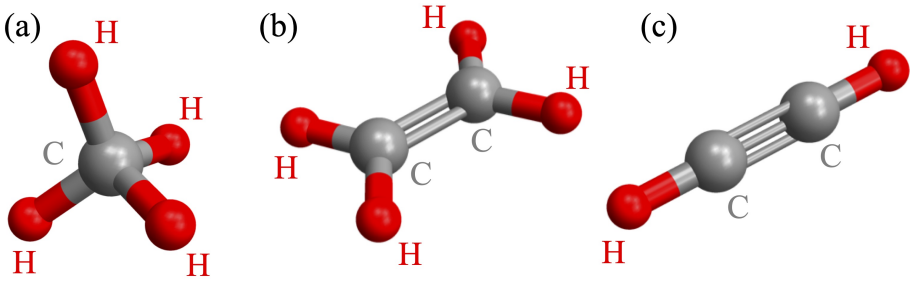

Figure 2.1: Carbon hybridization schemes. (a) The four σ bonds of methane (CH_4), generated from sp^3 hybrid orbitals. (b) Molecule of ethylene (C_2H_4), as an example of sp^2 hybridization with a carbon–carbon double bond, formed by one σ and one π hybrid orbitals. (c) Acethetylene (H–C≡C–H), as an example of molecule within the *sp* hybridization scheme. It displays two σ bonds and one carbon–carbon triple bond, which are generated from one σ and two π orbitals.

Single layer graphene, commonly known as graphene or monolayer graphite in the early works, is also a member of the family of carbon allotropes with sp^2 hybridization. It is composed of carbon atoms periodically arranged in an infinite 2D honeycomb lattice, shown in Fig. 2.2. As discussed above, the atomic structure is defined by two types of bonds. If *z* is the direction perpendicular to the graphene sheet,

the three in-plane C orbitals $2s$, $2p_x$ and $2p_y$ combine to form σ (bonding) and σ* (antibonding) orbitals which are even under reflections in the graphene plane. These hybrid orbitals form strong covalent bonds with the neighboring atoms. The out of plane $2p_z$ orbitals are odd with respect to the planar symmetry and decoupled from the σ states, which allows to treat them independently. They overlap with neighboring $2p_z$ states producing π and π* bands. The gap energy between the σ and σ* bands is large (~ 12 eV), so their contribution to the electronic properties is usually neglected [69]. The two remaining π and π* orbitals form the valence and conduction bands.

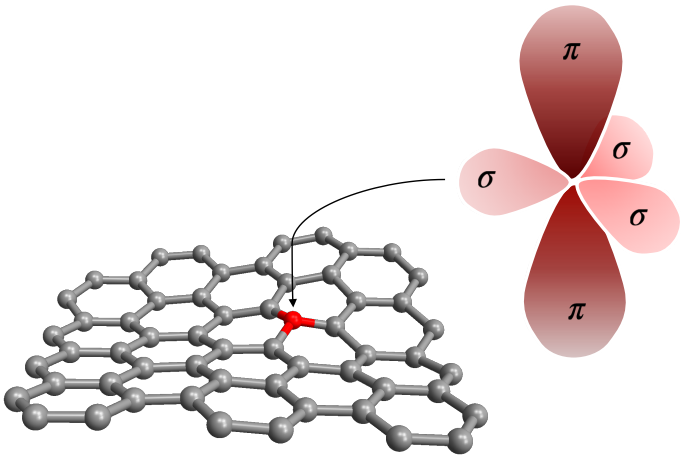

Figure 2.2: Scheme of the graphene arrangement and the hybrid orbitals: three in-plane σ orbitals and one π orbital, perpendicular to the graphene sheet.

2.1.1 *Structure and symmetries of the graphene lattice*

Figure 2.3 shows the triangular Bravais lattice of graphene with two atoms per unit cell, denoted as A (red circles) and B (blue circles) respectively, and constant $a = 2.46$ Å. The primitive vectors are $\mathbf{a}_1 = a(\sqrt{3}/2, 1/2)$ and $\mathbf{a}_2 = a(\sqrt{3}/2, -1/2)$. Note that the nearest neighbors to atom A (B) belong to sublattice B (A) and thus, the distance between any atom and its nearest neighbors is the carbon–carbon distance $a_{cc} = a/\sqrt{3}$.

Besides the translation symmetry stemming from the infinite periodic arrangement of carbon atoms, the graphene's 2D honeycomb lattice has twelve point symmetry operations, namely, six rotations by angles of $2\pi/n$, where $n = 1, ..., 6$, and six reflections, including three mirror planes bisecting the opposite sides of any hexagon and three mirror planes connecting opposite vertices. Therefore, graphene has a perpendicular six-fold rotational axis plus six in-plane two-fold axes and, in addition, it has a mirror plane. These symmetry elements form the point group of graphene, which is the dihedral group $\mathbf{D}_{6h}$.

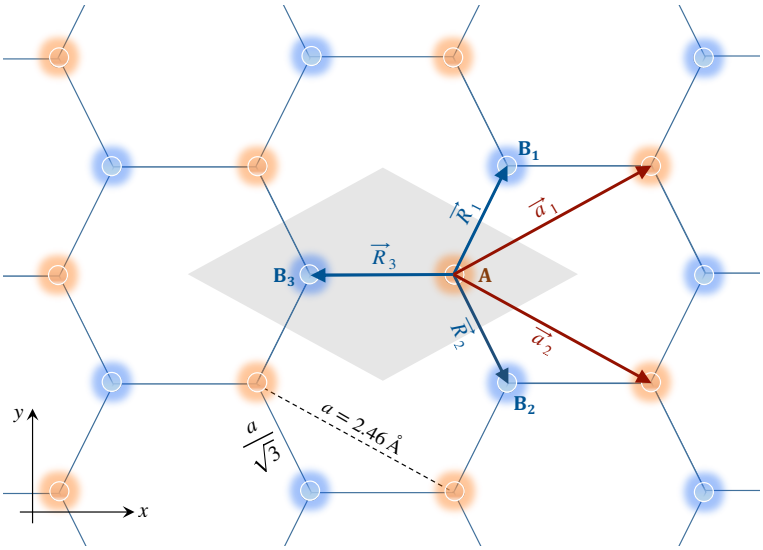

Figure 2.3: Hexagonal network of graphene with basis vectors $\mathbf{a}_1$ and $\mathbf{a}_2$. The grey-filled area in the background shows the primitive cell. Vectors $\mathbf{R}_j$ ($j = 1, 2, 3$) pointing to the location between nearest neighbors are also shown.

The point symmetry operations along with the translational symmetry form the space group of graphene, which is denoted as $\mathbf{P}6/mmm$ in Hermann-Mauguin notation [70].

The reciprocal lattice associated to the graphene's Bravais lattice is a hexagonal lattice rotated 90° with respect to the direct lattice, as shown in Figure 2.4. Therefore, the symmetry elements of the direct and reciprocal lattice are identical. The reciprocal basis vectors are $\mathbf{b}_1 = b(1/2, \sqrt{3}/2)$ and $\mathbf{b}_2 = b(1/2, -\sqrt{3}/2)$, where $b = 4\pi/\sqrt{3}a$. The first Brillouin zone is a hexagon and the six vertices can be grouped in two sets of inequivalent points (K and K'), since they are not related by any reciprocal lattice vector.

In general, any operation of the point group of graphene on the Brillouin zone other than the identity transforms a certain wave vector $\mathbf{k}$ into a distinct one. However, for certain values of $\mathbf{k}$, some of the operations of the symmetry group will leave $\mathbf{k}$ invariant. These particular operations form the group of the wave vector, which is a subgroup of the full symmetry group of the lattice. Lines in the BZ for which the group of $\mathbf{k}$ contains elements other than the identity are called *symmetry lines*. Besides, at certain points of the BZ the group of the wave vector may be larger than that of the symmetry lines. These points are called *symmetry points*.

The symmetry points in graphene are the BZ center Γ, points K and K', and points M, located at the middle of the hexagon's edges. The

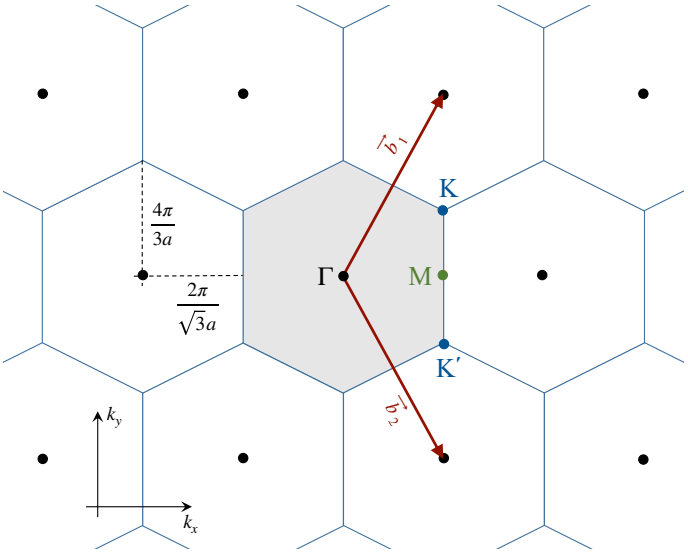

Figure 2.4: Reciprocal lattice of the graphene's Bravais lattice with basis vectors $\mathbf{b}_1$ and $\mathbf{b}_2$. The grey-filled area is the first Brillouin zone. The high symmetry points Γ (zone center), M and the two inequivalent corners K and K′ are also shown.

symmetry lines are Γ–K, Γ–M and K–M. The symmetry points can be written as:

$$\Gamma = (0,0); \qquad \mathrm{M} = \frac{2\pi}{\sqrt{3}a}(1,0);$$
$$\mathrm{K} = \frac{4\pi}{3a}\left(\frac{\sqrt{3}}{2}, \frac{1}{2}\right); \qquad \mathrm{K}' = \frac{4\pi}{3a}\left(\frac{\sqrt{3}}{2}, -\frac{1}{2}\right). \tag{2.1}$$

Note that any wave vector $\mathbf{k}$ of the Brillouin zone transforms under the symmetry operations according to the irreducible representation of the group at a given symmetry point. Such transformations are called the *small group* of $\mathbf{k}$ at the symmetry point. For example, the small group of $\mathbf{k}$ at point Γ is $\mathbf{D}_{6h}$, but it becomes $\mathbf{D}_{3h}$ at points K and K′, or $\mathbf{C}_{2v}$ at lines Γ–K. The electronic states of graphene at a given symmetry point can be therefore classified according to the corresponding representation of the group of the wave vector at that point. As $\mathbf{k}$ moves away from the symmetry point, the group of $\mathbf{k}$ becomes smaller and some of the degeneracies split. A detailed study on the symmetry classification of the electronic states of graphene from the point of view of the group theory can be found in [70–73].

2.1.2 *Tight-binding description of graphene*

Once we have described the atomic structure and symmetries of the graphene lattice, in this section we proceed to the calculation of the π-bands of graphene using the tight binding approximation, as first

done by Wallace in his seminal paper (1947) to describe the band theory of graphite [2]. Provided that the interaction between neighboring $2p_z$ electrons is weak, the orbitals can be regarded as atomic orbitals slightly modified by the periodic potential of graphene. Therefore, we can assume that the electrons are *tightly bound* to the atoms of the lattice. This tight-binding description allows to find an analytic solution for the energy of the π bands with a small number of parameters, in good agreement with the results of *ab initio* calculations [74]. Within this model, the Hamiltonian of the full lattice is given by:

$$H_o = \sum_{\mathbf{r}_n} \Big[H_{at}(\mathbf{r} - \mathbf{r}_n) + \Delta U(\mathbf{r} - \mathbf{r}_n) \Big], \tag{2.2}$$

where the sum is extended to the whole set of atomic sites $\mathbf{r}_n$, and ΔU includes small corrections to the atomic Hamiltonian H_{at} due to the interaction with neighboring ions and electrons. Taking into account that the overlap amongst the $2p_z$ orbitals and the rest of valence orbitals in each atom is zero, the A (or B) atom is uniquely defined by one orbital per atom site $\varphi_z(\mathbf{r} - \mathbf{r}_A)$, or $\varphi_z(\mathbf{r} - \mathbf{r}_B)$, that represents the carbon's $2p_z$ orbital in the periodic structure of graphene and therefore, is the eigenstate of the perturbed atomic Halmitonian $H_{at} + \Delta U$.

According to the Bloch's theorem [75], the eigenfunctions evaluated at two points $\mathbf{R}_i$ and $\mathbf{R}_j$ of the graphene's Bravais lattice only differ in a phase factor $\exp\big[i\,\mathbf{k}\cdot(\mathbf{R}_i - \mathbf{R}_j)\big]$. Consequently, the eigenstates of the Bloch electrons belonging to lattices A and B are given by:

Bloch's theorem: The eigenstates of the one-electron periodic Hamiltonian in a Bravais lattice can be chosen to have the form of a plane wave times a function with the periodicity of the Bravais lattice.

$$\phi_A(\mathbf{k}, \mathbf{r}) = \frac{1}{\sqrt{N}} \sum_{\mathbf{R}_A} e^{i\,\mathbf{k}\cdot\mathbf{R}_A} \varphi_z(\mathbf{r} - \mathbf{R}_A) = e^{i\,\mathbf{k}\cdot\mathbf{r}}\, u_A^{\mathbf{k}}(\mathbf{r}), \tag{2.3}$$

$$\phi_B(\mathbf{k}, \mathbf{r}) = \frac{1}{\sqrt{N}} \sum_{\mathbf{R}_B} e^{i\,\mathbf{k}\cdot\mathbf{R}_B} \varphi_z(\mathbf{r} - \mathbf{R}_B) = e^{i\,\mathbf{k}\cdot\mathbf{r}}\, u_B^{\mathbf{k}}(\mathbf{r}), \tag{2.4}$$

where $u_A^{\mathbf{k}}(\mathbf{r})$ and $u_B^{\mathbf{k}}(\mathbf{r})$ are periodic functions in the sublattices A and B, respectively, N is the number of unit cells in the graphene sheet, and $\mathbf{R}_A$ ($\mathbf{R}_B$) are lattice vectors connecting atomic sites of sublattice A (B). The sums in Eqs. (2.3) and (2.4) run over all the possible lattice vectors, i. e. all the atoms in sublattices A and B, respectively. Therefore, the eigenstates $|\psi_{\mathbf{k}}\rangle$ of the full Hamiltonian H_o are linear combinations of the Bloch states of each sublattice:

$$|\psi_{\mathbf{k}}\rangle = c_A(\mathbf{k})\,|\phi_A\rangle + c_B(\mathbf{k})\,|\phi_B\rangle\,. \tag{2.5}$$

For the sake of simplicity, in the following we only specify the dependence of the kets $|\phi_{A/B}\rangle$ and the coefficients $c_{A/B}$ on $\mathbf{k}$ when deemed necessary. Otherwise such dependence is implicitly understood.

To derive the electronic structure of the π-bands we have to solve the Schrödinger equation:

$$H_o\,|\psi_{\mathbf{k}}\rangle = E(\mathbf{k})\,|\psi_{\mathbf{k}}\rangle\,, \tag{2.6}$$

where $E(\mathbf{k})$ are the eigenvalues at a given $\mathbf{k}$ which constitute the electronic bands. Note that H_o has the whole symmetry of the graphene lattice and thus, the group of the Schrödinger equation (2.6) is the full space group of graphene. While in atoms or molecules the eigenvalues of the Schrödinger equation are well separated, for condensed matter systems such as graphene they form a continuous manifold whose topology is isomorphic to the representation of the full space group [76].

Multiplying both sides of Eq. (2.6) by $\langle\phi_A|$ and substituting $|\Psi_\mathbf{k}\rangle$ by the linear combination of Bloch states in Eq. (2.5), we obtain:

$$c_A \langle\phi_A|H_o|\phi_A\rangle + c_B \langle\phi_A|H_o|\phi_B\rangle = c_A E \langle\phi_A|\phi_A\rangle + c_B E \langle\phi_A|\phi_B\rangle . \tag{2.7}$$

A similar condition is obtained multiplying by $\langle\phi_B|$:

$$c_A \langle\phi_B|H_o|\phi_A\rangle + c_B \langle\phi_B|H_o|\phi_B\rangle = c_A E \langle\phi_B|\phi_A\rangle + c_B E \langle\phi_B|\phi_B\rangle . \tag{2.8}$$

Conditions (2.7) and (2.8) include both interaction $H_{ij} \equiv \langle\phi_i|H_o|\phi_j\rangle$ and overlapping integrals $S_{ij} \equiv \langle\phi_i|\phi_j\rangle$, with $i,j = A,B$. They can be expressed in matrix form as:

$$\begin{pmatrix} H_{AA} & H_{AB} \\ H_{BA} & H_{BB} \end{pmatrix} \begin{pmatrix} c_A \\ c_B \end{pmatrix} = E \begin{pmatrix} S_{AA} & S_{AB} \\ S_{BA} & S_{BB} \end{pmatrix} \begin{pmatrix} c_A \\ c_B \end{pmatrix}, \tag{2.9}$$

or, in the more compact form:

$$H_o \Psi = E S \Psi. \tag{2.10}$$

This equation has non trivial solutions if:

$$|H_o - E S| = 0, \tag{2.11}$$

which is the general form of the well-known secular equation of the π-orbitals of graphene [2]. Note that Eq. (2.11) is general in the sense that it has been obtained without making any further approximation to the tight-binding model. After some manipulation, we obtain:

$$E_\pm = \frac{1}{2E_3}\left\{2E_0 - E_1 \pm \left[(E_1 - 2E_0)^2 - 4E_2E_3\right]^{1/2}\right\}, \tag{2.12}$$

where:

$$\begin{aligned} E_0 &= H_{AA}S_{AA} & E_1 &= H_{AB}S^*_{AB} + H^*_{AB}S_{AB} \\ E_2 &= H^2_{AA} - H_{AB}H^*_{AB} & E_3 &= S^2_{AA} - S_{AB}S^*_{AB} \end{aligned} \tag{2.13}$$

and $E_\pm$ represents the eigenvalues of the conduction and valence bands, respectively.

2.1.3 *Electronic π and π* bands*

To calculate the interaction H_{ij} and overlapping S_{ij} integrals ($i, j = A, B$), we make use of the nearest neighbors approximation. Note that this approximation can be refined by including more neighbors to the calculations, but its simplest form gives reasonably good results at the vicinity of the high symmetry points K and K′ [74]. Let us then consider integrals of the form:

$$H_{AA} = \frac{1}{N} \sum_{\mathbf{R}'_A} \sum_{\mathbf{R}_A} e^{i\,\mathbf{k}\cdot(\mathbf{R}_A - \mathbf{R}'_A)} \langle \varphi_z(\mathbf{r} - \mathbf{R}'_A) | H_o | \varphi_z(\mathbf{r} - \mathbf{R}_A) \rangle \,. \tag{2.14}$$

Since the three neighboring atoms to any atom in sublattice A belong to sublattice B, see Fig. 2.3, the sum over $\mathbf{R}'_A$ has only one non-vanishing term at $\mathbf{R}'_A = \mathbf{R}_A$, so that:

$$H_{AA} = \frac{1}{N} \sum_{\mathbf{R}_A} \langle \varphi_z(\mathbf{r} - \mathbf{R}_A) | H_o | \varphi_z(\mathbf{r} - \mathbf{R}_A) \rangle = \langle \varphi_z(\mathbf{r} - \mathbf{R}_A) | H_o | \varphi_z(\mathbf{r} - \mathbf{R}_A) \rangle \,. \tag{2.15}$$

This term represents the average energy of the orbital $2p_z$ in the periodic potential of the graphene lattice and is independent of the wavevector $\mathbf{k}$. Its value $\varepsilon_{2p} = 0.28$ eV can be computed from the Hamiltonian and the atomic orbitals, or fitted by comparing the band structure to experimental or *ab-initio* results [74]. On the other hand, as atoms A and B are chemically identical, we have $H_{BB} = \varepsilon_{2p}$.

Let us now calculate the integrals:

$$\begin{aligned} H_{AB}(\mathbf{k}) = \frac{1}{N} \sum_{\mathbf{R}_A} \sum_{\mathbf{R}_B} e^{i\,\mathbf{k}\cdot(\mathbf{R}_B - \mathbf{R}_A)} \langle \varphi_z(\mathbf{r} - \mathbf{R}_A) | H_o | \varphi_z(\mathbf{r} - \mathbf{R}_B) \rangle = \\ \sum_{j=1}^{3} e^{i\,\mathbf{k}\cdot(\mathbf{R}_{B_j} - \mathbf{R}_A)} \langle \varphi_z(\mathbf{r} - \mathbf{R}_A) | H_o | \varphi_z(\mathbf{r} - \mathbf{R}_{B_j}) \rangle = \\ \sum_{j=1}^{3} e^{i\,\mathbf{k}\cdot\mathbf{R}_j} \langle \varphi_z(\mathbf{r} - \mathbf{R}_A) | H_o | \varphi_z(\mathbf{r} - \mathbf{R}_{B_j}) \rangle \,, \end{aligned} \tag{2.16}$$

where $\mathbf{R}_j = \mathbf{R}_{B_j} - \mathbf{R}_A$, being B_j the nearest neighbors to atom A. Note that the atomic orbitals φ_z are radially symmetric on the graphene plane and the integrals only depend on the distances $|\mathbf{R}_j|$, that are the same for the three nearest neighbors, see Fig. 2.3. This allows us to introduce the parameter:

Tight-binding integral

$$\gamma_0 = \langle \varphi_z(\mathbf{r} - \mathbf{R}_A) | H_0 | \varphi_z(\mathbf{r} - \mathbf{R}_B) \rangle \,, \tag{2.17}$$

which represents the average interaction energy between two neighboring carbon atoms (−2.97 eV) and is often known as the *tight-*

binding integral of graphene [74]. Thus, defining the complex form factor:

$$\begin{aligned} f(\mathbf{k}) &= e^{-\frac{i}{3}\mathbf{k}\cdot(\mathbf{a}_1+\mathbf{a}_2)}\left(e^{i\mathbf{k}\cdot\mathbf{a}_1}+e^{i\mathbf{k}\cdot\mathbf{a}_2}+1\right) \\ &= e^{-iak_x/\sqrt{3}}\left[1+2e^{\mathrm{i}\sqrt{3}ak_x/2}\cos\left(\frac{ak_y}{2}\right)\right], \end{aligned} \tag{2.18}$$

and taking into account that:

$$\begin{aligned} \mathbf{R}_1 = \frac{1}{3}(2\mathbf{a}_1-\mathbf{a}_2), \qquad \mathbf{R}_2 = \frac{1}{3}(-\mathbf{a}_1+2\mathbf{a}_2), \\ \mathbf{R}_3 = \frac{1}{3}(-\mathbf{a}_1-\mathbf{a}_2); \end{aligned} \tag{2.19}$$

we can write:

$$H_{AB}(\mathbf{k}) = \gamma_0 f(\mathbf{k}). \tag{2.20}$$

Similarly, it is easily found that $H_{BA} = H^*_{AB}$.

The integrals $\langle\phi_i|\phi_j\rangle$ $i,j = A,B$ can be calculated likewise assuming that the overlap between neighboring atoms belonging to the same lattice is zero and they are normalized, i. e. $\langle\varphi_z(\mathbf{r}-\mathbf{R}_A)|\varphi_z(\mathbf{r}-\mathbf{R}_B)\rangle = \delta_{AB}$. Therefore, we have:

$$\begin{aligned} S_{AA} \equiv \langle\phi_A|\phi_A\rangle = \\ \frac{1}{N}\sum_{\mathbf{R}'_A}\sum_{\mathbf{R}_A} e^{i\mathbf{k}\cdot(\mathbf{R}_A-\mathbf{R}'_A)}\,\langle\varphi_z(\mathbf{r}-\mathbf{R}'_A)|\varphi_z(\mathbf{r}-\mathbf{R}_A)\rangle = 1 \end{aligned} \tag{2.21}$$

and accordingly, $S_{BB} = 1$. As for the other integral, we have:

$$\begin{aligned} S_{AB}(\mathbf{k}) \equiv \langle\phi_A|\phi_B\rangle = \\ \frac{1}{N}\sum_{\mathbf{R}_A}\sum_{\mathbf{R}_B} e^{i\mathbf{k}\cdot(\mathbf{R}_B-\mathbf{R}_A)}\,\langle\varphi_z(\mathbf{r}-\mathbf{R}_A)|\varphi_z(\mathbf{r}-\mathbf{R}_B)\rangle = \\ \sum_{j=1}^{3} e^{i\mathbf{k}\cdot\mathbf{R}_j}\,\langle\varphi_z(\mathbf{r}-\mathbf{R}_A)|\,H_o\,|\varphi_z(\mathbf{r}-\mathbf{R}_{B_j})\rangle\,, \end{aligned} \tag{2.22}$$

which only depends on the distances $|\mathbf{R}_j|$. Introducing the *overlapping integral*, that represents the coupling between nearest neighboring orbitals:

Overlapping integral

$$s_0 = \langle\varphi_z(\mathbf{r}-\mathbf{R}_A)|\varphi_z(\mathbf{r}-\mathbf{R}_B)\rangle\,, \tag{2.23}$$

we obtain:

$$S_{AB}(\mathbf{k}) = s_0 f(\mathbf{k}), \tag{2.24}$$

and then, $S_{BA}(\mathbf{k}) = s_0 f^*(\mathbf{k})$. Therefore, we can write:

$$S(\mathbf{k}) = \begin{pmatrix} 1 & s_0 f(\mathbf{k}) \\ s_0 f^*(\mathbf{k}) & 1 \end{pmatrix} \tag{2.25}$$

Tight-binding Hamiltonian of SLG

and

$$H_o(\mathbf{k}) = \begin{pmatrix} \varepsilon_{2p} & \gamma_0 f(\mathbf{k}) \\ \gamma_0 f^*(\mathbf{k}) & \varepsilon_{2p} \end{pmatrix}, \tag{2.26}$$

which is the well-known tight-binding Hamiltonian of SLG within the nearest neighbors approximation. As we shall see later, this 2×2 matrix can be written in terms of Pauli matrices thus emphasizing the analogy with a spin Hamiltonian [69].

Constraining the parameters (2.13) to the nearest neighbors approximation, we obtain:

$$\begin{aligned} E_0 &= \varepsilon_{2p} & E_1(\mathbf{k}) &= 2\gamma_0 s_0 |f(\mathbf{k})|^2 \\ E_2(\mathbf{k}) &= \varepsilon_{2p}^2 - \gamma_0^2 |f(\mathbf{k})|^2 & E_3(\mathbf{k}) &= 1 - s_0^2 |f(\mathbf{k})|^2 \end{aligned} \tag{2.27}$$

where:

$$|f(\mathbf{k})| = \sqrt{1 + 4\cos\frac{\sqrt{3}ak_x}{2}\cos\frac{ak_y}{2} + 4\cos^2\frac{ak_y}{2}}, \tag{2.28}$$

being k_x and k_y the coordinates of $\mathbf{k}$ in the reciprocal space. Therefore, we have:

$$E_\pm(\mathbf{k}) = \frac{\varepsilon_{2p} \mp \gamma_0 |f(\mathbf{k})|}{1 \mp s_0 |f(\mathbf{k})|}. \tag{2.29}$$

Dispersion law

Since the overlap between wave functions centered in different atoms is small ($s_0 = 0.073$) [74], we can further approximate $s_0 \simeq 0$ and thus:

$$E_\pm(\mathbf{k}) = \varepsilon_{2p} \mp \gamma_0 |f(\mathbf{k})|, \tag{2.30}$$

which is the solution found by Wallace [2]. At the symmetry points K and K′ of the Brillouin zone, see Fig. 2.4, $f(\mathrm{K}) = f(\mathrm{K}') = 0$ and accordingly, the electronic bands are locally degenerated with energy ε_{2p}. Furthermore, as the $2p_z$ orbital is occupied by a single electron, the $(-)$ band in equation (2.30) is fully ocuppied, while the $(+)$ branch is empty. Thus, the Fermi level $E_\mathrm{F} = \varepsilon_{2p}$ and the Fermi surface is composed by the discrete set of K and K′ points, i. e. it has dimension zero. For this reason, graphene is usually referred as *semi-metal* or *zero-gap semiconductor* [69]. Choosing the Fermi level as the energy reference, the dispersion law (2.30) reads:

$$E_\pm(\mathbf{k}) = \mp\gamma_0 |f(\mathbf{k})|, \tag{2.31}$$

which allows to write the tight-binding Hamiltonian (2.26) in the simpler form:

$$H_o(\mathbf{k}) = \begin{pmatrix} 0 & \gamma_0 f(\mathbf{k}) \\ \gamma_0 f^*(\mathbf{k}) & 0 \end{pmatrix}. \tag{2.32}$$

Eigenstates of the π-orbitals

The eigenstates of H_o expressed in the basis $\{u_A^{\mathbf{k}}, u_B^{\mathbf{k}}\}$ are:

$$|\Phi_{\mathbf{k}}^{\pm}\rangle = \frac{e^{i\,\mathbf{k}\cdot\mathbf{r}}}{\sqrt{2}} \begin{pmatrix} \mp 1 \\ e^{-i\,\varphi_{\mathbf{k}}} \end{pmatrix}, \tag{2.33}$$

where $\varphi_{\mathbf{k}}$ is the phase of the complex function $f(\mathbf{k})$. Note that $\Phi_{\mathbf{k}}^{-}$ stands for the symmetric (bonding) combination of Bloch functions (valence band, π) and $\Phi_{\mathbf{k}}^{+}$ denotes the anti-symmetric or anti-bonding combination of Bloch states (conduction band, π^*).

Therefore, the wave function of the Bloch electron in Eq. (2.5) can be written in terms of the eigenstates (2.33) as:

$$|\psi_{\mathbf{k}}\rangle = C_-(\mathbf{k})\,|\Phi_{\mathbf{k}}^{-}\rangle + C_+(\mathbf{k})\,|\Phi_{\mathbf{k}}^{+}\rangle\,, \tag{2.34}$$

where the coefficients $C_\pm$ are normalized. The nearest-neighbor tight-biding description of graphene thereby leads to π and π^* energy bands which are symmetric with respect to the Fermi level. The energy E_- of the bonding π estates is negative, while the anti-bonding (π^*) states show positive values E_+. Figure 2.5 shows the dispersion law (2.31) along two different paths in the first Brillouin zone. Although the overall shape of the graphene band structure is quite satisfactorily described by the tight-binding model, the quantitative agreement with *ab initio* calculations is poor at the center of the Brillouin zone, see Fig. 2.6. Remarkably, values resulting from Eq. (2.31) at the vicinity of K and K′ are in good quantitative agreement with the *ab initio* results. Note that the optical properties of graphene, as well as the excitation mechanism for high-order harmonic generation is dominated by these regions near the valleys [1].

The dependence of H_o with the number of neighbors included in the calculation has been systematically studied by Reich *et al*. by including additional interaction energies γ_1 and γ_2 for the second and third nearest neighbors [77]. The method to construct the Hamiltonian is analogous to the one shown in this section, with new terms contributing to the calculation of the interaction integrals $\langle\phi_i|H_o|\phi_j\rangle$. Although the inclusion of new interaction terms with more distant neighbors qualitatively improves the tight-binding picture in the entire Brillouin zone, it does not substantially improve the first neighbors model at the vicinity of the K and K′ points.

Figure 2.7 depicts the 2D energy manifold at the first Brillouin zone of graphene stemming from the tight-binding model in the nearest-neighbors approximation, as given by Eq. (2.31). The figure is centered at the symmetry point Γ to highlight the isomorphism between the topology of the energy manifold and that of the 2D representation of the full space group of graphene, as discussed above in section 2.1.2. For any wave vector $\mathbf{k}$ at the BZ, the energy manifold has

1 Symmetry points K and K′ are often referred to as *valleys* in the literature because of the singular valley-like energy dispersion at their vicinity.

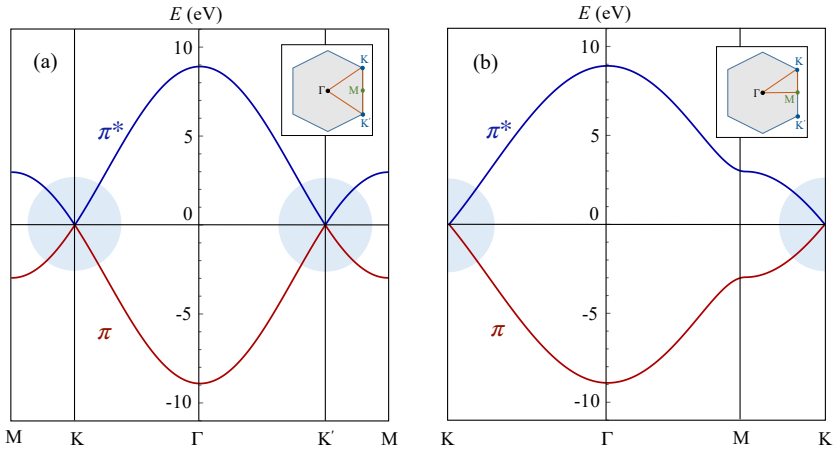

Figure 2.5: Nearest-neighbor tight-binding band structure of single layer graphene according to Eq. (2.31) along two different paths in the first Brillouin Zone: (a) M–K–Γ–K′–M and (b) K–Γ–M–K, see the insets in both panels. The solid blue (red) line is the π^* (π) band. In both panels s_0 and E_F are set to zero, and $\gamma_0 = -2.97$ eV. The light-blue circles in the background highlight the dispersion at the valleys, where the bands are degenerated.

two branches, corresponding to the valence and conduction bands. Within each branch, $E(\mathbf{k}) = E(\mathbf{k}')$ if $\mathbf{k}$ and $\mathbf{k}'$ are related by any of the elements of the dihedral group $\mathbf{D}_{6h}$. Finally, as a consequence of the translation symmetry, the pattern of the Brillouin zone is periodically repeated in the rest of the reciprocal space.

2.1.4 *Low energy excitations*

In this section we shall consider the properties of the graphene's band structure at the vicinity of the valleys. To keep a compact notation in what follows, we assume that $\mathbf{k} = (k_x, k_y)$ defines the location of the points in the reciprocal space relative to the corresponding valley, K or K′. Expanding $f(\mathbf{k})$ in Eq. (2.18) to the first order in $\mathbf{k}$, we obtain a linear approximation of the dispersion law close to those points [69]:

Linear dispersion law near points K and K′

$$E_{\pm}(\mathbf{k}) \simeq \pm\hbar v_F |\mathbf{k}|, \tag{2.35}$$

where v_F is the electronic group velocity:

$$v_F = \frac{|\gamma_0|}{\hbar}\frac{a\sqrt{3}}{2}. \tag{2.36}$$

Therefore, the dispersion is linear at the vicinity of the valleys with group velocity $v_F \simeq c/300$ and only depends on the $\mathbf{k}$-shift. The constant energy contours at the valleys are thereby circumferences of radius $|\mathbf{k}|$ and the band structure is cone-shaped, as illustrated in Fig. 2.7. This low-energy band structure extends over an energy range $\gtrsim 1$ eV [78].

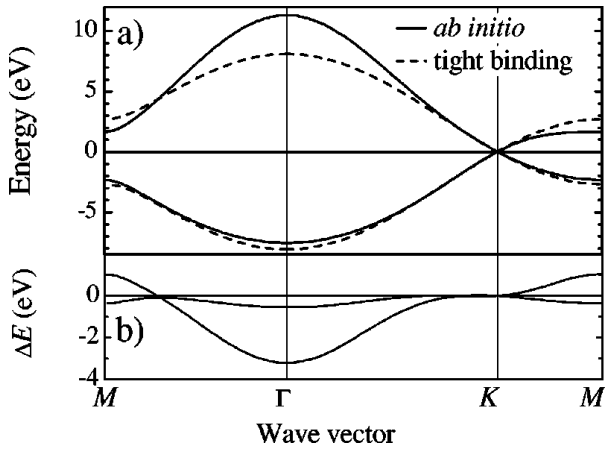

Figure 2.6: *Ab initio* and nearest-neighbor tight-binding dispersion of graphene. (a) The converged *ab initio* calculation π and π^* of graphene bands is shown by the full lines. The dashed lines represent the tight-binding dispersion of Eq. (2.31) with $\gamma_0 = -2.7$ eV. (b) Difference ΔE between the *ab initio* and tight-binding band structures (extracted from Reich *et al.* [77]).

Note that near K′ the Halmitonian H_o can be written as:

$$H_{o,K'} = \hbar v_F \begin{pmatrix} 0 & k_x - i\,k_y \\ k_x + i\,k_y & 0 \end{pmatrix}, \tag{2.37}$$

or in the more compact form [79]:

$$H_{o,K'} = v_F(\hat{\sigma}_x p_x + \hat{\sigma}_y p_y) = v_F\,\hat{\boldsymbol{\sigma}} \cdot \mathbf{p}, \tag{2.38}$$

where $\mathbf{p} = \hbar\mathbf{k}$ is the crystal momentum and $\hat{\boldsymbol{\sigma}} = (\hat{\sigma}_x, \hat{\sigma}_y, \hat{\sigma}_z)$ are the Pauli matrices:

$$\hat{\sigma}_x = \begin{pmatrix} 0 & 1 \\ 1 & 0 \end{pmatrix}, \quad \hat{\sigma}_y = \begin{pmatrix} 0 & -i \\ i & 0 \end{pmatrix}, \quad \hat{\sigma}_z = \begin{pmatrix} 1 & 0 \\ 0 & -1 \end{pmatrix}. \tag{2.39}$$

Likewise, it can be easily seen that at the inequivalent point K we obtain the transposed Halmitonian $H_{o,K} = H^t_{o,K'}$. Therefore, there is an extra degree of freedom related to the valleys, as for the point K the Halmitonian is proportional to $\hat{\boldsymbol{\sigma}}^t$ and involves left handed Pauli matrices, in contrast to the right-handed Pauli matrices operating at K′. This degree of freedom, known as *chirality*, is a reminiscence of the two underlying sublattices which conform the graphene's Bravais lattice, and is often referred in the literature as *pseudospin*, to highlight both the parallelism and differences with the spin.

Let us introduce the helicity (or chirality) operator as:

$$\hat{\mathbf{h}} = \hat{\boldsymbol{\sigma}} \cdot \frac{\mathbf{p}}{|\mathbf{p}|}, \tag{2.40}$$

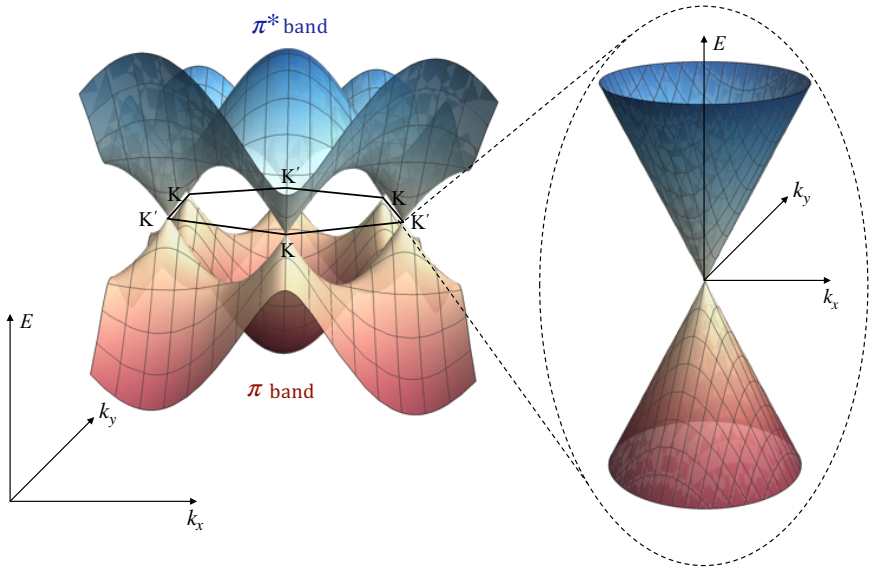

Figure 2.7: Scheme of the graphene's band structure within the nearest neighbors tight-binding approximation. The Fermi level is set to zero. The conduction and valence bands correspond to positive and negative values of the energy, respectively. Dirac points K and K′ are degenerated at the Fermi level. At the vicinity of those Dirac points the energy disperses linearly, configuring the Dirac cones shown in the right.

which represents the projection of the pseudospin operator $\hat{\boldsymbol{\sigma}}$ on the crystal momentum direction. Note that $\hat{\mathbf{h}}$ commutes with the Hamiltonian and the helicity is thereby a well defined quantity with eigenvalues $+1$ at K′ and -1 at K. As a consequence, electrons do not backscatter when crossing through the valleys [69, 80], since a change from $\mathbf{p}$ to $-\mathbf{p}$ would lead to a pseudospin reversion. Backscattering does not occur unless the Hamiltonian is perturbed by a term that flips pseudospin.

The Dirac-Weyl Halmintonian

To take into account pseudospin, we can rewrite the Halmitonian at the valleys as the result of the direct product of both subspaces [78]:

$$H_o = \begin{pmatrix} v_F\, \hat{\boldsymbol{\sigma}}^t \cdot \mathbf{p} & 0 \\ 0 & v_F\, \hat{\boldsymbol{\sigma}} \cdot \mathbf{p} \end{pmatrix} \tag{2.41}$$

where H_o acts now over the four-component spinor:

$$|\Psi\rangle = \begin{pmatrix} |\psi_{\mathrm{K}}\rangle \\ |\psi_{\mathrm{K}'}\rangle \end{pmatrix} \tag{2.42}$$

being $|\psi_{\mathrm{K}}\rangle$ and $|\psi_{\mathrm{K}'}\rangle$ the wave function of the Bloch electron at the vicinity of K and K′, respectively. In condensed matter physics the valleys are referred as *Weyl points* and the associated two-component

spinor, as the *Weyl spinor*. Formally, the term *Dirac point* should rather be used for the four-component spinor, thereby encompassing two Weyl points of opposite chirality at different locations in the reciprocal space [78]. Nevertheless, in the literature, the crossing points of 2D linearly dispersing bands are commonly referred to as Dirac points since the early works on graphene. For this reason, we shall maintain the common usage. The Hamiltonian in Eq. (2.41) is equivalent to the Dirac-Weyl Hamiltonian, which follows from the Dirac equation after setting the rest mass of the particle to zero. Therefore, the low-energy excitations in graphene emulate those of massless Dirac particles of spin 1/2 and are usually known as *massless Dirac fermions* [69, 77], though the group velocity of these quasiparticles is much smaller and the spin refers to the pseudospin.

Equation (2.38) makes explicit two outstanding discrete symmetries of the tight-binding Hamiltonian of graphene that are not directly related to the space group of the lattice. In particular, taking into account the 2D representation of the time-reversal operator $\mathcal{T} = i\,\hat{\sigma}_y K$, being K the complex conjugate operator, it is straightforward to show that $[\mathcal{T}, H_o] = 0$ and therefore, the tight-binding Hamiltonian is time-reversal invariant. On the other hand, a Hamiltonian is said to have electron-hole symmetry if there is a unitary transformation U such that $UH_oU^\dagger = -H_o$ in such a way that the energy spectrum is symmetric with respect to $E = 0$. Then, choosing $U = \hat{\sigma}_z$, is easily seen that H_o fulfills the electron-hole symmetry condition, which implies that for any eigenstate with positive energy E (electron) there is an eigenstate with energy $-E$ (hole). Note that this is not a symmetry of real graphene as it appears as a consequence of the nearest-neighbors tight-binding model, see Fig. 2.6.

The band degeneracy of graphene at the Dirac points is direct consequence of the inversion symmetry of the full space group of the lattice and hence, of the underlying sublattice symmetry, i. e. the possibility to divide the full lattice into two equivalent sublattices, as illustrated in Fig. 2.3. Therefore, the degeneracy at the Dirac points is protected if the sublattice symmetry is preserved. Mathematically, this constraint can be written as the anticommutation relation $\{H_o, \hat{\sigma}_z\} = 0$, which forbids the appearance of terms depending on $\hat{\sigma}_z$ in H_o. These terms are usually referred in the literature as *mass terms* since they produce a gap in the energy spectrum twice the rest mass of the quasiparticle. The $\hat{\sigma}_z$ mass term can be induced in graphene by interaction with certain substrate, or by making the two sublattices occupied by different atoms, as in the family of 2D transition metal dichalcogenides (TMDs), like MoS_2 or WSe_2 [81]. Note that, although the electron-hole and time reversal symmetries of H_o remain unaltered, the strong inversion symmetry breaking leads to a large mass term of the order of 1 eV [78]. Another means to break the inversion symmetry while preserving time reversal is by introducing the spin-

orbit coupling (SOCs) effect in the Hamiltonian H_o [82]. Meanwhile SOC in TMDs can be sizable, with strength of the order of $0.01 \sim 0.1$ eV, the intrinsic SOC term in graphene is negligibly small, due to a very weak atomic SOC strength for carbon and the planar structure, which effectively uncouples the π and σ electronic bands, as discussed above.

Notwithstanding, the tight-binding Hamiltonian developed in section 2.1.3 fully accounts for the remarkable properties of the low-energy excitations at the Dirac points, which, as we see, can be independently addressed using the Dirac formalism. In this sense, we can say that the Schrödinger equation is equivalent to massless Dirac's close to the Dirac points. Note that the tight-binding model accounts for the whole first Brillouin zone of the reciprocal space, thus encompassing the two inequivalent Dirac points. Therefore there is no need to work with the 4×4 Hamiltonian in Eq. 2.41, so the 2×2 matrix in Eq. (2.32) will be used instead.

2.2 ELECTRONIC PROPERTIES OF CARBON NANOTUBES

Single-wall carbon nanotubes, or carbon nanotubes in short, are carbon allotropic forms made from a single graphene layer, rolled up like a hollow cylinder. They have an impressively perfect crystalline structure and diameters up to few nanometers. Since there are infinite ways to roll a sheet as a cylinder, SWNTs display a wide variety of microscopic patterns that determine their electronic band structure and thus, their metallic or semiconducting character. These almost one-dimensional fairly complex configurations, with tens to hundreds of atoms in the unit cell, have well defined symmetries which simplify the understanding of their physical properties.

In this section we address the structural characteristics of SWNTs, paying special attention to their symmetries, which have a strong influence on the geometry of the electronic bands. We then compute the electronic band structure using the zone folding approach, and derive the time-independent Hamiltonian, that will be used in chapter 4 to study the interaction of these nanostructures with intense laser fields.

2.2.1 *Structural properties of carbon nanotubes*

The physical structure of single wall nanotubes can be understood as a rolled graphene strip [69, 74], see Fig. 2.8. The chiral vector $\mathbf{C}_h = n_1\mathbf{a}_1 + n_2\mathbf{a}_2$, being $\mathbf{a}_1, \mathbf{a}_2$ the graphene's lattice vectors and $n_1, n_2 \in \mathbb{Z}$, connects two equivalent sites on the graphene sheet and it is used to uniquely label the atomic structure of a given SWNT. The chiral indices (n_1, n_2) define the diameter $d_t = |\mathbf{C}_h|/\pi$, the chiral angle $\theta = \arctan \sqrt{3}n_2/(2n_1 + n_2)$, and the translational period along the tube axis a_0. The chiral angle is the angle between $\mathbf{C}_h$ and $\mathbf{a}_1$ and

lies in the range $0° \leqslant |\theta| \leqslant 30°$ as a consequence of the hexagonal symmetry of the graphene lattice. The translational period is given by the smallest graphene lattice vector $\mathbf{T}$ perpendicular to $\mathbf{C}_h$, such that $a_0 = \sqrt{3}a\sqrt{n_1^2 + n_1 n_2 + n_2^2}/N_R$, where N_R is the greatest common divisor of $(2n_1 + n_2, 2n_2 + n_1)$ and $a = 2.46\,\text{Å}$ is the graphene's lattice constant. The nanotube unit cell is thus a cylindrical surface with height a_0 and diameter d_t.

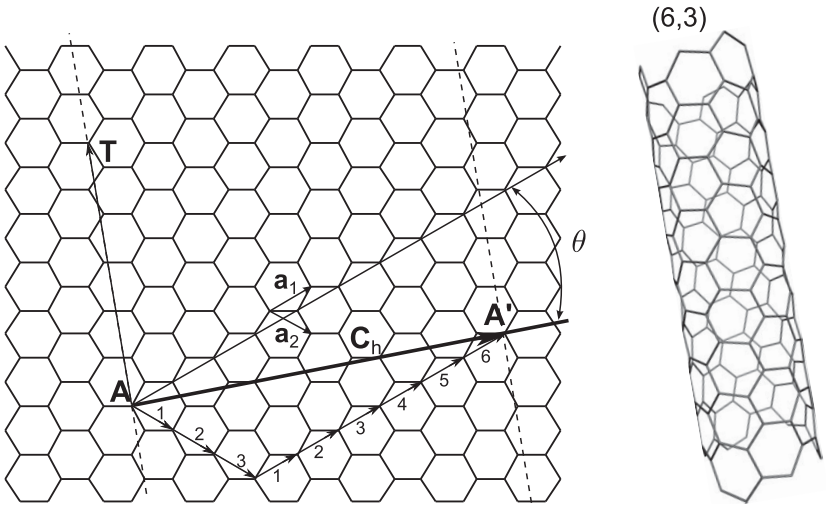

Figure 2.8: Example of SWNT in the graphene network. The lattice vectors are indicated by $\mathbf{a}_1$ and $\mathbf{a}_2$. In this example the chiral vector is $\mathbf{C}_h = 6\mathbf{a}_1 + 3\mathbf{a}_2$. The direction perpendicular to $\mathbf{C}_h$ is the tube axis (dashed lines), where the translational vector $\mathbf{T}$ is indicated. The angle between $\mathbf{C}_h$ and the $\mathbf{a}_1$ zigzag direction of the graphene lattice defines the chiral angle θ. The resulting $(6,3)$ nanotube is shown on the right (extracted from Foa *et al.* [69]).

Nanotubes of the type (n,n) have a chiral angle $\theta = 30°$ and display C–C bonds perpendicular to the nanotube axis, showing an armchair pattern along the circumference (*armchair* or $\mathcal{A}$-tubes). SWNTs of the type $(n,0)$, $\theta = 0°$, are called *zigzag* ($\mathcal{Z}$) tubes, as they exhibit a zigzag pattern along the circumference, displaying C–C bonds parallel to the nanotube axis. Both armchair and zigzag tubes are achiral species, in contrast with $(n_1, n_2 \neq n_1 \neq 0)$ chiral ($\mathcal{C}$) tubes. Figure 2.9 shows three examples of the different types of SWNTs. Although the diameters of the nanotubes shown in Fig. 2.9 are almost the same (~ 1.1 nm), their atomic structure is completely different due to the variation in both the chiral angle and the translational period. In the examples shown, tubes $(8,8)$ and $(14,0)$ present achiral symmetry, meanwhile $(12,3)$ is chiral. The unit cell of $(8,8)$ consist of 32 carbon atoms, while $(14,0)$ has 56 atoms in the unit cell and the number increase up to 84 in $(12,3)$. Chiral nanotubes often have a large number of atoms per unit cell.

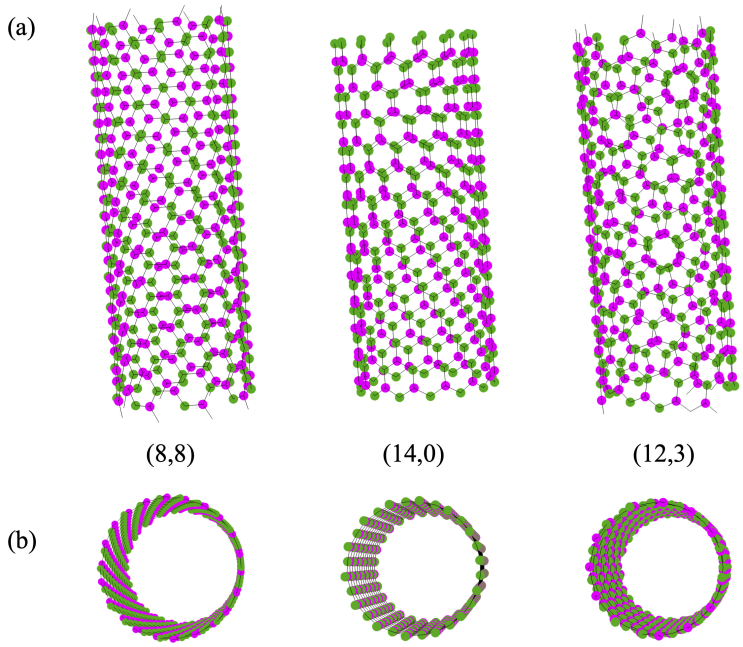

Figure 2.9: (a) Axial view of the atomic structure of $(8,8)$ armchair, $(14,0)$ zigzag and $(12,3)$ chiral nanotubes. Magenta and green circles represent the atoms in the two sublattices of the unrolled graphene sheet. (b) Zenith view of the three species. The chiral structure of $(12,3)$ contrast with the achiral $(8,8)$ and $(14,0)$.

Figure 2.10 shows the essential symmetry elements of (9,9) armchair. Symmetries of SWNTs are directly related to chirality. All species show a_0-period translational symmetry along the tube axis (z axis, by convention) and have a screw axis of pure rotational symmetries. Furthermore, both chiral and achiral tubes have π-rotational symmetry around the U-axis. In addition, $\mathcal{Z}$ and $\mathcal{A}$ tubes present mirror reflection symmetries on the horizontal xy-plane (σ_h) and on the vertical yz-plane (σ_v), which are not present in $\mathcal{C}$ tubes.

Line groups are the full space groups of one-dimensional systems which include translations in addition to the point-group operations (rotations and reflections). Thus, all the symmetries of SWNTs are gathered in line groups $\mathbf{L}_\mathcal{C}$ and $\mathbf{L}_{\mathcal{ZA}}$ given by the product of the dihedral point groups, $\mathbf{D}_n$ and $\mathbf{D}_{nh}$ (for chiral and achiral tubes, respectively), and the helical group [83, 84]:

$$\mathbf{L}_\mathcal{C} = \mathbf{T}_q^r \mathbf{D}_n, \tag{2.43}$$

$$\mathbf{L}_{\mathcal{ZA}} = \mathbf{T}_{2n}^1 \mathbf{D}_{nh}, \tag{2.44}$$

where $q = 2N$, being N the number of C-atoms in the unit cell; n is the greatest common divisor of the chiral indexes (n_1, n_2), and r is the helicity parameter for the screw axis transformations [74]. Note that for achiral tubes $q = 2n$ and $r = 1$. The elements of the groups are:

$$l(t,s,u,w) = (C_q^r | a_0 n/q)^t C_n^s U^u \sigma_v^w, \tag{2.45}$$

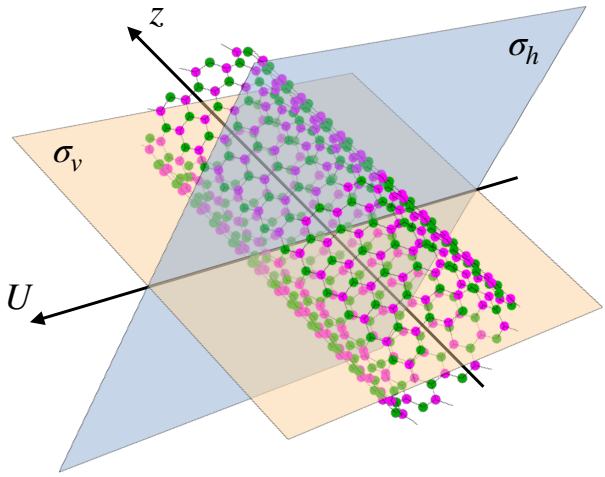

Figure 2.10: Symmetry elements of $(9,9)$ armchair. The full line group of this nanotube is $\mathbf{T}^1_{18}\mathbf{D}_{9h}$, whose generators are $(C^1_{18}|a_0/2)$ transformations, C_9 pure rotations, and the mirror reflections under σ_h and σ_v.

Elements of the SWNTs line groups

where $(C^r_q|a_0 n/q)^t$, $t = 0, \pm 1, \pm 2, ...$ are the elements of helical group $\mathbf{T}^r_q$; C^s_n, with $s = 0, 1, ..., n-1$ are the rotations around the z-axis and form the subgroup $\mathbf{C}_n$; U^u, $u = 0, 1$ are the π rotations around the U-axis for $\mathcal{C}$ tubes and the mirror σ_h reflections for achiral SWNTs; and finally, σ^w_v are the vertical mirror reflections for achiral tubes, so $w = 0$ for $\mathcal{C}$ tubes and $w = 0, 1$ for $\mathcal{A}$ and $\mathcal{Z}$ tubes [85]. Each SWNT is a line group in the sense that the relation between the carbon atoms and the symmetry operations of the tube is an isomorphism: starting with a single carbon atom and successively applying the elements of the group given by Eq. (2.45), the whole tube is constructed. In physical processes with translational symmetry there is no need to work with the full line groups $\mathbf{L}_\mathcal{C}$ or $\mathbf{L}_{\mathcal{ZA}}$, as the isogonal point groups are enough to describe the related phenomena. The point groups isogonal to the SWNTs line groups are $\mathbf{D}_q$ for $\mathcal{C}$-tubes and $\mathbf{D}_{2nh}$ for achiral tubes.

2.2.2 *Description of the band structure within the zone folding approach*

Noether's theorem: If a system has a continuous symmetry property, then there are corresponding quantities whose values are conserved in time.

According to Noether's theorem, each symmetry of a given system always implies the conservation law for a related physical magnitude. Therefore, group symmetry provides a set of quantum numbers with full physical meaning. The translational periodicity of the tube implies the conservation of the quasi-momentum k. Besides, rotational symmetry around the z-axis implies the conservation of m, the projection of the orbital angular momentum along the tube axis. The mirror reflection planes and the π-rotational symmetry around the U-axis impose additional conservation laws to the parities of the electronic

states, so that the parity with respect to σ_v is denoted by A for even states and B for odd ones, and the parity under U or σ_h transformations is denoted by $\pm$ for even and odd states, respectively. Therefore, the state of the electron $|k, m, \mathrm{A/B}, \pm\rangle$ corresponds to a particular irreducible representation of the line group and thus, its wave function transforms under the symmetry operations in the same way than the basis of the corresponding representation.

Provided that SWNTs are essentially one-dimensional structures, it is convenient to reduce their first Brillouin zone to 1D using the zone-folding approach. Therefore, we consider the nanotube as a graphene layer with periodic boundary conditions along the circumferential direction:

Periodic boundary conditions for SWNTs

$$\Psi_{\mathbf{k}}(\mathbf{r} + \mathbf{C}_h) = e^{i\,\mathbf{k}\cdot\mathbf{C}_h}\Psi_{\mathbf{k}}(\mathbf{r}) = \Psi_{\mathbf{k}}(\mathbf{r}), \tag{2.46}$$

being $\Psi_{\mathbf{k}}(\mathbf{r})$ the wave function of the electron in graphene as given by Eq. (2.34). This approach neglects curvature effects, but results a good approximation for tubes of radii large enough ($d_t > 1$ nm) [86, 87]. The condition expressed by Eq. (2.46) implies the quantization of the allowed wave vectors along the circumferential direction $\mathbf{k}\cdot\mathbf{C}_h = 2\pi m$, where $m \in \mathbb{Z}$ is the z-component of the orbital angular momentum. Since no condition is imposed to the wave vectors along the nanotube axis, they remain continuous. Strictly speaking, this choice is valid only for tubes of infinite length, but it is also found as a good approximation provided that the length-to-diameter ratio of the SWNTs is $> 10^3$. Thus, the BZ of the nanotube consists of a set of lines with length $2\pi/a_0$ parallel to the tube axis, as shown in Fig. 2.11 for the (8, 8) armchair case. The number of lines corresponds to the order of the isogonal point group $q = 2(n_1^2 + n_1 n_2 + n_2^2)/n\mathcal{R}$, where $\mathcal{R} = 3$ or $\mathcal{R} = 1$ depending on whether $(n_1 - n_2)/3n$ is integer or not [85]. Each line is labelled by the index m, which takes integer values in $(-q/2, q/2]$. According to the boundary condition Eq. (2.46), the q lines are separated by constant distances $2/d_t$.

The Hamiltonian describing the electron dynamics in the periodic potential of the nanotube is then given by the SLG Hamiltonian $H_o(\mathbf{k})$ in Eq. (2.32) with $\mathbf{k}$ fulfilling Eq. (2.46). The dispersion for each allowed wave vector in the circumferential direction of a given (n_1, n_2) nanotube is obtained by cutting the 2D band structure of graphene along q lines of length $2\pi/a_0$ separated by $2/d_t$ and parallel to the tube axis. The collection of these lines gives the electronic structure of the nanotube. By using the zone-folding approximation to describe the band structure, we assume that the wave function of graphene remains unaltered when rolling the tube. Therefore, within the nearest-neighbors tight-binding approximation, the dispersion is given by $E_m^{\pm}(k) = \mp\gamma_0\,|f_m(k)|$, where γ_0 is the tight-binding integral of graphene, see Sec. 2.1.3, and $f_m(k)$ is the complex function defined by Eq. (2.18)

Zone folding approach

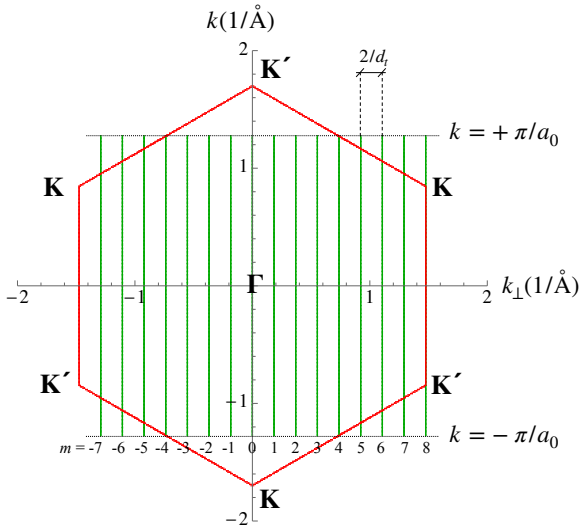

Figure 2.11: Allowed **k** vectors in the first Brillouin zone of (8, 8) armchair tube (green lines). This nanotube contains 32 C atoms in its unit cell, $q = 16$, $m = 0, \pm1, \pm2, ..., \pm7, 8$ and $d_t = 10.9$ Å. The red hexagon shows the boundary of the graphene's BZ along with the high symmetry points K and Γ. Note that for $\mathcal{A}$-type tubes, the translational period $a_0 = a$.

restricted to the 1D manifold correspondent to the nanotube's first Brillouin zone:

$$f_m(k) = e^{-iak_1^m/\sqrt{3}}\left(1 + 2e^{i\sqrt{3}ak_1^m/2}\cos\frac{ak_2^m}{2}\right), \tag{2.47}$$

where:

$$k_1^m = k_\perp^m \cos\theta' - k\sin\theta' \tag{2.48}$$

$$k_2^m = k_\perp^m \sin\theta' + k\cos\theta' \tag{2.49}$$

being $\theta' = \pi/6 - \theta$, and $k_\perp^m = 2m/d_t$ the set of allowed wave vectors along the circumferential direction

As discussed in Sec. 2.1.3, the Dirac points K and K′ are degenerated at the Fermi level. Accordingly, if K (K′) is an allowed wave vector for the SWNT, the corresponding bands are degenerated at the Fermi level and the nanotube is metallic, as it is the case of the (8,8) armchair tube shown in Fig. 2.11. Otherwise, the nanotube is a small-gap semiconductor. Based on this fact, Eq. (2.46) leads to the following general rule for the prediction of the metallicity: a given (n_1, n_2) SWNT is metallic if $(n_1 - n_2) \equiv 0 \pmod 3$ and small-gap semiconductor if $(n_1 - n_2) \equiv 1, 2 \pmod 3$. The tight-binding model in the nearest neighbors approximation predicts that the gap at the Fermi level for semiconducting nanotubes decreases as $1/d_t$ [88]. The metallicity rule is illustrated in the three examples of zigzag tubes shown in Figure 2.12.

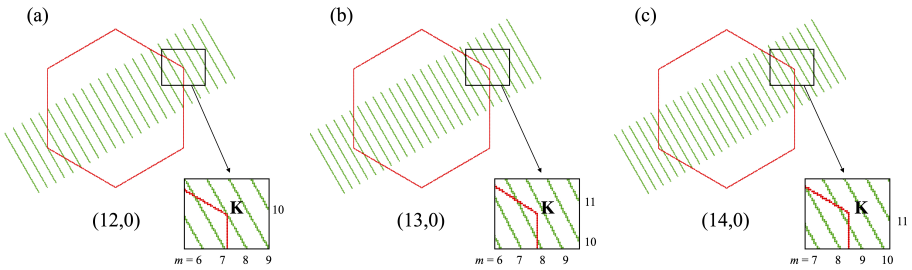

Figure 2.12: First Brillouin zone of $(12,0)$, $(13,0)$ and $(14,0)$ zigzag tubes. The diameters of these tubes are $d_t = 0.94, 1.02$ and 1.10 nm, respectively. Panel (a) shows the $(12,0)$ metallic tube $n \equiv 0 \pmod 3$ intersecting the K point at $m = -8$ and 8. In panels (b) and (c) we show the $(13,0)$ $n \equiv 1 \pmod 3$ and $(14,0)$ $n \equiv 2 \pmod 3$ semiconducting tubes.

In addition to the possible degeneracy of the valence and conduction bands at the Fermi level, symmetry imposes extra degeneracies to the electronic bands. The parities invoked by the U-axis, and the mirror planes for achiral tubes, combine the electronic states in degenerate multiplets, related to irreducible representations of the group (A or B for singlets, E for doublets, and G for quadruplets) [85]. Note that the degeneracy of k and $-k$ is shared by both chiral and achiral tubes. For this reason, the domain sufficient to characterize the entire band is $[0, \pi/a_0]$. Fig. 2.13 shows the band structure of (a) (8,8) armchair and (b) (14,0) zigzag tubes. In Fig. 2.13 singlets at $m = 0$ (n) are emphasized with solid (dashed) black lines for $k \in [0, \pi/a_0]$. The rest of bands correspond to double degenerated states consequence of the σ_v symmetry. The bands have specific symmetry with respect to $k = 0$ and $k = \pi/a_0$. For (n,n) armchair tubes, the conduction and valence bands with $m = 0$ and n have opposite σ_v parity, while in $\mathcal{Z}$-type tubes these states have always even parity. At $k = 0$ the singlets of the valence and conduction bands have sharp $\pm$ parity, which is always even for $\mathcal{A}$-tubes, while is reversed for $\mathcal{Z}$-tubes. Note that at $k = 0$ all the bands are zero-sloped, which results in strong van Hove singularities in the density of states (DOS) shown as a shaded area in the background of Fig. 2.13. The DOS is defined by $D(E) = (Na_0/2\pi)|dk/dE|$, being N the number of unit cells in the nanotube [89]. The DOS is negligible at $k = 2\pi/3a_0$ for armchair tubes, where the valence and conduction bands cross at the Fermi level, although these type of tubes present additional van Hove singularities in the interval $k \in (2\pi/3a_0, \pi/a_0)$ [85].

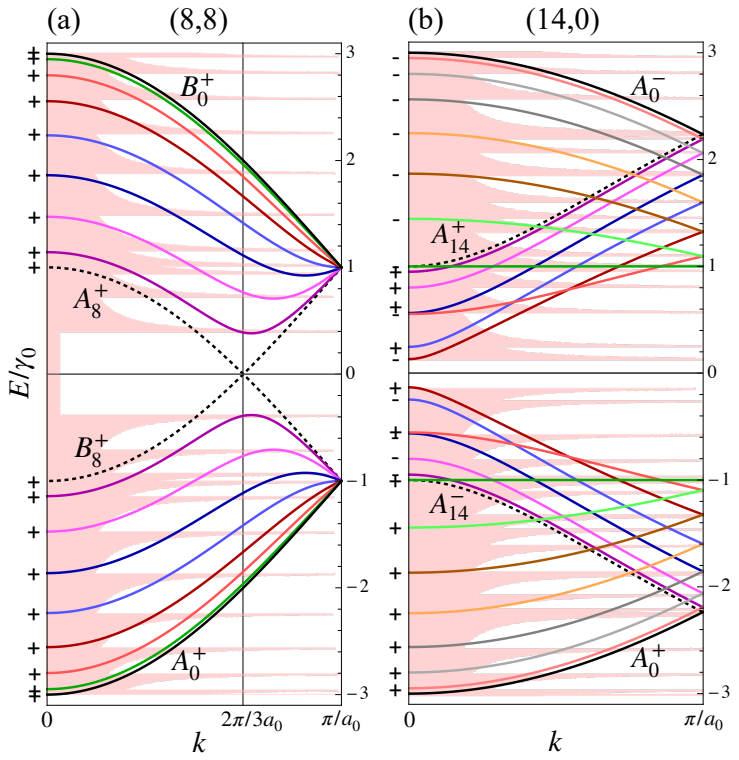

Figure 2.13: Band structure of (a) (8,8) armchair tube (metallic) and (b) (14,0) zigzag tube (semiconductor). The energy is given times the tight-binding integral γ_0. The solid (dashed) black lines in (a) emphasizes the $m = 0$ ($m = 8$) singlets of the valence and conduction bands labelled according to their irreducible representations. In (b) we represent the $m = 0$ ($m = 14$) singlet by solid (dashed) black lines labelled by the corresponding irreducible representations. In both panels, parities under σ_h reflections at $k = 0$ are denoted by $\pm$. The pink filled area in the background shows the density of states in arbitrary units.

2.3 THE INTERACTION HAMILTONIAN

Once we have derived the field-free Hamiltonian H_o, we shall devote this section to present the fundamentals of the description of the interaction between intense laser fields and matter. For this purpose, let us consider the electron subjected simultaneously to the crystal potential $V_C(\mathbf{r})$ and to an electromagnetic field described by the vector potential $\mathbf{A}(\mathbf{r}, t)$.

According to quantum electrodynamics, the Hamiltonian of the electromagnetic field H_{EM} can be written in terms of the creation and annihilation operators $\hat{a}^\dagger_{\mathbf{k},\mu}$ and $\hat{a}_{\mathbf{k},\lambda}$ as an expansion of normal modes $\mathbf{k}$ with frequency $\omega_\mathbf{k} = c|\mathbf{k}|$ confined in a volume V [90]:

$$H_{EM} = \sum_{\mathbf{k},\lambda} \hbar\omega_\mathbf{k} \left(\hat{a}^\dagger_{\mathbf{k},\lambda} \hat{a}_{\mathbf{k},\lambda} + \frac{1}{2} \right), \tag{2.50}$$

where $\lambda = \pm 1$ stands for the two possible polarization directions (spin) of the photons. We can thereby write the total Hamiltonian of the system as:

$$H = \frac{1}{2m_e}\left(\hat{\mathbf{p}} - q_e\hat{\mathbf{A}}\right)^2 + V_C(\mathbf{r}) + H_{EM}, \tag{2.51}$$

being m_e the electron mass, $q_e < 0$ the elementary charge, and $\hat{\mathbf{p}}$ the momentum operator, $-i\hbar\nabla_{\mathbf{r}}$. Since $\hat{\mathbf{A}}$ in general depends on $\mathbf{r}$, $\hat{\mathbf{A}}$ and $\hat{\mathbf{p}}$ do not commute. Therefore, the Hamiltonian (2.51) is expanded to:

$$H = \frac{\hat{p}^2}{2m_e} - \frac{q_e}{2m_e}\left(\hat{\mathbf{p}}\cdot\hat{\mathbf{A}} + \hat{\mathbf{A}}\cdot\hat{\mathbf{p}}\right) + \frac{{q_e}^2}{2m_e}\hat{A}^2 + V_C(\mathbf{r}) + H_{EM}. \tag{2.52}$$

The operator $\hat{\mathbf{A}}$ related to H_{EM} in a medium of volume V and dielectric permittivity ϵ can be written in terms of $\hat{a}^\dagger_{\mathbf{k},\lambda}$ and $\hat{a}_{\mathbf{k},\lambda}$ as:

$$\hat{\mathbf{A}}(t) = \sum_{\mathbf{k},\lambda} \mathbf{e}_{\mathbf{k},\lambda}\sqrt{\frac{\hbar}{2\epsilon V\omega_{\mathbf{k}}}}\left(\hat{a}^\dagger_{\mathbf{k},\lambda}e^{i\omega_k t}e^{-i\mathbf{k}\cdot\mathbf{r}} + \hat{a}_{\mathbf{k},\lambda}e^{-i\omega_k t}e^{i\mathbf{k}\cdot\mathbf{r}}\right), \tag{2.53}$$

being $\mathbf{e}_{\mathbf{k},\lambda}$ the polarization vectors. In the infrared regime $k \sim 10^7\ \mathrm{m}^{-1}$ and, since $|\mathbf{r}| \sim 10^{-10}$ m, we can assume $\mathbf{k}\cdot\mathbf{r} \ll$ and $e^{i\mathbf{k}\cdot\mathbf{r}} \sim 1$. This is the so called *dipole approximation*, where the plane wave expansion is considered only to the zeroth order. Implicitly to this approximation, the electron wave packet is assumed to remain in a neighborhood $\ll \lambda$ of its parent atom during the whole field cycle, therefore oscillating non-relativistically. This condition is not necessarily fullfilled for short wavelength radiation, such as X-rays, where additional terms of the plane wave expansion need to be considered, but the dipole approximation is extremely good for the mid-IR driving fields considered in this work. Therefore, in the dipole approximation $\left[\hat{\mathbf{p}}, \hat{\mathbf{A}}\right] = 0$, and thus:

$$H = \frac{\hat{p}^2}{2m_e} - \frac{q_e}{m_e}\hat{\mathbf{A}}\cdot\hat{\mathbf{p}} + \frac{{q_e}^2}{2m_e}\hat{A}^2 + V_C(\mathbf{r}) + H_{EM}. \tag{2.54}$$

The field of the single mode driving laser is described by the *coherent state* $|\alpha\rangle$. This minimum uncertainty wave packet results from the linear superposition of the Fock states $|n\rangle$ [91]:

$$|\alpha\rangle = e^{-\frac{1}{2}|\alpha|^2}\sum_{n=0}^{\infty}\frac{\alpha^n}{\sqrt{n!}}|n\rangle, \tag{2.55}$$

being $\alpha = |\alpha|e^{-i\Phi}$ a complex number. Note that the square value of the expansion coefficients in Eq. (2.55) is the Poisson distribution. It can be readily shown that $|\alpha\rangle$ is an eigenstate of the annihilation operator $\hat{a}$ and that the average number of photons in the coherent state is $\langle n\rangle_\alpha = |\alpha|^2$. Thus, the average energy is $\hbar\omega_o\left(\frac{1}{2} + |\alpha|^2\right)$, where ω_o is the frequency of the driving field.

Let us now consider the expression of a single mode electric field operator $\hat{\mathbf{F}}$ in terms of $\hat{a}_\lambda^\dagger$ and $\hat{a}_\lambda$ in the dipole approximation:

$$\hat{\mathbf{F}}(t) = i\sqrt{\frac{\hbar\omega_o}{2\epsilon V}}\sum_\lambda \mathbf{e}_\lambda\left(\hat{a}_\lambda e^{-i\omega_o t} - \hat{a}_\lambda^\dagger e^{i\omega_o t}\right), \tag{2.56}$$

where we assume that the field is contained in a volume V with dielectric permittivity ϵ. The average of $\hat{\mathbf{F}}$ in the coherent state $|\alpha\rangle$ is:

$$\langle\alpha\,|\,\hat{\mathbf{F}}\,|\,\alpha\rangle = \sqrt{\frac{2\hbar\omega_o|\alpha|^2}{V\epsilon}}\sum_\lambda \mathbf{e}_\lambda \sin(\omega_o t+\phi), \tag{2.57}$$

and the variance of $\hat{\mathbf{F}}$ in $|\alpha\rangle$:

$$\langle\alpha\,|\,\hat{\mathbf{F}}^2\,|\,\alpha\rangle = \frac{2\hbar\omega_o|\alpha|^2}{V\epsilon}\sin^2(\omega_o t+\phi) + \frac{\hbar\omega_o}{2V\epsilon}. \tag{2.58}$$

Consequently, the mean square deviation of $\hat{\mathbf{F}}$ in the coherent state is:

$$\langle\left(\hat{\mathbf{F}} - \langle\hat{\mathbf{F}}\rangle_\alpha\right)^2\rangle_\alpha = \langle\hat{\mathbf{F}}^2\rangle_\alpha - \langle\hat{\mathbf{F}}\rangle_\alpha^2 = \frac{\hbar\omega_o}{2V\epsilon}. \tag{2.59}$$

Therefore, any measurement of the electric field will be subject to an uncertainty

$$\Delta F = \sqrt{\frac{\hbar\omega_o}{2V\epsilon}}. \tag{2.60}$$

Similarly, the uncertainty of the magnetic field is:

$$\Delta B = \sqrt{\frac{\hbar\omega_o\mu}{2V}}, \tag{2.61}$$

being μ the magnetic permeability of the medium. Therefore, the residual noise energy of the electromagnetic field in the coherent state is given by:

$$\Delta E = \frac{1}{2}\epsilon(\Delta F)^2 V + \frac{1}{2\mu}(\Delta B)^2 V = \frac{\hbar\omega_o}{2}, \tag{2.62}$$

equivalent to the energy of the vacuum state mode. Note that in the classical limit (large $|\alpha|$) the relative weight of this residual energy is zero. Consequently, for large $|\alpha|$ we can consider the driving field unaffected by the interaction with the target, and use the effective Halmitonian:

$$\begin{aligned} H \sim \langle\alpha\,|\,H\,|\,\alpha\rangle = \frac{\hat{p}^2}{2m_e} - \frac{q_e}{m_e}\langle\alpha\,|\,\hat{\mathbf{A}}\,|\,\alpha\rangle\cdot\hat{\mathbf{p}} + \frac{{q_e}^2}{2m_e}\langle\alpha\,|\,\hat{A}^2\,|\,\alpha\rangle \\ + V_C(\mathbf{r}) + \hbar\omega_o\left(\frac{1}{2} + |\alpha|^2\right). \end{aligned} \tag{2.63}$$

By making the gauge transformation

$$\Psi(\mathbf{r},t) \rightarrow \Psi(\mathbf{r},t)e^{-i\frac{{q_e}^2}{2\hbar m_e}\int\langle\hat{A}^2(\tau)\rangle_\alpha d\tau - i\omega_o\left(\frac{1}{2}+|\alpha|^2\right)} \tag{2.64}$$

it is readily seen that the terms proportional to $\hat{A}^2$ and ω_o can be removed from the Schröndinger equation and then, the Hamiltonian in Eq. (2.63) can be written as:

$$H = \frac{\hat{p}^2}{2m_e} + V_C(\mathbf{r}) - \frac{q_e}{m_e}\mathbf{A}\cdot\hat{\mathbf{p}}, \tag{2.65}$$

being $\mathbf{A} = \langle\hat{\mathbf{A}}\rangle_\alpha$. The first two terms of H correspond to the unperturbed Hamiltonian H_o and the last term, involving $\mathbf{A}\cdot\hat{\mathbf{p}}$, is the interaction responsible for transitions between the eigenstates of H_o. Note that this later term can be expressed in the length gauge by performing the gauge transformation

$$\Psi(\mathbf{r},t) \rightarrow \Psi(\mathbf{r},t)e^{i\frac{q_e}{\hbar}\mathbf{A}\cdot\hat{\mathbf{r}}} \tag{2.66}$$

so that

$$H = \frac{\hat{p}^2}{2m_e} + V_C(\mathbf{r}) + V_{int}, \tag{2.67}$$

The interaction Hamiltonian

where

$$V_{int} = -q_e\,\mathbf{F}\cdot\hat{\mathbf{r}}, \tag{2.68}$$

which is the expression of the interaction Hamiltonian that we shall use throughout the rest of this work.

2.4 HIGH-ORDER HARMONIC GENERATION

The interaction of matter with sufficiently intense electromagnetic fields gives rise to a rich variety of physical processes, which are commonly known as *nonlinear* phenomena. One remarkable example is the emission of radiation at integer multiples of the driving field frequency, known as *harmonic generation*. Although nonlinear optical effects were predicted before the construction of the first laser in 1960 [38], the pioneer discoveries are considered to be two-photon absortion [92] and second-harmonic generation [42], that were first reported in 1961. Two and third order nonlinear phenomena include, among others, optical parametric oscillation, third-order harmonic generation, intensity-dependent refractive index, saturable absorption or stimulated Raman scattering [93–98]. High-order harmonic generation is an example of an extreme nonlinear optical process whereby a target (gas, plasma or solid) illuminated nonperturbatively by an intense laser beam emits harmonics of the laser frequency up to some cut-off order, most of them with comparable efficiency. HHG fundamentals will be later discussed in detail. First, we shall outline some introductory concepts of nonlinear phenomena.

2.4.1 *Remarks on nonlinear optical phenomena*

In general terms, when light interacts with matter, the time-dependent rearrangement of the atomic charge distribution causes the generation or modification of the electric multipole moments. Macroscopically, this implies the appearance of a polarization density $\mathbf{P}(t)$ in the material, induced by the electric field $\mathbf{F}(t)$, resulting from the superposition of the atomic dipole moments, which are the largest contributions to the atomic multipole expansion. Most nonlinear optical phenomena are described by expanding the polarization density as a power series in the applied electric field amplitude[2]:

$$P(t) = \epsilon_0 \left[\chi^{(1)}F(t) + \chi^{(2)}F^2(t) + \chi^{(3)}F^3(t) + \dots\right] \tag{2.69}$$

where $\chi^{(1)}$ is the linear susceptibility. The quantities $\chi^{(2)}$, $\chi^{(3)}$, ... are known as the second- and third-order non-linear optical susceptibilities, and so on. In general, the qth nonlinear susceptibility $\chi^{(q)}$ is a $(q+1)$-rank tensor and depends on the frequencies of the applied field. The role of matter polarization in nonlinear optical phenomena is explicit in the wave equation [98]:

$$\nabla^2\mathbf{F} - \frac{n^2}{c^2}\frac{\partial^2\mathbf{F}}{\partial t^2} = \frac{1}{\epsilon_0 c^2}\frac{\partial^2\mathbf{P}^{\mathrm{NL}}}{\partial t^2} \tag{2.70}$$

where n is the (linear) refractive index and $\mathbf{P}^{\mathrm{NL}}$ is the nonlinear part of $\mathbf{P}$. Therefore, a time-dependent polarization acts as the source of new components of the electromagnetic field.

A simple estimate of the order of magnitude of these quantities in condensed matter, where $\chi^{(1)} \sim 1$, leads to $\chi^{(2)} \sim 2\times10^{-12}$ m/V and $\chi^{(3)} \sim 4\times10^{-24}$ m^2/V^2 [98]. Then, a nonlinear optical process is said to be *perturbative* or a $\chi^{(q)}$ process if the efficiency of the optical response rapidly decreases with the harmonic order, as it happens in the weak-field regime. On the other hand, if the intensity of the field is strong enough as to maintain comparable the efficiency of the consecutive harmonic orders up to a certain cut-off, the process is understood as *non perturbative*, as it happens in HHG.

2.4.2 *High order harmonic generation*

High-order harmonic generation is a remarkable process resulting from the interaction of physical systems with intense electromagnetic radiation. In contrast to most of the conventional photon upconversion mechanisms, HHG is not based in the multiphoton excitation of atomic bound-state transitions, but on the dynamics of the unbound electrons. The spectrum generated by this nonlinear optical process has certain distinguishable features that were already

2 For the sake of simplicity, we assume $P(t)$ and $F(t)$ in Eq. (2.69) as scalar quantities.

observed in the earliest experimental and theoretical works in gases [39, 43, 44, 99, 100]. An scheme of the typical spectrum emitted by an atom upon irradiation with an electric field of frequency ω_o is shown in Fig. 2.14. It consists of a few low-order harmonics whose intensities decrease exponentially according to the perturbative scaling, followed by a *plateau*-like structure of harmonics with similar intensities, which ends up sharply at a cut-off frequency given by the law:

Cutt-off scaling law for atoms

$$\hbar\omega_{max} = I_p + 3.17U_p, \tag{2.71}$$

where I_p is the atomic ionization potential, and U_p the ponderomotive energy, i. e. the mean kinetic energy of a free electron in the electromagnetic field, which is given by $U_p = {q_e}^2{F_o}^2/4m_e\omega_o^2$, being q_e and m_e the charge and mass of the electron, respectively, and F_o the field amplitude. The plateau is characterized by a scaling of the efficiency of the qth-harmonic with the intensity I of the form $I^{q'}$, with $q' < q$, i. e. much weaker that the qth-power predicted by the perturbation theory. Therefore, HHG is not a $\chi^{(q)}$ process. The plateau can extend the harmonic emission up to thousands of harmonic orders, therefore conveying the possibility of generating coherent extreme ultraviolet (XUV) or even soft X-ray radiation [40, 41]. Beyond the cut-off frequency, the intensity of the harmonics decreases again exponentially, so that the highest-order harmonics are hardly visible.

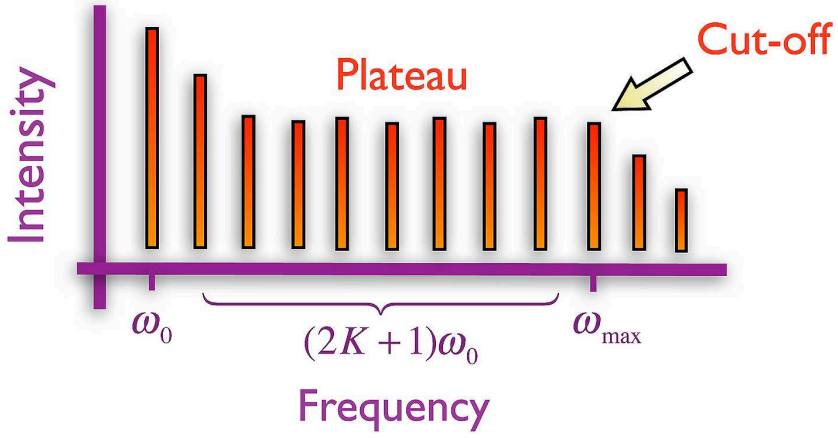

Figure 2.14: Scheme of the typical HHG spectrum emitted by an atom in the tunneling ionization regime. The spectrum consists of peaks at frequencies odd multiples of that of the driving field, ω_o.

The basic properties of the harmonic spectra generated by intense fields are well understood. The particular scaling law of the cut-off frequency with the intensity of the driver $\hbar\omega_{max} \propto \lambda^2 I$ reflects the physical underlying mechanism. HHG can be explained in classical terms by the *simpleman's model*. This model, also known as the *three-step model*, was first proposed by van Linden and Muller [101], and Gallagher [102], to study above-threshold ionization, and later used by

Kulander and Schafer [47], and Corkum [48], to explain the plateau extension in the harmonic spectrum.

The *simpleman's model* is based on three assumptions. First of all, the ionization probability depends on the instantaneous value of the electromagnetic field. Secondly, it is assumed that the electron is located right after ionization at the coordinate origin with zero velocity. These are reasonable assumptions in the tunneling ionization regime since zero is the mean value of the velocity and the origin can be assumed as the coordinate of the bound state previous to ionization. The third assumption consists in considering the dynamics subsequent to ionization as that of a classical free electron in the electromagnetic field, thus neglecting the influence of the Coulomb potential.

Let us consider a classical electron which is ionized at the coordinate origin at time t_o with zero velocity, evolving under the interaction with a monochromatic external field $F(t) = F_o \sin \omega t$ in the x direction. The classical equations of motion are:

$$\ddot{x}(t) = \frac{q_e F_o}{m_e} \sin \omega t \tag{2.72}$$

$$\dot{x}(t) = -\frac{q_e F_o}{m_e \omega} [\cos \omega t - \cos \omega t_o] \tag{2.73}$$

$$x(t) = -\frac{q_e F_o}{m_e \omega^2} [\sin \omega t - \sin \omega t_o - \omega (t - t_o) \cos \omega t_o] \tag{2.74}$$

Note that the velocity includes two different terms, a drift term, $v_{drift} = (q_e F_o / m_e \omega) \cos \omega t_o$, and a quiver term, $v_p = -(q_e F_o / m_e \omega) \cos \omega t$, which describes the oscillation in the external field. The drift term makes the trajectory to depend strongly on the initial phase of the electric field, ωt_o.

The simpleman's model for HHG in gas systems

According to the *simpleman's model*, the generation of the most energetic harmonics can be understood as depicted in Fig. 2.15. In a first step, the atomic electron appears in the continuum after tunneling through the Coulomb barrier. After the release, in a second step, the electron follows an oscillatory trajectory that returns to the atomic nucleus. Finally, the high frequency radiation is emitted in a last step, in which the electron recombines to the ground state of the parent ion. During this later step, the electron emits a photon whose energy equals the electron's total energy: kinetic plus ionization potential.

In order to determine the maximum photon energy that can be generated, we have to look at the maximum kinetic energy of the electron at re-scattering. It is readily found from Eqs. (2.73) and (2.74) that this maximum energy is $T_{max} = 3.17 U_p$, which straightforwardly yields the cut-off law in Eq. (2.71). As the largest tunnel probability occurs at the field maxima, the electron will be ionized twice every laser period. Consequently, the emitted radiation will consist of a sequence of bursts separated by half the optical period of the fundamental laser field. These pulses are mutually coherent, thus the spectrum of the emitted radiation corresponds to a comb of peaks separated

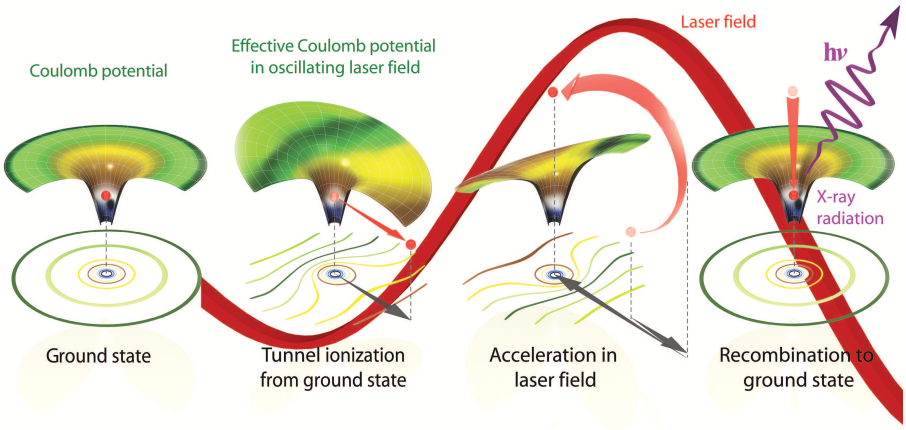

Figure 2.15: Classical scheme of HHG as described by the *simpleman's model*. The electric field of an intense laser extracts the electron from the atom by tunnel ionization through the Coulomb potential barrier. The laser field then accelerates the electron, which is driven back to the parent atom, liberating its excess energy as a high-energy photon when it recombines. Figure extracted from Popmintchev *et al.* [103].

by twice the laser frequency. Only odd harmonics will be emitted, in consistency with the general symmetry properties of centrosymmetric material media [98].

Fig. 2.16 depicts three pairs of electron trajectories corresponding to different re-collision energies and the kinetic energy of the particles as a function of the ionization and re-scattering times. The maximum re-collision energy takes the well-known value $T_{max} = 3.17U_p$ for the trajectory represented in blue, with an excursion time of approximately 0.63 times the period of the driving laser. Note that the other trajectories do not achieve this maximum kinetic energy. Remarkably, for harmonic frequencies below the cut-off, there are two possible electron trajectories at every half cycle of the laser pulse leading to the same kinetic energy at re-collision, which are known as *short* and *long* trajectories, according to the excursion time. Note also that for the short trajectory contributions, the less energetic harmonics are emitted earlier than the more energetic, thus imprinting a positive chirp in the harmonic radiation. This behavior is reversed for the long trajectories, that imprint a negative chirp.

The results of the interpretation of HHG in terms of semiclassical trajectories can be confirmed from the time-frequency analysis (TFA) of the harmonic signal, as calculated from the Schröndinger equation. The TFA consists in filtering the harmonic spectrum with a set of displaced Gaussian masks and computing the inverse Fourier transform of the masked spectra. It is thereby possible to resolve the time in which the different harmonics are emitted. As an example, in Fig. 2.17(c) we show the TFA for the HHG spectrum from hydrogen.

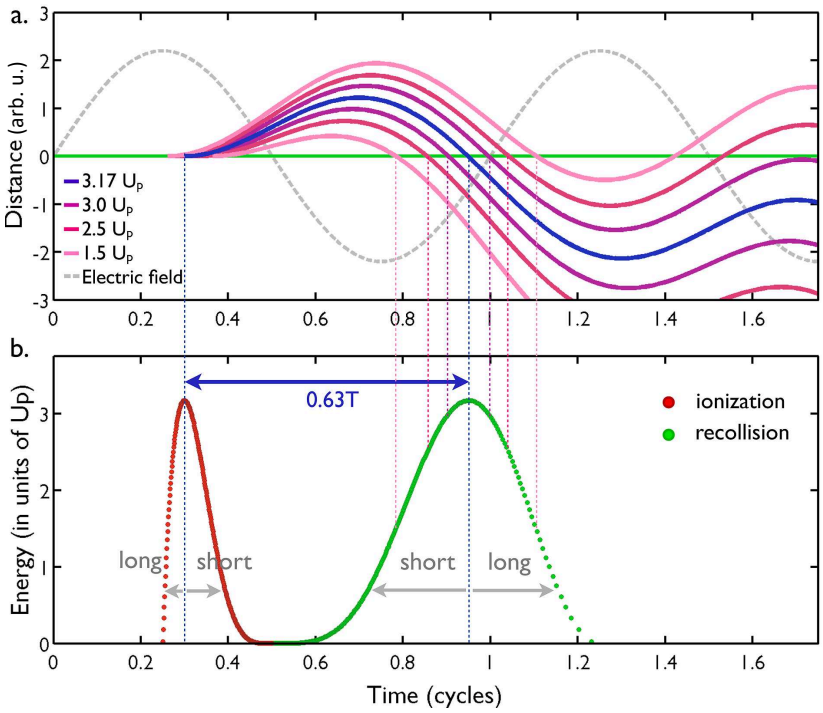

Figure 2.16: (a) Sample of electronic trajectories in a monochromatic laser field. The grey-dashed line represents the electric field in arbitrary units, and the green line, the nucleus position at the coordinate origin. Three pairs of short and long trajectories are represented for re-collision energies of $3.0U_p$ (purple), $2.5U_p$ (dark pink) and $1.5U_p$ (light pink), whereas the most energetic trajectory, $3.17U_p$ at re-collision, is represented in blue. The vertical axis represents the distance from the nucleus. (b) Returning kinetic energy of the particles at the instant of the first re-collision with the parent ion. The green points represent the re-collision time, and the red points, the ionization time. The blue arrow shows the excursion time for the most energetic trajectory, $0.63T$, where T is the laser period. Figure courtesy of C. Hernández-García [104].

Remarkably, the slopes of the TFA allows to identify the harmonics generated by the short (positive slope) and long trajectories (negative slope). Note that the efficiency of the harmonics generated by the short trajectories is greater, as a consequence of the limited spreading of the wave function of the recoiling electron, which is greater for long trajectories [105]. The re-collision energies of the semiclassical electron computed from Eq. 2.74 are also plotted in Fig. 2.17(c) as black dots. It can be observed that the results from TFA are in excellent agreement with the classical predictions.

For the case of solid targets, HHG is subjected to damage threshold, which is the main factor that limits the maximum intensity of the driving field. Due to this constraint, HHG is restricted to the pro-

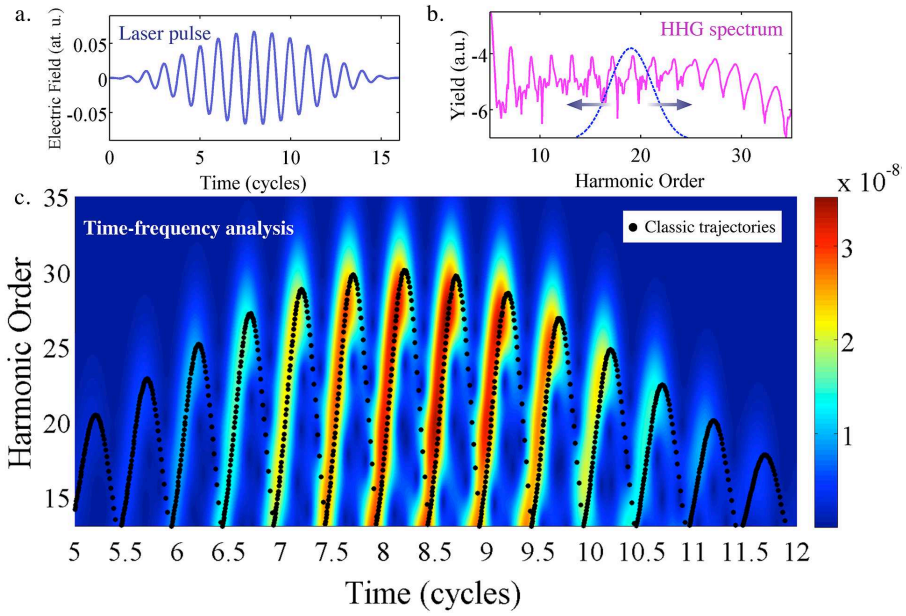

Figure 2.17: Time-frequency analysis for the HHG spectral yield showed in (b), which corresponds to an hydrogen atom irradiated by the laser pulse of panel (a), 800 nm wavelength, 5.8 cycles Full width at half maximum (FWHM) (15.5 fs) at 1.57×10^{14} W/cm^2 peak intensity. The gaussian spectral window is $3\omega_o$, see blue dashed line in (b). The black dots in (c) represent the short and long classical electron trajectories. Figure courtesy of C. Hernández-García [104].

duction of only several harmonics. This is shown in Fig. 2.18(a), that includes the spectra measured from ZnO by Ghimire *at al.* [52]. HHG in solids has been studied mainly in semiconductor materials, with energy gaps larger than mid-IR frequencies, in which the non-linear response is governed by tunneling excitation. In contrast to the atomic case, the first experiments of HHG in crystalline solids showed a linear cut-off frequency scaling with the driving field amplitude, see Fig. 2.18(b) [52]. Several theoretical models have been used to explain this linear response attending to the intraband dynamics of the quasi-free states, such as semiclassical models for intraband currents [63], semiconductor optical Bloch equations [64–67], or Bloch equations using Wannier localised functions [68].

Although the different scalings of the cut-off frequency imply that HHG in finite gap solids and gas targets has notable differences, these systems share some basic principles: harmonics are generated by electrons that are initially bound and promote to slightly bonded or unbound states through tunneling; once promoted, the electrons are accelerated by the field until they release the acquired kinetic energy in the form of high-frequency radiation. Nevertheless, in the case of solids, the first step leads to the creation of an electron-hole pair

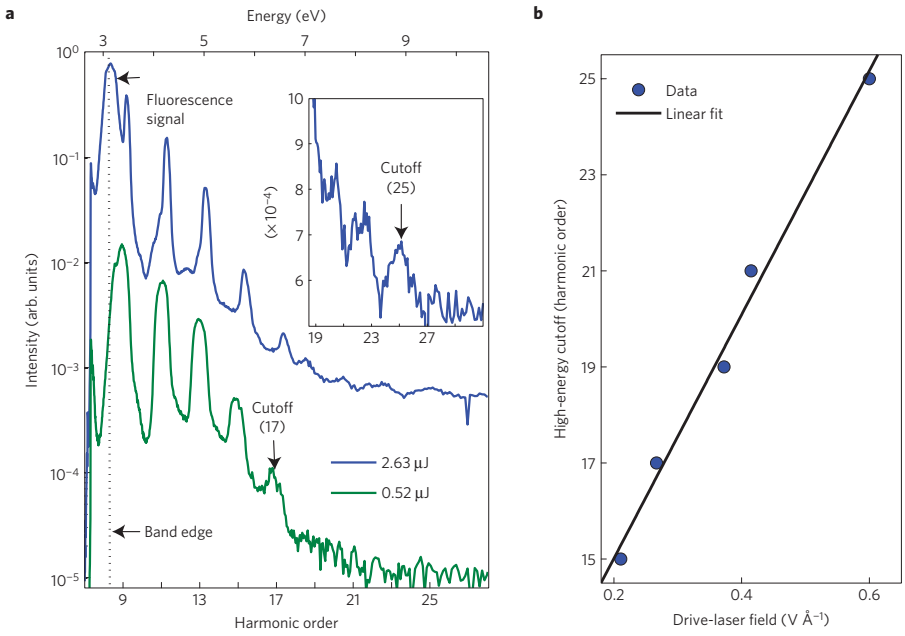

Figure 2.18: (a) Experimental spectra from a 500 μm-thick ZnO crystal driven by a laser field with 3.25 μm wavelength. The spectra represented by the green and blue curves correspond to an estimated vacuum field strength of 0.27 VÅ^{-1} and 0.6 VÅ^{-1}, respectively. The inset shows the expanded view at and near the cutoff of the 0.6 VÅ^{-1} spectrum on a linear scale. The dotted vertical line marks the approximate band edge of the crystal as indicated by the residual fluorescence signal. (b) The high-energy cut-off scales linearly with the driving laser field. Figure extracted from Ghimire *et al.* [52].

which quivers in the reciprocal space, therefore following real space trajectories that depend on the band structure. Thus, while in atoms the electron trajectories are universally defined, in solids this universality is lost, see Fig. 2.19. Also, re-collision can occur away from the origin, with the subsequent emission of a high-frequency photon resonant with the band gap at the recombination time [59].

As we shall see in the following chapters, HHG in graphene and carbon nanotubes obeys to a different mechanism, as the first step is not related to the tunneling ionization/excitation process found in the above referred systems, but rather to the particular geometry of the electronic band structure of these low dimensional carbon allotropes.

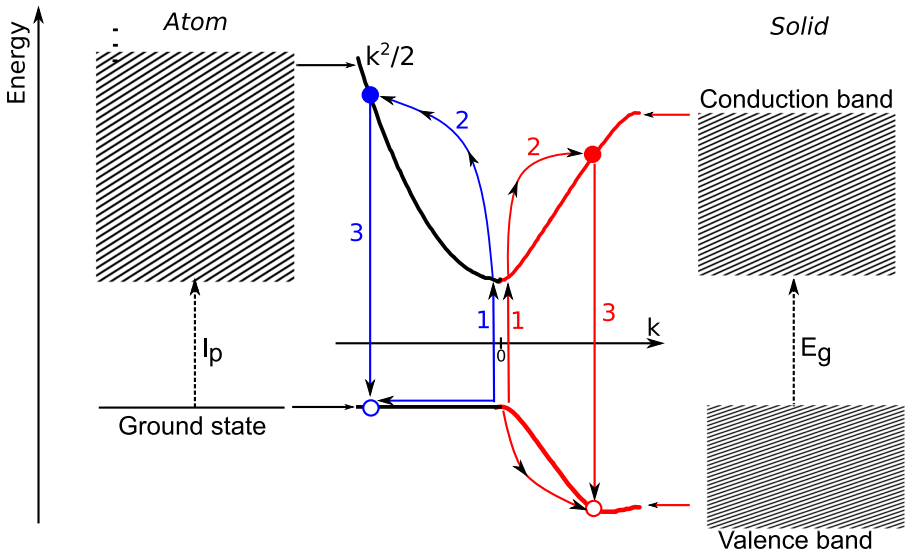

Figure 2.19: Energy diagrams of atoms and solids. In an atom (left), the ground state is a localized energy state, separated by the ionization potential I_p from the continuum states of vacuum (dashed square). In momentum space, the latter is a parabola (black line in the middle). In a solid (right), both ground and excited states form bands (valence and conduction, respectively), separated by the minimum energy gap E_g. They are more complicated functions of momentum (red lines in the middle). High harmonic generation proceeds through creation of an electron-hole pair, labelled (1), blue colors for the atomic case and red for the solid, acceleration of the pair to high momentum (2), and recombination of the electron with the hole (3). Figure extracted from Vampa and Brabec [59].

3

HIGH-ORDER HARMONIC GENERATION IN GAPLESS GRAPHENE

In this chapter we present our findings on the high-order harmonic response of graphene. Starting with the tight-binding hamiltonian of SLG, discussed in chapter 2, we derive in section 3.1 the dynamical equations of the interaction with an electromagnetic field. We also develop an integration approach that overcomes the numerical instabilities associated with the singular dipole matrix elements near the Dirac points, and discuss the dynamics of the Bloch electrons induced by the interaction. In section 3.2 we compute the emission dipole and the harmonic spectra. Sections 3.3 and 3.4 are devoted to study the spectral yield of graphene irradiated by mid-IR intense laser pulses linearly and elliptically polarized, respectively. Finally, we present in section 3.5 a semiclassical model to describe the mechanism for HHG in graphene.

The results and conclusions obtained in this comprehensive study were published in Refs. [106, 107]. These two articles are included as additional information at the end of the chapter in section 3.6.

3.1 THE DYNAMICAL EQUATIONS

Following the framework presented in chapter 2, the dynamics of the Bloch electrons in graphene interacting with an external electromagnetic field can be described by the time-dependent hamiltonian:

$$H(t) = H_o + V_{int}(t), \tag{3.1}$$

where H_o is the tight-binding hamiltonian in the nearest neighbors approximation as given by Eq. (2.32), and $V_{int}(t)$ describes the electric field coupling in the dipole approximation, Eq. (2.68). During the interaction, the electronic wave function can be expressed as a time-dependent superposition of the Bloch wave functions in Eq. (2.34):

$$\begin{aligned} |\Psi(t)\rangle &= \int |\psi_{\mathbf{k}}(t)\rangle \, d\mathbf{k} \\ &= \int \left[C_+(\mathbf{k},t)\,|\Phi^+_{\mathbf{k}}\rangle + C_-(\mathbf{k},t)\,|\Phi^-_{\mathbf{k}}\rangle \right] d\mathbf{k}. \end{aligned} \tag{3.2}$$

The integral is extended over the first Brillouin zone and thus fully includes the specific features of the low energy regions near the Dirac cones discussed in section 2.1.4.

When the duration of the laser pulse is less than the characteristic electron scattering time, which is of the order of several tens of

femtoseconds [108–110], the electron dynamics in the external field is coherent and can be described by the time-dependent Schrödinger equation (TDSE). Otherwise the density matrix formalism should be used instead [98, 111]. Therefore, in our case, the time evolution of the electronic wave function (3.2) is addressed by:

$$i\hbar\frac{\partial}{\partial t}|\Psi(t)\rangle = H(t)\,|\Psi(t)\rangle\,. \tag{3.3}$$

Projecting Eq. (3.3) on the basis of Bloch vectors, we have on the left hand-side:

$$i\hbar\,\langle\Phi^{\pm}_{\mathbf{k}}|\,\frac{\partial}{\partial t}|\Psi(t)\rangle = i\hbar\frac{\partial}{\partial t}C_{\pm}(\mathbf{k},t), \tag{3.4}$$

and, for the right-hand side,

$$\langle\Phi^{\pm}_{\mathbf{k}}|H(t)|\Psi(t)\rangle = \langle\Phi^{\pm}_{\mathbf{k}}|H_o|\Psi(t)\rangle - q_e\,\mathbf{F}(t)\,\langle\Phi^{\pm}_{\mathbf{k}}|\,\hat{\mathbf{r}}\,|\Psi(t)\rangle\,. \tag{3.5}$$

The first term of Eq. (3.5) is the eigenvalue $E_{\pm}(\mathbf{k})$ times the coefficient $C_{\pm}(\mathbf{k},t)$. The second integral involves a more elaborated calculation, but it is also straightforward. Indeed, using Eq. (3.2), we have:

$$\langle\Phi^{\pm}_{\mathbf{k}}|\,\hat{\mathbf{r}}\,|\Psi(t)\rangle = \int C_{+}(\mathbf{k}',t)\,\langle\Phi^{\pm}_{\mathbf{k}}|\,\hat{\mathbf{r}}\,|\Phi^{+}_{\mathbf{k}'}\rangle\,d\mathbf{k}' + \int C_{-}(\mathbf{k}',t)\,\langle\Phi^{\pm}_{\mathbf{k}}|\,\hat{\mathbf{r}}\,|\Phi^{-}_{\mathbf{k}'}\rangle\,d\mathbf{k}'. \tag{3.6}$$

Let us then calculate the first matrix element $\langle\Phi^{+}_{\mathbf{k}}|\,\hat{\mathbf{r}}\,|\Phi^{+}_{\mathbf{k}'}\rangle$. Using Eq. (2.33):

$$\begin{aligned}\langle\Phi^{+}_{\mathbf{k}}|\,\hat{\mathbf{r}}\,|\Phi^{+}_{\mathbf{k}'}\rangle &= \frac{1}{2}\left[1+e^{i(\varphi_{\mathbf{k}}-\varphi_{\mathbf{k}'})}\right]\int e^{-i(\mathbf{k}-\mathbf{k}')\cdot\mathbf{r}}\,\mathbf{r}\cdot d\mathbf{r}\\ &= \frac{1}{2i}\left[1+e^{i(\varphi_{\mathbf{k}}-\varphi_{\mathbf{k}'})}\right]\nabla_{\mathbf{k}'}\delta(\mathbf{k}-\mathbf{k}').\end{aligned} \tag{3.7}$$

Therefore, the first integral in Eq. (3.6) reads as:

$$\begin{aligned}&\int C_{+}(\mathbf{k}',t)\,\langle\Phi^{+}_{\mathbf{k}}|\,\hat{\mathbf{r}}\,|\Phi^{+}_{\mathbf{k}'}\rangle\,d\mathbf{k}' =\\ &\quad\frac{1}{2i}\nabla_{\mathbf{k}'}\left\{\int C_{+}(\mathbf{k}',t)\left[1+e^{i(\varphi_{\mathbf{k}}-\varphi_{\mathbf{k}'})}\right]\delta(\mathbf{k}-\mathbf{k}')d\mathbf{k}'\right\}\\ &\qquad-\frac{1}{2i}\int\nabla_{\mathbf{k}'}\left\{C_{+}(\mathbf{k}',t)\left[1+e^{i(\varphi_{\mathbf{k}}-\varphi_{\mathbf{k}'})}\right]\right\}\delta(\mathbf{k}-\mathbf{k}')d\mathbf{k}'\\ &\qquad= i\,\nabla_{\mathbf{k}}C_{+}(\mathbf{k},t)+\frac{1}{2}C_{+}(\mathbf{k},t)\nabla_{\mathbf{k}}\varphi_{\mathbf{k}}\,.\end{aligned} \tag{3.8}$$

Similarly, we have:

$$\begin{aligned}&\int C_{+}(\mathbf{k}',t)\,\langle\Phi^{-}_{\mathbf{k}}|\,\hat{\mathbf{r}}\,|\Phi^{+}_{\mathbf{k}'}\rangle\,d\mathbf{k}' =\\ &\quad\frac{1}{2i}\nabla_{\mathbf{k}'}\left\{\int C_{+}(\mathbf{k}',t)\left[-1+e^{i(\varphi_{\mathbf{k}}-\varphi_{\mathbf{k}'})}\right]\delta(\mathbf{k}-\mathbf{k}')d\mathbf{k}'\right\}\\ &\qquad-\frac{1}{2i}\int\nabla_{\mathbf{k}'}\left\{C_{+}(\mathbf{k}',t)\left[-1+e^{i(\varphi_{\mathbf{k}}-\varphi_{\mathbf{k}'})}\right]\right\}\delta(\mathbf{k}-\mathbf{k}')d\mathbf{k}'\\ &\qquad=\frac{1}{2}C_{+}(\mathbf{k},t)\nabla_{\mathbf{k}}\varphi_{\mathbf{k}}\,.\end{aligned} \tag{3.9}$$

In addition, note that the matrix elements of the second integral in Eq. (3.6) are calculated in the same way, leading to:

$$\int C_-(\mathbf{k}',t)\,\langle\Phi^-_{\mathbf{k}}|\,\hat{\mathbf{r}}\,|\Phi^-_{\mathbf{k}'}\rangle\,d\mathbf{k}' = i\,\nabla_{\mathbf{k}}C_-(\mathbf{k},t) + \frac{1}{2}C_-(\mathbf{k},t)\nabla_{\mathbf{k}}\varphi_{\mathbf{k}} \tag{3.10}$$

and

$$\int C_-(\mathbf{k}',t)\,\langle\Phi^+_{\mathbf{k}}|\,\hat{\mathbf{r}}\,|\Phi^-_{\mathbf{k}'}\rangle\,d\mathbf{k}' = \frac{1}{2}C_+(\mathbf{k},t)\nabla_{\mathbf{k}}\varphi_{\mathbf{k}}. \tag{3.11}$$

Grouping and rearranging terms, Eq. (3.4) corresponds to the following set of coupled two-level equations:

$$\begin{aligned} i\hbar\frac{\partial}{\partial t}C_+(\mathbf{k},t) &= [E_+(\mathbf{k}) - \mathbf{F}(t)\cdot\mathbf{D}(\mathbf{k})]\,C_+(\mathbf{k},t) \\ &\quad - i\,q_e\,\mathbf{F}(t)\cdot\nabla_{\mathbf{k}}C_+(\mathbf{k},t) - \mathbf{F}(t)\cdot\mathbf{D}(\mathbf{k})C_-(\mathbf{k},t), \end{aligned} \tag{3.12}$$

$$\begin{aligned} i\hbar\frac{\partial}{\partial t}C_-(\mathbf{k},t) &= [E_-(\mathbf{k}) - \mathbf{F}(t)\cdot\mathbf{D}(\mathbf{k})]\,C_-(\mathbf{k},t) \\ &\quad - i\,q_e\,\mathbf{F}(t)\cdot\nabla_{\mathbf{k}}C_-(\mathbf{k},t) - \mathbf{F}(t)\cdot\mathbf{D}(\mathbf{k})C_+(\mathbf{k},t), \end{aligned} \tag{3.13}$$

where

Transition matrix element

$$\mathbf{D}(\mathbf{k}) = \langle\Phi^+_{\mathbf{k}}|\,q_e\,\hat{\mathbf{r}}\,|\Phi^-_{\mathbf{k}}\rangle = \frac{q_e}{2}\nabla_{\mathbf{k}}\varphi_{\mathbf{k}}. \tag{3.14}$$

is the transition matrix element between the conduction and valence band states with wave vector $\mathbf{k}$ [112, 113].

The last term in the right hand side of both Eqs. (3.12) and (3.13) couples the conduction and valence bands and hence, leads to *interband* transitions, whilst the other terms in the equations are *intraband*. Therefore, the electric field $\mathbf{F}(t)$ of the optical pulse introduces both intraband and interband dynamics in the electron evolution. Physically, the interband dynamics couples states with the same wave vector $\mathbf{k}$ and results in the redistribution of the electronic population between the valence and conduction bands, whereas the intraband dynamics induced by the electric field quivers the electrons inside the bands according to the acceleration theorem, which describes the motion of Bloch electrons in external electomagnetic fields [114]:

$$\hbar\frac{d\mathbf{k}}{dt} = q_e\,\mathbf{F}(t). \tag{3.15}$$

Note that the acceleration theorem is universal and does not depend on the actual shape of the bands. Consequently, the intraband oscillations are the same for the conduction and valence bands [112]. The acceleration theorem can be used to simplify Eqs. (3.12) and (3.13) by re-expressing the wave functions in terms of the time-dependent basis of Houston states. Thus, a Bloch electron with initial quasimomentum $\mathbf{k}$ is described by the time-dependent wave vector $\boldsymbol{\kappa}_t$, the *kinetic quasimomentum*, which is given by the solution of Eq. (3.15) [115]:

$$\boldsymbol{\kappa}_t = \mathbf{k} + \frac{q_e}{\hbar}\int_{-\infty}^{t}\mathbf{F}(\tau)\,d\tau. \tag{3.16}$$

Therefore, the Bloch states can be rewritten as Houston states $|\Phi^{(H)}_{\pm,\mathbf{k}}(t)\rangle$ [115]:

$$|\Phi^{(H)}_{\pm,\mathbf{k}}(t)\rangle = e^{-\frac{i}{\hbar}\int_{-\infty}^{t} E_{\pm}(\boldsymbol{\kappa}_\tau)d\tau}\,|\Phi^{\pm}_{\boldsymbol{\kappa}_t}\rangle\,, \tag{3.17}$$

which allows to express the general solution of the TDSE as:

$$|\psi_{\mathbf{k}}(t)\rangle = C_+(\boldsymbol{\kappa}_t,t)\,|\Phi^{+}_{\boldsymbol{\kappa}_t}\rangle + C_-(\boldsymbol{\kappa}_t,t)\,|\Phi^{-}_{\boldsymbol{\kappa}_t}\rangle\,. \tag{3.18}$$

The dynamical equations

Inserting Eq. (3.18) in Eq. (3.3), and projecting onto $\langle\Phi^{(H)}_{\pm}|$ leads to the following system of differential equations:

$$\begin{aligned} i\hbar\frac{d}{dt}C_+(\boldsymbol{\kappa}_t,t) &= [E_+(\boldsymbol{\kappa}_t) - \mathbf{F}(t)\cdot\mathbf{D}(\boldsymbol{\kappa}_t)]\,C_+(\boldsymbol{\kappa}_t,t) \\ &\quad -\mathbf{F}(t)\cdot\mathbf{D}(\boldsymbol{\kappa}_t)C_-(\boldsymbol{\kappa}_t,t), \end{aligned} \tag{3.19}$$

$$\begin{aligned} i\hbar\frac{d}{dt}C_-(\boldsymbol{\kappa}_t,t) &= [E_-(\boldsymbol{\kappa}_t) - \mathbf{F}(t)\cdot\mathbf{D}(\boldsymbol{\kappa}_t)]\,C_-(\boldsymbol{\kappa}_t,t) \\ &\quad -\mathbf{F}(t)\cdot\mathbf{D}(\boldsymbol{\kappa}_t)C_+(\boldsymbol{\kappa}_t,t), \end{aligned} \tag{3.20}$$

which correspond to a driven parametric oscillator with a pumping operating through the periodic variation of the energy and the transition matrix elements. Note that, using the Houston transformation, the gradients $\nabla_{\mathbf{k}}$ in Eqs. (3.12) and (3.13) are not present in Eqs. (3.19) and (3.20), which greatly simplifies the integration. The Houston approach is equivalent to the Volkov transformation for Bloch states [116], as we highlighted in [106].

The components of interband coupling $\mathbf{D}(\mathbf{k})$ are given by [112, 113]:

$$D_x(\mathbf{k}) = -\frac{a\,q_e}{2\sqrt{3}}\frac{1+\cos\left(\frac{a\,k_y}{2}\right)\left[\cos\left(\frac{\sqrt{3}a\,k_x}{2}\right)-2\cos\left(\frac{a\,k_y}{2}\right)\right]}{1+4\cos\left(\frac{a\,k_y}{2}\right)\left[\cos\left(\frac{\sqrt{3}a\,k_x}{2}\right)+\cos\left(\frac{a\,k_y}{2}\right)\right]} \tag{3.21}$$

and

$$D_y(\mathbf{k}) = -\frac{a\,q_e}{2}\frac{\sin\left(\frac{a\,k_y}{2}\right)\sin\left(\frac{\sqrt{3}a\,k_x}{2}\right)}{1+4\cos\left(\frac{a\,k_y}{2}\right)\left[\cos\left(\frac{\sqrt{3}a\,k_x}{2}\right)+\cos\left(\frac{a\,k_y}{2}\right)\right]}. \tag{3.22}$$

The dependence of D_x with the wave vector $\mathbf{k}$ is shown in Fig. 3.1. The components of the matrix element are singular near the Dirac points K and K′ and take small values away from them, being zero at the center of the first Brillouin zone (point Γ). Therefore, there is a strong interband coupling near the Dirac points.

Off-diagonal transformation

The numerical integration of the dynamical equations (3.19) and (3.20) is of difficult convergence due to the singular values of $\mathbf{D}(\mathbf{k})$ near the Dirac points. Nevertheless, it is possible to recast these equations avoiding the explicit divergences of $\mathbf{D}(\boldsymbol{\kappa}_t)$ using the transformation introduced in Ref. [106], which effectively undoes the diagonalization of H_o:

$$C^M(\boldsymbol{\kappa}_t,t) = C_+(\boldsymbol{\kappa}_t,t) - C_-(\boldsymbol{\kappa}_t,t), \tag{3.23}$$

$$C^P(\boldsymbol{\kappa}_t,t) = e^{-i\varphi_{\boldsymbol{\kappa}_t}}\left[C_+(\boldsymbol{\kappa}_t,t) + C_-(\boldsymbol{\kappa}_t,t)\right], \tag{3.24}$$

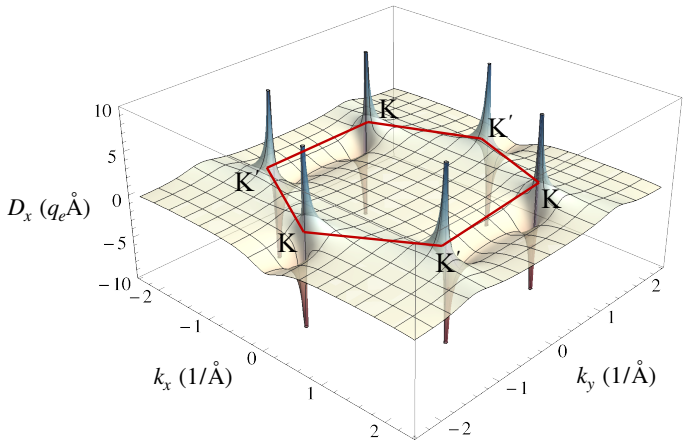

Figure 3.1: Interband transition matrix element D_x along graphene's first Brillouin zone. The red lines show the boundary of the BZ. The dipole matrix element is singular near the Dirac points.

where $\varphi_{\boldsymbol{\kappa}_t}$ is the phase of $f(\boldsymbol{\kappa}_t)$. With this transformation, Eqs. (3.19) and (3.20) can be recast into the following set of differential equations:

Integration scheme for the dynamical equations

$$i\hbar\frac{d}{dt}C^M(\boldsymbol{\kappa}_t,t) = \frac{E_+(\boldsymbol{\kappa}_t)+E_-(\boldsymbol{\kappa}_t)}{2}\,C^M(\boldsymbol{\kappa}_t,t) + \frac{E_+(\boldsymbol{\kappa}_t)-E_-(\boldsymbol{\kappa}_t)}{2}\,e^{i\varphi_{\boldsymbol{\kappa}_t}}C^P(\boldsymbol{\kappa}_t,t) \tag{3.25}$$

$$i\hbar\frac{d}{dt}C^P(\boldsymbol{\kappa}_t,t) = \frac{E_+(\boldsymbol{\kappa}_t)+E_-(\boldsymbol{\kappa}_t)}{2}\,C^P(\boldsymbol{\kappa}_t,t) + \frac{E_+(\boldsymbol{\kappa}_t)-E_-(\boldsymbol{\kappa}_t)}{2}\,e^{-i\varphi_{\boldsymbol{\kappa}_t}}C^M(\boldsymbol{\kappa}_t,t). \tag{3.26}$$

Note that this set of equations circumvent the numerical instabilities of Eqs. (3.19) and (3.20), since all the terms containing $\mathbf{D}(\mathbf{k})$ are removed. However, the interband coupling is still completely retained in the phase $\varphi_{\boldsymbol{\kappa}_t}$.

An example of the complex electron dynamics arising upon the interaction of graphene with an intense ultrashort laser pulse is shown in Fig. 3.2, where the occupation density $\mathcal{N}_{CB} = |C_+(\mathbf{k},t)|^2$ in the conduction band is depicted at different times during the interaction. The laser pulse is modeled using an 8-cycle (full width) $\sin^2$ temporal envelope, 2.9 cycles FWHM, linearly polarized along the x axis. The total field is then defined as:

$$F(t) = F_o \sin^2(\pi t/8T)\sin(\omega_o t), \tag{3.27}$$

for $0 \leqslant t \leqslant 8T$ and 0 elsewhere, being F_o the field amplitude, T the period, and $\omega_o = 2\pi/T$ the field frequency. As for Fig. 3.2 we have chosen a near infrared pulse 21.6 fs long, with $\lambda = 800$ nm and $F_o = 2.0$ V/Å, corresponding to a peak intensity of 5.5×10^{13} W/cm^2.

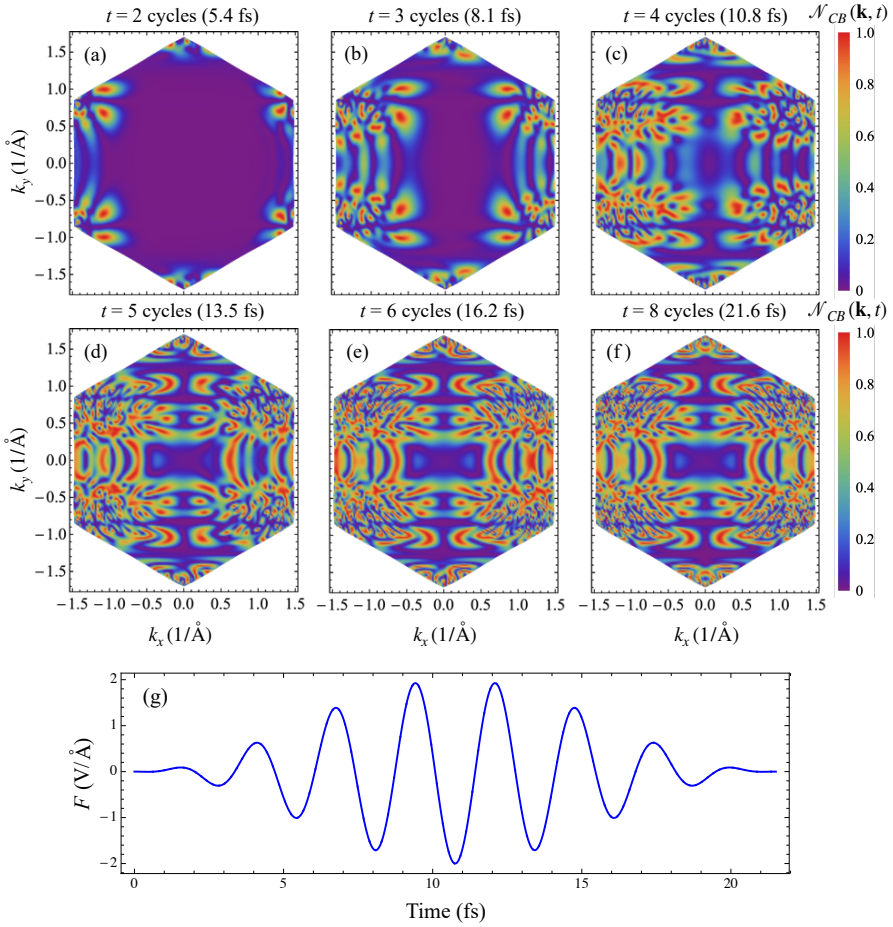

Figure 3.2: (a)-(f) Conduction band population $\mathcal{N}_{CB}$ as a function of the wave vector at different moments of the interaction between the graphene sheet and an ultrashort intense laser pulse linearly polarized along the x direction, shown in panel (g). Only the first Brillouin zone of the reciprocal space is shown. Different colors correspond to different values of the conduction band population.

According to the discussion above, the electrons are accelerated by the field along its polarization direction, as given by Eq. (3.16), quivering in the reciprocal space with amplitude $-q_e\mathbf{A}(t)/\hbar c$. Eventually, the electrons in the valence band that reach the vicinity of the Dirac points are kicked to the conduction band by the singularity of the interband matrix element $\mathbf{D}(\mathbf{k})$ near these points. During the first two cycles of the pulse – panel (a) – when the field amplitude is not too large, this dynamics is clearly observed with areas of high electron population near the Dirac points and interference fringes generated as the electrons quiver back and forth. Additional electrons are promoted as the pulse evolves and the field amplitude increases, see panels (b) and (c) corresponding to three and four field cycles, causing the dispersion of the high populated areas. Panels (d) to (f) correspond to

the last half of the pulse, when the field has reached its maximum amplitude and the high-population areas are spread over the whole first Brillouin zone. After the sixth cycle – panel (e) – the excitation saturates the probability distribution, becoming completely symmetric at the end of the pulse (21.6 fs), see panel (f). The remaining population at the conduction band after the pulse ends is modulated by interference fringes and it is relatively long lived, decaying by electron collisions in times of the order of tens of femtoseconds [113].

As a final remark to this section, we may point out that it is considered that the derivation of the dynamical equations (3.19) and (3.20), which are independent of the intraband gradients, and the approach to their integration by means of the transformation (3.23) and (3.24), are fundamental original achievements of this predoctoral work and were published in Ref. [106], see section 3.6.1.

3.2 THE EMISSION DIPOLE OF GRAPHENE

As shown in section 3.1, the wave function $\Psi(\mathbf{r}, t)$ of the electron in the periodic potential of graphene during the interaction with an external electric field is given by Eq. (3.2) upon resolution of the dynamical equations (3.19) and (3.20) for the probability coefficients $C_+(\mathbf{k}, t)$ and $C_-(\mathbf{k}, t)$ at every point in the first Brillouin zone. The electron is accelerated back and forth under the combination of the Coulomb interaction with the graphene network and the force exerted by the driving field. As a consequence, the electron emits radiation in the form of electromagnetic waves. In the dipole approximation and in the non-relativistic regime, the power radiated $P(t)$ is given by the Larmor's semiclassical formula [117]:

$$P(t) = \frac{2}{3c^3}|\mathbf{a}(t)|^2 \tag{3.28}$$

where $\mathbf{a}(t)$ is the acceleration of the electric dipole, i. e. the second time derivative of the expectation value

$$\mathbf{d}(t) = \langle \Psi(t)|\, q_e\, \hat{\mathbf{r}}\, |\Psi(t)\rangle\,. \tag{3.29}$$

The emission spectra is then given in terms of the Fourier transform of the dipole acceleration by [118]:

$$P(\omega) = \frac{4}{3c^3}|\mathbf{a}(\omega)|^2. \tag{3.30}$$

Let us calculate the expectation value of $\mathbf{d}(t)$ as given by Eq. (3.29):

$$\begin{aligned}\mathbf{d}(t) = &\int C_+^*(\mathbf{k},t)C_+(\mathbf{k}',t)\,\langle\Phi_{\mathbf{k}}^+|\,q_e\,\hat{\mathbf{r}}\,|\,\Phi_{\mathbf{k}'}^+\rangle\,d\mathbf{k}d\mathbf{k}' \\ &+\int C_+^*(\mathbf{k},t)C_-(\mathbf{k}',t)\,\langle\Phi_{\mathbf{k}}^+|\,q_e\,\hat{\mathbf{r}}\,|\,\Phi_{\mathbf{k}'}^-\rangle\,d\mathbf{k}d\mathbf{k}' \\ &+\int C_-^*(\mathbf{k},t)C_+(\mathbf{k}',t)\,\langle\Phi_{\mathbf{k}}^-|\,q_e\,\hat{\mathbf{r}}\,|\,\Phi_{\mathbf{k}'}^+\rangle\,d\mathbf{k}d\mathbf{k}' \\ &+\int C_-^*(\mathbf{k},t)C_-(\mathbf{k}',t)\,\langle\Phi_{\mathbf{k}}^-|\,q_e\,\hat{\mathbf{r}}\,|\,\Phi_{\mathbf{k}'}^-\rangle\,d\mathbf{k}d\mathbf{k}'. \end{aligned} \tag{3.31}$$

The integrals in $d\mathbf{k}'$ have been already calculated above, see Eqs. (3.8) and (3.9), so that we can write:

$$\begin{aligned}\mathbf{d}(t) = i\,q_e &\int \left[C_+^*(\mathbf{k},t)\nabla_{\mathbf{k}}C_+(\mathbf{k},t) + C_-^*(\mathbf{k},t)\nabla_{\mathbf{k}}C_-(\mathbf{k},t)\right]d\mathbf{k} \\ &+\int \mathbf{D}(\mathbf{k})\left[C_+^*(\mathbf{k},t)C_+(\mathbf{k},t) + C_-^*(\mathbf{k},t)C_-(\mathbf{k},t)\right]d\mathbf{k} \\ &+\int \mathbf{D}(\mathbf{k})\left[C_+(\mathbf{k},t)C_-^*(\mathbf{k},t) + C_+^*(\mathbf{k},t)C_-(\mathbf{k},t)\right]d\mathbf{k}. \end{aligned} \tag{3.32}$$

The first term of Eq. (3.32), which does not depend on $\mathbf{D}(\mathbf{k})$, can be interpreted as the intraband component of the emission dipole. On the other hand, note that the second term is independent of time as a consequence of the normalization condition $|C_+(\mathbf{k},t)|^2 + |C_-(\mathbf{k},t)|^2 = 1$, therefore it does not contribute to the dipole acceleration. Finally, the third term is associated to interband transitions. We can write $\mathbf{d}(t)$ in a more compact form in terms of the kinetic quasimomentum $\boldsymbol{\kappa}_t$ and the off-diagonal coefficients C^M and C^P. Thus, substituting $\mathbf{k} \to \boldsymbol{\kappa}_t$ and introducing Eqs. (3.23) and (3.24) in Eq. (3.32), we obtain after some manipulation:

Emission dipole

$$\mathbf{d}(t) = i\,\frac{q_e}{2}\int \left[C^{M*}(\boldsymbol{\kappa}_t,t)\nabla_{\boldsymbol{\kappa}_t}C^M(\boldsymbol{\kappa}_t,t) + C^{P*}(\boldsymbol{\kappa}_t,t)\nabla_{\boldsymbol{\kappa}_t}C^P(\boldsymbol{\kappa}_t,t)\right]d\mathbf{k}. \tag{3.33}$$

Intraband component

The intraband contribution to the total acceleration $\mathbf{a}_{\leftrightarrow}$ can be computed as:

$$\mathbf{a}_{\leftrightarrow}(t) = \frac{{q_e}^2}{\hbar^2}\mathbf{F}(t)\int \left[|C_+(\boldsymbol{\kappa}_t,t)|^2\frac{\partial^2 E_+(\boldsymbol{\kappa}_t)}{\partial\boldsymbol{\kappa}_t^2} + |C_-(\boldsymbol{\kappa}_t,t)|^2\frac{\partial^2 E_-(\boldsymbol{\kappa}_t)}{\partial\boldsymbol{\kappa}_t^2}\right]d\mathbf{k}. \tag{3.34}$$

3.3 HIGH-ORDER HARMONIC SPECTRA OF GRAPHENE

The red-filled area in Fig. 3.3(a) shows a typical high-order harmonic spectrum from graphene, calculated after integration of Eqs. (3.25), (3.26) and (3.33), considering a driving field of 3 μm wavelength at 5.1×10^{12} W/cm^2 peak intensity, linearly polarized along the y direction. The laser pulse is modeled as given by Eq. (3.27), with $F_o = 0.6$

V/Å. The spectrum shows the characteristic non-perturbative features of HHG, with a clear emergence of the spectral plateau extending, in this case, up to a maximum (cut-off) frequency $\sim 41\omega_o$, being ω_o the driving laser's fundamental frequency. Note that the spectral

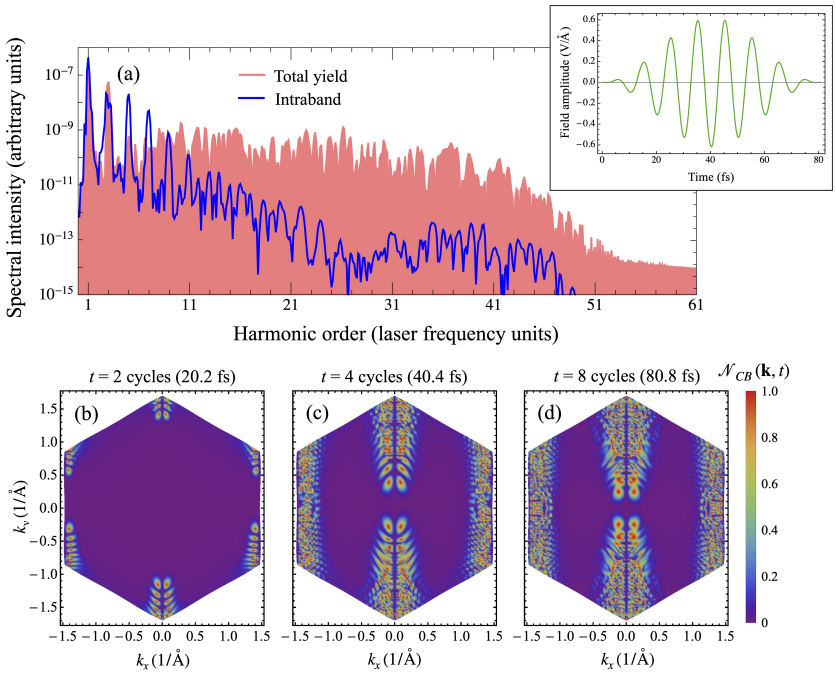

Figure 3.3: (a) HHG spectrum from SLG driven by a 3 μm wavelength, 28 fs (2.9 cycles) FWHM pulse at 5.1×10^{12} W/cm^2 peak intensity and linearly polarized along the y direction (red-filled area). The intraband component of the total yield is represented as a blue line. The inset shows the amplitude of the electric field of the pulse as a function of time. (b)–(d) Conduction band population $\mathcal{N}_{CB}$ as a function of the wave vector at different moments of the interaction between graphene and the ultrashort laser pulse.

content in Fig. 3.3(a) is quite rich, as a result of different electron-hole pair's trajectories leading to the same harmonic, as we shall discuss in section 3.5, and also due to the interference of the intraband and interband contributions to the emission dipole. The intraband component (blue line) has a strong influence in the lower-order harmonic response, but becomes negligible with respect to the interband contribution in the region of the spectral plateau, where it exhibits a typical perturbative behaviour. This result is consistent with the findings of previous studies on finite gap crystals, which show that the intraband contribution dominates the harmonic emission of low order harmonics, while the interband dominates for the higher frequency spectrum [17, 65, 66].

Panels (b)–(d) of Fig. 3.3 show the occupation density $\mathcal{N}_{CB}$ in the conduction band at different times during the interaction. Consistent to the case presented in Fig. 3.2, electrons are accelerated by the field

along the polarization direction. During the first two cycles of the pulse, when the field amplitude is not too large, the electrons populate the conduction band close to the Dirac points and generate interference fringes along the y direction, see panel (b). As the pulse evolves and the intensity increases, more electrons are promoted to the conduction band, see panels (c) and (d). The high-population areas and the interference fringes disperse up to almost reach the center of the Brillouin zone, where the energy gap is maximum. Note that the distribution becomes symmetric at the end of the pulse, as it happens in Fig. 3.2(f).

The time-frequency analysis of the spectrum gives us further insight into the HHG process. As can be seen in Fig. 3.4, during the first three cycles the harmonics are emitted at every half-cycle of the field. As the intensity increases, high-order harmonics are being emitted over the whole cycle. Note that the lower harmonics are clearly observed every half-cycle during the whole pulse, but the higher orders only appear at the central part of the pulse, once the population of electrons in the conduction band is spread over the Brillouin zone. Noticeably, the time-frequency chart obtained from graphene is much more complex and less structured than that obtained from gas systems, as shown in Fig. 2.17. The spectral efficiency in the former shows no particular trend as a function of the generation time, as it is the case of the latter. This evidence suggests that the underlying physics behind HHG in graphene is different from that of these other well-studied systems. This topic will be later discussed in section 3.5.

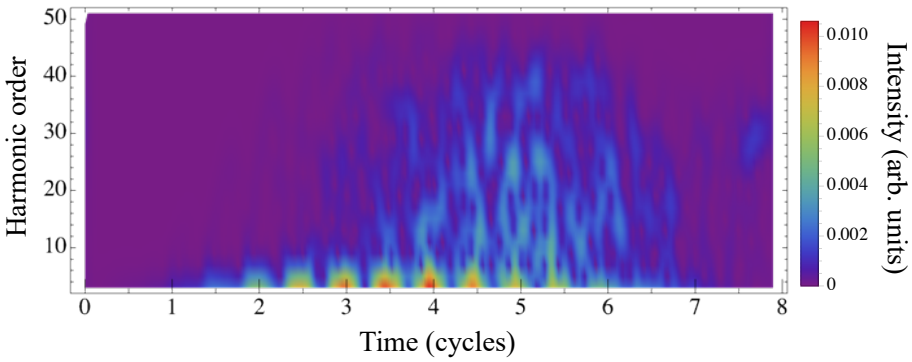

Figure 3.4: Time-frequency analysis for the spectral yield shown in Fig. 3.3(a), calculated with a $3\omega_o$ gaussian spectral window.

As discussed in [119], the power scaling p_q of HHG in graphene is lower than the harmonic order ($p_q < q$) and almost constant for all the harmonics in the plateau region ($p_q = q$), a behaviour also found in gases, which reflects the non-perturbative nature of the process [120–123].

We show in Figs. 3.5, 3.6 and 3.7 the high-harmonic spectra at different peak intensities of the driving field for laser wavelengths 800 nm, 1.6 μm and 3.0 μm, respectively. In the near infrared regime (Fig. 3.5), the HHG spectrum shows the typical perturbative behavior for the lowest intensity: a monotonous decrease of efficiency with increasing harmonic order, see panel (a). This behaviour changes drastically in

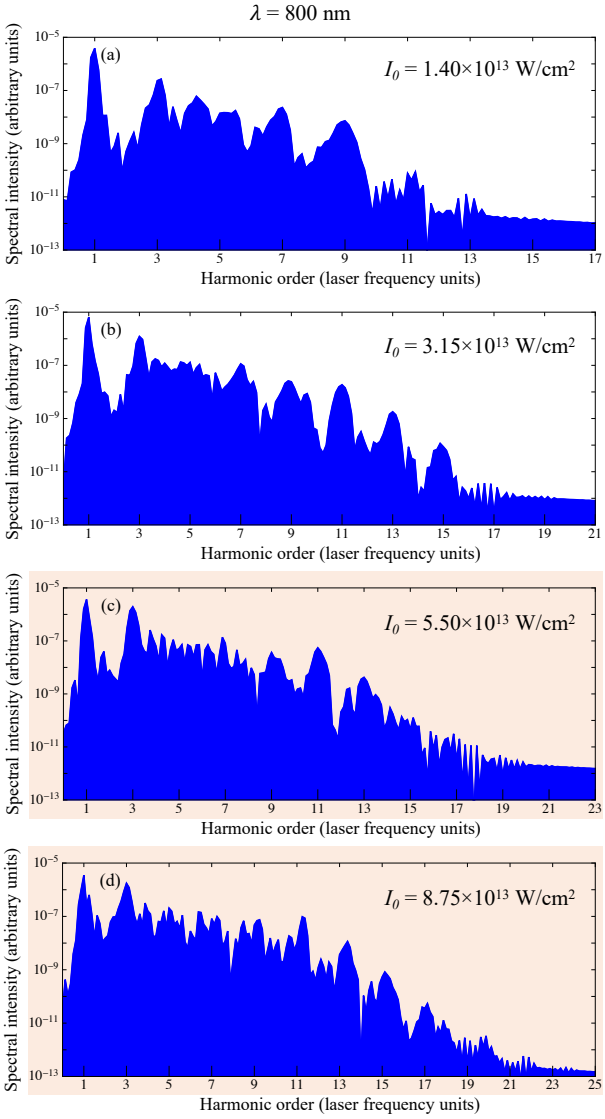

Figure 3.5: High-order harmonic yield from single layer graphene driven by an 800 nm, 8 fs FWHM pulse at different peak intensities. The colored background of panels (c) and (d) indicates intensities above the threshold damage of graphene. For 800 nm, therefore, the saturated cut-off frequency $\sim 11\omega_o$ is reached above the threshold damage.

panels (b)–(d) for driving fields at higher intensities, where the emergence of the non-perturbative plateau is clearly observed. Notwithstanding, this characteristic feature of the HHG spectra appears, even

at lower laser intensities, if the wavelength of the driving field is increased to the mid-infrared regime, as shown in Figs. 3.6 and 3.7.

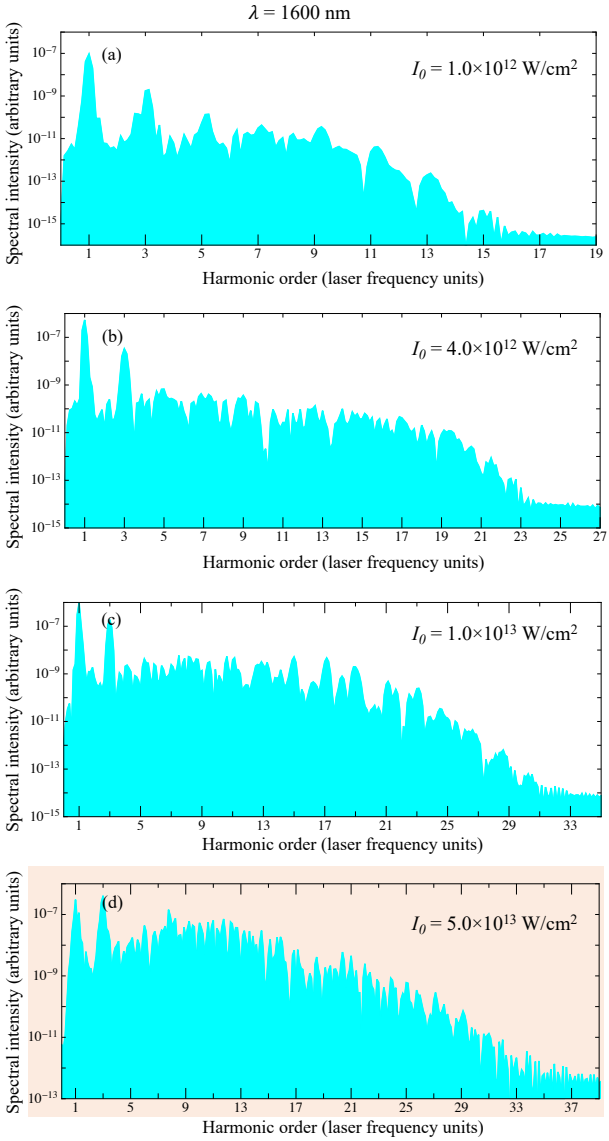

Figure 3.6: HHG spectra from single layer graphene driven by a 1600 nm, 16 fs FWHM pulse at different peak intensities. The saturated cut-off is this case $\sim 23\omega_0$. The colored background of panel (d) indicates that the intensity is above the threshold damage.

Fig. 3.8 depicts the scaling of the cut-off frequency with the driving field intensity for pulses with 3.0 μm wavelength.[1] Note that the cut-off frequency saturates at the largest intensities, the saturated cut-off corresponding to a photon energy of $\simeq$ 17.8 eV, which coincides with the maximum gap in the BZ (point Γ). This saturation has also been

1 The cut-off scalings with intensity for all pulses discussed in this section are shown in Fig. 3 of Ref. [106], which is one of the papers produced in this research. The full text is included at the end of this chapter in section 3.6.1.

described in gap semiconductors [59] and, unlike the gaseous systems discussed in section 2.4.2, there is no simple law (linear or quadratic) describing the dependence of the scaling of the cut-off frequency with the field intensity. This is another clear indication that the mechanism for HHG in solids is different to that reported for simpler systems.

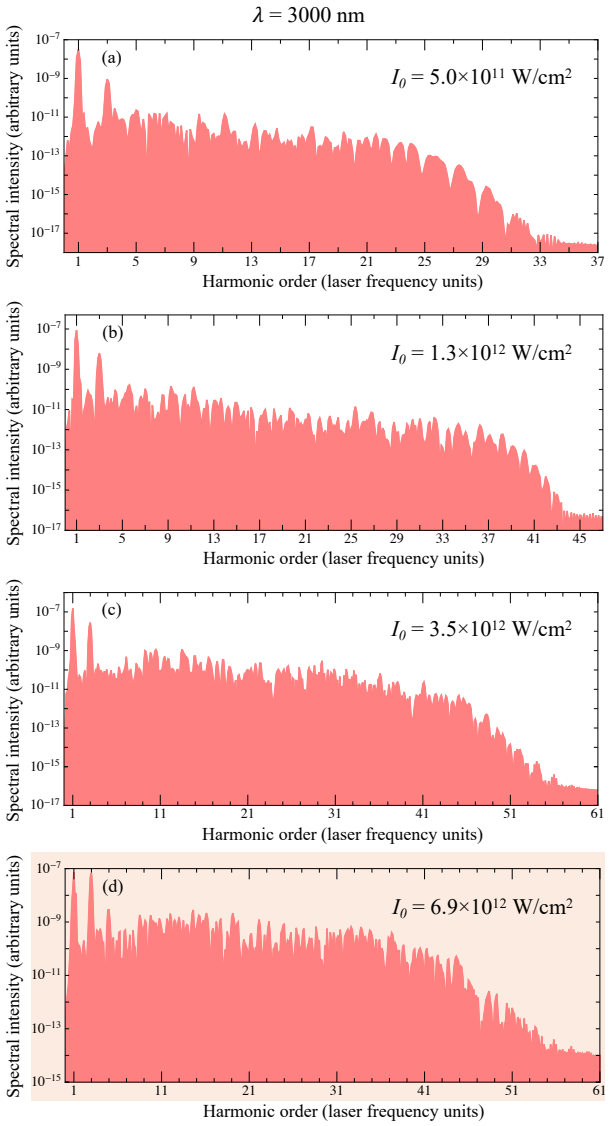

Figure 3.7: Harmonic yield from single layer graphene for $\lambda = 3\mu m$. In this case, the pulse is the same as that used for Fig. 3.3. The cut-off is reached at $\sim 41\omega_0$. Only panel (d) is above the threshold damage.

Note however that the use of arbitrary large intensities is precluded by the damage of the sample. We indicate with a colored background of Figs. 3.5 to 3.8 the intensities for which the material is expected to be damaged, assuming a damage fluence-threshold of 150 mJ/cm^2 [124]. Observe that in the mid-infrared regime it is possible to reach the saturated cut-off at intensities below the damage threshold. How-

ever, as the laser period increases, the decoherence due to carrier collisions, typically of several tens of fs [125], becomes a limitation. This trade-off indicates that the HHG production is more favorable at mid-IR wavelengths in the short-cycle regime.

In summary, three main conclusions can be already drawn from our study of HHG in graphene: (i) the emergence of a spectral plateau at large intensities, (ii) a nontrivial cut-off dependence with the intensity, and (iii) a saturation of the photon energy with the intensity, close to the maximum energy gap of the material. As we shall see in section 3.5, the interpretation of these conclusions will guide us to unveil the fundamental mechanism for HHG in graphene.

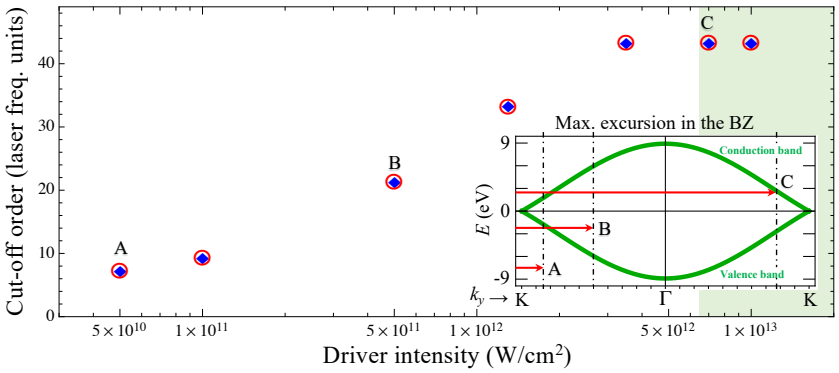

Figure 3.8: Cut-off scaling with intensity in graphene irradiated by an 8-cycle mid-IR pulse with 3µm wavelength. The blue diamonds are the result of the numerical integration of the TDSE. The red circles are given by the semiclassical SPAM considering that the electron-hole pair is created at the Dirac points. The green filled area corresponds to intensities above damage threshold. The inset shows the gap energy during the e-h excursion. The maximum excursion at intensity points A, B and C in the main panel is represented by red arrows in the inset.

3.4 POLARIZATION CONTROL OF HIGH-ORDER HARMONICS

High harmonic generation in atomic or molecular targets also provides a robust mechanism to produce coherent ultrashort pulses with controllable polarization in the extreme-ultraviolet. Although for a long time HHG was thought to be restricted to produce linearly polarized harmonics, several techniques have recently succeeded in generating elliptically and circularly polarized harmonics in atomic gases, using rather sophisticated configurations [126, 127]. It has been reported that HHG in solids is sensitive to the orientation of the electric field relative to the crystal axis [128]. Recent reports revealed also that HHG in graphene is enhanced by elliptically polarized excitations [16], and that circular-polarized harmonics can be obtained from circular-polarized drivers [130]. In this context, we have carried on

a detailed theoretical study of the polarization characteristics of the harmonics induced by few-cycle infrared laser pulses, as a function of the driver polarization parameters. We have analyzed the ellipticity, tilt angle and intensity of the harmonics when driven by laser pulses with different polarizations and orientations. The calculations have been performed considering a 3 μm wavelength, 8-cycle (full width) driving pulse with $\sin^2$ temporal envelope, modeled as:

$$\mathbf{F}(t) = \sin^2(\pi t/8T)\left[F_x \sin(\omega_o t)\mathbf{u}_x + F_y \sin(\omega_o t + \Delta\phi)\mathbf{u}_y\right] \tag{3.35}$$

where F_x and F_y are the cartesian components of the field amplitude, T is the period, $\omega_o = 2\pi/T$ the field frequency, and $\Delta\phi$ the relative phase between the field components. The pulse duration is 28 fs (2.9 cycles) FWHM, smaller than the decoherence time due to carrier collisions [108–110]. We have considered a peak intensity of 5×10^{10} W/cm^2, well below the threshold damage [124].

We first have focused in the dependence of the non-linear response of SLG to a linearly-polarized field, i. e. $\Delta\phi = 0$ in Eq. (3.35), with different tilts. Figure 3.9(a) shows the calculated spectra for different values of the tilt angle $\theta = \arctan(F_x/F_y)$, obtained by the addition of the spectral components $I_x(\theta, \omega)$ and $I_y(\theta, \omega)$. The response shows the typical non-perturbative behaviour up to the seventh harmonic order, followed by a cut-off. These results are in good agreement with the experimental observations reported in [16], where HHG was observed up to the ninth harmonic. The fact that the spectra shown in Fig. 3.9(a) are not identical demonstrates the anisotropic nature of the optical response of SLG under intense laser fields.

Figure 3.9(b) shows the dependence of the harmonic ellipticity ε_q with respect to the driver's linear polarization direction. The ellipticity of the q-th harmonic is derived from the Stokes parameters $\{S_0^q, S_1^q, S_2^q, S_3^q\}$, computed from the intensity of the different polarization components, integrated over a spectral window of width ω_o around each harmonic frequency. The ellipticity is defined by:

$$\varepsilon_q = \tan\left[\frac{1}{2}\arctan\left(\frac{S_3^q}{\sqrt{{S_1^q}^2 + {S_2^q}^2}}\right)\right]. \tag{3.36}$$

Inspection of Fig. 3.9(b) reveals that all harmonic orders are linearly polarized when the driving field is aligned with a symmetry axis of the SLG lattice ($\theta = 0$, 30°, etc.), and elliptically polarized elsewhere. As a consequence of the symmetry of the graphene lattice, the optical response with respect to the driver's polarization follows a periodic pattern with period $\Delta\theta = 60°$. The harmonic ellipticity for tilt angles $\theta < 30°$ and $> 30°$ are related by mirror symmetry. We find a remarkable difference between the lower and higher-order harmonics: for angles $\theta < 30°$ the third, fifth and seventh harmonics present left-handed elliptical polarization, whilst the ninth and the eleventh

are right handed. These results demonstrate that the ellipticity of the high-order harmonics generated in SLG can be tuned by changing the tilt angle of the linearly polarized driver, without the need of complex driving configurations.

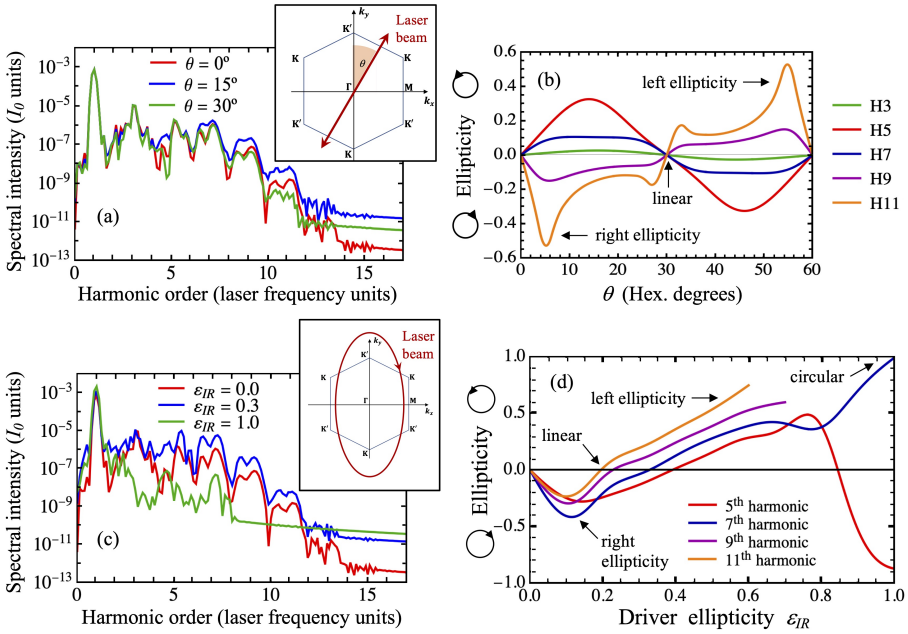

Figure 3.9: (a) Total harmonic yield from SLG for different angles of linear polarization of the driving laser, measured from the vertical axis, as shown in the inset. (b) Ellipticity of the harmonic yield as a function of θ. (c) Harmonic yield from SLG for three different values of the ellipticity of the input beam. (d) Ellipticity of the harmonic yield from SLG as a function of the driver's ellipticity ε_{IR}.

We have also investigated the variation of the HHG response of SLG to changes in the ellipticity of the driving pulse. We consider a right-handed elliptically polarized driving pulse, as described by Eq. (3.35) with $\Delta\phi = \pi/2$. The ellipticity of the driver is, therefore, $\varepsilon_{IR} = F_x/F_y$. The rest of the driving field's parameters are defined as in the linear case, so that $\varepsilon_{IR} = 0$ corresponds to a vertical linearly polarized driver. Fig. 3.9(c) shows the calculated harmonic yield for different values of ε_{IR}. The spectra also show the non-perturbative characteristics (*plateau* and cut-off) observed for linear polarization. A main observation from Fig. 3.9(c) is the drop in the efficiency of the HHG for circularly polarized drivings (green line, $\varepsilon_{IR} = 1$). This is also observed in atoms, where the number of re-scattering trajectories drops drastically with the ellipticity of the driver [129]. Complementary, Fig. 3.9(d) shows the dependence of the ellipticity of each harmonic field as a function of the driver's ellipticity. Remarkably, for circularly polarized input signal the fifth and seventh harmonics are nearly circularly polarized [130], and with opposite handeness,

also as found in atomic HHG driven by counter-rotating fields [127, 131–133]. Note that for smaller values of ε_{IR} the polarization is right-handed (as it is the input beam), whilst it turns to left-handed for higher ellipticities.

As a further observation, Fig. 3.9(c) also shows that the harmonic intensity does not decrease monotonically with the driver's ellipticity, as can be noticed by comparing the red ($\varepsilon_{IR} = 0$) and blue ($\varepsilon_{IR} = 0.3$) curves. To further explore this phenomena, we plot in Fig. 3.10(a) the normalized harmonic intensity as a function of the driver's ellipticity, for different harmonics. The harmonic response is split into two components: $I_y(\varepsilon_{IR}, \omega)$, parallel to the major axis of the driver's polarization ellipse (dotted lines), and $I_x(\varepsilon_{IR}, \omega)$, parallel to the minor axis (solid lines), see the inset of Fig. 3.9(c). All the intensities are normalized by I_y at $\varepsilon_{IR} = 0$. Note that, while I_y decreases with the ellipticity for all the harmonic orders, I_x shows a pronounced increase with a maximum for the driver's ellipticity in the interval $0.3 < \varepsilon_{IR} < 0.4$. As shown in Fig. 3.10(b), these results are in good agreement with the experimental data presented in [16], where it was demonstrated that the efficiency of the harmonic response parallel to the major axis of the polarization ellipse, which corresponds to I_x in 3.10(b), decreases gradually as the ellipticity of the laser increases, while the perpendicular component I_y is greatly enhanced with elliptically polarized excitations and reaches a maximum value at a finite ellipticity $\varepsilon_{IR} \sim 0.3$.

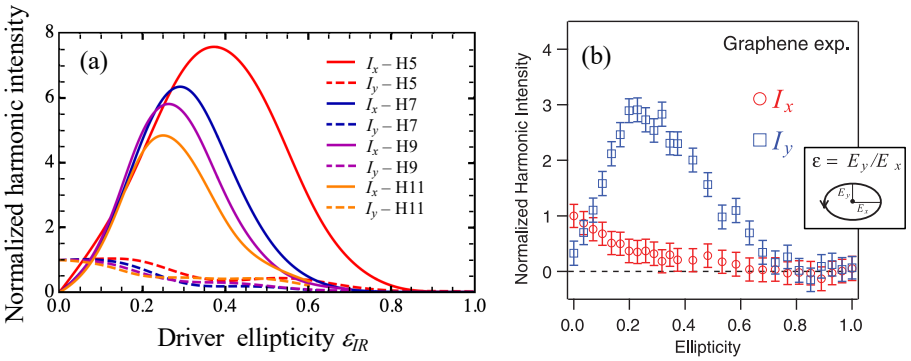

Figure 3.10: (a) Normalized intensities for the harmonic yield as a function of the laser ellipticity. (b) Experimental data for the normalized intensities of the seventh-harmonic radiation from SLG as a function of laser ellipticity (extracted from *Yoshikawa et al.* [16]).

The results of our simulations demonstrate that graphene exhibits an extraordinarily complex photon-spin conversion, leading to a rich scenario for harmonic polarization control. Although depolarization in the response to circularly polarized drivers has been observed in atomic systems [126, 134], we observe that this phenomenon is even stronger for SLG. In addition, our results also reveal that the harmonic pulses are produced with femtosecond time-varying ellipticity,

thus showing the ultrafast change of the harmonic polarization state. This work is another original contribution to this PhD thesis and was published in Ref. [107]. The full article is included in section 3.6.2.

3.5 PHYSICAL MECHANISM FOR HIGH-ORDER HARMONIC GENERATION IN GRAPHENE

In this section we develop in detail a model (SPAM), based on the saddle point approximation, that provides a simple description of HHG in single layer graphene and was published in Ref. [106]. As we shall see, the SPAM allows to identify the fundamental mechanism and predicts the spectral cut-off energies, in excellent agreement with the numerical calculations showed in section 3.3. The following discussion applies to driving pulses linearly polarized. For simplicity, we shall assume that the pulse is polarized along the y axis, so that $\mathbf{F}(t) = F(t)\mathbf{u}_y$, though the conclusions are also applicable to any polarization direction parallel to the main symmetry axes of graphene.

Let us consider once again the system of dynamical equations derived in sec 3.1. Multiplying by $e^{\frac{i}{\hbar}\int_{t_o}^{t}[E_+(\boldsymbol{\kappa}_\tau)-F(\tau)D_y(\boldsymbol{\kappa}_\tau)]d\tau}$ both sides of Eq (3.19) and rearranging terms, we obtain:

$$\frac{d}{dt}\left[e^{\frac{i}{\hbar}\int_{t_o}^{t}[E_+(\boldsymbol{\kappa}_\tau)-F(\tau)D_y(\boldsymbol{\kappa}_\tau)]d\tau}C_+(\boldsymbol{\kappa}_t,t)\right] = \frac{i}{\hbar}e^{\frac{i}{\hbar}\int_{t_o}^{t}[E_+(\boldsymbol{\kappa}_\tau)-F(\tau)D_y(\boldsymbol{\kappa}_\tau)]d\tau}F(t)D_y(\boldsymbol{\kappa}_t)C_-(\boldsymbol{\kappa}_t,t). \tag{3.37}$$

Integrating between t and t_o and after some manipulation, we have:

$$C_+(\boldsymbol{\kappa}_t,t) = e^{-\frac{i}{\hbar}\int_{t_o}^{t}[E_+(\boldsymbol{\kappa}_\tau)-F(\tau)D_y(\boldsymbol{\kappa}_\tau)]d\tau}C_+(\boldsymbol{\kappa}_{t_o},t_o) + \frac{i}{\hbar}\int_{t_o}^{t}e^{-\frac{i}{\hbar}\left[\int_{\tau_1}^{t}[E_+(\boldsymbol{\kappa}_\tau)-F(\tau)D_y(\boldsymbol{\kappa}_\tau)]d\tau\right]}F(\tau_1)D_y(\boldsymbol{\kappa}_{\tau_1})C_-(\boldsymbol{\kappa}_{\tau_1},\tau_1)d\tau_1. \tag{3.38}$$

A similar equation for $C_-(\boldsymbol{\kappa}_t,t)$ is obtained following the same procedure with Eq. (3.20). Introducing the action integral between t and t_o:

$$S_\pm(\mathbf{k},t,t_o) = -\int_{t_o}^{t}\left[E_\pm(\boldsymbol{\kappa}_\tau) - F(\tau)D_y(\boldsymbol{\kappa}_\tau)\right]d\tau, \tag{3.39}$$

we can write the probability coefficients in the following form:

$$C_+(\boldsymbol{\kappa}_t,t) = e^{\frac{i}{\hbar}S_+(\mathbf{k},t,t_o)}C_+(\boldsymbol{\kappa}_{t_o},t_o) + \frac{i}{\hbar}\int_{t_o}^{t}e^{\frac{i}{\hbar}S_+(\mathbf{k},t,\tau)}F(\tau)D_y(\boldsymbol{\kappa}_\tau)C_-(\boldsymbol{\kappa}_\tau,\tau)d\tau, \tag{3.40}$$

$$C_-(\boldsymbol{\kappa}_t,t) = e^{\frac{i}{\hbar}S_-(\mathbf{k},t,t_o)}C_-(\boldsymbol{\kappa}_{t_o},t_o) + \frac{i}{\hbar}\int_{t_o}^{t}e^{\frac{i}{\hbar}S_-(\mathbf{k},t,\tau)}F(\tau)D_y(\boldsymbol{\kappa}_\tau)C_+(\boldsymbol{\kappa}_\tau,\tau)d\tau, \tag{3.41}$$

which constitute the formal solutions of the TDSE during the interaction interval $\Delta t = t - t_o$. Now, assume that the interaction begins at

$t_o = 0$, with initial conditions $C_-(\mathbf{k}, 0) = 1$ and $C_+(\mathbf{k}, 0) = 0$, i. e. we focus on the dynamics of the valence electron initially located at the point $\boldsymbol{\kappa}_{t=0} = \mathbf{k}$, that follows the quiver trajectory in the BZ given by $\boldsymbol{\kappa}_t$. Then, the solutions of the TDSE are:

$$C_+(\boldsymbol{\kappa}_t, t) = \frac{i}{\hbar}\int_0^t e^{\frac{i}{\hbar}S_+(\mathbf{k},t,\tau)}F(\tau)D_y(\boldsymbol{\kappa}_\tau)C_-(\boldsymbol{\kappa}_\tau,\tau)d\tau, \tag{3.42}$$

$$C_-(\boldsymbol{\kappa}_t, t) = e^{\frac{i}{\hbar}S_-(\mathbf{k},t,0)} + \frac{i}{\hbar}\int_0^t e^{\frac{i}{\hbar}S_-(\mathbf{k},t,\tau)}F(\tau)D_y(\boldsymbol{\kappa}_\tau)C_+(\boldsymbol{\kappa}_\tau,\tau)d\tau. \tag{3.43}$$

As we saw in section 3.1, $D_y(\boldsymbol{\kappa}_t)$ presents singularities near the Dirac points. We model this behavior defining $D_y(\boldsymbol{\kappa}_t)$ as an impulse function $D_y(\boldsymbol{\kappa}_t) \simeq \mathcal{D}_0\delta(\boldsymbol{\kappa}_t - \mathbf{k}_D)$, where $\mathbf{k}_D$ is the coordinate of the Dirac point at K, see Fig. 2.4, though the following discussion applies as well to the K' Dirac point, due to the inversion symmetry. Since the integrals in Eqs. (3.42) and (3.43) run over time, we use:

$$1 = \int \delta(\boldsymbol{\kappa}_t - \mathbf{k}_D)d\boldsymbol{\kappa}_t = \int \delta(t - t_{D,\mathbf{k}})dt, \tag{3.44}$$

where $t_{D,\mathbf{k}}$ is the time when the electron crosses through the Dirac point leaving a hole and thus, $\boldsymbol{\kappa}_{t_{D,\mathbf{k}}} = \mathbf{k}_D$. From Eq. (3.44), we have:

$$\int \delta(\boldsymbol{\kappa}_t - \mathbf{k}_D)d\boldsymbol{\kappa}_t = \int \delta(\boldsymbol{\kappa}_t - \mathbf{k}_D)\frac{d\boldsymbol{\kappa}_t}{dt}dt = \int \delta(t - t_{D,\mathbf{k}})dt \rightarrow$$
$$\delta(\boldsymbol{\kappa}_t - \mathbf{k}_D)\frac{d\boldsymbol{\kappa}_t}{dt} = \delta(t - t_{D,\mathbf{k}}). \tag{3.45}$$

Taking into account the definition of $\boldsymbol{\kappa}_t$, Eq (3.16), this condition can be written as:

$$\delta(\boldsymbol{\kappa}_t - \mathbf{k}_D) = \frac{\hbar}{q_e F(t)}\delta(t - t_{D,\mathbf{k}}), \tag{3.46}$$

which allows us to write the impulse *ansatz* in terms of time:

$$D_y(\boldsymbol{\kappa}_t) \simeq \frac{\hbar\mathcal{D}_0}{q_e F(t)}\delta(t - t_{D,\mathbf{k}}). \tag{3.47}$$

The model assumes than before $t_{D,\mathbf{k}}$ the electron remains in the valence band, so $C_+(\mathbf{k}_D, t') = 0$ if $t' \leqslant t_{D,\mathbf{k}}$. Then, using the impulse function, the probability coefficients in Eqs. (3.42) and (3.43) can be written in the much simpler form:

$$C_+(\boldsymbol{\kappa}_t, t) = \frac{i\mathcal{D}_0}{q_e}e^{\frac{i}{\hbar}S_+(\mathbf{k},t,t_{D,\mathbf{k}})}C_-(\mathbf{k}_D, t_{D,\mathbf{k}}), \tag{3.48}$$

$$C_-(\boldsymbol{\kappa}_t, t) = e^{\frac{i}{\hbar}S_-(\mathbf{k},t,0)}. \tag{3.49}$$

The interpretation of (3.48) and (3.49) is straightforward and provides insight into the excitation mechanism that occurs in graphene

Excitation mechanism

after the interaction with an intense laser field, as shown in Fig. 3.11: an electron, initially at point $\mathbf{k}$ in the valence band, quivers in momentum space with amplitude $\boldsymbol{\kappa}_t$ due to the interaction with the field; at time $t_{\mathrm{D},\mathbf{k}}$ the electron's trajectory approximates the Dirac point, and the electron is promoted to the conduction band through the non-adiabatic interaction represented by the singular matrix element $D_y(\mathbf{k}_\mathrm{D})$, leaving a hole; after the promotion, the electron and the hole continue oscillating following the trajectories given by $\boldsymbol{\kappa}_t$. Most remarkably, this mechanism differs from that described for finite-gap semiconductor solids [65], where the excitation of the e-h pair is due to tunneling, rather than to the non-adiabatic crossing near the Dirac point. This fact is of paramount importance, since it implies that electrons in graphene can be promoted to the conduction band at any time during the interaction, as long as their semiclassical trajectories pass near the Dirac points. Hence, excitation is not restricted to the field's maxima, as it is the case of tunnel excitation in finite-gap materials.

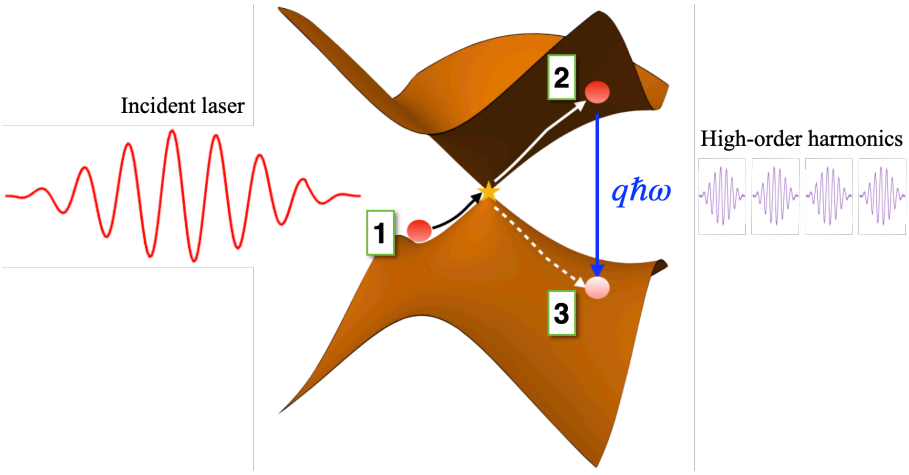

Figure 3.11: Mechanism for high-order harmonic generation in graphene. (1) As the interaction begins, the electron starts quivering in the valence band following the trajectory defined by $\boldsymbol{\kappa}_t$. Eventually, the electron reaches the proximity of the Dirac point and is promoted to the conduction band, leaving a hole. (2) The electron keeps quivering in the conduction band while the hole oscillates in the valence band. (3) The harmonic emission takes place when the electron and hole trajectories overlap in direct space emitting a photon resonant with the band gap.

As discussed in section 3.3, the lower-order harmonic emission is dominated by intraband dynamics, while interband transitions are responsible for the higher frequency spectrum [17, 65, 66]. Note that from Eq. (3.32) we can extract the interband component of the complex amplitude of the emission dipole, which is given by:

$$\tilde{\mathbf{d}}_{\updownarrow}(\boldsymbol{\kappa}_t, t) = \mathbf{D}(\boldsymbol{\kappa}_t)\mathrm{C}_+(\boldsymbol{\kappa}_t, t)\mathrm{C}_-^*(\boldsymbol{\kappa}_t, t). \tag{3.50}$$

Using equations (3.48) and (3.49), it can be readily seen that:

$$\tilde{d}_{y,\updownarrow}(\boldsymbol{\kappa}_t, t) = \frac{i\mathcal{D}_0}{q_e} e^{\frac{i}{\hbar} S_g(\mathbf{k}, t, t_{D,\mathbf{k}})} D_y(\boldsymbol{\kappa}_t), \tag{3.51}$$

where $S_g(\mathbf{k}, t, t_{D,\mathbf{k}}) = S_+(\mathbf{k}, t, t_{D,\mathbf{k}}) - S_-(\mathbf{k}, t, t_{D,\mathbf{k}})$. Therefore, the total amplitude of the q-th harmonic of the interband dipole is given by the Fourier transform of the k-space integral of Eq. (3.51):

$$\tilde{d}_{y,\updownarrow}(q\omega_o) = \frac{i\mathcal{D}_0}{q_e} \int_{-\infty}^{\infty} \int_{\mathbf{k}} e^{\frac{i}{\hbar}\left[S_g(\mathbf{k}, t, t_{D,\mathbf{k}}) + q\hbar\omega_o t\right]} D_y(\boldsymbol{\kappa}_t) \, d\mathbf{k} dt. \tag{3.52}$$

Since $D_y(\boldsymbol{\kappa}_t)$ is a smooth function in the reciprocal space except in the proximity of the Dirac points, the complex exponential of the action $S_g(\mathbf{k}, t, t_{D,\mathbf{k}})$ oscillates much faster than $D_y(\boldsymbol{\kappa}_t)$. As a consequence, the relevant contributions to the integral in Eq. (3.52) result from the stationary points of the semiclassical action, i.e. from those points satisfying the conditions:

The saddle-point approximation model for high-order harmonic emission

$$\frac{\partial}{\partial t}\left[S_g(\mathbf{k}, t, t_{D,\mathbf{k}}) + q\hbar\omega_o t\right] = 0 \rightarrow E_+(\boldsymbol{\kappa}_t) - E_-(\boldsymbol{\kappa}_t) = q\hbar\omega_o, \tag{3.53}$$

$$\nabla_{\mathbf{k}} S_g(\mathbf{k}, t, t_{D,\mathbf{k}}) = 0 \rightarrow \int_{t_{D,\mathbf{k}}}^{t} \mathbf{v}_+(\boldsymbol{\kappa}_\tau) d\tau = \int_{t_{D,\mathbf{k}}}^{t} \mathbf{v}_-(\boldsymbol{\kappa}_\tau) d\tau, \tag{3.54}$$

where the terms $\mathbf{v}_\pm(\boldsymbol{\kappa}_t) = (1/\hbar)\nabla_{\mathbf{k}} E_\pm(\boldsymbol{\kappa}_\tau)$ represent the velocity of the electrons. The first condition can be interpreted as the resonant emission of a photon by interband relaxation at the point $\boldsymbol{\kappa}_t$. Thus, according to this, after the non-adiabatic crossing through the Dirac point, the electron and the hole oscillate until time t, when they recombine emitting a photon resonant with the band gap at $\boldsymbol{\kappa}_t$. The second condition Eq. (3.54) implies that recombination only occurs at times when the electron and hole trajectories overlap in the direct space.

The main limitation of the SPAM is the assumption that the polarization of the driving beam is parallel to the main symmetry axes of graphene. Although significant effort has been made to extend the model to other linear and elliptical polarizations, we have not yet been able to succeed.

3.6 PUBLICATIONS

To finalize this chapter, we include the full text of the two articles published from the results and conclusions of our study on high-order harmonic generation in graphene. The first one was issued in 2018 in the *New Journal of Physics*, under the title *"Theory of high-order harmonic generation for gapless graphene"* [106], and includes the results discussed in sections 3.1 to 3.3 and 3.5. The second article develops in detail the contents of section 3.4 and was published in 2019 in the journal *Optics Express* with the title *"Optical anisotropy of non-perturbative*

high-order harmonic generation in gapless graphene" [107]. In order to comply with the regulations of the University of Salamanca, before each article we include an abstract in Spanish language.

3.6.1 *Theory of high-order harmonic generation for gapless graphene*

Resumen

La generación de armónicos orden elevado (HHG) resulta de la interacción de la materia con radiación electromagnética intensa. A diferencia de la mayoría de los mecanismos convencionales, la HHG no se basa en la excitación multifotónica de las transiciones atómicas entre estados ligados, sino en la dinámica de los electrones no ligados. El carácter no perturbativo de la HHG tiene como firma la aparición de una estructura en forma de meseta o *plateau* en el espectro de intensidad de los armónicos, seguida de un corte abrupto [39]. Se han observado armónicos de orden superior en una amplia variedad de blancos, incluyendo gases, sólidos y plasmas. Recientemente, también se ha observado la HHG en el grafeno [16, 17]. En este trabajo presentamos nuevos resultados teóricos de HHG en grafeno monocapa (SLG) inducida por pulsos de láser ultracortos en longitudes de onda infrarrojas. En primer lugar, desarrollamos un método computacional basado en la descripción *tight-binding* del grafeno que soslaya las inestabilidades numéricas asociadas al carácter singular de los elementos de matriz de la transición dipolar en el entorno de los puntos de Dirac. Utilizamos este método para integrar la ecuación de Schrödinger dependiente del tiempo con diferentes longitudes de onda e intensidades del campo incidente, con el fin de caracterizar la aparición de características espectrales no perturbativas. Finalmente, desarrollamos un modelo semiclásico para la emisión dipolar basado en la aproximación del punto de silla (SPAM), que retiene las principales contribuciones a la HHG y que revela el mecanismo fundamental de la emisión armónica: excitación en el entorno de los puntos de Dirac y creación de un par electrón-hueco que, posteriormente, emite un fotón de alta frecuencia tras la recombinación del electrón y del hueco cuando éstos se superponen en el espacio directo. Las predicciones del SPAM para el escalado de la frecuencia de corte con la intensidad están en excelente acuerdo con los resultados de los cálculos numéricos basados en la ecuación de Schrödinger. Por tanto, como conclusión principal, demostramos que el grafeno presenta un mecanismo particular para la generación de armónicos de orden elevado que se inicia por la transición no adiabática de las trayectorias de los electrones de valencia a través de los puntos de Dirac. Este mecanismo de excitación es radicalmente diferente del proceso de ionización/excitación por efecto túnel observado en átomos, moléculas y sólidos semiconductores [65].

New Journal of Physics
The open access journal at the forefront of physics

Deutsche Physikalische Gesellschaft DPG
IOP Institute of Physics

Published in partnership with: Deutsche Physikalische Gesellschaft and the Institute of Physics

OPEN ACCESS

RECEIVED
31 October 2017

REVISED
9 April 2018

ACCEPTED FOR PUBLICATION
17 April 2018

PUBLISHED
11 May 2018

PAPER

Theory of high-order harmonic generation for gapless graphene

Óscar Zurrón, Antonio Picón and Luis Plaja

Grupo de Investigación en Aplicaciones del Láser y Fotónica, Departamento de Física Aplicada, University of Salamanca, E-37008, Salamanca, Spain

E-mail: ozurronci@usal.es

Keywords: graphene, high order harmonic generation, intense fields, two-dimensional systems

Abstract

We study the high-harmonic spectrum emitted by a single-layer graphene, irradiated by an ultrashort intense infrared laser pulse. We show the emergence of the typical non-perturbative spectral features, harmonic *plateau* and cut-off, for mid-infrared driving fields, at fluences below the damage threshold. In contrast to previous works, using THz drivings, we demonstrate that the harmonic cut-off frequency saturates with the intensity. Our results are derived from the numerical integration of the time-dependent Schrödinger equation using a nearest neighbor tight-binding description of graphene. We also develop a saddle-point analysis that reveals a mechanism for harmonic emission in graphene different from that reported in atoms, molecules and finite gap solids. In graphene, the first step is initiated by the non-diabatic crossing of the valence band electron trajectories through the Dirac points, instead of tunneling ionization/excitation. We include a complete identification of the trajectories contributing to any particular high harmonic and reproduce the harmonic cut-off scaling with the driving intensity.

1. Introduction

High-order harmonic generation (HHG) is a remarkable process resulting from the interaction of physical systems with intense electromagnetic radiation. In contrast to most of the conventional photon up-conversion mechanisms, HHG is not based in the multiphoton excitation of atomic bound-state transitions, but on the dynamics of the unbound electrons. The non-perturbative character of HHG has as a distinguishable signature: the emergence of a *plateau*-like structure in the harmonic intensity spectrum, followed by an abrupt cut-off [1]. This *plateau* is characterized by a dependence of the harmonic intensity with the harmonic order, q, much weaker that the qth-power predicted by the perturbation theory. This structure extends the harmonic emission up to thousands of harmonic orders, therefore conveying the possibility of generating coherent extreme ultraviolet (XUV) or even soft x-ray radiation [2, 3].

High-order harmonics have been observed from a wide variety of targets, including gases, solids, and plasmas. In the latter case HHG arises from the collective response at relativistic intensities [4]. For the atomic or molecular gases and finite-gap solids, high harmonic radiation is produced by intense pulses, yet below the relativistic limit. In these systems, HHG shares some common basic principles [5]. In particular, harmonics are generated by electrons initially bounded, that are promoted into free or quasi-free states by tunneling excitation. Once freed, the electrons are accelerated by the electric field to, subsequently, release the acquired kinetic energy in the form of high-frequency radiation. HHG leads to a wide range of applications, from imaging and spectroscopy with sub-femtosecond resolution to sources of XUV/soft x-ray coherent pulses [6, 7]. Recently, HHG from solids has burgeoned a great interest, mainly motivated by the quadratic scaling of the harmonic conversion efficiency with the density of the target, as a result of the coherent nature of the process [5, 8–14].

Despite those similarities, the first experiment of HHG in solid state [8] noticed substantial differences in the laws governing the spectral *plateau* and cut-off frequency, compared to the atomic case. In atoms and molecules, the cut-off frequency scales with the product of the laser intensity and the squared wavelength, $\hbar\omega_c \propto I\lambda^2$. This law reflects the mechanism underlying HHG: the cut-off frequency corresponds to the maximum kinetic energy

of an ionized electron recolliding with the parent ion. In contrast, the cut-off frequency has been found to scale linearly with the driving field amplitude for semiconductors [8]. This kind of behavior may remind the HHG from simple two-level systems, where the cut-off energy reflects the maximum instantaneous Stark shift [15, 16]. However, two-level systems are not sufficient to explain the complex dynamics introduced by the intraband contributions. Several theoretical models have been used to explain this linear response, including the intraband dynamics of the quasi-free states, such as semiclassical models for intraband currents [17], semiconductor optical Bloch equations [18–21], and Bloch equations using Wannier localized functions [22]. HHG in 2D materials with field polarization perpendicular to the plane has been recently explored theoretically [23].

Remarkably enough, electron tunneling plays a fundamental role as the first step in the HHG process for systems presenting an energy gap, or ionization potential, larger than mid-IR photon energy. In this sense, the gapless structure of graphene presents a new scenario, and the actual details of the mechanism underlying HHG remain unaddressed.

The gapless band structure of single-layer graphene (SLG) allows the optical resonant excitation at all frequencies, up to the vacuum ultraviolet. This conveys graphene particular optical properties, as a strong broadband linear response with a comparatively large optical absorption (>2%) of visible light [24], and a strong nonlinear response for THz radiation [25, 26]. While the generation of the second harmonic is forbidden in the dipole approximation, due to the centrosymmetric structure of ideal SLG, it can be observed in stacked samples [27]. Third-order nonlinearities are found to be also remarkably strong in SLG, with nonlinear susceptibilities several orders of magnitude above those of transparent materials, and of the same order as in other resonant materials, such as metal nanoparticles. The third harmonic has been observed in few-layer graphene for transitions occurring near the K and M points of the Brillouin zone (BZ) [28–30]. Nonlinear effects arising from induced plasma have been predicted to enhance HHG [31, 32]. HHG in gapless graphene has not been reported until recently [33, 34], observing the generation of up to the 9th harmonic using a mid-infrared driving laser. This demonstrates the experimental feasibility of producing HHG in monolayer graphene.

Despite these promising characteristics, current theoretical models for gapless graphene are not complete in describing the nonlinear dynamics induced by short intense laser pulses. Some models have been used for dopped graphene with a small energy gap [35], which do not include the important effects induced by the singular coupling near the Dirac cone [36]. Other models accounting for the Dirac singularity do not consider the entire BZ, therefore limiting the cut-off scaling predictions [37]. Questions as the role of the spectrally ubiquitous resonance, the singular transition matrix elements at the Dirac points, the cut-off scaling, or the underlying physical mechanism in HHG remain unveiled.

In this paper we present new theoretical results of HHG in SLG induced by few-cycle laser pulses at infrared wavelengths. On one side, we develop an exact computational method that overcomes the numerical instabilities associated with the singular dipole transition elements near the Dirac points. We use this method to integrate the time-dependent Schrödinger equation (TDSE) for different driving field wavelengths and intensities, in order to characterize the emergence of the non-perturbative spectral features (a *plateau* in the harmonic intensities, followed by a cut-off). Finally, we develop an approximated model that retains the main contributions to HHG and reveals the fundamental mechanism of harmonic emission: excitation near the Dirac points and creation of an electron–hole pair that subsequently emits a high-frequency photon upon recombination, when the electron and hole overlap in direct space. Therefore, as a main conclusion, we demonstrate that graphene presents its particular mechanism of HHG, in which the first step is initiated by the non-adiabatic crossing of the valence electron trajectories through the Dirac points. This first step is radically different from the tunneling ionization/excitation process found in atoms, molecules and finite gap materials [19]. Our trajectory analysis accounts exactly for the cut-off scaling with the intensity.

The manuscript is organized as follows. In section 2 we present our theoretical framework. In section 3 we present our method for the numerical integration of the TDSE in SLG, showing HHG spectra and the scaling of the cut-off harmonic frequency with the intensity for different wavelengths. In section 4 we develop our approximate description and derive the physical conditions for the harmonic emission, as well as the rules governing the harmonic cut-off frequency. Finally, we present our conclusions in section 5.

2. Theory

We consider the standard tight-binding description of SLG [38], where the wavefunctions of the conduction (+) and valence (−) bands can be written as linear combinations of Bloch states from two neighboring sublattices,

$$\Phi_{\pm}(\mathbf{k};\,\mathbf{r}) = \sqrt{\frac{1}{2}}\,\mathrm{e}^{\mathrm{i}\mathbf{k}\cdot\mathbf{r}}\begin{pmatrix}\pm 1\\ \mathrm{e}^{-\mathrm{i}\phi(\mathbf{k})}\end{pmatrix}. \tag{1}$$

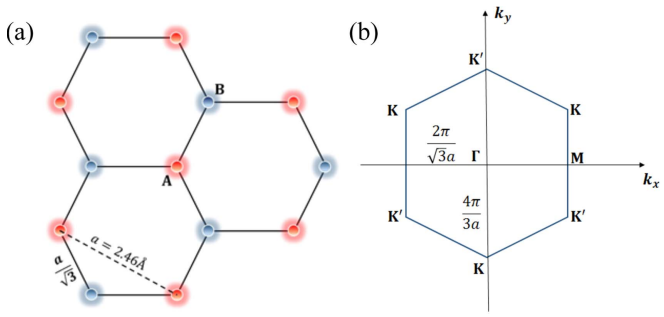

Figure 1. Scheme of graphene's structure in (a) direct and (b) reciprocal space. The unit cell is composed by two carbon atoms (red and blue). In the reciprocal space, points K and K′ correspond to the location of the Dirac cones. In our study the laser pulse is linearly polarized along the y direction and it is aimed perpendicularly to the graphene layer (x–y plane).

$\phi(\mathbf{k})$ being the argument of the complex function

$$f(\mathbf{k}) = \mathrm{e}^{-\mathrm{i}ak_x/\sqrt{3}}\left(1 + 2\mathrm{e}^{\mathrm{i}\sqrt{3}ak_x/2}\cos\frac{ak_y}{2}\right) \tag{2}$$

and $a = 2.46$ Å the lattice constant. Figures 1(a) and (b) show the structure of SLG in the direct and reciprocal space, respectively. The Dirac points are located in points K and K′ in the reciprocal space. K is related to K′ by inversion symmetry. The Γ point, at the center of the BZ, corresponds to the maximum gap ≃17.8 eV in the tight-binding description. The driving electric field is assumed polarized in the y direction, and aimed perpendicularly to the graphene layer. Dirac cones result from the overlap of atomic p_z orbitals, and are coupled when the field polarization is parallel to the graphene sheet. The interaction with a field perpendicular to the layer has been studied recently elsewhere for the case of 2D materials, and found to resemble HHG in atoms [23].

The vectors in equation (1) are eigenstates of the system's Hamiltonian H_G with energies $E_{\pm}(\mathbf{k}) = \pm\gamma|f(\mathbf{k})|$ ($\gamma = 2.97$ eV). The interaction of the laser pulse $F(t)$ with the system is described by the time-dependent Hamiltonian $H(t) = H_G + V_i(t)$, where $V_i(t) = -q_e F(t)\, y$ is the electric field coupling within the dipole approximation.

During the interaction, the time-dependent wavefunction can be expressed as a superposition of the eigenstates (1):

$$\begin{aligned}\Psi(\mathbf{r}, t) &= \int \Psi(\mathbf{k}; \mathbf{r}, t)\mathrm{d}\mathbf{k} \\ &= \int [C_+(\mathbf{k}, t)\Phi_+(\mathbf{k}; \mathbf{r}) + C_-(\mathbf{k}, t)\Phi_-(\mathbf{k}; \mathbf{r})]\mathrm{d}\mathbf{k}.\end{aligned} \tag{3}$$

Inserting (3) into the TDSE, $\mathrm{i}\hbar\partial\Psi(\mathbf{r}, t)/\partial t = H(t)\Psi(\mathbf{r}, t)$ and projecting, we find the following set of coupled two-level equations

$$\begin{aligned}\mathrm{i}\hbar\frac{\partial}{\partial t}C_+(\mathbf{k}, t) &= [E_+(\mathbf{k}) - F(t)D_y(\mathbf{k})]C_+(\mathbf{k}, t) \\ &\quad - \mathrm{i}q_e F(t)\frac{\partial}{\partial k_y}C_+(\mathbf{k}, t) - F(t)D_y(\mathbf{k})C_-(\mathbf{k}, t),\end{aligned} \tag{4}$$

$$\begin{aligned}\mathrm{i}\hbar\frac{\partial}{\partial t}C_-(\mathbf{k}, t) &= [E_-(\mathbf{k}) - F(t)D_y(\mathbf{k})]C_-(\mathbf{k}, t) \\ &\quad - \mathrm{i}q_e F(t)\frac{\partial}{\partial k_y}C_-(\mathbf{k}, t) - F(t)D_y(\mathbf{k})C_+(\mathbf{k}, t)\end{aligned} \tag{5}$$

with $D_y(\mathbf{k}) = (q_e/2)\partial\phi(\mathbf{k})/\partial k_y$ [39]. For ultrashort pulses (<30 fs full-width at half maximum, FWHM), it is possible to remain in the Schrödinger representation instead of using the density-matrix formalism, as the carrier collisional diffusion has characteristic times of several tens of femtoseconds [40–42]. Furthermore, it is also possible to draw a parallelism between equation (4) and the standard strong-field formulation for atoms [43], replacing the band structure, $E_+(\mathbf{k})$, by the parabolic shape of the free electron energy, including the energy term $-F(t)D_y$ as a phase-shift, and taking $C_-(\mathbf{k}, t) = 1$.

Equations (4) and (5) include interband and intraband couplings, the intraband contribution corresponding to derivatives in the reciprocal space. The computational complexity introduced by these gradients can be removed introducing the kinetic momentum:

$$\hbar\boldsymbol{\kappa}_t = \hbar\mathbf{k} - q_e\mathbf{A}(t)/c, \tag{6}$$

$\mathbf{A}(t)$ being the vector potential. The equations (4) and (5) are then reduced to:

$$\begin{aligned} \mathrm{i}\hbar\frac{\mathrm{d}}{\mathrm{d}t}C_+(\boldsymbol{\kappa}_t, t) = &[E_+(\boldsymbol{\kappa}_t) - F(t)D_y(\boldsymbol{\kappa}_t)]C_+(\boldsymbol{\kappa}_t, t) \\ &- F(t)D_y(\boldsymbol{\kappa}_t)C_-(\boldsymbol{\kappa}_t, t), \end{aligned} \tag{7}$$

$$\begin{aligned} \mathrm{i}\hbar\frac{\mathrm{d}}{\mathrm{d}t}C_-(\boldsymbol{\kappa}_t, t) = &[E_-(\boldsymbol{\kappa}_t) - F(t)D_y(\boldsymbol{\kappa}_t)]C_-(\boldsymbol{\kappa}_t, t) \\ &- F(t)D_y(\boldsymbol{\kappa}_t)C_+(\boldsymbol{\kappa}_t, t). \end{aligned} \tag{8}$$

This set of equations corresponds to a driven two-level parametric oscillator.

3. Numerical results

The numerical integration of equations (7) and (8) is of difficult convergence due to the singular values of $D_y(\mathbf{k})$ near the Dirac points. It is possible to recast these equations and renormalize the terms containing $D_y(\mathbf{k})$ using the following transformation, which effectively undoes the diagonalization of H_G:

$$C^M(\boldsymbol{\kappa}_t, t) = C_+(\boldsymbol{\kappa}_t, t) - C_-(\boldsymbol{\kappa}_t, t), \tag{9}$$

$$\tilde{C}^P(\boldsymbol{\kappa}_t, t) = \mathrm{e}^{-\mathrm{i}\phi(\boldsymbol{\kappa}_t)}[C_+(\boldsymbol{\kappa}_t, t) + C_-(\boldsymbol{\kappa}_t, t)]. \tag{10}$$

Now, from (7) and (8), we derive the following set of equations

$$\begin{aligned} \mathrm{i}\hbar\frac{\mathrm{d}}{\mathrm{d}t}C^M(\boldsymbol{\kappa}_t, t) = &\frac{E_+(\boldsymbol{\kappa}_t) + E_-(\boldsymbol{\kappa}_t)}{2}C^M(\boldsymbol{\kappa}_t, t) \\ &+ \frac{E_+(\boldsymbol{\kappa}_t) - E_-(\boldsymbol{\kappa}_t)}{2}\mathrm{e}^{\mathrm{i}\phi(\boldsymbol{\kappa}_t)}\tilde{C}^P(\boldsymbol{\kappa}_t, t), \end{aligned} \tag{11}$$

$$\begin{aligned} \mathrm{i}\hbar\frac{\mathrm{d}}{\mathrm{d}t}\tilde{C}^P(\boldsymbol{\kappa}_t, t) = &\frac{E_+(\boldsymbol{\kappa}_t) + E_-(\boldsymbol{\kappa}_t)}{2}\tilde{C}^P(\boldsymbol{\kappa}_t, t) \\ &+ \frac{E_+(\boldsymbol{\kappa}_t) - E_-(\boldsymbol{\kappa}_t)}{2}\mathrm{e}^{-\mathrm{i}\phi(\boldsymbol{\kappa}_t)}C^M(\boldsymbol{\kappa}_t, t). \end{aligned} \tag{12}$$

According to Larmor's semiclassical formula, the harmonic emission is given by the dipole acceleration. The mean value of the dipole can be written as the sum of two contributions, corresponding to intraband ($\mathbf{d}_{\leftrightarrow}$) and interband ($\mathbf{d}_{\updownarrow}$) transitions [20],

$$\begin{aligned} \mathbf{d}(t) &= \langle\Psi(t)|q_e\mathbf{r}|\Psi(t)\rangle \\ &= \int[\mathbf{d}_{\leftrightarrow}(\boldsymbol{\kappa}_t, t) + \mathbf{d}_{\updownarrow}(\boldsymbol{\kappa}_t, t)]\,\mathrm{d}\mathbf{k}, \end{aligned} \tag{13}$$

where

$$\begin{aligned} \mathbf{d}_{\leftrightarrow}(\boldsymbol{\kappa}_t, t) = \mathrm{i}q_e[&C_+^*(\boldsymbol{\kappa}_t, t)\nabla_{\boldsymbol{\kappa}_t}C_+(\boldsymbol{\kappa}_t, t) \\ &+ C_-^*(\boldsymbol{\kappa}_t, t)\nabla_{\boldsymbol{\kappa}_t}C_-(\boldsymbol{\kappa}_t, t)] \end{aligned} \tag{14}$$

and

$$\begin{aligned} \mathbf{d}_{\updownarrow}(\boldsymbol{\kappa}_t, t) = \mathbf{D}(\boldsymbol{\kappa}_t)[&C_-^*(\boldsymbol{\kappa}_t, t)C_+(\boldsymbol{\kappa}_t, t) \\ &+ C_-(\boldsymbol{\kappa}_t, t)C_+^*(\boldsymbol{\kappa}_t, t)]. \end{aligned} \tag{15}$$

Using (9) and (10), the total dipole can also be written as

$$\mathbf{d}(t) = \mathrm{i}\frac{q_e}{2}\int[C^{M*}\nabla_{\boldsymbol{\kappa}_t}C^M + \tilde{C}^{P*}\nabla_{\boldsymbol{\kappa}_t}\tilde{C}^P]\,\mathrm{d}\mathbf{k}. \tag{16}$$

We have integrated numerically equations (11), (12) and (16), considering few-cycle driving pulses at different intensities and wavelengths. The driving pulses are modeled using an 8 cycle (full width) $\sin^2$ temporal envelope, 2.9 cycles FWHM. The total field is defined as $F(t) = F_0\sin^2(\pi t/8T)\sin(\omega_0 t)$ for $0 \leqslant t \leqslant 8T$, and 0 elsewhere, where F_0 is the field amplitude, T is the period, and $\omega_0 = 2\pi/T$ the field frequency. Figure 2 shows the calculated HHG spectra at two different intensities for a driving field of 3 μm wavelength. For the lowest intensity, figure 2(a), the HHG spectrum shows the typical perturbative behavior: a monotonous decrease of efficiency with increasing harmonic order. This behavior changes drastically for driving fields at higher intensity, figure 2(b), with a clear emergence of a spectral *plateau*, extending up to a maximum (cut-off) frequency. It has been reported that the inclusion of additional energy bands results in the appearance of secondary plateaus, with higher cut-off frequencies, but with efficiencies smaller in various orders of magnitude [20], not affecting

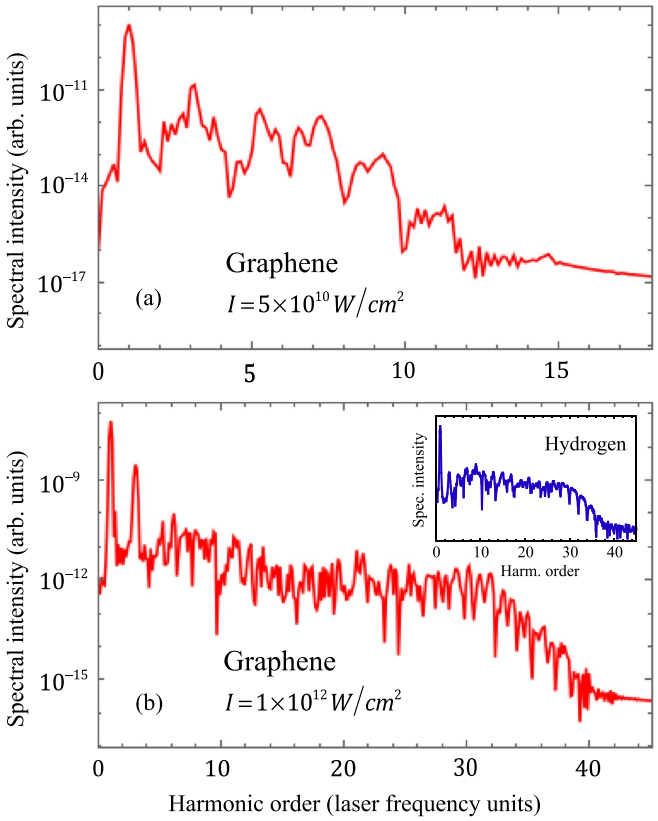

Figure 2. HHG spectra from SLG driven by a 3 μm wavelength, 28 fs (2.9 cycles) FWHM pulse at two different intensities: (a) 5×10^{10} W cm^{-2} and (b) 1×10^{12} W cm^{-2}. As a reference, the inset shows the HHG spectrum emitted by the hydrogen atom, driven by a 800 nm pulse with the same number of cycles, at an intensity of 1.57×10^{14} W cm^{-2}.

therefore our conclusions. It is interesting to note also that the spectral content in figure 2 is quite rich, even for the lower intensity case. This results from the interference of two different contributions to the same radiated energy, namely, the intraband and interband components of the emission dipole, and from the different electron–hole pair's trajectories leading to the same harmonic, as we shall describe below. For the sake of comparison, we show in the inset of figure 2(b) the HHG spectrum corresponding to the hydrogen atom, driven by a 800 nm laser with the same pulse width. We will show that the mechanism of electron excitation in graphene differs substantially from the tunnel ionization in atoms. The efficiency in the latter case is much lower, and HHG typically occurs for laser intensities one or two orders of magnitude above those required in graphene. Note that, although the spectra is quite complex in both cases, atoms present a more regular structure after the cut-off frequency. This difference will be discussed in the following section.

We show in figure 3 the scaling of the cut-off frequency with the driving field intensity for laser wavelengths 800 nm, 1.6 μm and 3.0 μm. Note that for the three cases the cut-off frequency saturates at the largest intensities, and the saturated cut-off corresponds to a photon energy of $\simeq$17.8 eV, i.e. the maximum gap in the BZ. This saturation has also been described in gap semiconductors [5]. Unlike the other physical systems mentioned in the introduction (atoms, molecules or two-level systems), there is no simple law (linear or quadratic) describing the scaling of the cut-off frequency with the field amplitude.

The use of arbitrary large intensities is precluded by the damage of the sample. We indicate with a colored area in figure 3 the intensities for which the material is expected to have damage, assuming a damage fluence-threshold of 150 mJ cm^{-2} [44]. Observe that for longer wavelengths it is possible to reach the saturated cut-off at intensities below the damage threshold. Note however that, as the laser period increases, the decoherence due to carrier collisions, typically of several tens of fs, becomes a limitation. This tradeoff indicates that the HHG production is more favorable at mid-IR wavelengths in the short-cycle regime.

Our numerical findings reflect some fundamental properties of the harmonic emission: (i) emergence of a spectral *plateau* at large intensities, (ii) a nontrivial cut-off dependence with the intensity, and (iii) a limiting photon energy close to the maximum energy gap of the material. In the following section, we develop a saddle-point approximation model (SPAM) that provides a simple description of HHG in SLG. The SPAM allows to identify the fundamental mechanism and predicts the spectral cut-off energies, in excellent agreement with our numerical calculations.

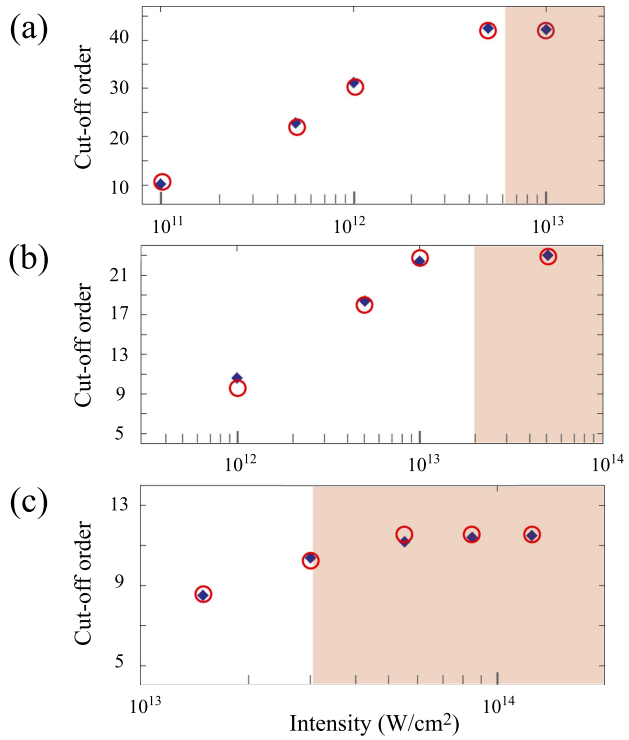

Figure 3. Cut-off scalings with intensity for a 8 cycle pulse with wavelengths (a) 3 μm, (b) 1.6 μm and (c) 800 nm. The blue diamonds correspond to the numerical integration of the TDSE. The red circles are given by the semiclassical model SPAM (more details are given in the text). Filled areas correspond to intensities above damage threshold.

4. Underlying mechanism

Our description starts with the integral form of the dynamical equations (7) and (8):

$$C_-(\boldsymbol{\kappa}_t,\, t) = C_-(\mathbf{k},\, 0)\mathrm{e}^{\frac{\mathrm{i}}{\hbar}S_-(\mathbf{k},t,0)} + \frac{\mathrm{i}}{\hbar}\int_0^t \mathrm{e}^{\frac{\mathrm{i}}{\hbar}S_-(\mathbf{k},t,t_1)}F(t_1)D_y(\boldsymbol{\kappa}_{t_1})C_+(\boldsymbol{\kappa}_{t_1},\, t_1)\mathrm{d}t_1, \tag{17}$$

$$C_+(\boldsymbol{\kappa}_t,\, t) = C_+(\mathbf{k},\, 0)\mathrm{e}^{\frac{\mathrm{i}}{\hbar}S_+(\mathbf{k},t,0)} + \frac{\mathrm{i}}{\hbar}\int_0^t \mathrm{e}^{\frac{\mathrm{i}}{\hbar}S_+(\mathbf{k},t,t_1)}F(t_1)D_y(\boldsymbol{\kappa}_{t_1})C_-(\boldsymbol{\kappa}_{t_1},\, t_1)\mathrm{d}t_1, \tag{18}$$

where we define the action term $S_\pm(\mathbf{k},\, t,\, t_1) = -\int_{t_1}^t [E_\pm(\boldsymbol{\kappa}_\tau) - F(\tau)D_y(\boldsymbol{\kappa}_\tau)]\mathrm{d}\tau$. Note that for the initial time, $\boldsymbol{\kappa}_{\tau=0} = \mathbf{k}$. In SLG, $D_y(\boldsymbol{\kappa}_t)$ presents singularities near the Dirac points. We model this behavior defining $D_y(\boldsymbol{\kappa}_t)$ as an impulse function $D_y(\boldsymbol{\kappa}_t) = \mathcal{D}_0\delta(\boldsymbol{\kappa}_t - \mathbf{k}_\mathbf{D})$, where $\mathbf{k}_\mathbf{D}$ is the coordinate of the Dirac point at K. The following discussion applies as well to the K′ Dirac point, due to the inversion symmetry, assuming a change of sign in the electric field amplitude. Using the impulse ansatz, we focus on the dynamics of the valence electron initially located at the point $\mathbf{k}$, that follows the quiver trajectory in the BZ given by $\boldsymbol{\kappa}_t$. Using the impulse function, the probability amplitudes (17) and (18) can be then written as

$$C_-(\boldsymbol{\kappa}_t,\, t) = \mathrm{e}^{\frac{\mathrm{i}}{\hbar}S_-(\mathbf{k},t,0)}, \tag{19}$$

$$C_+(\boldsymbol{\kappa}_t,\, t) = \mathrm{i}\frac{\mathcal{D}_0}{q_e}\mathrm{e}^{\frac{\mathrm{i}}{\hbar}S_+(\mathbf{k},t,t_{D,\mathbf{k}})}C_-(\mathbf{k}_\mathbf{D},\, t_{D,\mathbf{k}}), \tag{20}$$

where we use the initial conditions $C_-\,(\mathbf{k}, 0) = 1$ and $C_+(\mathbf{k}, 0) = 0$. $t_{D,\mathbf{k}}$ is the time instant when the electron crosses the Dirac point and is promoted to the conduction band leaving a hole, i.e. $\boldsymbol{\kappa}_{t_{D,\mathbf{k}}} = \mathbf{k}_\mathbf{D}$.

High-harmonics in solids, including graphene, are dominated by interband dynamics [20, 34]. Using equations (19) and (20), the complex amplitude of the interband dipole (15) is given by

$$\tilde{d}_{y,\updownarrow}(\boldsymbol{\kappa}_t,\, t) = D_y(\boldsymbol{\kappa}_t) C_-^*(\boldsymbol{\kappa}_t,\, t) C_+(\boldsymbol{\kappa}_t,\, t)$$
$$= \mathrm{i}\frac{\mathcal{D}_0}{q_e} \mathrm{e}^{\frac{\mathrm{i}}{\hbar} S_g(\mathbf{k}, t, t_{D,\mathbf{k}})} D_y(\boldsymbol{\kappa}_t), \tag{21}$$

where $S_g(\mathbf{k},\, t,\, t_{D,\mathbf{k}}) = S_+(\mathbf{k},\, t,\, t_{D,\mathbf{k}}) - S_-(\mathbf{k},\, t,\, t_{D,\mathbf{k}})$. The amplitude of the qth harmonic of the interband dipole is then given by the Fourier transform of the k-space integral

$$\tilde{d}_{y,\updownarrow}(q\omega_0) = \mathrm{i}\frac{\mathcal{D}_0}{q_e} \int_{\mathbf{k}} \int_{-\infty}^{\infty} \mathrm{e}^{\frac{\mathrm{i}}{\hbar}[S_g(\mathbf{k}, t, t_{D,\mathbf{k}}) + q\hbar\omega_0 t]} D_y(\boldsymbol{\kappa}_t) \mathrm{d}\mathbf{k}\mathrm{d}t. \tag{22}$$

Following [19, 43] (in the context of solids), we can identify that the main contributions to the integral in (22) are the stationary phase points. Therefore, the harmonic emission takes place predominantly at those times that fulfill the equation,

$$\frac{\partial}{\partial t}[S_g(\mathbf{k},\, t,\, t_{D,\mathbf{k}}) + q\hbar\omega_0 t] = 0$$
$$\rightarrow E_+(\boldsymbol{\kappa}_t) - E_-(\boldsymbol{\kappa}_t) = q\hbar\omega_0. \tag{23}$$

This condition can be interpreted as the emission of a photon by interband relaxation at the point $\boldsymbol{\kappa}_t$, where the gap is resonant with the emitted photon. This condition, together with equations (19) and (20), leads to a simple picture of the qth order harmonic emission in SLG: an electron, initially at point $\mathbf{k}$ in the valence band, quivers in momentum space with amplitude $\boldsymbol{\kappa}_t$ due to the interaction with the field; at time $t_{D,\mathbf{k}}$ the electron's trajectory approximates the Dirac point, and the electron is promoted to the conduction band through the non-adiabatic interaction with the singular matrix element D_y, leaving a hole; finally, the electron and the hole oscillate until time t, when they recombine emitting a photon resonant with the band gap at $\boldsymbol{\kappa}_t$. This mechanism for SLG differs from the one described for finite-gap semiconductor solids [19], as the excitation in the latter is dominated by tunneling, rather than by the non-adiabatic crossing. The SPAM predicts that only those states with initial momentum vertically aligned near the Dirac points can be promoted to the conduction band, as these are the only trajectories that cross the Dirac points. As these states are also vertically aligned with the Γ point, the maximum energy of the photon emission will be limited by the gap at this point (≃17.8 eV), which matches with the value of the saturated cut-off energy mentioned above.

We obtain an additional condition by applying the saddle-point analysis in momentum space to (22), which leads to

$$\nabla_{\mathbf{k}} S_g(\mathbf{k},\, t,\, t_{D,\mathbf{k}}) = 0$$
$$\rightarrow \int_{t_{D,\mathbf{k}}}^{t} \mathbf{v}_+(\boldsymbol{\kappa}_\tau)\mathrm{d}\tau = \int_{t_{D,\mathbf{k}}}^{t} \mathbf{v}_-(\boldsymbol{\kappa}_\tau)\mathrm{d}\tau, \tag{24}$$

where the terms $\mathbf{v}_\pm(\boldsymbol{\kappa}_t) = (1/\hbar)\nabla_{\mathbf{k}} E_\pm(\boldsymbol{\kappa}_\tau)$ represent the velocity of the electrons. The time integral of the velocities corresponds to classical electron trajectories. The interpretation in terms of semiclassical trajectories is at the core of the present understanding of HHG from atoms [43], and it is also extended to solids in [5] or used for the description of the dynamics of hot free carriers in graphene [30]. In this semiclassical framework the interpretation of equation (24) is straightforward: once the electron–hole pair is created at time $t_{D,\mathbf{k}}$ near the Dirac point, both are driven by the field; condition (24) states that the pair recombines emitting a photon at time t, only when their trajectories intersect in real space.

Figure 4(b) shows the classical trajectories of two electrons, with different initial positions in the BZ ($\mathbf{k}_A$ and $\mathbf{k}_B$), which cross the Dirac point at times $t_{D,\mathbf{k}_A}$ and $t_{D,\mathbf{k}_B}$. The trajectories correspond to a 3 μm wavelength pulse, with intensity 10^{11} W cm^{-2}. Note that for the trajectory A, the electron and the hole created at $t_{D,\mathbf{k}_A}$ meet in direct space at the final time t. In contrast, in B, the electron and the hole do not meet at t. According to equation (24), the photon emission at t is effective only for the case A. Figure 4(a) shows a map of the energy gap at the moment t where the photon may be emitted, as a function of the time in which the electron–hole pair is created, $t_{D,\mathbf{k}}$. The points A and B in the map correspond to the cases shown in figure 4(b). We have colored in red the points $(t_{D,\mathbf{k}}, t)$ corresponding to electron–hole pairs, created at $t_{D,\mathbf{k}}$, that are driven to overlap in the same direct-space unit cell at the emission time t. These colored areas are, therefore, in compliance with both conditions (23) and (24), and correspond to the situations when the harmonic photon is effectively emitted. According to this map, point A corresponds to an electron–hole pair created at $t_{D,\mathbf{k}} \simeq 0.3T$, which emits a $\simeq 10\hbar\omega_0$ photon when recombined at $t \simeq 0.9T$. Note that, as it happens in B, other points in the map may potentially emit higher frequency harmonics (up to $\simeq 14\hbar\omega_0$, i.e. the maximum gap energy attained during the electron–hole excursion). However, the photon emission is not possible since the electron–hole pairs are spatially apart at t. The maximal photon energy is, therefore, given by the energy maxima in the map of figure 4(a), constrained to the colored zone, which corresponds to the trajectories ending with an electron–hole intersection and therefore, having the possibility of recombination. In figure 4, the cut-off harmonic corresponds to point A, with an energy $\simeq 10\hbar\omega_0$, smaller than the maximum gap ($\simeq 14\hbar\omega_0$ at the Γ point). In

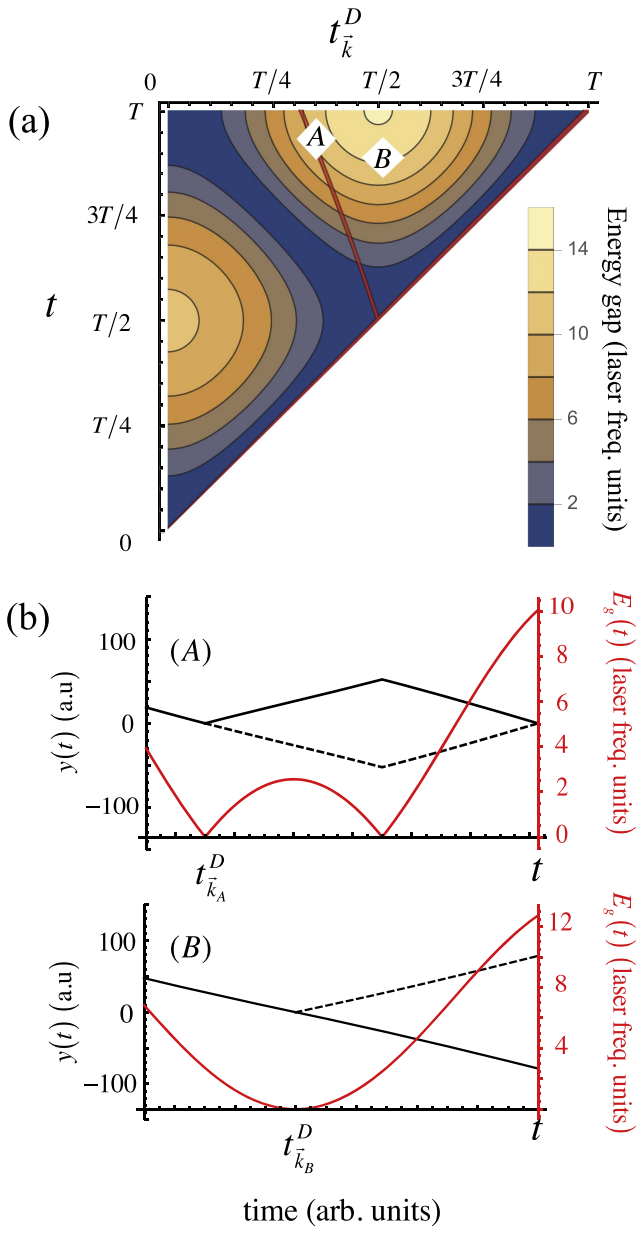

Figure 4. (a) Map of the energy of the emitted photon for different classical trajectories computed with the SPAM, $t^D_{\vec{k}}$ being the time of the electron–hole pair creation and t the potential time of photon emission. The points where the electron–hole pair trajectories intersect in direct-space at time t are represented by the red area. (b) Two electron trajectories corresponding to points A and B illustrated in (a). The trajectory of the electron (black line) and hole (dashed line) are represented as a function of time. This figure corresponds to a 3 μm wavelength laser pulse with peak intensity of 10^{11} W cm^{-2}.

figure 3(a) we compare this cut-off prediction (red circle) with the results of the exact integration of equations (4) and (5) (blue diamonds). As it can be noticed, this cut-off prediction is in excellent agreement with the results of the numerical calculations.

We show in figure 5 the SPAM energy maps at 3 μm wavelength for the four additional intensities used in figure 3(a). We observe that for increasing intensity, the topology of the colored region, i.e. the condition for the electron–hole overlapping at the emission time, becomes more complex. It is interesting to note that the same harmonic may be emitted by two or more trajectories within the same driving field's half cycle. These interfering contributions are also found in HHG by atoms and molecules [45], although in SLG their characteristics, i.e. the number of trajectories, initial and final times, etc reveal a more intricate scenario. Note, in particular, that figures 5(c) and (d) reveal three or more path contributions for the maximum (cut-off) frequency. In contrast, there is a single electron trajectory emitting cut-off harmonics in atoms and molecules. As a result, in these latter systems, the HHG spectrum becomes regular at the cut-off, while in graphene remains, still, complex (see figure 2(b) and its inset).

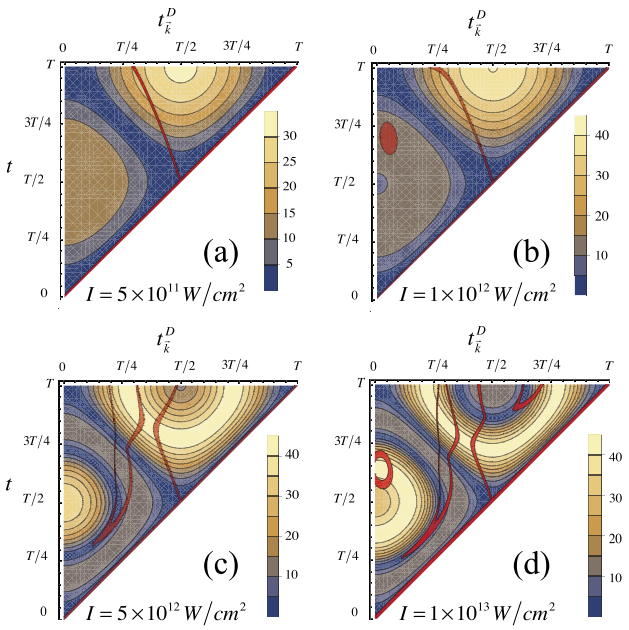

Figure 5. Energy maps for the emitted harmonic photon according to the SPAM, for the 3 μm wavelength driving pulse and the intensities used in figure 3(a). The points corresponding to intersecting electron–hole trajectories at time t are highlighted in red.

As described, we can use these maps to identify the cut-off harmonic order at each intensity. The predicted values are plotted in figure 3(a), and show an excellent agreement with the results of the numerical computations. Figures 3(b) and (c) show the cut-off extracted from the SPAM maps in comparison with the TDSE results, for different intensities and 1.6 μm and 800 nm wavelengths, demonstrating a similar accuracy of the SPAM for the whole range of parameters.

Before concluding, let us comment the harmonic emission associated with the intraband transitions from this simplified perspective. Substituting equations (17) and (18) in (14), and discarding the terms that vanish after the integration over the BZ (due to the graphene's inversion symmetry), we find,

$$\mathbf{d}_{\leftrightarrow}(\boldsymbol{\kappa}_t,\, t) = \frac{|\mathcal{D}_0|^2}{q_e}\left(\int_{t_{D,\mathbf{k}}}^{t} \mathbf{v}_{+}(\boldsymbol{\kappa}_\tau)\,\mathrm{d}\tau + \int_{0}^{t_{D,\mathbf{k}}} \mathbf{v}_{-}(\boldsymbol{\kappa}_\tau)\,\mathrm{d}\tau\right). \tag{25}$$

This corresponds to the time-dependent dipole associated to the position of a valence electron in direct-space, initially with pseudomomentum $\mathbf{k}$, that undergoes an excitation to the conduction band at time $t_{D,\mathbf{k}}$. The intraband dipole, therefore, is also a source of harmonics due to the non-parabolic shape of the electronic bands. Previous studies in finite gap crystals show that the intraband contribution dominates the harmonic emission of low order harmonics, while the interband dominates for the higher frequency spectrum [19, 20].

5. Conclusions

We have studied the HHG in SLG irradiated by intense few-cycle infrared laser pulses. The study is two-fold. First, we integrate exactly the TDSE using a non-diagonal basis to circumvent the numerical instabilities associated to the Dirac points. Our method allows, therefore, to account the singular non-adiabatic coupling near the Dirac cones without approximation. Our numerical results demonstrate the emergence of the non-perturbative signatures in the harmonic spectrum (intensity *plateau*, followed by an abrupt cut-off) at mid-infrared wavelengths, below the damage threshold. In contrast to the atomic case, we show that in graphene the harmonic cut-off frequency saturates with increasing intensity. In a second part, we develop a SPAM to unveil the basic mechanism of HHG in graphene. According to the SPAM, harmonics are generated by electron–hole pairs produced during the non-adiabatic crossing of the electron trajectories near the Dirac points. This mechanism differs from the tunnel excitation giving rise to HHG in atoms, molecules and solids with finite gaps. Once generated, the electron and hole are driven by the field until their trajectories intersect in real space, allowing recombination, and thus emitting a high-frequency photon. This electron–hole recombination mechanism is analogous to the rescattering process found in atoms and molecules. In this latter case, however, the hole remains static in the ion, while in solids, it quivers with the electric field. Our SPAM reproduces the

scaling of the harmonic cut-off frequency with the driving field intensity with excellent agreement with the numerical results, and fully characterizes the trajectories, their number, and the electron–hole creation and recombination times leading to the emission of harmonics.

The theory presented in this manuscript can be extended to other two-dimensional materials. Our SPAM results are encouraging for the development and design of new materials, and of methods to control the electron dynamics to tailor the HHG emission [46]. This work paves the way for further investigations in the understanding of the nonlinear optical response of gapless materials and in the manipulation of electron carriers at the petahertz domain. The formalism presented here is also specially suitable to study the interplay of nonlinearly polarized pulses and the role of strong electron–hole correlations in the production of HHG [47].

Acknowledgments

We acknowledge fruitful discussions with I J Sola, H Crespo, E Pinsanty, J Biegert, J M Pérez-Iglesias, R Rengel, M J Martín and C Hernández García. We acknowledge support from Junta de Castilla y León (Project SA046U16) and MINECO (FIS2013-44174-P, FIS2016-75652-P) and European Union (FEDER). AP acknowledges support from the European Union's Horizon 2020 research and innovation programme under the Marie Sklodowska-Curie grant agreement No. 702565.

References

[1] Krause J L, Schafer K J and Kulander K C 1992 High-order harmonic generation from atoms and ions in the high intensity regime *Phys. Rev. Lett.* **68** 3535
[2] Popmintchev T *et al* 2012 Bright coherent ultrahigh harmonics in the keV x-ray regime from mid-infrared femtosecond lasers *Science* **336** 1287
[3] Silva F, Teichmann S M, Cousin S L and Biegert J 2015 Spatio-temporal isolation of attosecond soft x-ray pulses in the water window *Nat. Commun.* **6** 6611
[4] Teubner U and Gibbon P 2009 High-order harmonics from laser-irradiated plasma surfaces *Rev. Mod. Phys.* **81** 445
[5] Vampa G and Brabec T 2017 Merge of high harmonic generation from gases and solids and its implications for attosecond science *J. Phys. B: At. Mol. Opt. Phys.* **50** 083001
[6] Plaja L, Torres R and Zaïr A 2013 Attosecond physics *Attosecond Measurements and Control of Physical Systems* (Berlin: Springer)
[7] Krausz F and Ivanov M 2009 Attosecond physics *Rev. Mod. Phys.* **81** 163
[8] Ghimire S, DiChiara A D, Sistrunk E, Agostini P, DiMauro L F and Reis D A 2011 Observation of high-order harmonic generation in a bulk crystal *Nat. Phys.* **7** 138
[9] Schubert O *et al* 2014 Sub-cycle control of terahertz high-harmonic generation by dynamical bloch oscillations *Nat. Photon.* **8** 119
[10] Luu T, Garg M, Kruchinin S Y, Moulet A, Hassan M T and Goulielmakis E 2015 Extreme ultraviolet high-harmonic spectroscopy of solids *Nature* **521** 498
[11] Hohenleutner M, Langer F, Schubert O, Knorr M, Huttner U, Koch S W, Kira M and Huber R 2015 Real-time observation of interfering crystal electrons in high-harmonic generation *Nature* **523** 572
[12] Vampa G, Hammond T J, Thiré N, Schmidt B E, Légaré F, McDonald C R, Brabec T and Corkum P B 2015 Linking high harmonics from gases and solids *Nature* **522** 462
[13] Ndabashimiye G, Ghimire S, Wu M, Browne D A, Schafer K J, Gaarde M B and Reis D A 2016 Solid-state harmonics beyond the atomic limit *Nature* **534** 520
[14] Liu H, Li Y, You Y S, Ghimire S, Heinz T F and Reis D A 2017 High-harmonic generation from an atomically thin semiconductor *Nat. Phys.* **13** 262
[15] Plaja L and Roso-Franco L 1992 High-order harmonic generation in a crystalline solid *Phys. Rev.* B **45** 8334
[16] Picón A, Roso L, Mompart J, Varela O, Ahufinger V, Corbalán R and Plaja L 2010 Dipole spectrum structure of nonresonant nonpertubative driven two-level atoms *Phys. Rev.* A **81** 033420
[17] Ghimire S, DiChiara A D, Sistrunk E, Ndabashimiye G, Szafruga U B, Mohammad A, Agostini P, DiMauro L F and Reis D A 2012 Generation and propagation of high-order harmonics in crystals *Phys. Rev.* A **85** 043836
[18] Golde D, Meier T and Koch S W 2008 High harmonics generated in semiconductor nanostructures by the coupled dynamics of optical inter- and intraband excitations *Phys. Rev.* B **77** 075330
[19] Vampa G, McDonald C R, Orlando G, Klug D D, Corkum P B and Brabec T 2014 Theoretical analysis of high-harmonic generation in solids *Phys. Rev. Lett.* **113** 073901
[20] Wu M, Ghimire S, Reis D A, Schafer K J and Gaarde M B 2015 High-harmonic generation from Bloch electrons in solids *Phys. Rev.* A **91** 043839
[21] Luu T T and Wörner H J 2016 High-order harmonic generation in solids: a unifying approach *Phys. Rev.* B **94** 115164
[22] Osika E N, Chacón A, Ortmann L, Suárez N, Pérez-Hernández J A, Szafran B, Ciappina M F, Sols F, Landsman A S and Lewenstein M 2017 Wannier–Bloch approach to localization in high-harmonics generation in solids *Phys. Rev.* X **7** 021017
[23] Tancogne-Dejean N and Rubio A 2018 Atomic-like high-harmonic generation from two-dimensional materials *Sci. Adv.* **4** eaao5207
[24] Buna M and Borini S 2009 Optical constants of graphene layers in the visible range *Appl. Phys. Lett.* **94** 031901
[25] Mikhailov S A and Ziegler K 2008 Nonlinear electromagnetic response of graphene: frequency multiplication and the self-consistent-field effects *J. Phys.: Condens. Matter* **20** 384204
[26] Ishikawa K L 2010 Nonlinear optical response of graphene in time domain *Phys. Rev.* B **82** 201402
[27] Dean J J and van Driel H M 2009 Second harmonic generation from graphene and graphitic films *Appl. Phys. Lett.* **95** 261910
[28] Kumar N, Kumar J, Gerstenkorn C, Wang R, Chiu H Y, Smirl A L and Zhao H 2013 Third harmonic generation in graphene and few-layer graphite films *Phys. Rev.* B **87** 121406
[29] Hong S Y, Dadap J I, Petrone N, Yeh P C, Hone J and Osgood R M 2013 Optical third-harmonic generation in graphene *Phys. Rev.* X **3** 021014

[30] Baudisch M et al 2017 Petahertz optical response in graphene arXiv:1703.10945
[31] Ni G X et al 2016 Ultrafast optical switching of infrared plasmon polaritons in high-mobility graphene Nat. Photon. 10 244
[32] Cox J D, Marini A and García de Abajo F J 2017 Plasmon-assisted high-harmonic generation in graphene Nat. Commun. 8 14380
[33] Yoshikawa N, Tamaya T and Tanaka K 2017 High-harmonic generation in graphene enhanced by elliptically polarized light excitation Science 356 736
[34] Taucer M et al 2017 Nonperturbative harmonic generation in graphene from intense midinfrared pulsed light Phys. Rev. B 96 195420
[35] Dimitrovski D, Madsen L B and Pedersen T G 2017 High-order harmonic generation from gapped graphene: perturbative response and transition to nonperturbative regime Phys. Rev. B 95 035405
[36] Kelardeh H K, Apalkov V and Stockman M I 2015 Graphene in ultrafast and superstrong laser fields Phys. Rev. B 91 045439
[37] Chizhova L A, L Florian and Burgdörfer J 2017 High-harmonic generation in graphene: interband response and the harmonic cutoff Phys. Rev. B 95 085436
[38] Reich S, Thomsen C and Maultzsch J 2004 Carbon Nanotubes: Basic Concepts and Physical Properties (Weinheim: Wiley)
[39] Kelardeh H K, Apalkov V and Stockman M I 2014 Wannier–Stark states of graphene in strong electric field Phys. Rev. B 90 085313
[40] Breusing M, Ropers C and Elsaesser T 2009 Ultrafast carrier dynamics in graphite Phys. Rev. Lett. 102 086809
[41] Brida D et al 2013 Ultrafast collinear scattering and carrier multiplication in graphene Nat. Commun. 4 611
[42] Iglesias J M, Martín M J, Pascual E and Rengel R 2015 Carrier-carrier and carrier-phonon interactions in the dynamics of photoexcited electrons in graphene J. Phys.: Conf. Ser. 647 012003
[43] Lewenstein M, Balcou Ph, Ivanov M Y, L'Huillier A and Corkum P B 1994 Theory of high-harmonic generation by low-frequency laser fields Phys. Rev. A 49 2117
[44] Roberts A, Cormode D, Reynolds C, Newhouse-Illige T, LeRoy B J and Sandhu A S 2011 Response of graphene to femtosecond high-intensity laser irradiation Appl. Phys. Lett. 99 051912
[45] Antoine P, l'Huillier A and Lewenstein M 1996 Attosecond pulse trains using high-order harmonics Phys. Rev. Lett. 77 1234
[46] Sivis M, Taucer M, Vampa G, Johnston K, Staudte A, Naumov A Y, Villeneuve D M, Ropers C and Corkum P B 2017 Tailored semiconductors for high-harmonic optoelectronics Science 357 303–6
[47] Golde D, Meier T and Koch S W 2006 Microscopic analysis of extreme nonlinear optics in semiconductor nanostructures J. Opt. Soc. Am. B 23 2559

3.6.2 *Optical anisotropy of non-perturbative high-order harmonic generation in gapless graphene*

Resumen

La generación de armónicos de orden elevado (HHG) en sistemas atómicos o moleculares es un mecanismo robusto para producir pulsos ultracortos coherentes en la región del ultravioleta extremo y con polarización controlable. Aunque durante mucho tiempo se creyó que la HHG estaba restringida a la producción de armónicos polarizados linealmente, varias técnicas han logrado generar armónicos con polarización elíptica y circular en gases atómicos, aunque utilizando configuraciones bastante sofisticadas [126, 127]. Por otra parte, existe un creciente interés por la utilización de sólidos cristalinos para la HHG, debido a su mayor eficiencia en la conversión armónica y la flexibilidad que exhiben para ser utilizados como blancos de alta densidad [58]. Se ha reportado que la HHG en los sólidos es sensible a la orientación del campo eléctrico en relación con el eje del cristal [128]. Otros trabajos recientes revelan también que la HHG en el grafeno es más eficiente mediante excitaciones polarizadas elípticamente, y que los armónicos con polarización circular se pueden obtener a partir de pulsos con polarización circular [16]. En este contexto, hemos realizado un estudio teórico detallado de las características de polarización de los armónicos inducidos al irradiar grafeno con pulsos láser ultracortos infrarrojos, en función de los parámetros de polarización del láser. Así, hemos analizado la elipticidad, el ángulo de inclinación y la intensidad de los armónicos generados por pulsos láser con diferentes polarizaciones y orientaciones. Nuestros resultados demuestran una conversión de la polarización de los armónicos extraordinariamente compleja, que conduce a un amplio abanico de posibilidades para su control: rotación óptica, polarización sintonizable y polarización transitoria ultrarrápida. Por otra parte, nuestros resultados revelan que los pulsos armónicos se producen con elipticidad variable en la escala del femtosegundo, mostrando así al existencia de cambios ultrarrápidos en el estado de polarización. Además, aunque ya se ha observado despolarización en la respuesta a pulsos polarizados circularmente en sistemas atómicos [126, 134], nuestros resultados muestran que este fenómeno es aún más acusado en el grafeno.

Research Article | Vol. 27, No. 5 | 4 Mar 2019 | OPTICS EXPRESS 7776
Optics EXPRESS

Optical anisotropy of non-perturbative high-order harmonic generation in gapless graphene

Óscar Zurrón-Cifuentes,[1,*] Roberto Boyero-García,[1] Carlos Hernández-García,[1] Antonio Picón,[2] and Luis Plaja[1]

[1] *Grupo de Investigación en Aplicaciones del Láser y Fotónica, Departamento de Física Aplicada, University of Salamanca, Salamanca E-37008, Spain*
[2] *Departamento de Química, Universidad Autónoma de Madrid, Madrid 28049, Spain*
[*] *ozurronci@usal.es*

Abstract: High harmonic generation in atomic or molecular targets stands as a robust mechanism to produce coherent ultrashort pulses with controllable polarization in the extreme-ultraviolet. However, the production of elliptically or circularly-polarized harmonics is not straightforward, demanding complex combinations of elliptically or circularly-polarized drivers, or the use of molecular alignment techniques. Nevertheless, recent studies show the feasibility of high-harmonic generation in solids. In contrast with atoms and molecules, solids are high-density targets and therefore more efficient radiation sources. Among solid targets, 2D materials are of special interest due to their particular electronic structure, which conveys special optical properties. In this paper, we present theoretical calculations that demonstrate an extraordinary complex light-spin conversion in single-layer graphene irradiated at non perturbative intensities. Linearly-polarized drivings result in the emission of elliptically-polarized harmonics, and elliptically-polarized drivings may result in linearly-polarized or ellipticity-reversed harmonics. In addition, we demonstrate the ultrafast temporal modulation of the harmonic ellipticity.

1. Introduction

High-order harmonic generation (HHG) results from the interaction of physical systems with intense electromagnetic radiation and has led to a large number of relevant applications in attosecond science [1]. HHG is based on the dynamics of the unbound electrons rather than in bound-state transitions, as in conventional perturbative photon up-conversion schemes. As a non-perturbative process, HHG has a noticeable feature: the harmonic spectra show a *plateau*-like structure, followed by a steep drop in efficiency beyond certain cut-off frequency [2]. The *plateau* may extend up to thousands of harmonic orders, allowing the generation of coherent extreme ultraviolet (XUV) or even soft x-ray radiation [3].

High-order harmonics have been observed from a wide diversity of materials. For gas-phase systems, HHG arises from ionized electrons pulled away from their parent atoms or molecules and recolliding back as the field reverses its sign. During recollision electrons may recombine, emitting coherent high-energy photons [4, 5]. For a long time, HHG was thought to be restricted to produce linearly polarized harmonics due to the weak rescattering efficiency when driven by circularly polarized IR pulses [6]. However, several techniques have recently succeeded in generating elliptically and circularly polarized harmonics in atomic gases, using rather sophisticated configurations: HHG driven by a two-color counter-rotating circularly polarized field [7–10]; HHG driven by single-color noncollinear counter-rotating beams [11, 12]; HHG in a double gas jet configuration irradiated by orthogonally polarized beams [13]; or by using molecular targets irradiated by ellipticaly and linearly polarized driving pulses [14–17].

#356082 https://doi.org/10.1364/OE.27.007776
Journal © 2019 Received 26 Dec 2018; revised 6 Feb 2019; accepted 19 Feb 2019; published 1 Mar 2019

Optics EXPRESS

Anisotropic molecules have been also demonstrated to produce elliptical-polarized harmonics out of linear-polarized drivings, after being strongly aligned [18].

High density targets, as crystalline solids, have become increasingly interesting due to their higher efficiency in harmonic conversion and the flexible design of target geometries. HHG in solids, however, is limited by photoinduced damage, which restricts the maximum intensity of the driving field. Until recently, only bulk solids were considered for HHG, with energy gaps larger than the driver photons [19]. HHG from finite-gap solids follows a similar process to atoms or molecules, where ionization is replaced by tunnel excitation from the valence to the conduction band at the driving field maxima, and harmonics are radiated upon electron-hole recombination [20].

Modern materials, such as topological insulators and 2D materials, present a wide variety of electronic structure configurations, controlled by manufacturing, that make them interesting candidates for HHG [21, 22]. Specifically, single-layer graphene (SLG) shows a potential due to the presence of degenerate points in the reciprocal space, that convey extraordinary electronic and optical properties. The singular band-structure provides graphene with a strong non-linear optical response [23, 24]. For instance, second and third harmonics have been observed in multilayer graphene [22, 25–27], and harmonics up to the 9th-order in SLG driven by mid-infrared laser pulses have also been reported [28, 29]. In contrast with the finite-gap case, HHG in graphene relies on the excitation of electron-hole pairs at the Dirac points, which is not associated to tunnel excitation [30]. Dirac points at topological-phase boundaries have been also associated to the enhancement of harmonic conversion [31, 32].

It has been reported that HHG in solids is sensitive to the orientation of the electric field relative to the crystal axis [21, 33, 34]. Recent reports revealed also that HHG in graphene is enhanced by elliptically polarized excitations [28, 35, 36], and that circular-polarized harmonics can be obtained from circular-polarized drivers [36, 37]. In this paper we present a detailed theoretical study of the polarization characteristics of the harmonics induced by a few-cycle infrared laser pulse, as a function of the driver polarization parameters. We analyze the ellipticity, tilt angle and intensity of the harmonics when driven by a laser pulse with different polarizations and orientations. Our results demonstrate an extraordinarily complex photon-spin conversion, leading to a rich scenario for harmonic polarization control: optical rotation, tunable polarization and ultrafast transient polarization. Although time-dependent ellipticity has been observed in the response to circularly and elliptically-polarized drivers in atomic systems [12, 38], here we show that this phenomenon is even stronger for SLG.

2. Methods

Single layer graphene is composed of carbon atoms arranged in an 2D-hexagonal honeycomb lattice, with the first Brillouin Zone as shown in Fig. 1(a). According to the standard tight-binding description of SLG within the nearest-neighbor aproximation [39], the out-of-plane atomic p_z orbitals overlap resulting in π-type bands. Taking the energy of the carbon $2p$ orbitals as reference ($\epsilon_{2p} = 0$), the hamiltonian which describes the electron dynamics in the periodic potential of the crystal is a 2×2 matrix of the form

$$H_0 = \begin{pmatrix} 0 & \gamma f(\mathbf{k}) \\ \gamma f^*(\mathbf{k}) & 0 \end{pmatrix} \tag{1}$$

where $\gamma = 2.97$ eV is the hopping integral and $f(\mathbf{k})$ the complex function:

$$f(\mathbf{k}) = e^{-iak_x/\sqrt{3}} \left(1 + 2e^{i\sqrt{3}ak_x/2} \cos \frac{ak_y}{2} \right), \tag{2}$$

being $a = 2.46$ Å the lattice constant. The band structure of SLG is obtained upon diagonalization of H_0, which yields to eigenvalues $E_\pm(\mathbf{k}) = \pm\gamma|f(\mathbf{k})|$. The wave functions of the corresponding eigenstates of the conduction (+) and valence (-) bands can be written as

$$\Phi_\pm(\mathbf{k};\mathbf{r}) = \sqrt{\frac{1}{2}}e^{i\mathbf{k}\cdot\mathbf{r}}\begin{pmatrix}\pm 1\\ e^{-i\phi(\mathbf{k})}\end{pmatrix}, \tag{3}$$

being $\phi(\mathbf{k})$ the argument of the complex function $f(\mathbf{k})$. $E_\pm(\mathbf{k})$ describe the conduction and valence bands of graphene shown in Fig. 1(b). In the reciprocal space, the high-symmetry points K and K' are degenerated at the energy origin (Dirac points). At their vicinity the band dispersion is linear: electrons and holes behave as massless fermions with constant velocity $v_F \simeq 10^6$ m/s. The maximum energy gap, $\simeq 17.8$ eV, occurs at the center of the Brillouin Zone, labeled Γ in Fig. 1(a). We note that, in practical situations, the chemical potential of graphene can be shifted by electrostatic fields or introducing chemicals. If constant fields are applied near the breakdown threshold, energy shifts of few hundred meV (charge density of few 10^{13} electrons per cm^2) are induced. These values of the chemical potential have a small effect in the optical properties of graphene [40]. Note also that the conduction band occupation with chemical potentials of 100 meV is still very low in comparison with the valence band occupation ($> 10^{15}$ electrons per cm^2) and thus, Pauli blocking is not likely to be relevant. As a result of these considerations, we do not expect that chemical potential shifts affect substantially our results.

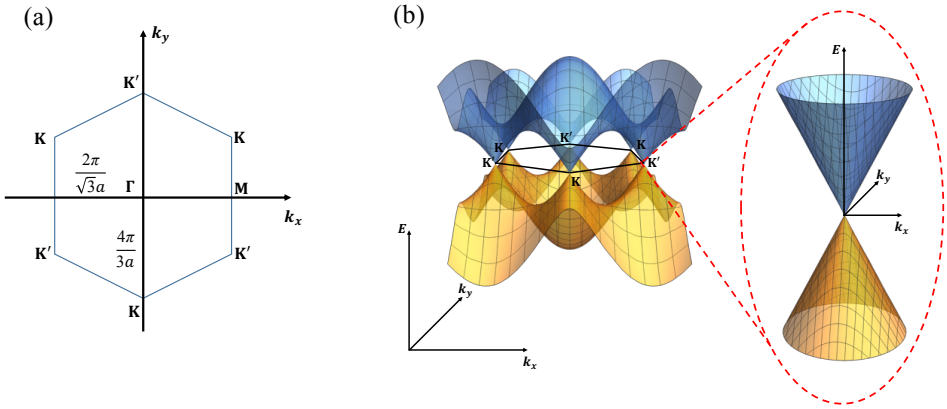

Fig. 1. (a) Scheme of graphene's first Brillouin Zone in the reciprocal space. (b) Graphene's band structure within the nearest-neighbor tight-binding approximation. The Fermi level is set to zero. The conduction and valence bands correspond to positive and negative values of energy, respectively. Dirac points K and K' are degenerated in energy at the Fermi level.

The interaction of the laser pulse $\mathbf{F}(t)$ with the system is described by the time-dependent Hamiltonian $H(t) = H_0 + V_i(t)$, where H_0 is the SLG hamiltonian (1), and $V_i(t) = -q_e\mathbf{F}(t)\cdot\mathbf{r}$ is the electric field coupling in the dipole approximation, being q_e the elementary charge. The time-dependent wave function can be expressed as a superposition of the eigenstates (3):

$$\Psi(\mathbf{r},t) = \int \Psi(\mathbf{k};\mathbf{r},t)d\mathbf{k} = \int \left[C_+(\mathbf{k},t)\Phi_+(\mathbf{k};\mathbf{r}) + C_-(\mathbf{k},t)\Phi_-(\mathbf{k};\mathbf{r})\right]d\mathbf{k}. \tag{4}$$

Following [30], the dynamics can be computed from the integration of the following two-level

Optics EXPRESS

equations at each point of the Brillouin Zone:

$$i\hbar\frac{d}{dt}C^M(\boldsymbol{\kappa}_t,t) = \frac{E_+(\boldsymbol{\kappa}_t)+E_-(\boldsymbol{\kappa}_t)}{2}C^M(\boldsymbol{\kappa}_t,t)+\frac{E_+(\boldsymbol{\kappa}_t)-E_-(\boldsymbol{\kappa}_t)}{2}e^{i\phi(\boldsymbol{\kappa}_t)}\tilde{C}^P(\boldsymbol{\kappa}_t,t) \quad (5)$$

$$i\hbar\frac{d}{dt}\tilde{C}^P(\boldsymbol{\kappa}_t,t) = \frac{E_+(\boldsymbol{\kappa}_t)+E_-(\boldsymbol{\kappa}_t)}{2}\tilde{C}^P(\boldsymbol{\kappa}_t,t)+\frac{E_+(\boldsymbol{\kappa}_t)-E_-(\boldsymbol{\kappa}_t)}{2}e^{-i\phi(\boldsymbol{\kappa}_t)}C^M(\boldsymbol{\kappa}_t,t) \quad (6)$$

where $\hbar\boldsymbol{\kappa}_t = \hbar\mathbf{k} - q_e\mathbf{A}(t)/c$, $\mathbf{A}(t)$ being the vector potential, and

$$C^M(\boldsymbol{\kappa}_t,t) = C_+(\boldsymbol{\kappa}_t,t) - C_-(\boldsymbol{\kappa}_t,t) \quad (7)$$

$$C^P(\boldsymbol{\kappa}_t,t) = e^{-i\phi(\boldsymbol{\kappa}_t)}\left[C_+(\boldsymbol{\kappa}_t,t) + C_-(\boldsymbol{\kappa}_t,t)\right]. \quad (8)$$

We take as initial condition the SLG in its ground state, i.e. $C_-(\mathbf{k},0) = 1$ and $C_+(\mathbf{k},0) = 0$. The harmonic emission is given by the dipole acceleration, i.e. the second time derivative of

$$\mathbf{d}(t) = \langle\Psi(\mathbf{r},t)|q_e\mathbf{r}|\Psi(\mathbf{r},t)\rangle = i\frac{q_e}{2}\int\left[C^{M*}\nabla_{\boldsymbol{\kappa}_t}C^M + C^{P*}\nabla_{\boldsymbol{\kappa}_t}C^P\right]d\mathbf{k}. \quad (9)$$

We have integrated numerically Eqs. (5), (6), and (9), considering an 8-cycle (full extend) driving pulse with $\sin^2$ temporal envelope, modeled as:

$$\mathbf{F}(t) = \sin^2(\pi t/8T)\left[F_x\sin(\omega_0 t)\mathbf{e}_x + F_y\sin(\omega_0 t+\Delta\phi)\mathbf{e}_y\right] \quad (10)$$

where F_x and F_y are the cartesian components of the field amplitude, T is the period, $\omega_0 = 2\pi/T$ the field frequency, and $\Delta\phi$ the relative phase between the field components. We neglect local field corrections to the driving field amplitude, as the field is aimed perpendicularly to the graphene layer and, therefore, propagates through an atomic-size thickness. For the calculations presented in this work, we have considered a wavelength of 3 μm, resulting in a pulse duration of 28 fs (2.9 cycles) at full-width-half-maximum in intensity, ensuring that the pulse length is smaller than the decoherence time due to carrier collisions [41]. We have considered a peak intensity of 5×10^{10} W/cm^2, well below the threshold damage, assuming damage for fluences above 150 mJ/cm^2 [42].

3. Results and discussion

3.1. Linearly polarized laser driver

We first have studied the dependence of the non-linear response of SLG to a linearly-polarized field, i.e. $\Delta\phi = 0$ in Eq. (10), as a function of the tilt angle, $\theta = \arctan(F_x/F_y)$. Figure 2(a) shows the calculated spectra for different values of θ, obtained by the addition of the spectral components $\mathcal{S}_x(\theta,\omega)$ and $\mathcal{S}_y(\theta,\omega)$. The response shows the typical non-perturbative behaviour (*plateau*) up to the seventh harmonic order, followed by a cut-off. These results are in good agreement with the experimental observations reported in [28], where HHG was observed up to the ninth harmonic. As a consequence of the symmetry, the optical response with respect to the driver's polarization follows a periodic pattern with period $\Delta\theta = 60°$. Thus, the harmonic spectrum for $\theta = 30°$ is indistinguible from the one corresponding to $\theta = 90°$ (horizontally polarized driver). Note that the spectra shown in Fig. 2(a) are particularly rich. This is a consequence of the interference of the two different contributions, intraband and interband, as well as of the contributions of different electron-hole pair's trajectories leading to the same harmonic [30].

The fact that the spectra in Fig. 2(a) are not identical demonstrates the anisotropic nature of the optical response of SLG under intense laser fields. As noted previously, anisotropy in HHG is also expected for aligned molecular targets due to the non-spherical symmetry of the molecular orbitals [43]. However, crystalline solids include an additional source of anisotropy, as the dynamics of the electrons in the conduction band are still subjected to the details of the crystal

Optics EXPRESS

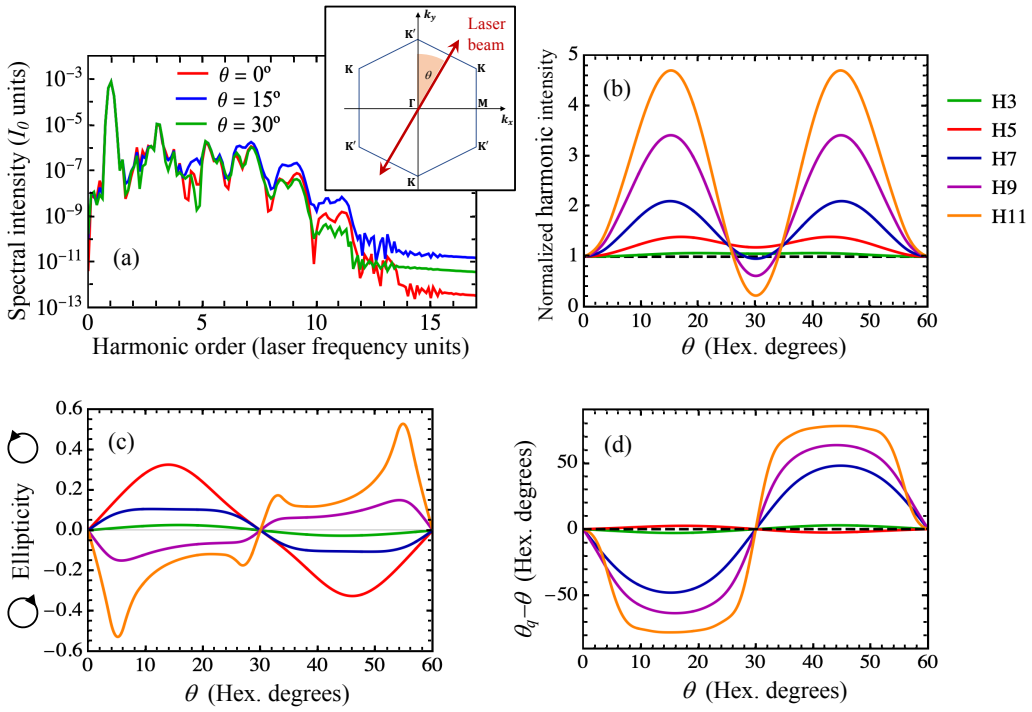

Fig. 2. (a) Total harmonic yield from SLG for different angles of linear polarization of the driving laser, measured from the vertical axis, as shown in the inset. The total yield for each angle is obtained by the addition of the spectral components $\mathcal{S}_x(\theta, \omega)$ and $\mathcal{S}_y(\theta, \omega)$ and it is given in units of the driver's intensity I_0. (b) Intensities of the harmonic yield of SLG as a function of θ. For each harmonic, intensities are normalized to the value at $\theta = 0$. (c) Ellipticity of the harmonic yield as a function of θ. Positive values of the ellipticity indicate left handed polarization. (d) Harmonic tilt angle shift with respect to the driver's tilt, as a function of θ.

potential. In contrast, ionized electrons in molecules behave approximately as free particles and therefore, respond to the field isotropically.

Figure 2(b) shows the variation of the intensity of the harmonic yield with the driver's polarization angle θ. The intensity of each harmonic is normalized to the corresponding value at $\theta = 0$. All the harmonics present a maximum intensity value for $\theta = 15°$ and $45°$, which increases with the harmonic order. On the other hand, the harmonic yield finds a minimum efficiency at $\theta = 30°$ for the higher-order harmonics. Note, therefore, that the crystal symmetry axes do not correspond to the optimal driver polarization directions to generate harmonics efficiently.

Figures 2(c) and 2(d) show the dependence of the harmonic ellipticity ε_q and relative tilt angle $\theta_q - \theta$ with respect to the driver's polarization direction. The ellipticity and tilt angle of the q-th harmonic are derived from the Stokes parameters $\{S_0^q, S_1^q, S_2^q, S_3^q\}$, computed from the intensity of the different polarization components, integrated over a spectral window of width ω_0 around

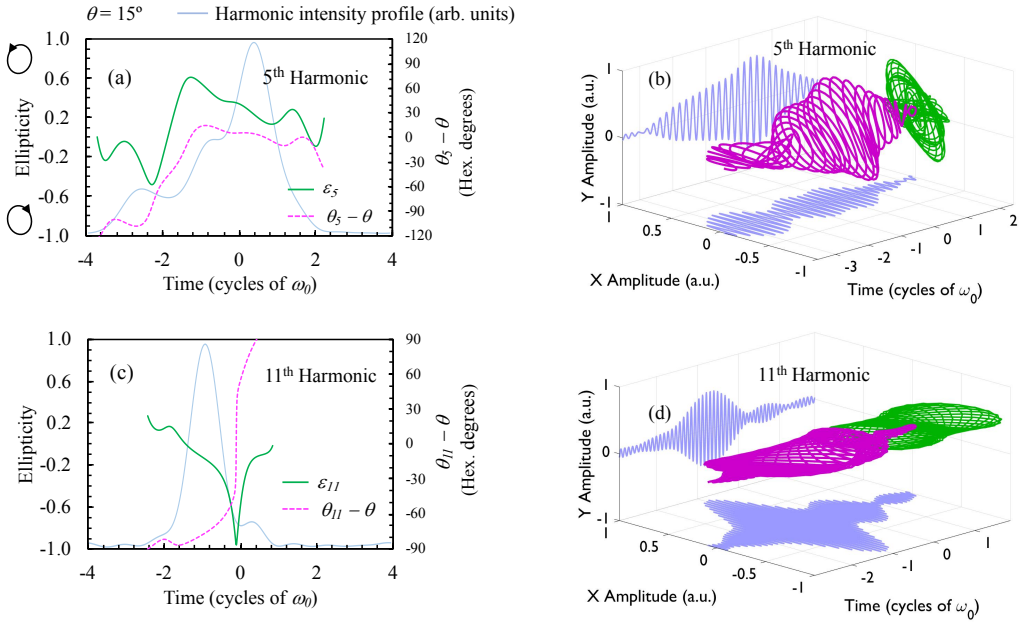

Fig. 3. Time dependent ellipticity for a tilt angle $\theta = 15^\circ$ of the input beam. Panels (a) and (c) show the time dependence of the ellipticity parameter ε_q and relative tilt angle $\theta_q - \theta$ for the fifth and eleventh harmonics, respectively. The blue line in the background of each panel represents the intensity profile of the harmonic emission. Panels (b) and (d) show the 3D plots of the electric field for the fifth and eleventh harmonic pulses along with their ortogonal X and Y components.

each harmonic frequency. Then, the ellipticity and tilt angle are defined as:

$$\varepsilon_q = \tan\left[\frac{1}{2}\arctan\left(\frac{S_3^q}{\sqrt{S_1^{q\,2} + S_2^{q\,2}}}\right)\right], \tag{11}$$

$$\theta_q = \frac{\pi}{2} - \frac{1}{2}\arctan\frac{S_2^q}{S_1^q}. \tag{12}$$

Inspection of Fig. 2(c) reveals that all harmonic orders are linearly polarized when the driving field is aligned with a symmetry axis of the SLG lattice ($\theta = 0$, 30°, etc.), and elliptically polarized elsewhere. The harmonic ellipticity for angles $\theta < 30^\circ$ and $> 30^\circ$ are related by mirror symmetry. We find a remarkable difference between the lower and higher-order harmonics: for angles $\theta < 30^\circ$ the third, fifth and seventh harmonics present left-handed elliptical polarization, whilst the ninth and eleventh are right handed. In contrast, in the case of aligned molecules, the harmonic ellipticity against the driver's tilt behaves similarly for all harmonic orders. According to [20, 30] the frequency of the emitted harmonic corresponds to the instantaneous energy of the electron-hole pair when recombining. This suggests that the third harmonic is generated near the Dirac points, where the band structure is isotropic and therefore, the third-harmonic emission becomes insensitive to the orientation of the driver's polarization.

The combination of the results shown in Figs. 2(b) and 2(c) leaves the conclusion that SLG behaves most efficiently as a source of elliptically polarized harmonics when the driver's

Optics EXPRESS

polarization axis is rotated 15° from the crystal symmetry axes. It also demonstrates that the ellipticity of the harmonics generated in SLG can be easily tuned by changing the tilt angle of the linearly polarized driver, without the need of complex driving configurations.

The orientation of the polarization ellipse (i.e. the tilt angle θ_q of its main axis), is analyzed in Fig. 2(d). The major axis is almost parallel to the signal's polarization for the lower harmonics, while it rotates gradually as the harmonic order increases, reaching a maximal angular difference around $\theta = 15°$ and 45°. For these tilt angles, the main axis of the polarization ellipse of the eleventh harmonic is almost perpendicular to the direction of the driver polarization.

We plot in Fig. 3 the time evolution of the polarization of the harmonics generated at a driver's tilt of 15°, which corresponds to the maximum conversion efficiency, see Fig. 2(b). Our computations show a clear evidence of ultrafast polarization changes both in ellipticity, at the scale of 0.2 per cycle, and tilt angle. The time-dependent harmonic ellipticities are also found in collinear [38] and non-collinear [12] schemes in atomic targets. However, we show that the range and rate of ellipticity variation in SLG are considerable higher. As a general trend, the rate of variation is shown to increase with the harmonic order. This suggests possible applications in ultrafast pump-probe transient absorption experiments.

3.2. *Elliptically polarized laser driver*

We have also investigated the variation of the HHG response to changes in the ellipticity of the driving pulse. We consider a right-handed elliptically polarized driving pulse, as described by Eq. (10) with $\Delta\phi = \pi/2$. The ellipticity of the driver is, therefore, $\varepsilon_{IR} = F_x/F_y$. The rest of the driving field's parameters are defined as in the linear case, so that $\varepsilon_{IR} = 0$ corresponds to the (vertical) linearly polarized driver of the preceding section.

Figure 4(a) shows the calculated harmonic yield for different values of ε_{IR}. The spectra also show the non-perturbative characteristics (*plateau* and cut-off) observed for linear polarization in the previous section. A main observation from Fig. 4(a) is the drop in the efficiency of the HHG for circularly polarized drivings (green line, $\varepsilon_{IR} = 1$). This trend is also observed in atoms, where the number of rescattering trajectories drops drastically with the ellipticity of the driver [44]. However, in comparison with the atomic case, the drop in efficiency in SLG is much weaker. Most interestingly, for $\varepsilon_{IR} = 1$, the three-fold rotational symmetry of graphene forbids the generation of one every three harmonic orders, as it has been recently reported in [36], much in the same way as in atomic HHG driven by two-color counter-rotating fields [7–10].

As a further observation, Fig. 4(a) also shows that the harmonic intensity does not decrease monotonically with the driver's ellipticity, as can be noticed by comparing the red ($\varepsilon_{IR} = 0$) and blue ($\varepsilon_{IR} = 0.3$) curves. We further explore this phenomena in Fig. 4(b), where we plot the normalized harmonic intensity as a function of the driver's ellipticity for different harmonics. The harmonic response is split into two components, parallel to the major axis $\mathcal{S}_y(\varepsilon, \omega)$, dotted lines, and minor axis $\mathcal{S}_x(\varepsilon, \omega)$, solid lines, of the driver's polarization ellipse. All the intesities are normalized by $\mathcal{S}_y$ at $\varepsilon_{IR} = 0$. Note that, while $\mathcal{S}_y$ decreases with the ellipticity for all the harmonic orders, $\mathcal{S}_x$ shows a pronounced increase with a maximum for the driver's ellipticity in the interval $0.3 < \varepsilon_{IR} < 0.4$. This result is in agreement with the experimental data presented in [28]. Complementary, Fig. 4(d) shows the dependence of the ellipticity of each harmonic field as a function of the driver's ellipticity. Note that the region of optimal harmonic conversion in Fig. 4(b) corresponds to harmonics with polarization close to linear. This behavior is the opposite of what we found for the linear-polarized driving in the preceding section, where the optimal conversion efficiency is associated with the generation of elliptically polarized harmonics. Note also that for smaller values of ε_{IR} the polarization is right-handed (as it is the input beam), whilst it turns to left-handed for higher ellipticities. Remarkably enough, for circularly polarized input signal ($\varepsilon_{IR} = 1.0$) the fifth and seventh harmonics are nearly circularly polarized [36], and with opposite handeness, also as found in atomic HHG driven by counter-rotating fields [7–10].

Optics EXPRESS

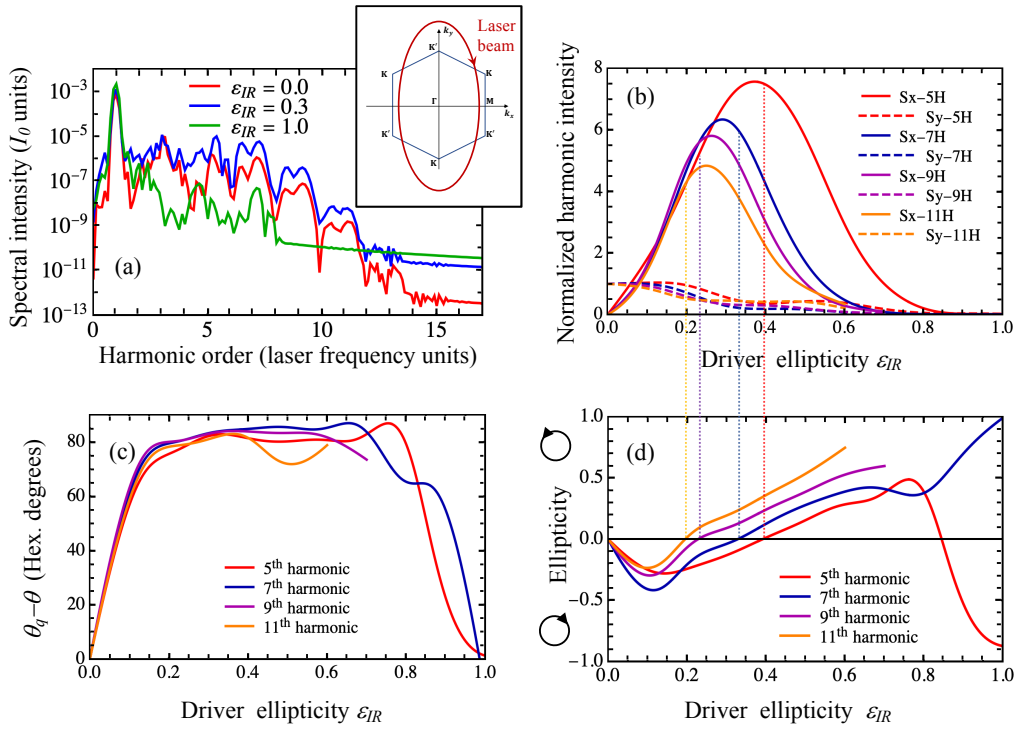

Fig. 4. (a) Harmonic yield from SLG for three different values of the ellipticity of the input beam. The total yield is obtained by the addition of the spectral components $\mathcal{S}_x$ and $\mathcal{S}_y$ parallel to the axes of the laser polarization ellipse and it is given in units of the driver's intensity I_0. (b) Normalized intensities for the harmonic yield as a function of the laser ellipticity. (c) Tilt angle of the harmonic response as a function of ε_{IR}. The tilt angle of the input laser is always zero. (d) Ellipticity of the harmonic yield from SLG as a function of ε_{IR}. Positive values of the ellipticity indicate left handed polarization. The lines connecting graphics (b) and (d) are eye guides. In (b), (c) and (d) the highest harmonics are not plotted for the largest ellipticities because they are not resolved in the spectra.

As additional information, we plot in Fig. 4(c) the tilt angle of the major axis polarization ellipse of each harmonic as a function of the driving field's ellipticity. Our results show that the main axis of the response is almost perpendicular to the main axis of the driving for ellipticity values of maximal efficiency. As shown in Fig. 4(b), this is a consequence of the steep increase of $\mathcal{S}_x$ in these cases. Together with the data shown in Fig. 4(d), we can conclude that the harmonic emission efficiency shows a maximum for driving ellipticities in the range $0.3 < \varepsilon_{IR} < 0.4$, where the harmonics are emitted with polarization close to linear and tilt angles perpendicular to the main axis of the driver's polarization ellipse.

Finally, Fig. 5 shows the time dependent polarization for $\varepsilon_{IR} = 0.3$, i.e. a value corresponding to maximal conversion efficiency according to Fig. 4(b), and for $\varepsilon_{IR} = 1.0$. In the case of the elliptically-polarized drivers, the polarization of the harmonic field varies at the femtosecond scale, in the same way than for linearly-polarized drivings. Note however that the ellipse tilt remains approximately constant at each pulse component of the harmonic field. On the other hand, the ellipticity remains close to pure circular in time when the driving field is circularly-polarized.

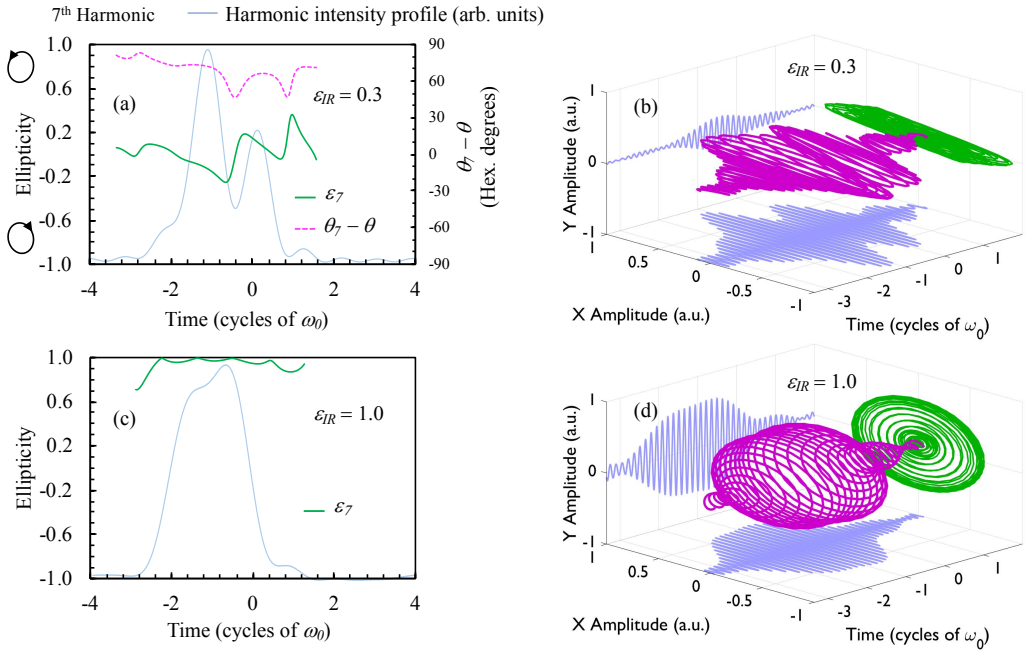

Fig. 5. Panels (a) and (c) show the time dependence of the ellipticity for $\varepsilon_{IR} = 0.3$ and 1.0, respectively. The blue line in the background of each panel represents the intensity profile of the harmonic emission within the laser pulse. Panels (b) and (d) show the 3D plots of the electric field for the harmonic pulses along with its ortogonal X and Y components.

4. Conclusions

We have studied the polarization properties of the high-harmonic emission from single-layer graphene irradiated by intense few-cycle infrared laser pulses with different polarizations. Our numerical results demonstrate that the anisotropic response of SLG induces a complex photon-spin conversion, and thus the production of ellipticaly polarized harmonics from linear-polarized infrared pulses, and linearly polarized harmonics from elliptical-polarized infrared pulses. For the case of elliptically polarized drivers, we have confirmed the increasing role of the polarizability in the x direction, revealing a strong sensitivity of the polarization characteristics of the harmonics field to variations on the driver's ellipticity. Our results also reveal the ultrafast change of the harmonic polarization state, producing pulses with femtosecond time-varying ellipticity. This dynamics may be resolved experimentally using spatial-spectral interferometry [45]. These pulses convey an extraordinary tool for ultrafast pump-probe experiments, ultrafast chiral dichroism [46, 47] and spin/charge dynamics in magnetic materials [48, 49].

Funding

Junta de Castilla y León (SA287P18); Agencia Estatal de Innovación (FIS2016-75652-P, EQC2018-004117-P); Comunidad de Madrid (2017-T1/IND-5432); Agencia Estatal de Investigación (RYC-2017-22745).

References

1. L. Plaja, R. Torres, and A. Zaïr, *Attosecond Physics. Attosecond Measurements and Control of Physical Systems* (Springer-Verlag, 2013).

Optics EXPRESS

2. J. L. Krause, K. J. Schafer, and K. C. Kulander, Phys. Rev. Lett. **68**, 3535-3538 (1992).
3. T. Popmintchev, M. C. Chen, D. Popmintchev, P. Arpin, S. Brown, S. Alisauskas, G. Andriukaitis, T. Balciunas, O. Mücke, A. Pugzlys, A. Baltuska, B. Shim, S. E. Schrauth, A. Gaeta, C. Hernández-García, L. Plaja, A. Becker, A. Jaron-Becker, M. M. Murnane, and H. C. Kapteyn, "Bright Coherent Ultrahigh Harmonics in the keV X-ray Regime from Mid-Infrared Femtosecond Lasers," Science **336**, 1287-1291 (2012).
4. P. B. Corkum, "Plasma perspective on strong field multiphoton ionization," Phys. Rev. Lett. **71**, 1994-1997 (1993).
5. K. J. Schafer, B.Yang, L. F. DiMauro, and K. C. Kulander, "Above threshold ionization beyond the high harmonic cutoff," Phys. Rev. Lett. **70**, 1599-1602 (1993).
6. P. Dietrich, N. H. Burnett, M. Ivanov, P. B. Corkum, "High-harmonic generation and correlated two-electron multiphoton ionization with elliptically polarized light," Phys. Rev. A **50**, R3585-R3588 (1994).
7. D. B. Milosevic, W. Becker, R. Kopold, "Generation of circularly polarized high-order harmonics by two-color coplanar field mixing," Phys. Rev. A **61**, 063403 (2000).
8. A. Fleischer, O. Kfir, T. Diskin, P. Sidorenko, O. Cohen, "Spin angular momentum and tunable polarization in high-harmonic generation," Nat. Photonics **8**, 543-549 (2014).
9. C. Chen, Z. Tao, C. Hernández-García, P. Matyba, A. Carr, R. Knut, O. Kfir, D. Zusin, C. Gentry, P. Grychtol, O. Cohen, L. Plaja, A. Becker, A. Jaron-Becker, H. Kapteyn, M. Murnane, "Tomographic reconstruction of circularly polarized high-harmonic fields: 3D attosecond metrology," Sci. Adv. **2**, e1501333 (2016).
10. K. M. Dorney, L. Rego, N. J. Brooks, J. San-Román, C.T. Liao, J. L. Ellis, D. Zusin, C. Gentry, Q. L. Nguyen, J. M. Shaw, A. Picón, L. Plaja, H. C. Kapteyn, M. M. Murnane, C. Hernández-García, "Controlling the polarization and vortex charge of attosecond high-harmonic beams via simultaneous spin-orbit momentum conservation," Nat. Photonics **13**, 123-130 (2019).
11. D. D. Hickstein, F. J. Dollar, P. Grychtol, J. L. Ellis, R. Knut, C. Hernández-García, D. Zusin, C. Gentry, J. M. Shaw, T. Fan, K. M. Dorney, A. Becker, A. Jaron-Becker, H. C. Kapteyn, M. M. Murnane, C. G. Durfee, "Non-collinear generation of angularly isolated circularly polarized high harmonics," Nat. Photonics **9**, 743-750 (2015).
12. P. C. Huang, C. Hernández-García, J. T. Huang, P. Y. Huang, C. H. Lu, L. Rego, D. D. Hickstein, J. L. Ellis, A. Jaron-Becker, A. Becker, S. D. Yang, C. G. Durfee, L. Plaja, H. C. Kapteyn, M. M. Murnane, A. H. Kung, M. C. Chen "Polarization control of isolated high-harmonic pulses," Nat. Photonics **12**, 349-354 (2018).
13. J. L. Ellis, K. M. Dorney, D. D. Hickstein, N. J. Brooks, C. Gentry, C. Hernández-García, D. Zusin, J. M. Shaw, Q. L. Nguyen, C. A. Mancuso, G. S. M. Jansen, S. Witte, H. C. Kapteyn, M. M. Murnane,"High harmonics with spatially varying ellipticity," Optica **5**, 479-485 (2018).
14. K. J. Yuan, A. D. Bandrauk, "Circularly polarized molecular high-order harmonic generation in H2+ with intense laser pulses and static fields," Phys. Rev. A **83**, 063422 (2011).
15. G. Lambert, B. Vodungbo, J. Gautier, B. Mahieu, V. Malka, S. Sebban, P. Zeitoun, J. Luning, J. Perron, A. Andreev, S. Stremoukhov, F. Ardana-Lamas, A. Dax, C. P. Hauri, A. Sardinha, M. Fajardo "Towards enabling femtosecond helicity-dependent spectroscopy with high-harmonic sources," Nat. Commun. **6**, 6167 (2015).
16. A. Ferré, C. Handschin, M. Dumergue, F. Burgy, A. Comby, D. Descamps, B. Fabre, G. A. Garcia, R. Géneaux, L. Merceron, E. Mével, L. Nahon, S. Petit, B. Pons, D. Staedter, S. Weber, T. Ruchon, V. Blanchet, Y. Mairesse "A table-top ultrashort light source in the extreme ultraviolet for circular dichroism experiments," Nat. Photonics **9**, 93-98 (2015).
17. A. Etches, Ch. B. Madsen, and L. B. Madsen, "Inducing elliptically polarized high-order harmonics from aligned molecules with linearly polarized femtosecond pulses," Phys. Rev. A **81**, 013409 (2010).
18. X. Zhou, R. Lock, N. Wagner, W. Li, H. C. Kapteyn, and M. M. Murnane, "Elliptically Polarized High-Order Harmonic Emission from Molecules in Linearly Polarized Laser Fields," Phys. Rev. Lett. **102**, 073902 (2009).
19. S. Ghimire, A.D. DiChiara, E. Sistrunk, P. Agostini, L.F. DiMauro, and D.A. Reis, "Observation of high-order harmonic generation in a bulk crystal," Nat. Phys. **7**, 138-141 (2011).
20. G. Vampa, C. R. McDonald, G. Orlando, D. D. Klug, P. B. Corkum, and T. Brabec, "Theoretical analysis of High Harmonic Generation in solids," Phys. Rev. Lett. **113**, 073901 (2014).
21. H. Liu, Y. Li, Y.S. You, S. Ghimire, T. F. Heinz, and D. A. Reis, "High-harmonic generation from an atomically thin semiconductor," Nat. Phys. **13**, 262-265 (2017).
22. M. Baudisch, A. Marini, J. D. Cox, T. Zhu, F. Silva, S. Teichmann, M. Massicotte, F. Koppens, L. S. Levitov, F. J. García de Abajo, J. Biegert, "Petahertz optical response in graphene", Nat. Commun. **9**, 1018 (2018)
23. S. A. Mikhailov and K. Ziegler, "Nonlinear electromagnetic response of graphene: frequency multiplication and the self-consistent-field effects," J. Phys.: Condens. Matter **20**, 384204 (2008).
24. K. L. Ishikawa, "Nonlinear Optical Response of Graphene in Time Domain," Phys. Rev. B **82**, 201402 (2010).
25. J. J. Dean and H. M. van Driel, "Second harmonic generation from graphene and graphitic films," Appl. Phys. Lett. **95**, 261910 (2009).
26. N. Kumar, J. Kumar, C. Gerstenkorn, R. Wang, H.Y. Chiu, A.L. Smirl, and H. Zhao, "Third harmonic generation in graphene and few-layer graphite films," Phys. Rev. B **87**, 121406 (2013).
27. S.Y. Hong, J.I. Dadap, N. Petrone, P.C. Yeh, J. Hone, and R.M. Osgood, "Optical Third-Harmonic Generation in Graphene," Phys. Rev. X **3**, 021014 (2013).
28. N. Yoshikawa, T. Tamaya, and K. Tanaka, "High-harmonic generation in graphene enhanced by elliptically polarized light excitation," Science **356**, 736-738 (2017).
29. M. Taucer, T. J. Hammond, P. B. Corkum, G. Vampa, C. Couture, N. Thiré, B. E. Schmidt, F. Légaré, H. Selvi, N.

Optics EXPRESS

Unsuree, B. Hamilton, T. J. Echtermeyer and M. A. Denecke, "Nonperturbative harmonic generation in graphene from intense midinfrared pulsed light," Phys. Rev. B **96**, 195420 (2017).
30. O. Zurrón, A. Picón, and L. Plaja, "Theory of high-order harmonic generation for gapless graphene," New J. Phys. **20** 053033 (2018).
31. A. Chacón, W. Zhu, Sh. P. Kelly, A. Dauphin, E. Pisanty, A. Picón, Ch. Ticknor, M. F. Ciappina, A. Saxena, M. Lewenstein "Observing Topological Phase Transitions with High Harmonic Generation," arXiv:1807.01616 [cond-mat.mes-hall] (2018).
32. R. E. F. Silva, A. Jiménez-Galán, B. Amorim, O. Smirnova, and M. Ivanov, "Topological strong field physics on sub-laser cycle time scale," arXiv:1806.11232v2 [physics.optics] (2018).
33. F. Langer, M. Hohenleutner, C. P. Schmid, C. Poellmann, P. Nagler, T. Korn, C. Schüller, M. S. Sherwin, U. Huttner, J. T. Steiner, S. W. Koch, M. Kira, and R. Huber, "Lightwave-driven quasiparticle collisions on a subcycle timescale," Nature **533**, 225-229 (2016).
34. Y. S. You, J. Lu, E. Cunningham, Ch. Roedel, and S. Ghimire, "Crystal orientation-dependent polarization state of high-order harmonics," arXiv:1810.11567v1 (2018).
35. C. Liu, Y. Zheng, Z. Zeng, and R. Li "Driving-laser ellipticity dependence of high-order harmonic generation in graphene." Phys. Rev. A **97**, 063412 (2018).
36. Z.Y. Chen and R. Qin,"Circularly polarized extreme ultraviolet high harmonic generation in graphene," arXiv:1808.07346v2 (2018).
37. S. A. Sørngård, S. I. Simonsen, and J. P. Hansen, "High-order harmonic generation from graphene: Strong attosecond pulses with arbitrary polarization," Phys. Rev. A **87**, 053803 (2013).
38. L. Barreau, K. Veyrinas, V. Gruson, S. J. Weber, T. Auguste, J. F. Hergott, F. Lepetit, B. Carré, J. C. Houver, D. Dowek, and P. Salières, Pascal, "Evidence of depolarization and ellipticity of high harmonics driven by ultrashort bichromatic circularly polarized fields," Nat. Commun. **9**, 4727 (2018).
39. S. Reich and Ch. Thomsen, and J. Maultzsch, *Carbon Nanotubes: Basic Concepts and Physical Properties* (Wiley-Vch Verlag, 2004).
40. F. Zhou and W. Du, "The graphene Mach-Zehnder modulator based on sandwiched structure," Res J Opt Photonics **2**, 1000110 (2018).
41. M. Breusing, C. Ropers and Th. Elsaesser, "Ultrafast carrier dynamics in graphite," Phys. Rev. Lett. **102** 086809 (2009).
42. A. Roberts, D. Cormode, C. Reynolds, T. Newhouse-Illige, B. J. LeRoy, and A. S. Sandhu, "Response of graphene to femtosecond high-intensity laser irradiation," Appl. Phys. Lett. **99**, 051912 (2011).
43. E. Skantzakis, S. Chatziathanasiou, P. A. Carpeggiani, G. Sansone, A. Nayak, D. Gray, P. Tzallas, D. Charalambidis, E. Hertz and O. Faucher, "Polarization shaping of high-order harmonics in laser-aligned molecules," Scientific Reports **6**, 39295 (2016).
44. K. S. Budil, P. Salières, A. L' Huillier, T. Ditmire, and M. D. Perry, "Influence of ellipticity on harmonic generation,", Phys. Rev. A **48**, R3437-R3440 (1993).
45. M. W. Lin and I. Jovanovic, "Single-Shot Measurement of Temporally-Dependent Polarization State of Femtosecond Pulses by Angle-Multiplexed Spectral-Spatial Interferometry," Scientific Reports **6**, 32839 (2016).
46. R. Cireasa, A. E. Boguslavskiy, B. Pons, M. C. H. Wong, D. Descamps, S. Petit, H. Ruf, N. Thiré, A. Ferré, J. Suarez, J. Higuet, B. E. Schmidt, A. F. Alharbi, F. Légaré, V. Blanchet, B. Fabre, S. Patchkovskii, O. Smirnova, Y. Mairesse, V. R. Bhardwaj. "Probing molecular chirality on a sub-femtosecond timescale," Nat. Phys. **11**, 654-658 (2015).
47. S. Beaulieu, A. Comby, D. Descamps, B. Fabre, G. A. Garcia, R. Géneaux, A. G. Harvey, F. Légaré, Z. Masín, L. Nahon, A. F. Ordonez, S. Petit, B. Pons, Y. Mairesse, O. Smirnova, V. Blanchet, "Photoexcitation circular dichroism in chiral molecule," Nat. Phys. **14**, 484-489 (2018).
48. C. Boeglin, E. Beaurepaire, V. Halté, V. López-Flores, C. Stamm, N. Pontius, H. A. Durr, J.-Y. Bigot, "Distinguishing the ultrafast dynamics of spin and orbital moments in solids," Nature **465**, 458-461 (2010).
49. P. Tengdin, W. You, C. Chen, X. Shi, D. Zusin, Y. Zhang, C. Gentry, A. Blonsky, M. Keller, P. M. Oppeneer, H. C. Kapteyn, Z. Tao, M. M. Murnane, "Critical behavior within 20 fs drives the out-of-equilibrium laser-induced magnetic phase transition in nickel," Sci. Adv. **4**, 9744 (2018).

4

HIGH-ORDER HARMONIC GENERATION IN CARBON NANOTUBES

This chapter is devoted to study HHG in single wall carbon nanotubes irradiated by intense ultrashort IR laser pulses. Using the tight-binding and zone folding approximations, discussed in chapter 2, we first derive in section 4.1 the dynamical equations and the expression for the emission dipole governing the harmonic generation. Next, in section 4.2 we focus in the study of the harmonic spectra, which show the emergence of the typical non-perturbative features at fluences below the damage threshold. We demonstrate that the harmonic cut-off frequency saturates with the intensity, as it occurs in the case of graphene. We discuss the results for the different types of SWNTs attending to the differences between them. Finally, in section 4.3 we apply our saddle-point approximation model (SPAM) to show that the mechanism for harmonic emission is similar to that reported for graphene in section 3.5, although now is triggered by the non-adiabatic crossing of electrons through van Hove singularities instead of Dirac points. These results have been partially published in Ref. [135], which is fully included in section 4.4.

4.1 MODEL AND MAIN EQUATIONS

The symmetries of SWNTs discussed in section 2.2.2 determine the selection rules for the optical transitions between electronic states. If the wavelength of the incident beam is large compared to the translational period a_0, the conservation of the linear quasi-momentum leads to almost direct transitions ($\Delta k \approx 0$). Furthermore, within the dipole approximation the interaction Hamiltonian is proportional to the momentum operator and consequently, it transforms according to the polar vector representation D^{pv} of the symmetry group of the nanotube. Therefore, any optical transition from the state $|i\rangle$ into the state $|f\rangle$ is allowed if the direct product of the representations of the polar vector and those of the electronic states have a common component, i. e. if $D^{|f\rangle} \subseteq D^{|i\rangle} \otimes D^{pv}$ [74]. The z component of a polar vector belongs to the non-degenerate representation ${}_0A_0^-$, since it has even parity with respect to σ_v and odd parity under σ_h reflections and U-axis transformations [136].[1] Consequently, z-polarized light changes

1 We will consider only drivers with polarization parallel to the tube axis (z). If another polarization direction was to be considered, note that the x- and y- components of the polar vector are double-degenerate and have even parity under σ_h but odd parity under U-axis transformations. Therefore the irreducible representations are given by ${}_0E_{\pm 1}^+$ for achiral tubes and ${}_0E_1^-$ for chiral SWNTs [136].

neither the angular momentum m nor the σ_v parity quantum numbers, but it does reverse the σ_h parity of the state it interacts with. Therefore, for the transition $|i\rangle \to |f\rangle$ to be allowed, the states must have same k, m and σ_v-parity, and opposite σ_h-parity quantum numbers [89]. In addition, the electronic intraband dynamics is subjected to *umklapp* rules, that govern the jump of the quantum number m when the **k**-trajectories exceed the first Brillouin zone [74]. We shall discuss such *umklapp* rules in more detail in the following sections.

Let us begin considering a nanotube (n_1, n_2) irradiated by an intense laser pulse, linearly polarized along its axis, $\mathbf{F}(t) = F(t)\mathbf{u}_z$. The electron dynamics is governed by the time-dependent hamiltonian $H(k, m, t) = H_o(k, m) + V_{int}(t)$, where $H_o(k, m)$ is the unperturbed hamiltonian of graphene constrained to the 1D **k**-space manifold of the nanotube (see chapter 2), and $V_{int}(t) = -q_e F(t) z$ is the electric field coupling in the dipole approximation. If $|\Phi^{\pm}_{k,m}\rangle$ are the eigenstates of the conduction and valence bands in the zone-folding approximation, the time-dependent wave function of the Bloch electron can be written as:

$$\begin{aligned}\Psi(\mathbf{r}, t) &= \sum_m \int \psi_{k,m}(\mathbf{r}, t) dk \\ &= \sum_m \int \left[C^+_m(k, t)\Phi^+_{k,m}(\mathbf{r}) + C^-_m(k, t)\Phi^-_{k,m}(\mathbf{r}) \right] dk. \end{aligned} \tag{4.1}$$

Inserting Eq. (4.1) into the TDSE, Eq. (3.3), and following the procedure described in section 3.1 for graphene, we obtain the following set of coupled two-level equations:

Dynamical equations of SWNTs

$$\begin{aligned} i\hbar \frac{d}{dt} C^+_m(\kappa_t, t) = &\left[E^+_m(\kappa_t) - F(t) D_m(\kappa_t) \right] C^+_m(\kappa_t, t) \\ &- F(t) D_m(\kappa_t) C^-_m(\kappa_t, t), \end{aligned} \tag{4.2}$$

$$\begin{aligned} i\hbar \frac{d}{dt} C^-_m(\kappa_t, t) = &\left[E^-_m(\kappa_t) - F(t) D_m(\kappa_t) \right] C^-_m(\kappa_t, t) \\ &- F(t) D_m(\kappa_t) C^+_m(\kappa_t, t), \end{aligned} \tag{4.3}$$

where $\hbar\kappa_t = \hbar k - q_e A(t)/c$, being $A(t)$ the vector potential, $E^{\pm}_m$ are the energy eigenvalues for band index m, see section 2.2.2, and D_m is the component of the transition matrix element of graphene parallel to the nanotube axis, Eq. (3.22), constrained to the set of allowed wave vectors. That is:

$$D_m(k) = \frac{q_e}{2} \frac{\partial \varphi_m}{\partial k}, \tag{4.4}$$

being $\varphi_m(k)$ the phase of the complex function $f_m(k)$ defined by Eq. (2.47). To integrate equations (4.2) and (4.3) we follow the approach used for graphene in section 3.1. Introducing the off-diagonal coefficients $C^M_m(\kappa_t, t)$ and $C^P_m(\kappa_t, t)$

$$C^M_m(\kappa_t, t) = C^+_m(\kappa_t, t) - C^-_m(\kappa_t, t), \tag{4.5}$$

$$C^P_m(\kappa_t, t) = e^{-i\varphi_m(\kappa_t)} \left[C^+_m(\kappa_t, t) + C^-_m(\kappa_t, t) \right], \tag{4.6}$$

it is thereby also possible to recast the equations to overcome the numerical instabilities that appear as a consequence of the divergence of D_m at the vicinity of the Dirac points K and K′:

Integration scheme for the dynamical equations of SWNTs

$$i\hbar\frac{d}{dt}C_m^M(\kappa_t,t) = \frac{E_m^+(\kappa_t)+E_m^-(\kappa_t)}{2}\,C_m^M(\kappa_t,t) + \frac{E_m^+(\kappa_t)-E_m^-(\kappa_t)}{2}\,e^{i\,\varphi_m(\kappa_t)}C_m^P(\kappa_t,t) \tag{4.7}$$

$$i\hbar\frac{d}{dt}C_m^P(\kappa_t,t) = \frac{E_m^+(\kappa_t)+E_m^-(\kappa_t)}{2}\,C_m^P(\kappa_t,t), + \frac{E_m^+(\kappa_t)-E_m^-(\kappa_t)}{2}\,e^{-i\,\varphi_m(\kappa_t)}C_m^M(\kappa_t,t). \tag{4.8}$$

As discussed in section 3.2, the harmonic emission is proportional to the second derivative of the emission dipole, which is given by the restriction of Eq. (3.33) to the Brillouin zone of the nanotube:

Emission dipole of SWNTs

$$d(t) = i\,\frac{q_e}{2}\sum_m\int\left[C_m^{M*}\frac{\partial C_m^M}{\partial\kappa_t}+C_m^{P*}\frac{\partial C_m^P}{\partial\kappa_t}\right]dk. \tag{4.9}$$

In addition, note that the intraband component of the emission spectra can be also computed as the restriction of Eq. (3.34) to the BZ of the nanotube:

$$a_m^{intra}(t) = \frac{{q_e}^2}{\hbar^2}F(t)\int\left[|C_m^+|^2\frac{\partial^2E_m^+}{\partial\kappa_t^2}+|C_m^-|^2\frac{\partial^2E_m^-}{\partial\kappa_t^2}\right]dk. \tag{4.10}$$

4.2 HIGH-ORDER HARMONIC SPECTRA

We have integrated numerically Eqs. (4.7)–(4.10), considering mid-IR few-cycle driving pulses at different intensities targeting SWNTs of different types and diameters. The driving pulses are modeled using an 8-cycle (full width) $\sin^2$ temporal envelope as defined by Eq. (3.27). We neglect local field corrections to the driving field amplitude, as the beam is aimed perpendicularly to the nanotube and, therefore, propagates through walls of atomic-size thickness. The spectra thereby computed are discussed in the following sections.

4.2.1 *Armchair nanotubes*

All (n,n) type tubes exhibit the π-band structure shown in Fig. 4.1(a), with the valence and conduction bands crossing at $a_0k = 2\pi/3$, so they are always metallic. Optical transitions $A_0^+ \to B_0^+$ and $B_n^+ \to A_n^+$ induced by z-polarized drivers are forbidden in any (n,n) $\mathcal{A}$-type tube as a consequence of the σ_h-parity selection rule. The rest of bands $|m| = 1,\ldots,n-1$ are doublets where optical transitions are allowed for any $a_0k \in (0,\pi]$, but forbidden at $a_0k = 0$. Furthermore, the intraband dynamics is also subjected to the *umklapp* rule $m' = m \pm n$ (mod

$2n$), so that m shifts to m' when the first Brillouin zone is exceeded through $a_0 k = \pi$ [137]. The pink-filled area in the background of Fig. 4.1(a) shows the DOS for a $(9,9)$ tube, which is dominated by the van Hove singularities at the zero-slope points of the band's diagram, and has a small non-null value nearby the Fermi level. This structure is common to all $\mathcal{A}$-tubes.

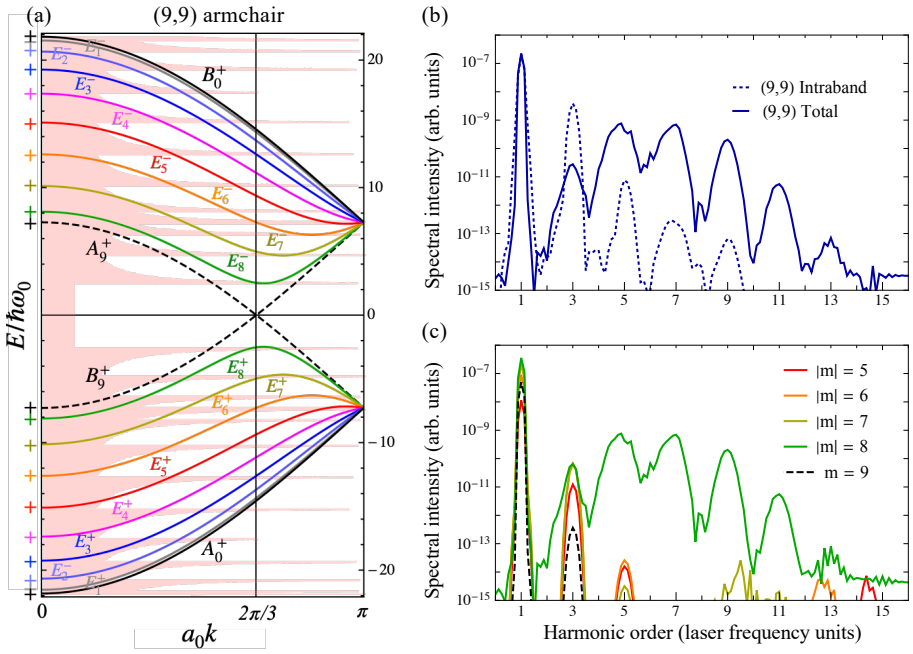

Figure 4.1: (a) Band structure of $(9,9)$ $\mathcal{A}$-type tube. The energy is given in units of the frequency of a 3 μm laser ($\hbar\omega_o = 0.41$ eV). The horizontal axis represents the wave vector times the translational period $a_0 = 2.46$ Å. The pink-filled area in the background shows the DOS. (b) Harmonic yield from $(9,9)$ armchair driven by a 3 μm wavelength, 28 fs (2.9 cycles) FWHM pulse at 5×10^{10} W/cm^2 peak intensity. The solid (dashed) line represents the total (intraband) harmonic spectrum. (c) Contribution to the total harmonic yield from transitions between m bands.

Figure 4.1(b) shows the calculated HHG yield from a (9,9) $\mathcal{A}$-tube at a driving peak intensity of 5×10^{10} W/cm^2 and 3 μm wavelength.[2] The emergence of a spectral plateau extending up to a cut-off frequency corresponding to the seventh harmonic is clearly observed. Only odd-order harmonics are present in the spectrum, as a consequence of the centrosymmetric structure of the system. All harmonics are linearly polarized in the direction of the tube axis. In Fig. 4.1(c) we show the contributions to the emission spectra corresponding to different values of m. The coherent addition of the contributions from all m-values results in the spectra shown in (b). Note that the higher order harmonics are given by the contribution from bands $|m| = 8$,

2 The results included in this section were reported in our publication of Ref. [135].

which include the first van Hove singularity. Remarkably, the band gap at the first van Hove singularity is nearly resonant with a $5\omega_o$ transition, thus enhancing the interband component of the high harmonic emission around this resonance. The other points of the BZ contribute to the lower order harmonics mainly with intraband radiation.

According to Eqs. (4.2) and (4.3), the valence and conduction bands are coupled during the interaction with the laser field by the matrix element D_m, which in the case of $\mathcal{A}$-type tubes has the form [138, 139]:

Transition matrix element for $\mathcal{A}$-type tubes

$$D_m(k) = -\frac{a_0 q_e}{2} \frac{\sin\left(\frac{a_0 k}{2}\right) \sin\left(\frac{m\pi}{n}\right)}{1 + 4\cos\left(\frac{a_0 k}{2}\right)\left[\cos\left(\frac{m\pi}{n}\right) + \cos\left(\frac{a_0 k}{2}\right)\right]}. \tag{4.11}$$

Fig. 4.2 depicts D_m in the $(9,9)$-armchair tube for different band indices m. Note that D_m is null for $m = 0, n$ at any $a_0 k \in (-\pi, \pi]$, thus decoupling the dynamical equations (4.2) and (4.3). We assume that initially the states bellow the Fermi level are fully occupied, $C_m^-(k,0) = 1$, and those at the conduction band are empty, $C_m^+(k,0) = 0$. Since the

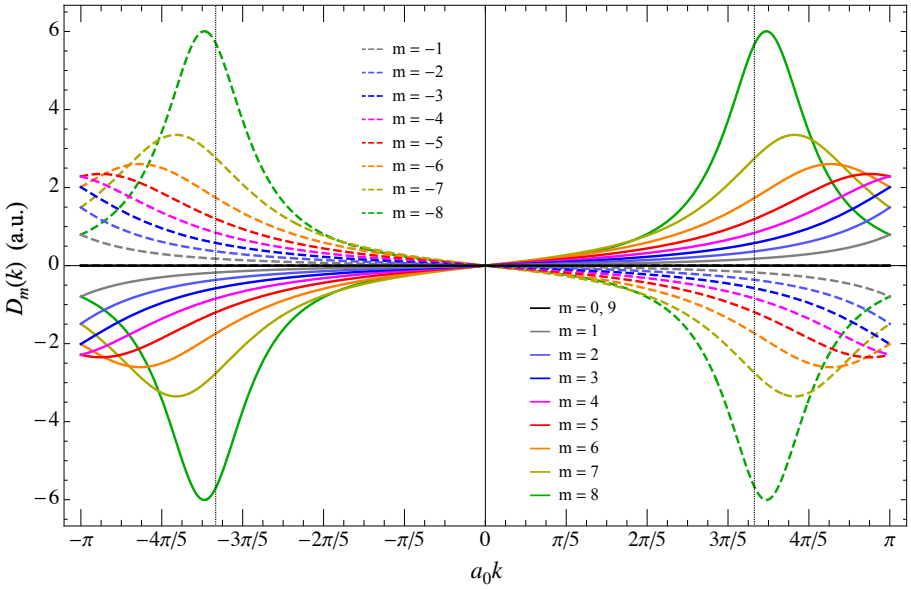

Figure 4.2: Matrix element $D_m(k)$ corresponding to the (9,9) armchair tube for different m values. The vertical dotted lines at $a_0 k = \pm 2\pi/3$ indicate the band's crossing at the Dirac points for $m = 9$.

states B_n^+ (A_0^+) and A_n^+ (B_0^+) are decoupled, their population remains in B_n^+ (A_0^+) and contributes to HHG only through intraband transitions. This conclusion is a consequence of the σ_h symmetry-induced selection rule. The coupling is symmetric with respect to $a_0 k = 0$ for bands with equal $|m|$, and shows peaks of magnitude increasing with $|m|$ at the wave vectors corresponding to the first four van Hove singularities in the DOS. The absolute maximum of D_m is reached at the

first van Hove singularity, which in the zone folding approach corresponds to the bands located closest to the Dirac points, $|m| = n - 1$. This suggests that the interaction with the driver laser is much more efficient for these states and, therefore, that the interband emission spectra is mainly due to transitions within states $|m| = n - 1$. Note that the increased band curvature near the Dirac points entails sharper van-Hove singularities, which also enhances the efficiency of the interband transitions. In contrast, in 1D models with finite gaps intraband currents are the main source of harmonic radiation [64].

Figure 4.3 shows the harmonic yield from $\mathcal{A}$-tubes of different diameters. The basic features of the spectra are maintained, although the efficiency of the harmonics near resonance (5^{th} and 7^{th}) increase with the tube diameter. Note that the slope of the bands closest to $a_0 k = \pm 2\pi/3$ increases with the tube diameter, and the number of electronic states available at the maximal values of D_m also increases. As the diameter increases, the BZ points of bands $|m| = n - 1$ fall closer to the Dirac points and, therefore, D_m approaches the singularity, which explains the higher efficiency of the harmonics. In addition, as the diameter increases, the resonance near the 5^{th} harmonic is red-shifted since the gap energy of the $|m| = n - 1$ bands is reduced. Finally, note also that the cut-off barely changes, independently of the size of the nanotube.

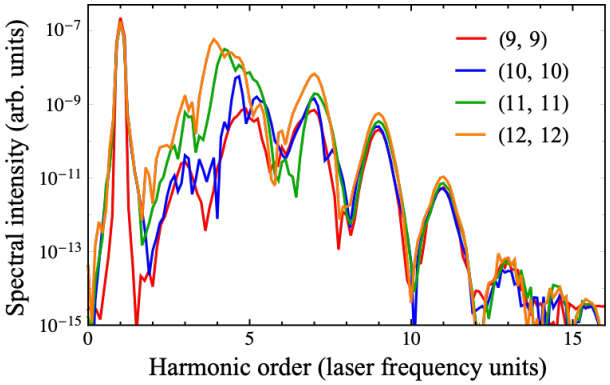

Figure 4.3: Harmonic yield from $(9,9)$, $(10,10)$, $(11,11)$ and $(12,12)$ armchair tubes. The diameters of these tubes are $d_t = 1.22, 1.36, 1.50$ and 1.63 nm, respectively. The electric field parameters are those in Fig. 4.1.

4.2.2 *Zigzag nanotubes*

While armchair tubes correspond to a chiral angle $\theta = 30°$ and always have metallic character, zigzag nanotubes ($\mathcal{Z}$-tubes) are defined by $\theta = 0°$ and can be either metallic or semiconducting, depending on the chiral index $(n, 0)$. The anisotropic dispersion of the graphene bands at the vicinity of the Dirac points results in three different types

of $\mathcal{Z}$-tubes. In metallic tubes with $n \equiv 0 \pmod 3$ the valence and conduction bands $|m_F| = 2n/3$ are degenerated at the Fermi level, and the non-degenerated bands closest to them, $m = m_F \pm 1$, present different dispersion despite being located symmetrically with respect to K, as can be seen in Figs. 2.12(a) and 4.4(a). The same dispersion asymmetry leads to a variation of the transition energies for semiconducting tubes, with different behavior depending on whether $n \equiv 1$ or $n \equiv 2 \pmod 3$, as shown in Figs. 2.12(b) and 4.4(b), and Figs. 2.12(c) and 4.4(c), respectively.

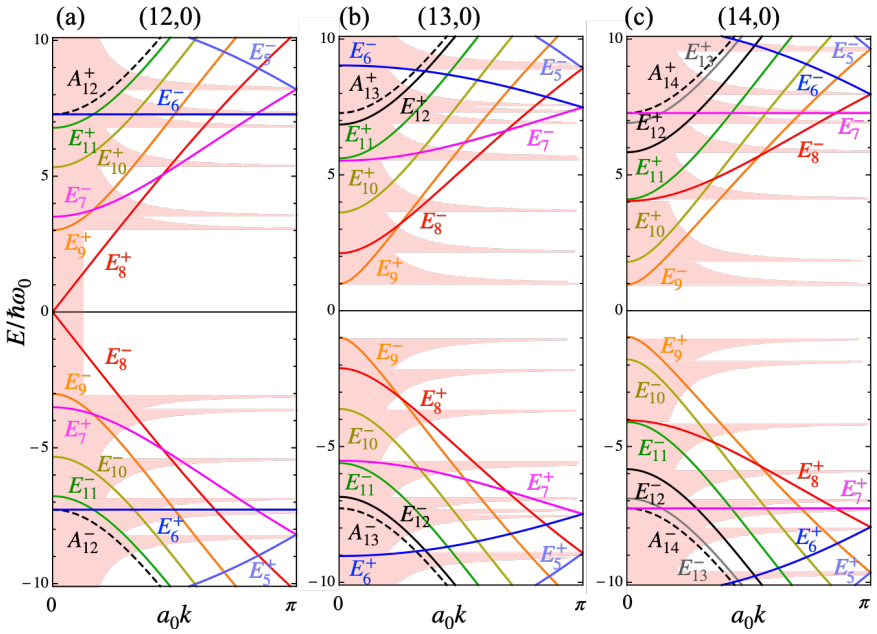

Figure 4.4: π-band structure of (a) $(12,0)$, (b) $(13,0)$ and (c) $(14,0)$ zigzag nanotubes. The energy is given in units of the frequency of a 3 μm laser driver ($\hbar\omega_o = 0.41$ eV). The horizontal axis represent the wavevector times the translational period a_0. Note that for all $\mathcal{Z}$-tubes, $a_0 = 4.26$ Å. The pink colored area in the background is the DOS.

All $\mathcal{Z}$-tubes present band diagrams similar to those shown in Fig. 4.4. The zero-slope points are always at $a_0k = 0$, where the DOS shows the van Hove singularities. A remarkable feature of zigzag tubes is the absence of symmetry-related restrictions to interband transitions for z-polarized beams, as valence and conduction bands conform multiplets or singlets with same σ_v and opposite σ_h parities. The *umklapp* rule applicable to intraband transitions exceeding the first Brillouin is the same than for $\mathcal{A}$-type tubes: $m' = m \pm n \pmod{2n}$ [137]. In the vicinity of the Fermi level, the DOS is null for semiconducting species and present a small non-null value for metallic tubes, much alike the $\mathcal{A}$-type nanotubes.

Transition matrix element for $\mathcal{Z}$-type tubes

For $\mathcal{Z}$-tubes, the matrix element that couples the valence and conduction bands in Eqs. (4.2) and (4.3) is:

$$D_m(k) = -\frac{aq_e}{2}\frac{\sin\Theta_m^k \sin\Xi_m^k}{1+4\cos\Theta_m^k\left[\cos\Xi_m^k+\cos\Theta_m^k\right]} \tag{4.12}$$

where

$$\Theta_m^k = \frac{\pi m}{2n} + \frac{\sqrt{3}ak}{4} \tag{4.13}$$

$$\Xi_m^k = \frac{3\pi m}{2n} - \frac{\sqrt{3}ak}{4} \tag{4.14}$$

being a the lattice constant of graphene. As happens in $\mathcal{A}$-type species, in zigzag nanotubes D_m is symmetric with respect to $a_0k = 0$ for bands with equal $|m|$. Fig. 4.5(a) shows the matrix element D_m for the $(12,0)$ metallic tube, which diverges at $a_0k = 0$ for $|m| = m_F$ and reaches maxima of decreasing magnitude for the rest of m values. Note that the maximal values of D_m are always located at the proximity of $a_0k = 0$. Semiconducting species show a similar behavior, except for that the matrix element remains finite in all bands, as can

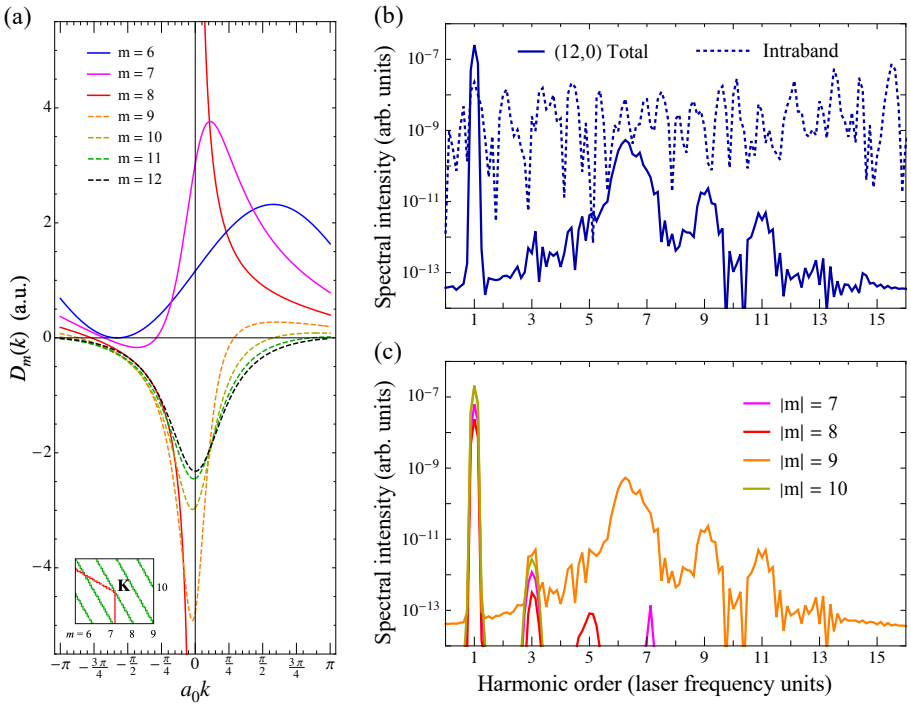

Figure 4.5: (a) Matrix element $D_m(k)$ corresponding to the $(12,0)$ zigzag tube for different m values. The inset shows the relative location of the different bands with respect to K. (b) Harmonic yield from $(12,0)$ $\mathcal{Z}$-tube driven by a 3µm wavelength, 28 fs (2.9 cycles) FWHM pulse at 5×10^{10} W/cm^2 peak intensity. (c) Contribution to the harmonic yield from the different values of $|m|$.

be seen from Figs. 4.6(a) and 4.7(a). Since D_m is in general nonzero in $\mathcal{Z}$-tubes, the dipole emission consists of both intraband and interband contributions for all m. As happens also in $\mathcal{A}$-tubes, interband transitions take place mostly in the vicinity of $a_0k = 0$, where both D_m and the DOS reach maximal values.

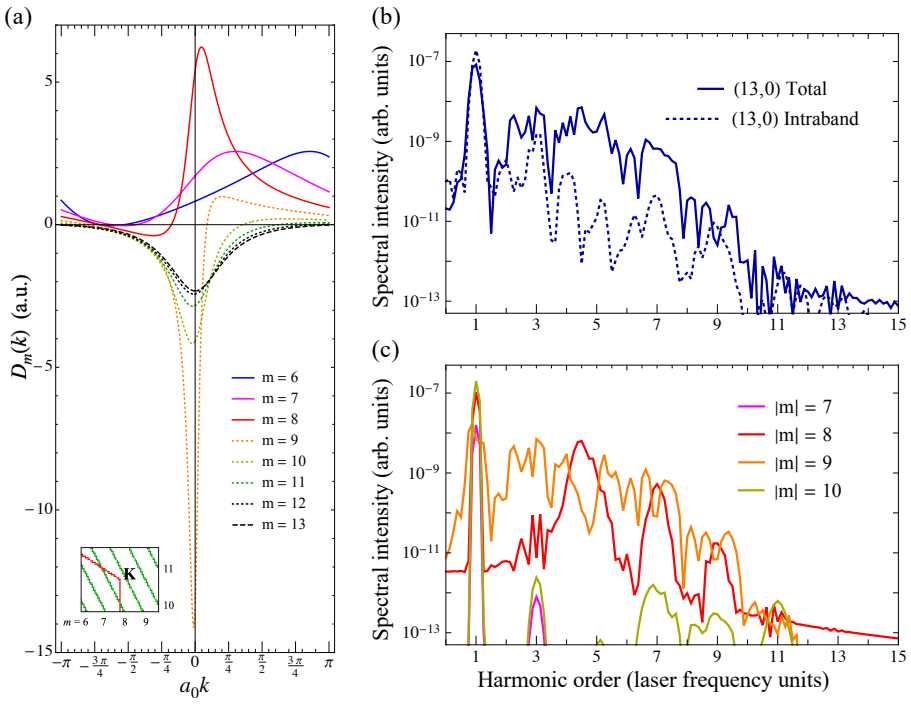

Figure 4.6: (a) $D_m(k)$ corresponding to the $(13, 0)$ semiconducting zigzag tube for different m values. The location of the different bands with respect to the point K is shown in the inset. (b) Harmonic yield from $(13, 0)$ $\mathcal{Z}$-tube. The contributions to the total harmonic yield from the different values of $|m|$ are shown in panel (c). The parameters of the drivers are the same than those in Fig. 4.5.

Fig. 4.5(b) shows the harmonic yield from the metallic $(12, 0)$ $\mathcal{Z}$-tube at a driving peak intensity of 5×10^{10} W/cm^2 and 3 μm wavelength. The spectrum shows the clear emergence of the 6-photon resonance, the lower harmonics (3^{rd} and 5^{th}) almost suppressed, and the higher ones well resolved. The intraband component of the emission spectra shows a noisy structure extending to arbitrary high frequencies, which is a consequence of the divergence of the transition matrix element at the Dirac points. This unphysical spectrum is cancelled by the interband emission, so that the total spectrum remains finite.

In Fig. 4.5(c) we show the contributions related to the different values of $|m|$. Note that the total yield is almost entirely due to the contribution from $|m| = 9$ bands and corresponds to states packed at the first van Hove singularity, where D_m presents its maximal value. As for the $\mathcal{A}$-type case, the other bands, where D_m is weaker, contribute only to the lower harmonics. As a conclusion, the high-order emis-

sion spectra in metallic $\mathcal{Z}$-type nanotubes is mainly due to transitions between states $|m| = |m_F| + 1$ at wave vectors near the first van Hove singularity, similarly to what happens in armchair tubes.

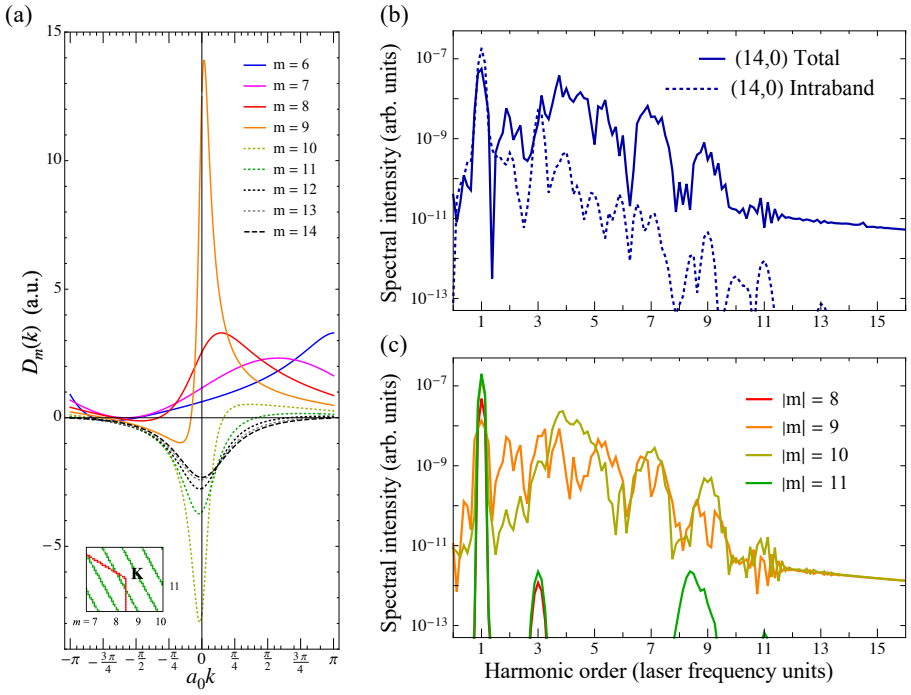

Figure 4.7: (a) $D_m(k)$ corresponding to the semiconducting $(14, 0)$ $\mathcal{Z}$-type tube. The inset shows the location of the different bands relative to the point K. (b) Harmonic yield from $(14, 0)$ $\mathcal{Z}$-tube. (c) Contributions to the total harmonic yield from the different values of m. The parameters of the drivers are the same than those in Fig. 4.5.

The emission spectra from semiconducting tubes belonging to the two different types, $n \equiv 1$ and $n \equiv 2$ (mod 3), are shown in Figs. 4.6(b) and 4.7(b), respectively. The peak intensity and wavelength of the driving field remain the same as those employed in the cases previously discussed in this section. We find that both spectra are similar, but the efficiency is lower for the tube with smaller radius $(13, 0)$. Subtle differences between the spectra are caused by the different band dispersion at the two first van Hove singularities, since they appear at opposite sides of the K point. Note that the intraband component does not contribute to the higher harmonic orders in either case, as it also happens in metallic $\mathcal{A}$ and $\mathcal{Z}$ nanotubes. Note also that the spectra of these two semiconducting tubes show signals near the 2^{nd} and 4^{th} harmonics, which are resonant with the band gap at the two first van Hove singularities, see Figs. 4.4(b) and (c).

Finally, Figs. 4.6(c) and 4.7(c) show the contributions from the different bands. In both cases, the total yield is effectively given by the coherent addition of two contributions, corresponding to bands at the

first and second van Hove singularities, where D_m presents maximal values. This feature is not observed in armchair or metallic zigzag tubes, where only the contribution from the band crossing the first van Hove singularity is relevant to HHG. The resonances at the first and second van Hove singularities (near the 2^{nd} and 4^{th} harmonics, respectively) are clearly observed in both figures. These resonances cause the complex structure of the spectral region below the 5^{th} harmonic.

Figure 4.8 shows additional information on the dependence of HHG with the nanotube's diameter. As a first result, note that the cut-off

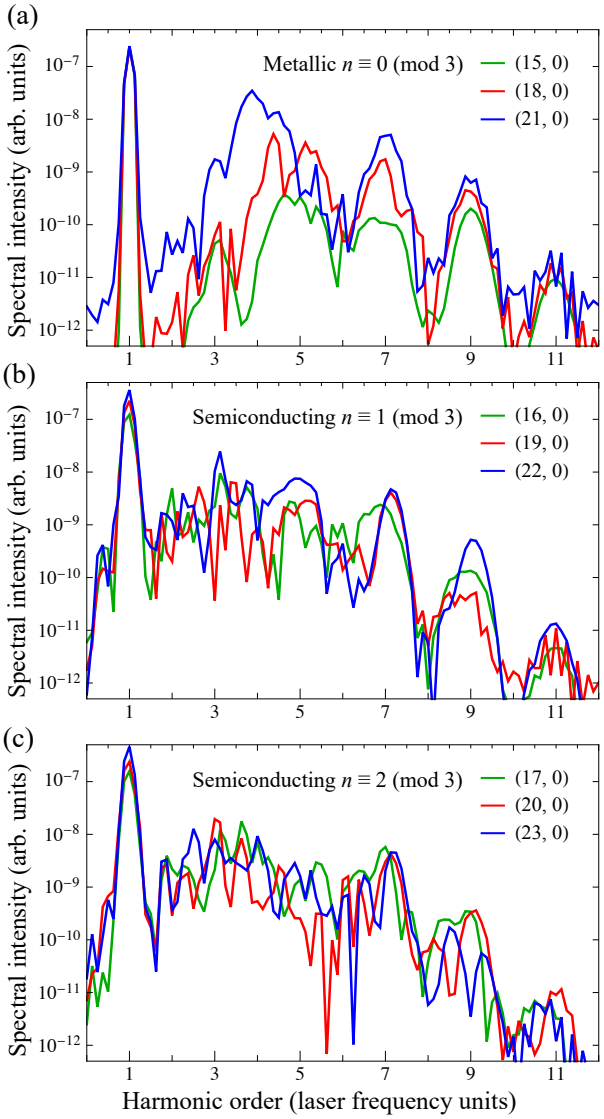

Figure 4.8: Harmonic yield from metallic and semiconducting zigzag tubes of different diameters. (a) Metallic tubes with diameters 1.18, 1.41 and 1.65 nm, respectively. (b) Semiconducting type $n \equiv 1$ tubes with $d_t = 1.24$, 1.49 and 1.73 nm. (c) Type $n \equiv 2$ tubes with diameters 1.33, 1.57 and 1.81 nm.

frequency is barely affected by the diameter, as it was also the case in armchair tubes. For metallic tubes, shown in Fig. 4.8(a), the spectral efficiency is found to increase with the tube diameter. The lower order harmonics are better resolved and red-shifted as the diameter increases, since the resonance with the gap energy of the bands $m = m_F \pm 1$ is reduced. These results are in line with those already obtained for $\mathcal{A}$-tubes and suggest, as a general rule, that in metallic tubes the interband component of the emission dipole becomes more relevant as the diameter increases, since the first van Hove singularity is located closer to the Dirac points and, therefore, the band gap is smaller and the matrix element is stronger. For semiconducting tubes, there is no clear correlation between the nanotube diameter either with the spectral efficiency or the harmonic peak resolution, see Figs. 4.8(b) and (c). The basic features of the spectra are maintained, and the same spectral complexity at the low frequency spectrum is observed, independently of the diameter. Note that, as the diameter increases, the differences amongst the band structure of the tubes become less relevant at the vicinity of the Fermi level, as it also happens in metallic nanotubes. This conclusion explains why we do not observe a monotonous increase of the spectral efficiency with the diameter.

4.2.3 *The effect of chirality*

Let us now study the dependence of the variation the chiral angle $0° < |\theta| < 30°$ on HHG. General $\mathcal{C}$-type tubes correspond to indices (n_1, n_2) such that $n_1 \neq n_2$ and $n_1, n_2 \neq 0$. Like zigzag species, chiral tubes can be either metallic or semiconducting, though they do not posses mirror reflection planes. Therefore, in the domain $a_0 k \in (0, \pi)$, the electronic bands are singlets with opposite $(\pm)$ U-parity, and there are no symmetry-related restrictions to optical transitions with z-polarized light, as was the case of the $\mathcal{Z}$-type tubes.

Fig. 4.9 shows the BZ, the band structure and the transition matrix element corresponding to the metallic $(8, 2)$ $\mathcal{C}$-type tube. Metallic chiral SWNTs with $n_1 - n_2 \equiv 0 \pmod 3$ exhibit band degeneracy at the Fermi level at $a_0 k_F = 2\pi/3$ and $m_F = nr \pmod q$ when $\mathcal{R} = 3$, or $a_0 k_F = 0$ and $m_F = \pm q/3$ if $\mathcal{R} = 1$ [85], where the parameters n, r, q and $\mathcal{R}$ are defined in section 2.2. The matrix element D_m diverges at these points where the DOS presents a small non-zero value, much alike $\mathcal{Z}$-tubes. The van Hove singularities are located at wave vectors where D_m reaches finite maximal values. Similarly, semiconducting $\mathcal{C}$-type tubes show the same behavior than their achiral counterparts, with D_m maximal at the proximity of the van Hove singularities. Therefore, the conclusions drawn above for the $\mathcal{Z}$-species are also applicable to $\mathcal{C}$-type tubes.

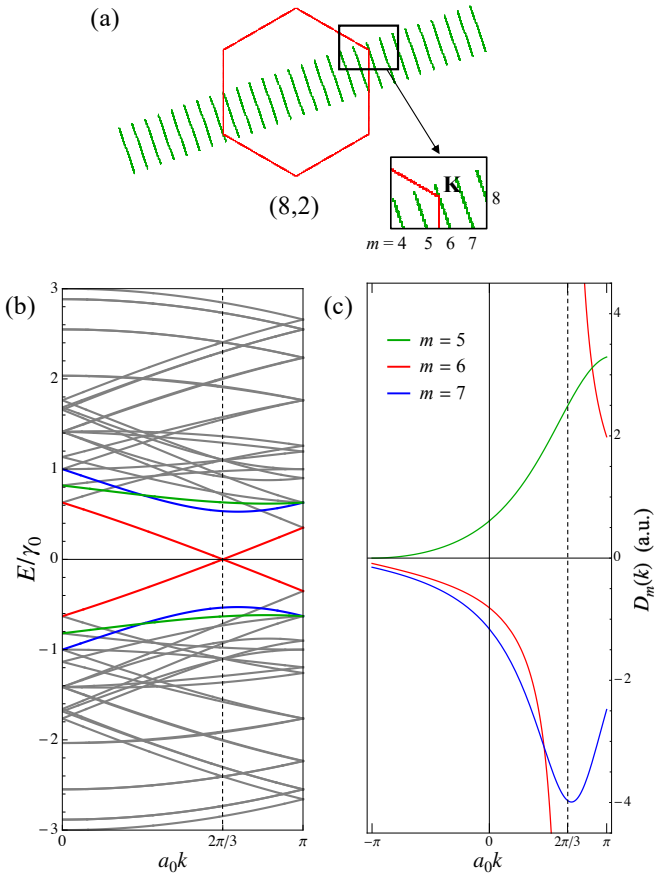

Figure 4.9: (a) First Brillouin zone of the $(8,2)$ $\mathcal{C}$-type tube. The structural parameters of this nanotube are: $d_t = 7.18$ Å, $a_0 = 6.51$ Å, $\theta = 11°$, $n = 2$, $r = 11$, $q = 28$ and $\mathcal{R} = 3$. (b) Band structure of the chiral tube $(8,2)$. The energy is given times the tight binding integral γ_0. The red line emphasizes the degenerated $|m| = 6$ bands, while bands at the first, $|m| = 7$, and second, $|m| = 5$, van Hove singularities are indicated by blue and green lines, respectively. (c) The transition matrix element $D_m(k)$ corresponding to these highlighted bands is shown in (c).

Figure 4.10(a) shows the comparison of the harmonic yields from $\mathcal{A}$, $\mathcal{Z}$ and $\mathcal{C}$-type SWNTs of diameters ~ 0.95 nm at a driving peak intensity of 5×10^{10} W/cm^2 and wavelength 3 μm. The yield from the semiconducting chiral species $(10,3)$, $\theta = 13°$, is clearly distinguishable from the spectra of the other two metallic tubes $(7,7)$ and $(12,0)$, which are very similar. All the spectra maintain the features already observed in metallic and semiconducting nanotubes, namely, (i) similar cut-off frequency, (ii) higher harmonic yield for the semiconducting species, and (iii) enhancement of the low harmonic spectrum in semiconducting species due to resonance. Additionally, Fig. 4.10(b) shows the harmonic yield from three tubes of greater diameter ~ 1.10 nm, generated by the same laser pulse. Again, it is the semiconducting tube which gives the most efficient spectra. In this case, the chiral

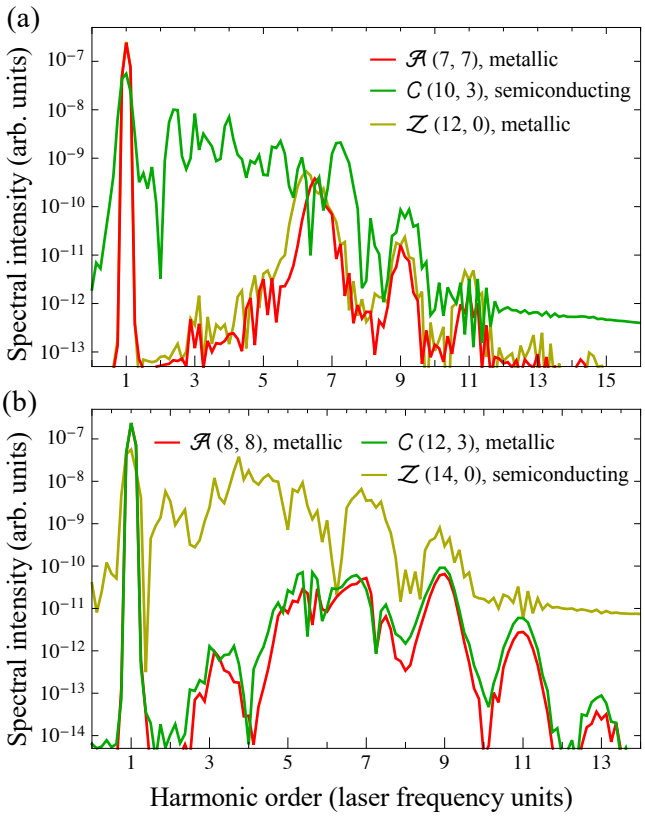

Figure 4.10: (a) Comparison of harmonic yields from (7, 7) armchair, (10, 3) chiral and (12, 0) zigzag. The achiral species are metallic, while the chiral is semiconducting. The diameters of the three tubes are similar: 0.95 nm, 0.93 and 0.94 nm, respectively. (b) Harmonic yields from $\mathcal{A}$ (8, 8), $\mathcal{C}$ (12, 3) and $\mathcal{Z}$ (14, 0). In this case, the zigzag tube is semiconducting, whilst the other two are metallic. The diameters of the three tubes are 1.09, 1.08 and 1.10 nm, respectively. In both panels, the driving pulse is the same than for the rest of cases analyzed in this section.

tube (12, 3), $\theta = 11°$, is metallic and its harmonic yield is quite similar to that produced by the metallic (8, 8) armchair. Finally, in Fig. 4.11 we compare the harmonic yield from two semiconducting nanotubes of different chirality with diameters $\sim$ 0.85 nm. The spectral structure and overall efficiency of all harmonic orders is quite similar in both cases, though they show some differences in the 5^{th} order and in the perturbative spectral tail. In any case, those differences are much less significative than the ones observed between semiconducting and metallic tubes of the same diameter.

As a conclusion, for nanotubes of the similar diameter, semiconducting species lead to more efficient HHG than their metallic counterparts. In fact, tubes with similar diameter and same conducting character generate similar spectra, independently of their chirality. Thus, the harmonic spectra is very sensitive to the variation of the

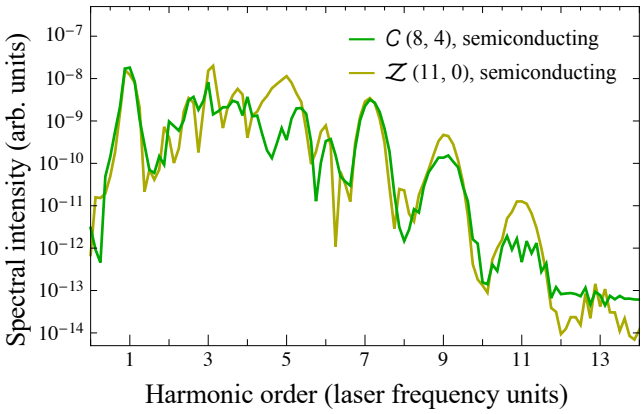

Figure 4.11: Harmonic yield from $(8,4)$, $\theta = 19°$ chiral and $(11,0)$ zigzag. Both nanotubes are semiconducting species with diameters 0.83 and 0.86 nm, respectively. The parameters of the driver are the same than in Fig. 4.10.

chiral angle θ only if *it changes the tube from semiconducting to metallic and vice versa*. Otherwise, variation of θ has little impact on the harmonic response.

4.2.4 *Dependence on the driving intensity*

All the spectra obtained so far have been calculated using the same mid-IR 8-cycle pulse with 5×10^{10} W/cm^2 peak intensity and 3 μm wavelength. Note that the cut-off frequency is $7\omega_o$ in all cases, regardless the size, chirality or conducting character of the nanotube. In order to explore the dependence of HHG with intensity, we plot in Fig. 4.12(a) the spectral yield from $(16,0)$ $\mathcal{Z}$-tube irradiated by a driving pulse of the same duration and wavelength, but with peak intensity of 5×10^{12} W/cm^2. The spectral plateau is extended towards the XUV, although the tangled structure already observed for lower intensities is even more pronounced.

We show in Fig. 4.12(b) the scaling of the cut-off frequency with the driving field intensity. As the use of arbitrary large intensities is precluded by the damage of the sample, we indicate with a green background the intensities for which nanotubes are expected to have damage, assuming that the damage fluence threshold is 150 mJ/cm^2 [124]. The dependence of the cut-off frequency with the intensity is similar to that found in graphene, see section 3.3. Note that the cut-off frequency saturates at the largest intensities. The saturated cut-off corresponds to a photon energy of $\simeq$ 12.7 eV, which is the gap corresponding to the maximum oscillation of the quasimomentum κ_t of electron-hole pairs generated at the first van Hove singularity, corresponding to the interband transition $E_5^- \rightarrow E_5^+$, see the inset

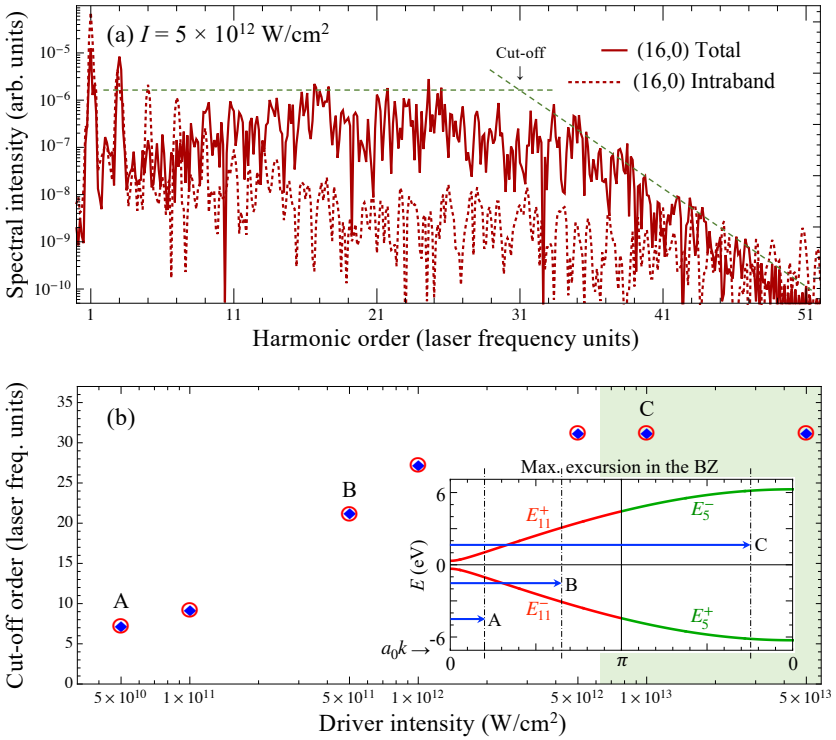

Figure 4.12: (a) Harmonic yield from $(16,0)$ z-tube driven by a 3μm wavelength, 28 fs (2.9 cycles) FWHM pulse at 5×10^{12}W/cm^2 peak intensity. (b) Cut-off scaling with intensity from $(16,0)$ zigzag irradiated by an 8-cycle mid-IR pulse with 3μm wavelength. The blue diamonds are the result of the numerical integration of the TDSE. The red circles are given by the semiclassical SPAM considering the the electron-hole pair is created at the first van Hove singularity: $a_0k = 0$, $|m| = 11$. The green filled area area corresponds to intensities above damage threshold. The inset shows the band structure at $|m| = 5$ and 11, and the maximum excursion of the e-h hole pair in the BZ corresponding to intensity points A, B and C.

of Fig. 4.12(b).[3] As in graphene, there is no simple law relating the cut-off frequency with the field amplitude. In Fig. 6 of section 4.4 we present similar results for the $(9,9)$ armchair nanotube that were reported in our publication of Ref. [135].

To summarize our findings in this section, for SWNTs of the same diameter, semiconducting tubes are more efficient sources of high-order harmonics than metallic species. In the former, the spectral yield is the result of the coherent addition of contributions from states packed at the first and second van Hove singularities, while only states at the first van Hove singularity contribute in the latter.

3 According to the *umklapp* rule, band $m = 11$ shifts to $m' = 5$ if the intraband oscillation exceeds the first Brillouin zone through $a_0k = \pi$.

While the lower order harmonics are caused both by intraband and interband dynamics, the higher-orders are due to interband transitions. The spectra obtained from tubes of the same diameter are vey similar for SWNTs with the same conduction character (semiconducting or metallic). Therefore, it is metallicity rather than chirality what influences the spectral yield. Although it is observed that for metallic tubes the spectral efficiency increases with the diameter up to a certain value, the spectra of semiconducting tubes does not show any significative correlation with the tube diameter, neither in the efficiency nor in the resolution of the harmonics. As intensity increases, the spectral plateau is extended towards the XUV regime, with a non-trivial dependence of the cut-off scaling, but showing a saturation of the cut-off photon energy, corresponding to the maximum gap reachable for electron-hole pairs generated at the first van Hove singularity in their quiver motion through the BZ.

4.3 THE GENERATION MECHANISM

As in the case of graphene, we have found that the spectral features of the radiated harmonics can also be explained in semiclassical terms. For this purpose we use the saddle-point approach model (SPAM) introduced for graphene in section 3.5 [106, 140]. The SPAM demonstrated that the high-harmonic spectra in graphene results from the recombination of electron-hole pairs, created during the non-adiabatic crossing near the Dirac points. To extend this description to SWNTs, we shall replace this condition by the non-adiabatic crossing through the first van Hove singularity, which we consider located at band m. In nanotubes, therefore, the SPAM describes the q-th order harmonic emission as the Fourier transform of the dipole acceleration, and is computed from the $\mathbf{k}$-space integral

$$\tilde{d}_m^{\updownarrow}(q\omega_o) = \frac{i\mathcal{D}_0^m}{q_e}\int_{-\infty}^{\infty}\int_k e^{\frac{i}{\hbar}[S_m(k,t,t_H)+q\hbar\omega_o t]} D_m(\kappa_t)\,dk\,dt, \tag{4.15}$$

where $S_m(k,t,t_H) = \int_{t_H}^{t}[E_m^+(\kappa_\tau) - E_m^-(\kappa_\tau)]\,d\tau$, κ_t is the kinetic quasi-momentum as defined by Eq. (3.16), $\mathcal{D}_0^m$ is a constant, and t_H is the time of crossing the first van Hove singularity, when the electron-hole pairs are generated. Note that Eq. 4.15 is the restriction of Eq. 3.52, derived in section 3.5 for graphene, to the SWNT's one-dimensional manifold. However, there is the important difference that the role of the Dirac points in graphene is replaced by that of the first van Hove singularity. Bearing this in mind, the derivation of Eq.4.15 is straightforward following the methodology described in section 3.5.

Taking into account that the main contributions to the integral in Eq. (4.15) are the stationary-phase points [49, 65, 140], the saddle-

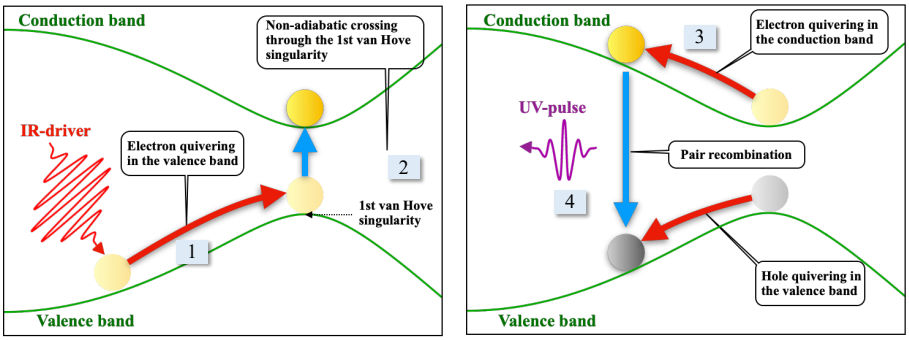

Figure 4.13: Mechanism for high-order harmonic generation in SWNTs. (1) Upon interaction with the electromagnetic field, the electron quivers in the valence band following the trajectory defined by κ_t. (2) Eventually, the electron reaches the first van Hove singularity and is promoted to the conduction band, leaving a hole. (3) The electron-hole pair oscillates in momentum space. (4) The harmonic emission takes place when the electron and hole trajectories overlap in direct space emitting a photon resonant with the band-gap.

point analysis results in the harmonic emission occurring when the following conditions are fulfilled:

$$\int_{t_H}^{t} v_m^+(\kappa_\tau)\, d\tau = \int_{t_H}^{t} v_m^-(\kappa_\tau)\, d\tau, \tag{4.16}$$

and

$$E_m^+(\kappa_t) - E_m^-(\kappa_t) = q\hbar\omega_o, \tag{4.17}$$

where the terms $v_m^\pm(\kappa_t) = \frac{1}{\hbar}\frac{\partial}{\partial k}E_m^\pm(\kappa_t)$ correspond to the velocities of the valence and conduction band electrons, respectively. In this semiclassical framework, conditions (4.16) and (4.17) define the generation mechanism for HHG in SWNTs, see Fig. 4.13: (i) as a consequence of the interaction with the field, the electron initially at point k in the valence band oscillates with amplitude $\kappa_t - k$; (ii) at time t_H the electron crosses the first van Hove singularity, where D_m reaches its maximal value, and is promoted to the conduction band, leaving a hole; (iii) according to Eq. (4.16), the electron-hole pair will quiver in the momentum space until time t, when their trajectories intersect in the real space; and (iv) upon recombination, a photon resonant with the band gap at κ_t is emitted, thus fulfilling Eq. (4.17).

Figure 4.14 shows the classical trajectories corresponding to two electrons, with different initial positions in the Brillouin zone, k_A and k_B, which reach the first van Hove singularity of a semiconducting $(16,0)$ z-tube at times t_{H_A} and t_{H_B}. The trajectories correspond to a 3 μm wavelength pulse, with intensity 5×10^{11} W/cm^2. Note that for the trajectory A, the electron and the hole created at t_{H_A} meet in

direct space at the final time t. In contrast, in B, the electron and the hole do not meet at t. According to Eq. (4.16), the photon emission at t is effective only for the case A.

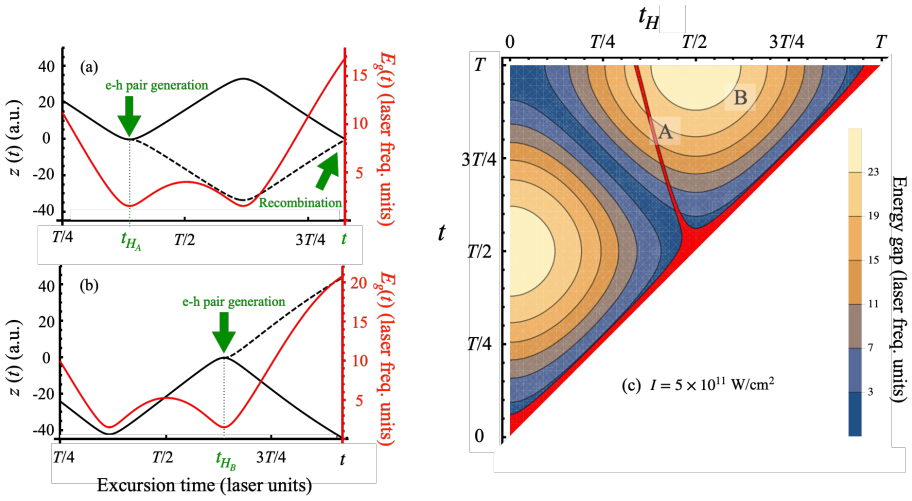

Figure 4.14: (a)–(b) Electron and hole trajectories corresponding to points A and B illustrated in (c). The trajectory of the electron (black solid line) and hole (dashed line) are represented as a function of time. The figure corresponds to a driving laser pulse of 3 μm wavelength with peak intensity of 5×10^{11} W/cm^2 targeting a $(16, 0)$ zigzag tube. (c) Energy map of the maximum gap energy of the quivering electron for the classical trajectories computed with the SPAM, being t_{H} the time of the creation of the electron-hole pair and t the time of the potential photon emission. The red area represents the points where the electron-hole trajectories intersect in direct space at time t and, therefore, where there is an actual photon emission.

Figure 4.14(c) shows a map of the energy gap as a function of the initial time t_{H}, when the electron-hole pair is created, and the final time t, when the pair annihilates. Points A and B in the energy map correspond to the cases shown in Figs. 4.14(a) and (b), respectively. We have colored in red the points (t_{H}, t) corresponding to electron-hole pairs, created at t_{H}, whose trajectories overlap in the same crystal cell at time t and, therefore, are allowed to recombine. These colored areas are, therefore, in compliance with both conditions (4.16) and (4.17), and correspond to situations when the harmonic photon can be effectively emitted. According to this map, point A corresponds to an electron-hole pair created at $t_{\mathrm{H}} \simeq 0.4\mathrm{T}$ which emits a $\simeq 17\hbar\omega_o$ photon when recombined at $t \simeq 0.9\mathrm{T}$. Note that, as it happens in B, other points in the map may potentially emit higher frequency harmonics at time t, but the photon emission is not possible, since the electron-hole pairs are spatially apart. The maximal photon energy is therefore given by the energy maxima in the map of Fig. 4.14(c) constrained to the red area. According to this, Fig. 4.14(c) predicts the harmonic cut-

off at $\simeq 21\hbar\omega_o$, smaller than the maximum gap that the electron-hole pair access during its oscillation in the reciprocal space ($\simeq 23\hbar\omega_o$). In Figure 4.12(b) we have already shown this cut-off prediction (red circles) in comparison with the results of the integration of the TDSE, Eqs. (4.2) and (4.3). As it can be noticed, this cut-off prediction is in excellent agreement with the results of the numerical calculations.

We show in figure 4.15 the SPAM energy maps at 3 μm wavelength for two additional intensities. As it also happens with single layer graphene, we observe that for increasing intensity the topology of the red-colored region, i. e. the condition for the electron-hole overlap at time t, becomes more complex. It is interesting to note that the same harmonic may be emitted by two or more trajectories within the same half cycle of the driving field. In particular, Fig. 4.15(b) shows four contributions, labelled from a to d, for the maximum (cut-off) frequency. In the publication included in section 4.4 we show similar maps for the metallic nanotube (9, 9) armchair.

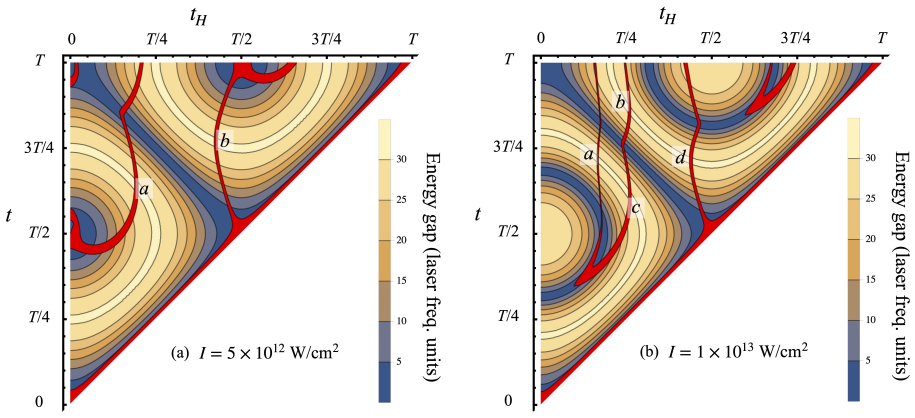

Figure 4.15: Energy map for the emitted harmonic photon from a (16, 0) zigzag tube according to SPAM for driver peak intensities of (a) 5×10^{12} and (b) 10^{13}W/cm^2. The points corresponding to intersecting electron-hole trajectories are highlighted in red.

4.4 PUBLICATIONS

To conclude the chapter, we include the full version of the article published in 2020 in the journal *Optics Express* under the title *"High harmonic generation in armchair carbon nanotubes"* [135]. In this article we reported the results and conclusions drawn from the study of HHG in $\mathcal{A}$-type nanotubes. According to the requirements of the University of Salamanca, the Spanish version of the abstract is also included.

High harmonic generation in armchair carbon nanotubes

Resumen

En este trabajo presentamos un estudio sobre la generación de armónicos de orden elevado (HHG) en nanotubos de carbono de pared simple (SWNT) tipo *armchair* generados por pulsos láser ultracortos en el infrarrojo medio. Para un SWNT con índices quirales (n, n), demostramos que el proceso de HHG está dominado por las bandas $|m| = n - 1$ y que la frecuencia de corte se satura al incrementar la intensidad del láser, como ocurre en el caso del grafeno. En consecuencia, la HHG en los nanotubos *armchair* se describe a partir de un sistema periódico unidimensional, cuya emisión de alta frecuencia puede modificarse mediante el control de sus parámetros estructurales. Además, mostramos que el mecanismo de HHG en nanotubos tiene similitudes con el del grafeno. Sin embargo, como diferencia principal, observamos que la excitación del par electrón-hueco en los SWNT está conectada con transiciones no adiabáticas de los electrones de valencia de las bandas $|m| = n - 1$ a través de la primera singularidad de van Hove, que tiene un rol similar al de los puntos de Dirac en el grafeno.

Research Article | Vol. 28, No. 13 / 22 June 2020 / Optics Express 19760
Optics EXPRESS

High harmonic generation in armchair carbon nanotubes

ÓSCAR ZURRÓN-CIFUENTES,* ROBERTO BOYERO-GARCÍA, CARLOS HERNÁNDEZ-GARCÍA, AND LUIS PLAJA

Grupo de Investigación en Aplicaciones del Láser y Fotónica, Departamento de Física Aplicada, University of Salamanca, E-37008, Salamanca, Spain
*ozurronci@usal.es

Abstract: We study high-order harmonic generation (HHG) in armchair-type single-wall carbon nanotubes (SWNTs) driven by ultrashort, mid-infrared laser pulses. For a SWNT with chiral indices (n, n), we demonstrate that HHG is dominated by bands $|m| = n - 1$ and that the cut-off frequency saturates with intensity, as it occurs in the case of single layer graphene. As a consequence, HHG in SWNTs can be described effectively as a one-dimensional periodic system, whose high-frequency emission can be modified through the proper control of the structural parameters. Additionally, we show that the HHG mechanism in nanotubes has some similarities to that previously reported in single layer graphene. However, as a main difference, the electron-hole pair excitation in SWNTs is connected to the non-adiabatic crossing through the first van Hove singularity of the $|m| = n - 1$ bands, instead of the crossing through the Dirac point that takes place in graphene.

1. introduction

Carbon nanotubes are carbon allotropes with quasi-one dimensional periodic structure. Their remarkable mechanical, electrical and thermal properties have attracted considerable interest since their discovery at the early 90's. They were first reported as carbon microtubules, made of concentric shells and diameters ranging from a few to several hundred nanometers [1]. Some years later, single-wall carbon nanotubes (SWNTs) were synthesized rolling monolayer graphene [2,3]. SWNTs have diameters around the nanometer and an extraordinarily perfect crystalline structure. SWNTs are also interesting topological objects, with electronic, optical and structural properties depending on the rolling direction (chiral angle) of the graphene sheet. These somewhat complex structures, which exhibit tens to hundreds of atoms in the unit cell, have well defined symmetries that easy the understanding of their physical properties [4,5].

Recently, the nonlinear optical response of periodic systems to intense mid-infrared radiation has captivated the interest of the scientific community. High-order harmonic generation (HHG) in crystalline solids has been a subject of interest already at the early days of the study of strong-field phenomena, either in realistic bulk solids [6] or dimensionally reduced models [7,8]. Experiments in crystalline solids subjected to intense fields have been demonstrated to emit high harmonics [9], resulting from the non-perturbative electronic response to the driving field. HHG has been extensively studied in atomic and molecular systems [10]. In gases, harmonics are radiated upon the recollision of electrons, that are first ionized, next accelerated and finally, redirected to the parent ion by the electromagnetic field [11,12]. The absence of a privileged resonance results in well defined *plateau* structures in the harmonic spectra extending up to cut-off frequencies at the extreme ultraviolet (UV) or even, at the soft x-rays regime [13,14]. In finite-gap solids, interband HHG follows a mechanism similar to that in gases or molecules, but ionization is replaced by the tunnel excitation from the valence to the conduction band, and the harmonic radiation occurs when the exited electron recombines with its hole [15]. Single layer (gapless) graphene has also been recently demonstrated to produce high order harmonics when interacting

#394714 https://doi.org/10.1364/OE.394714
Journal © 2020 Received 8 Apr 2020; revised 7 Jun 2020; accepted 8 Jun 2020; published 19 Jun 2020

Optics EXPRESS

with a strong mid-infrared (IR) field [16]. It has been shown that HHG in this system differs from bulk solids, as the first step (tunnel excitation) is replaced by electron-hole pair creation during the non-adiabatic crossing of the momentum-space trajectories near the Dirac points [17]. This fact introduces an extraordinary complexity, since the initiation of the HHG process is not linked to the field's amplitude maxima, when tunnel excitation is more likely. Graphene shows also an interesting non-linear anisotropy, allowing for photon spin conversion and ultrafast polarization changes in the emitted harmonic spectra [18].

Despite the considerable effort in the study of HHG in graphene and other 2D materials, similar studies for technologically feasible lower dimensional geometries —quasi 1D— are not abundant [19]. In this paper we present theoretical results of HHG in armchair-type SWNTs induced by few-cycle IR laser pulses. We demonstrate that, in this context, SWNTs behave effectively as one-dimensional two-band systems, whose properties can be modified with the choice of the SWNT's geometry. Remarkably enough, a recent experimental report shows that the high order harmonic emission spectra can be controlled either by tuning the electronic structure of SWNTs or carrier injection using electrolyte gating approaches, with up to the 11^{th}-order harmonic being observed in semiconductor tubes of relative large band gap ~ 1.26 eV [20].

The paper is organized as follows: First, we briefly review the structural characteristics of SWNTs, with special emphasis on their symmetries and the zone-folded electronic band structure. Next, in section 3 we present our method for the numerical integration of the time-dependent Schrödinger equation (TDSE) in SWNTs. In section 4 we present and discuss our results for the high harmonic spectra and, using a semiclassical model, we describe the HHG mechanism along with the dependence of the cut-off frequency with the intensity. Finally, we present our conclusions.

2. Structure of $\mathcal{A}$-type single-wall carbon nanotubes

For diameters above one nanometer, the effects of curvature can be neglected and the SWNT's electronic structure can be derived from that of single-layer graphene [21,22]. The nanotube corresponds to a graphene sheet rolled along the direction pointed by the chiral vector $\mathbf{C}_h = n_1\mathbf{a}_1 + n_2\mathbf{a}_2$, $(n_1, n_2) \in \mathbb{Z}^2$ being the tuple of chiral indices, and $\mathbf{a}_1 = a_0(\sqrt{3}/2, 1/2)$ and $\mathbf{a}_2 = a_0(\sqrt{3}/2, -1/2)$ the graphene's primitive vectors, with $a_0 = 2.46$ Å. The chiral indices (n_1, n_2) define the nanotube diameter $d_t = |\mathbf{C}_h|/\pi$, the chiral angle θ between $\mathbf{C}_h$ and $\mathbf{a}_1$, $0° \leq |\theta| \leq 30°$, and the translational period along the tube axis $a = \sqrt{3}a_0\sqrt{n_1^2 + n_1n_2 + n_2^2}/N_R$, where $N_R = \gcd(2n_1 + n_2, 2n_2 + n_1)$. $\mathcal{A}$-type —armchair— nanotubes correspond to chiral indices (n, n) and $|\theta| = 30°$, while $(n, 0)$ denotes $\mathcal{Z}$-type —zigzag— tubes, with $|\theta| = 0°$. Both zigzag and armchair tubes are achiral species, unlike $\mathcal{C}$ —chiral— nanotubes, where $n_2 \neq n_1$ $(n_i \neq 0)$.

Figure 1 shows the structure of a $(9, 9)$ armchair SWNT in (a) real and (b) reciprocal space, respectively. Symmetries of SWNTs are directly related to chirality. All nanotube species show a-period translational symmetry along the tube axis (z axis, by convention), a screw axis of pure rotational symmetries, which in the case of $\mathcal{A}$-type nanotubes coincides with the tube axis, and π-rotational symmetry around the U-axis, transverse to z. In addition, $\mathcal{Z}$ and $\mathcal{A}$-type tubes present mirror symmetries in the horizontal xy-plane (σ_h) and vertical yz-plane (σ_v). Figure 1(a) shows the essential symmetry elements of armchair nanotubes. Note that $\sigma_h = U \cdot \sigma_v$.

The translational periodicity implies the conservation of the quasi-momentum along the nanotube axis k. Besides, the rotational symmetry around the z-axis implies the conservation of m, the z-projection of the electron's orbital angular momentum. For $\mathcal{A}$-type nanotubes, the mirror reflection planes impose well-defined parities to the electronic states: the parity with respect to σ_v is denoted as A for even states, and B, for odd ones, while the parity under σ_h reflections is denoted by $\pm$ for even and odd states, respectively. Therefore, the state of the

Optics EXPRESS

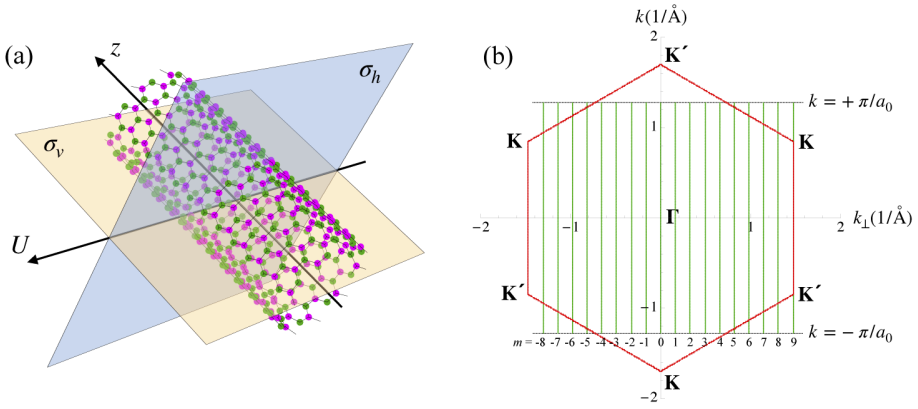

Fig. 1. (a) View of the structure and symmetries of a (9,9) armchair nanotutube. Magenta and green circles represent the atoms in the two sublattices of the unrolled graphene sheet. (b) Allowed **k** vectors in the first Brillouin zone of (9,9) armchair tube (green lines). This nanotube has 36 C-atoms in its unit cell, $q = 18$, $m = 0, \pm1, \pm2, \ldots, \pm8, 9$ and $d_t = 12.2$ Å. The red hexagon shows the boundary of the graphene's BZ along with the high symmetry points K and Γ.

electron corresponds to a particular irreducible representation of the line group, characterized by the set $\{k, m, A/B, \pm\}$.

Curvature effects being neglected, SWNT's Brillouin zone (BZ) can be constructed from graphene's using the zone-folding approach, i.e. considering the nanotube as graphene with periodic boundary conditions along the circumferential direction [4,5]. As a result, the BZ of the nanotube corresponds to a set of q —the number of hexagons in the unit cell— straight lines with length $2\pi/a$, parallel to the tube axis and separated by constant distances $2/d_t$. Each line is labelled by the index m, which takes integer values in $(-q/2, q/2]$. As an example, Fig. 1(b) depicts the BZ of (9,9) armchair. Note that for $\mathcal{A}$-type tubes, the translational period is $a = a_0$.

Within the nearest-neighbor tight-binding approximation, the energy dispersion is given by $E_\pm(\mathbf{k}) = \pm\gamma|f(\mathbf{k})|$, where $\gamma = 2.97$ eV is the hopping parameter and $f(\mathbf{k})$ the complex function

$$f(\mathbf{k}) = e^{-ia_0k_\perp/\sqrt{3}}\left(1 + 2e^{i\sqrt{3}a_0k_\perp/2}\cos\frac{a_0k}{2}\right), \tag{1}$$

being $k_\perp = 2m/d_t$ the set of wave vectors along the circumferential direction. Figure 2 shows the band structure of the (9,9) nanotube. Bands are labelled according to the value of $|m|$ and the parities upon the vertical and horizontal mirror symmetries, A/B and $+/-$ respectively. Bands with $m = 0$ and 9, drawn in black, are singlets with + parity, while the rest of bands are doubly degenerated in the interval $a_0k \in [0, \pi)$, with $E = A$ or B parity, and converge at $a_0k = \pi$. For $ka_0 = 0$ all states have + parity. $\mathcal{A}$-type (n, n) nanotubes are semimetals, as both valence and conduction bands are degenerated at the point $a_0k = \pm2\pi/3$ of the band $m = n$, corresponding to the Dirac points K and K' of the graphene's Brillouin zone, see Fig. 1(b). The density of states (DOS) profile is shown as a shaded area in the background of Fig. 2. Van Hove singularities correspond to points where the slope of the energy bands is null.

Optics EXPRESS

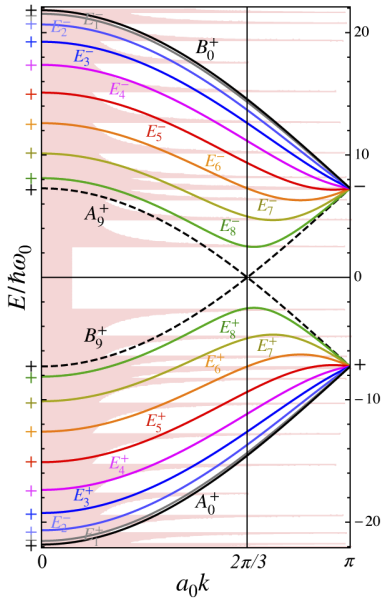

Fig. 2. Band structure of (9,9) armchair. The energy is given in units of the frequency of a 3μm driving field ($\hbar\omega_0 = 0.41$ eV). The horizontal axis represents the wave vector times the translational period a_0. The solid (dashed) black lines indicate the $m = 0$ ($m = 9$) singlets. The rest of the bands represent double degenerated states $E^{\pm}_{|m|}$, with $E = A/B$. Parities under σ_h reflections at $a_0k = 0$ and π are also indicated. The pink-filled profile in the background shows the density of states, dominated by the van Hove singularities.

3. Interaction with an electromagnetic field

Symmetries of $\mathcal{A}$-type SWNTs impose selection rules for the optical transitions between electronic states. If the incident electric field is linearly polarized along the nanotube axis, optical transitions are essentially vertical, conserve m and A/B, while swap $\pm$. As a result, transitions $A_0^+ \rightarrow B_0^+$ and $B_n^+ \rightarrow A_n^+$ are forbidden in any (n,n) $\mathcal{A}$-type tube. The rest of transitions involving bands $|m| = 1, \ldots, n-1$ are allowed for any $a_0k \in (0,\pi]$, but they are forbidden at $a_0k = 0$. Furthermore, the electronic intraband dynamics are also subjected to the *Umklapp* rule $m' = m \pm n \pmod{2n}$, so that m shifts to m' when the first Brillouin zone is exceeded through $a_0k = \pi$ [4,23].

Let us consider an $\mathcal{A}$-type SWNT being irradiated by a laser pulse $\mathbf{F}(t)$ linearly polarized along the direction of its axis. Within the dipole approximation, the interaction is described by the time-dependent Hamiltonian $H(t) = H_0 - q_eF(t)z$, where q_e is the elementary charge. If $\Phi_m^{\pm}(k;\mathbf{r})$ are the eigenstates of the conduction and valence bands, the time-dependent wavefunction can be expressed as:

$$\Psi(\mathbf{r},t) = \sum_m \int \Psi_m(k;\mathbf{r},t)dk = \sum_m \int \left[C_m^+(k,t)\Phi_m^+(k;\mathbf{r}) + C_m^-(k,t)\Phi_m^-(k;\mathbf{r})\right] dk. \tag{2}$$

As shown for graphene in [17], introducing the oscillating frame $\hbar\kappa_t = \hbar k - q_eA(t)/c$, where $A(t)$ is the vector potential, and using the transformation:

$$C_m^M(\kappa_t,t) = C_m^+(\kappa_t,t) - C_m^-(\kappa_t,t) \tag{3}$$

$$\tilde{C}_m^P(\kappa_t,t) = e^{-i\phi_m(\kappa_t)}\left[C_m^+(\kappa_t,t) + C_m^-(\kappa_t,t)\right], \tag{4}$$

Optics EXPRESS

the dynamical equations can be written in the following form:

$$i\hbar\frac{d}{dt}C_m^M(\kappa_t,t) = \frac{E_m^+(\kappa_t)+E_m^-(\kappa_t)}{2}C_m^M(\kappa_t,t) + \frac{E_m^+(\kappa_t)-E_m^-(\kappa_t)}{2}e^{i\phi_m(\kappa_t)}\tilde{C}_m^P(\kappa_t,t) \tag{5}$$

$$i\hbar\frac{d}{dt}\tilde{C}_m^P(\kappa_t,t) = \frac{E_m^+(\kappa_t)+E_m^-(\kappa_t)}{2}\tilde{C}_m^P(\kappa_t,t) + \frac{E_m^+(\kappa_t)-E_m^-(\kappa_t)}{2}e^{-i\phi_m(\kappa_t)}C_m^M(\kappa_t,t), \tag{6}$$

where $E_m^{\pm}$ is the energy of the valence (-) and conduction (+) bands with index m, and ϕ_m is the phase of the complex function $f(\mathbf{k})$ in Eq. (1). The harmonic emission is then proportional to the second derivative of the emission dipole, which is given by:

$$d(t) = i\frac{q_e}{2}\sum_m\int\left[C_m^{M*}\frac{\partial C_m^M}{\partial\kappa_t} + \tilde{C}_m^{P*}\frac{\partial\tilde{C}_m^P}{\partial\kappa_t}\right]dk. \tag{7}$$

In addition, we compute the intraband fraction of the harmonic spectra as:

$$a_m^{\text{intra}}(t) = \frac{q^2}{\hbar^2}F(t)\int\left[|C_m^+|^2\frac{\partial^2E_m^+}{\partial\kappa_t^2} + |C_m^-|^2\frac{\partial^2E_m^-}{\partial\kappa_t^2}\right]dk. \tag{8}$$

4. Results and discussion

Equations (5), (6), (7) and (8) have been integrated numerically considering mid-IR 8-cycle driving pulses. The electric field is assumed linearly polarized along the nanotube axis and defined as $F(t) = F_0\sin^2(\pi t/8T)\sin(\omega_0 t)$ for $0 \le t \le 8T$ and 0 at any other t, being F_0 the field's amplitude, T the period, and $\omega_0 = 2\pi/T$ the frequency. The beam is aimed perpendicularly to the nanotube, thus traversing an atomic-size thickness and therefore, we neglect propagation effects.

Figure 3 shows the calculated HHG yield from (9,9) $\mathcal{A}$-tube at a driving peak intensity of 5×10^{10} W/cm^2 and 3 μm wavelength. The pulse duration is 28 fs (2.9 cycles) at full width at half maximum (FWHM), which is smaller than the decoherence time due to carrier collisions [24–26]. Figure 3 shows clearly the emergence of a spectral plateau extending up to a cut-off frequency, which corresponds to the seventh harmonic. Note that the intensity used here is about two-orders of magnitude below the "transition intensity" to non-perturbative HHG, predicted in 1D models [7]. Only odd-order harmonics are present in the spectrum, as a consequence of centrosymmetric structure of the system. All harmonics are linearly polarized in the direction of the tube axis.

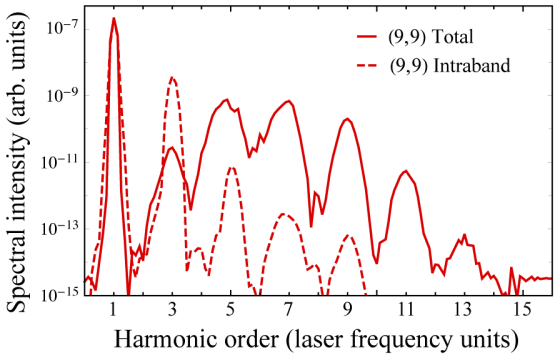

Fig. 3. The solid line represents the total harmonic yield from (9,9) $\mathcal{A}$-tube driven by a 3μm wavelength, 28 fs (2.9 cycles) FWHM pulse at 5×10^{10} W/cm^2 peak intensity. The dotted line indicates the intraband spectral component.

Optics EXPRESS

We can analyze the contribution of the different m bands to the harmonic spectra by considering the specific form of the component parallel to the nanotube axis of the interband matrix element in the length gauge [27–29]:

$$D_m(k) = -\frac{a_0 q_e}{2} \frac{\sin\left(\frac{a_0 k}{2}\right) \sin\left(\frac{m\pi}{n}\right)}{1 + 4\cos\left(\frac{a_0 k}{2}\right)\left[\cos\left(\frac{m\pi}{n}\right) + \cos\left(\frac{a_0 k}{2}\right)\right]}. \tag{9}$$

Figure 4(a) shows the magnitude of the matrix element $|D_m(k)|$ in the $(9,9)$-armchair tube for different band indices m. Consistent with the symmetry considerations discussed above, $|D_m(k)|$ is null for $m = 0, 9$. As a consequence, the contribution of these bands to the total HHG corresponds solely to the intraband dynamics. For the rest of bands, the coupling shows peaks of magnitude increasing with $|m|$, corresponding to the first four van Hove singularities in the DOS. The absolute maximum of $|D_m(k)|$ is reached at the first van Hove singularity. This suggests that the interaction with the driver laser is much stronger for the states packed at the first van Hove singularity than for others and therefore, that the interband emission spectra is mainly due to transitions within such states. Note that the increased band curvature near the Dirac points entails sharper van-Hove singularities and, therefore, enhances the efficiency of the interband transitions in HHG. In contrast, 1D models with finite gaps demonstrate intraband currents as the main source of harmonic radiation [30]. This behavior is further illustrated in Fig. 4(b), where

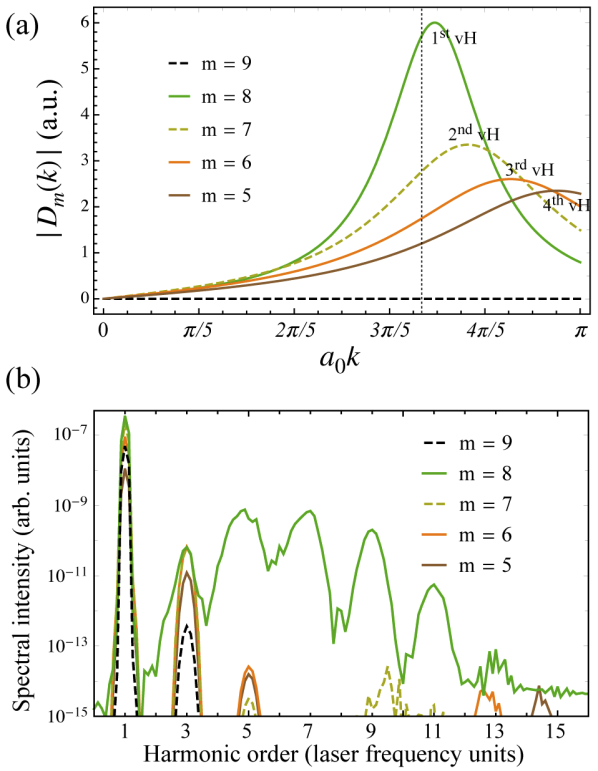

Fig. 4. (a) Matrix element $|D_m(k)|$ corresponding to the (9,9) armchair tube for different m values. The dotted line at $a_0k = 2\pi/3$ indicates the band's crossing point for $m = 9$. (b) Contribution to the harmonic yield from the different values of m. The driver's parameters are the same as in Fig. 3.

Optics EXPRESS

we show the different contributions to the emission spectra from the (9,9)-$\mathcal{A}$-tube corresponding to several values of m. The coherent addition of the contributions from all m-values gives the spectrum shown in Fig. 3. Nevertheless, note that the higher order harmonics are given by the contribution from the slices $|m| = 8$ of the Brillouin Zone shown in Fig. 1(b), which are connected with the first van Hove singularity. The other points of the BZ, where $|D_m(k)|$ and the curvature of the bands are weaker, contribute to the lower order harmonics mainly with intraband radiation. Note that the band gap at the first van Hove singularity is near resonant with a $5\omega_0$ transition, thus enhancing the interband component of the high harmonic emission.

Figure 5 shows the harmonic yield from several $\mathcal{A}$-tubes of different diameters. The basic features of the spectra are maintained, although the efficiency of the higher order harmonics in the spectral non-perturbative area (5^{th} and 7^{th}) increases with the tube diameter. Note that the slope of the bands closest to $a_0 k = 2\pi/3$ increases with the tube diameter, which implies that the number of electronic states available at the maximal values of $D_m(k)$ also increases. Also, the value of $|D_m(k)|$ approaches the singularity at the Dirac points, which explains the higher efficiency of the harmonics. It is also observed that, as the diameter increases, the 5^{th} harmonic is red-shifted since the resonance with the gap energy of the $m = n - 1$ band is reduced. Note that the cut-off barely changes, independently of the size of the nanotube.

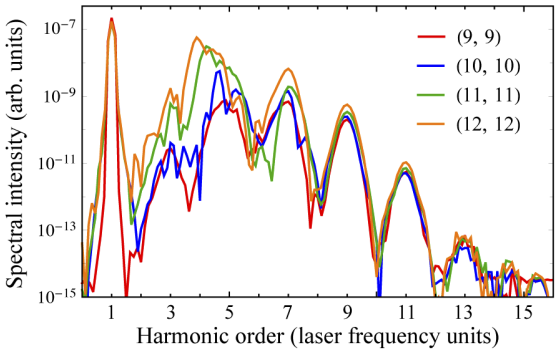

Fig. 5. Harmonic yield from (9,9), (10,10), (11,11) and (12,12) armchair tubes. The diameters of these tubes are $d_t = 1.22, 1.36, 1.50$ and 1.63 nm, respectively. The electric field parameters are those in Figs. 3 and 4(b).

Figure 6(a) shows the spectral yield from the (9,9) $\mathcal{A}$-tube irradiated by a driving pulse of the same duration and wavelength, but with peak intensity of 5×10^{12} W/cm^2. As intensity increases, the spectral *plateau* is extended towards the extreme UV. In Fig. 6(b) we show the scaling of the cut-off frequency with the driving field intensity. The filled area in the background corresponds to intensities above the damage threshold, assuming that the damage threshold fluence is 150 mJ/cm^2 [31]. Note that the cut-off frequency saturates at the largest intensities to a photon energy of $\simeq 16.7$ eV, which is the gap corresponding to the maximum oscillation of the coupled quasimomentum κ_t. This saturation has also been described in graphene [17] and in gap semiconductors [32].

The spectral features of the radiated harmonics can be described in semiclassical terms. For this purpose we use the saddle-point approach model (SPAM) introduced for single layer graphene [17,33]. The SPAM demonstrated that the high-harmonic spectra in graphene results from the recombination of electron-hole pairs, created during the non-adiabatic crossing of the Dirac points by the electron trajectories. For the description of SWNTs, we shall replace this condition by the non-adiabatic crossing through the first van Hove singularity. In nanotubes, therefore, the SPAM describes the q-th order harmonic emission as the Fourier transform of the dipole

Optics EXPRESS

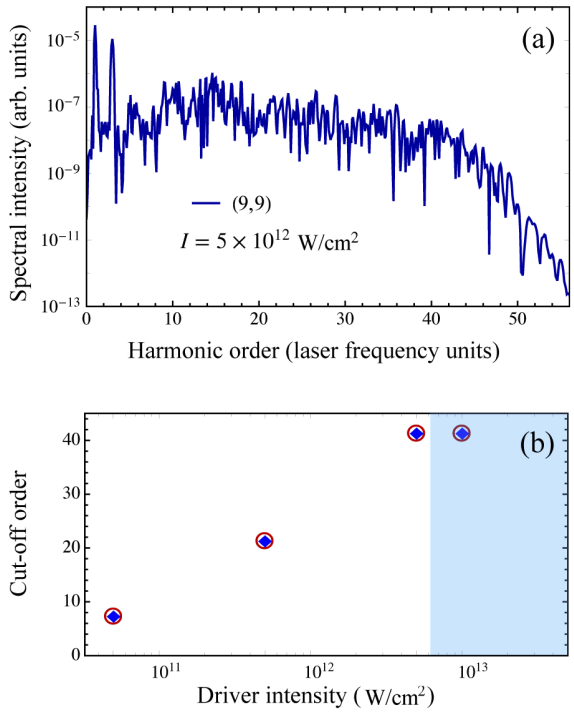

Fig. 6. (a) Harmonic yield from (9,9) $\mathcal{A}$-tube driven by a 3μm wavelength, 28 fs (2.9 cycles) FWHM pulse at 5×10^{12} W/cm^2 peak intensity. (b) Cut-off scaling with intensity from (9,9) armchair. The blue diamonds are the result of the numerical integration of the TDSE. The red circles are predicted by the semiclassical SPAM considering electron-hole creation at the first van Hove singularity: $a_0 k = 2\pi/3$, $m = 8$. The filled area in the background corresponds to intensities above the damage threshold.

acceleration, computed from the k-space integral:

$$\tilde{d}_m^{\updownarrow}(q\omega_0) = i\frac{\mathcal{D}_0^m}{q_e}\int_k\int_{-\infty}^{\infty} e^{\frac{i}{\hbar}[S_m(k,t,t_H)+q\hbar\omega_0 t]} D_m(\boldsymbol{\kappa}_t)dkdt, \tag{10}$$

where $S_m(k,t,t_H) = \int_{t_H}^{t}\left[E_m^+(\kappa_\tau) - E_m^-(\kappa_\tau)\right]d\tau$, $\mathcal{D}_0^m$ is a constant, and t_H is the time of crossing the first van Hove singularity, when the electron-hole pairs are generated. Taking into account that the main contributions to the integral in Eq. (10) are the stationary-phase points [15,33,34], from saddle-point analysis we find that the harmonic emission occurs when the following conditions are fulfilled:

$$\int_{t_H}^{t} v_m^+(\kappa_\tau)d\tau = \int_{t_H}^{t} v_m^-(\kappa_\tau)d\tau, \tag{11}$$

and

$$E_m^+(\kappa_t) - E_m^-(\kappa_t) = q\hbar\omega_0, \tag{12}$$

where $v_m^{\pm}(\kappa_t) = \frac{1}{\hbar}\frac{\partial}{\partial k}E_m^{\pm}(\kappa_\tau)$ are the velocities of the valence and conduction band electrons. In this semiclassical framework, conditions (11) and (12) define the generation mechanism for HHG in SWNTs: (i) as a consequence of the interaction with the field, the electron initially at point k in the valence band oscillates with amplitude $\kappa_t - k$; (ii) at time t_H the electron crosses the first van Hove singularity, where D_m reaches its maximal value, and is promoted to the conduction band,

Optics EXPRESS

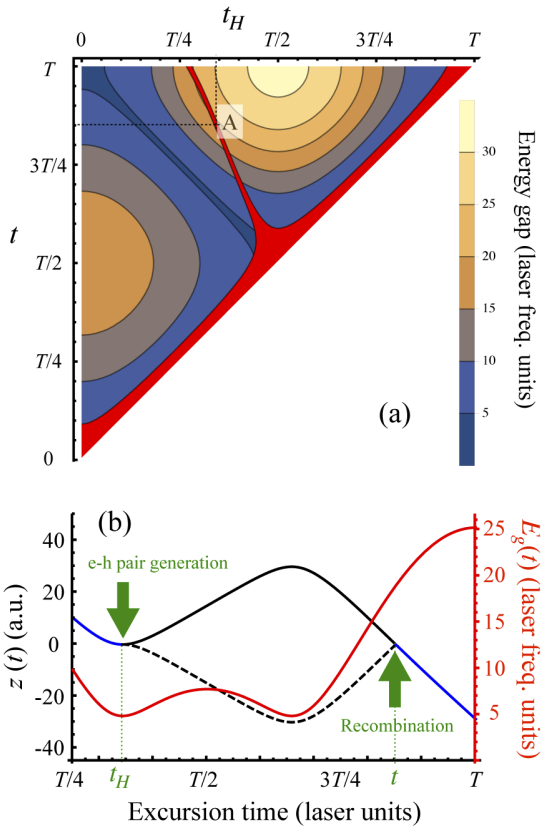

Fig. 7. (a) Map of the energy of the emitted photon for different classical trajectories computed with the SPAM, being t_H the time of creation of the electron-hole pair and t the potential time of the photon emission. The points where the electron-hole trajectories intersect in direct space at time t are represented by the red area. (b) Electron and hole trajectories corresponding to point A illustrated in panel (a). The trajectories of the electron (black solid line) and the hole (dashed line) are represented as a function of time. The red curve represents the energy gap $E_g(t)$ between the electron and the hole during their oscillation in the bands. The figure corresponds to a driving laser pulse of 3 μm wavelength with constant intensity of 5×10^{11} W/cm^2 targeting a (9,9) armchair tube.

leaving a hole; (iii) according to Eq. (11), the electron-hole pair will quiver in the momentum space until time t, when their trajectories intersect in the real space; and (iv) upon recombination, a photon resonant with the band gap at κ_t is emitted, thus fulfilling Eq. (12).

The SPAM predicts that the maximum energy of the photon emission will be the maximum gap experienced by the electron-hole pair during its oscillation in the reciprocal space. For (n, n) tubes, the first van Hove singularity is located at the band $m = n - 1$ and therefore, this band holds the relevant contribution to the total HHG, as shown in Fig. 4(b). If the driving pulse is strong enough, the electron-hole pair originated in the band $m = n - 1$ will eventually exceed the first Brillouin zone at $a_0 k = \pi$ and shift the oscillation to band $m = 0$ according to the *Umklapp* rule. In particular, for (9,9) $\mathcal{A}$-type tubes the maximum gap experienced by the electron-hole pairs created at $m = 8$ corresponds to 16.7 eV, which matches with the value of the saturated cut-off energy shown in Fig. 6(b). As the nanotube diameter increases, the contributions from

Optics EXPRESS

the second and third van Hove singularities become more relevant, increasing the efficency of the HHG (as shown Fig. 5).

Figure 7(a) shows a map of the energy gap experienced by an electron-hole pair, created at the first van Hove singularity in time t_H, as a function of time t. The map corresponds to a 3 μm wavelength pulse with constant intensity of 5×10^{11} W/cm^2 targeting an (9,9) $\mathcal{A}$-tube, thus representing in a simple way the phenomenology during the cycle of maximum amplitude of the 8-cycle laser pulse considered above for the quantum mechanical model. The red-colored areas correspond to electron-hole trajectories created at t_H that overlap in the same unit cell in the real space at time t. As an example, in point A the electron-hole pair is created at $t_H \simeq 0.35T$ and emits a $\simeq 19\hbar\omega_0$ photon when recombined at $t \simeq 0.85T$. Figure 7(b) shows the classical trajectories of this electron. Note that, for the laser parameters in Fig. 7(a), the maximal photon energy is given by the highest contour constrained to the red-colored area. Therefore, we can use these kind of maps to identify the cut-off frequency of the HHG spectra at each intensity and wavelength. Figure 6(b) shows a comparison between the SPAM cut-off prediction (red circles) and the results of the exact integration of TDSE (blue diamonds). Both results are in excellent agreement.

Additionally, we show in Fig. 8 the SPAM energy map at 3 μm wavelength for a pulse of larger intensity 10^{13} W/cm^2. As it also happens in single layer graphene [17], when the driver's intensity increases, the topology of the red-colored region becomes more complex, so the same harmonic may be emitted by two or more sets of trajectories within the same half cycle of the field. In particular, note that Fig. 8 shows four sets of contributions, labelled from a to d, for the maximum (cut-off) frequency.

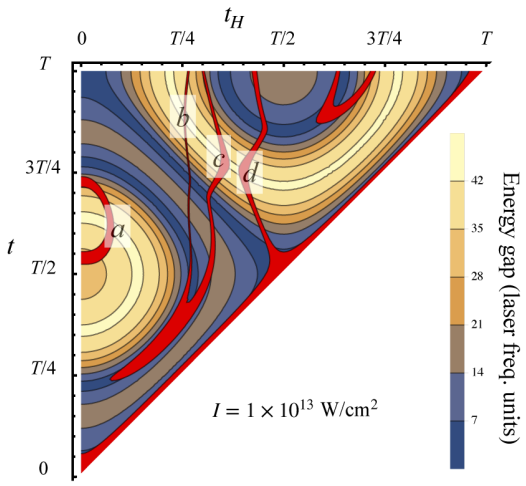

Fig. 8. Energy map for the emitted harmonic photon from a (9,9) armchair tube according to SPAM for a driver peak intensity of 10^{13} W/cm^2. The points corresponding to intersecting electron-hole trajectories are highlighted in red.

5. Conclusions

We have studied the non-perturbative emission of armchair (n, n) carbon nanotubes irradiated by intense few-cycle infrared laser pulses, both from the numerical integration of the TDSE and using a semiclassical model. We have found that the harmonic spectrum follows the typical non-pertubative characteristics, a *plateau* followed by a cut-off frequency. We show that high-harmonics are generated mainly from interband —valence to conduction— transitions

Optics EXPRESS

between nanotube bands with index $|m| = n - 1$. According to our semiclassical model, HHG is initiated by electrons initially quivering in the valence band, that are promoted to the conduction band during the non-adiabatic excursion across the first van Hove singularity. This first step shares similarities with the case of graphene, and departs strongly from the tunnel picture, valid for atoms, molecules and bulk solids. After the excitation to the conduction band, the generated electron-hole pair evolves under the influence of the electric field. The harmonic emission takes place upon recombination of the pair when both electron and hole overlap in real space. In comparison with graphene, HHG in nanotubes is constrained by their one-dimensional nature, i.e. the discrete nature of the reciprocal space: nanotubes with larger diameters emit harmonics more efficiently, since the $|m| = n - 1$ band is closer to the Dirac points, the first van Hove singularity becomes more pronounced and the dipole matrix element is increased. Our semiclassical model predicts the scaling of the harmonic cut-off frequency with the driving field intensity and fully characterizes the electron-hole pairs' creation and recombination times leading to the emission of harmonics. The results presented in this manuscript may be extended in future works to the analysis of the influence of chirality and driver's polarization on the high harmonic emission spectra.

Funding

Junta de Castilla y León, European Regional Development Fund(SA287P18); Ministerio de Ciencia, Innovación y Universidades (FIS2016-75652-P, RYC-2017-22745, PID2019-106910GB-I00); European Research Council (851201).

Acknowledgments

The authors acknowledge V. Marcos for exciting infusions. This project has received funding from the European Research Council (ERC) under the European Union's Horizon 2020 research and innovation program.

Disclosures

The authors declare no conflicts of interest.

References

1. S. Iijima, "Helical microtubules of graphitic carbon," Nature **354**(6348), 56–58 (1991).
2. S. Iijima and T. Ichihashi, "Single-shell carbon nanotubes of 1 nm diameter," Nature **363**(6430), 603–605 (1993).
3. D. S. Bethune, C. H. Klang, M. S. de Vries, G. Gorman, R. Savoy, J. Vazquez, and R. Beyers, "Cobalt-catalysed growth of carbon nanotubes with single-atomic-layer walls," Nature **363**(6430), 605–607 (1993).
4. S. Reich, C. Thomsen, and J. Maultzsch, *Carbon nanotubes: basic concepts and physical properties* (WILEY-CVH Verlag GmbH & Co. KGaA, 2004).
5. L. E. F. Foa-Torres, S. Roche, and J. C. Charlier, *Introduction to graphene-based nanomaterials: from electronic structure to quantum transport* (Cambridge University, 2014).
6. L. Plaja and L. Roso, "High-order harmonic generation in a crystalline solid," Phys. Rev. B **45**(15), 8334–8341 (1992).
7. F. H. M. Faisal and J. Z. Kamiński, "Floquet theory of high-harmonic generation in periodic structures," Phys. Rev. A **56**(1), 748–762 (1997).
8. K. A. Pronin, A. D. Bandrauk, and A. A. Ovchinnikov, "Harmonic generation by a one-dimensional conductor: Exact results," Phys. Rev. B **50**(5), 3473–3476 (1994).
9. S. Ghimire, A. D. DiChiara, E. Sistrunk, P. Agostini, L. F. DiMauro, and D. A. Reis, "Observation of high-order harmonic generation in a bulk crystal," Nat. Phys. **7**(2), 138–141 (2011).
10. L. Plaja, R. Torres, and A. Zaïr, *Attosecond Physics. Attosecond Measurements and Control of Physical Systems* (Springer-Verlag, 2013).
11. P. B. Corkum, "Plasma perspective on strong field multiphoton ionization," Phys. Rev. Lett. **71**(13), 1994–1997 (1993).
12. K. J. Schafer, B. Yang, L. F. DiMauro, and K. C. Kulander, "Above threshold ionization beyond the high harmonic cutoff," Phys. Rev. Lett. **70**(11), 1599–1602 (1993).

Optics EXPRESS

13. J. L. Krause, K. J. Schafer, and K. C. Kulander, "High-order harmonic generation from atoms and ions in the high intensity regime," Phys. Rev. Lett. **68**(24), 3535–3538 (1992).
14. T. Popmintchev, M. C. Chen, D. Popmintchev, P. Arpin, S. Brown, S. Alisauskas, G. Andriukaitis, T. Balciunas, O. Mücke, A. Pugzlys, A. Baltuska, B. Shim, S. E. Schrauth, A. Gaeta, C. Hernández-García, L. Plaja, A. Becker, A. Jaron-Becker, M. M. Murnane, and H. C. Kapteyn, "Bright Coherent Ultrahigh Harmonics in the keV X-ray Regime from Mid-Infrared Femtosecond Lasers," Science **336**(6086), 1287–1291 (2012).
15. G. Vampa, C. R. McDonald, G. Orlando, D. D. Klug, P. B. Corkum, and T. Brabec, "Theoretical Analysis of High-Harmonic Generation in Solids," Phys. Rev. Lett. **113**(7), 073901 (2014).
16. N. Yoshikawa, T. Tamaya, and K. Tanaka, "High-harmonic generation in graphene enhanced by elliptically polarized light excitation," Science **356**(6339), 736–738 (2017).
17. O. Zurrón, A. Picón, and L. Plaja, "Theory of high-order harmonic generation for gapless graphene," New J. Phys. **20**(5), 053033 (2018).
18. O. Zurrón-Cifuentes, R. Boyero-García, C. Hernández-García, A. Picón, and L. Plaja, "Optical anisotropy of non-perturbative high-order harmonic generation in gapless graphene," Opt. Express **27**(5), 7776–7786 (2019).
19. S. de Vega, J. D. Cox, F. Sols, and F. J. García de Abajo, "Strong-field-driven dynamics and high-harmonic generation in interacting one dimensional systems," Phys. Rev. Res. **2**(1), 013313 (2020).
20. H. Nishidome, K. Nagai, K. Uchida, Y. Ichinose, Y. Yomogida, K. Tanaka, and K. Yanagi, "*Control of high-harmonic generation by tuning the electronic structure and carrier injection*," arXiv:2004.11000v1 [physics.optics] (2020).
21. N. Hamada, S. I. Sawada, and A. Oshiyama, "New one-dimensional conductors: Graphitic microtubules," Phys. Rev. Lett. **68**(10), 1579–1581 (1992).
22. R. Saito, M. Fujita, G. Dresselhaus, and M. S. Dresselhaus, "Electronic structure of chiral graphene tubules," Appl. Phys. Lett. **60**(18), 2204–2206 (1992).
23. N. Bozović, I. Bozović, and M. Damnjanović, "Selection rules for polymers and quasi-one-dimensional crystals: IV. Kronecker products for the line groups isogonal to Dnh," J. Phys. A: Math. Gen. **18**(6), 923–937 (1985).
24. M. Breusing, C. Ropers, and T. Elsaesser, "Ultrafast Carrier Dynamics in Graphite," Phys. Rev. Lett. **102**(8), 086809 (2009).
25. J. M. Iglesias, M. J. Martín, E. Pascual, and R. Rengel, "Carrier-carrier and carrier-phonon interactions in the dynamics of photoexcited electrons in graphene," J. Phys.: Conf. Ser. **647**, 012003 (2015).
26. D. Brida, A. Tomadin, C. Manzoni, Y. J. Kim, A. Lombardo, S. Milana, R. R. Nair, K. S. Novoselov, A. C. Ferrari, G. Cerullo, and M. Polini, "Ultrafast collinear scattering and carrier multiplication in graphene," Nat. Commun. **4**(1), 1987 (2013).
27. S. V. Goupalov, "Optical transitions in carbon nanotubes," Phys. Rev. B **72**(19), 195403 (2005).
28. S. V. Goupalov, A. Zarifi, and T. G. Pedersen, "Calculation of optical matrix elements in carbon nanotubes," Phys. Rev. B **81**(15), 153402 (2010).
29. H. K. Kelardeh, V. Apalkov, and M. I. Stockman, "Wannier-Stark states of graphene in strong electric field," Phys. Rev. B **90**(8), 085313 (2014).
30. D. Golde, T. Meier, and S. W. Koch, "High harmonics generated in semiconductor nanostructures by the coupled dynamics of optical inter- and intraband excitations," Phys. Rev. B **77**(7), 075330 (2008).
31. A. Roberts, D. Cormode, C. Reynolds, T. Newhouse-Illige, B. J. LeRoy, and A. S. Sandhu, "Response of graphene to femtosecond high-intensity laser irradiation," Appl. Phys. Lett. **99**(5), 051912 (2011).
32. G. Vampa and T. Brabec, "Merge of high harmonic generation from gases and solids and its implications for attosecond science," J. Phys. B: At., Mol. Opt. Phys. **50**(8), 083001 (2017).
33. A. Nayak, M. Dumergue, S. Kühn, S. Mondal, T. Csizmadia, N. G. Harshitha, M. Füle, M. U. Kahaly, B. Farkas, B. Major, V. Szaszkó-Bogár, P. Földi, S. Majorosi, N. Tsatrafyllis, E. Skantzakis, L. Neoričić, M. Shirozhan, G. Vampa, K. Varjú, P. Tzallas, G. Sansone, D. Charalambidis, and S. Kahaly, "Saddle point approaches in strong field physics and generation of attosecond pulses," Phys. Rep. **833**, 1–52 (2019).
34. M. Lewenstein, P. Balcou, M. Y. Ivanov, A. L'Huillier, and P. B. Corkum, "Theory of high-harmonic generation by low-frequency laser fields," Phys. Rev. A **49**(3), 2117–2132 (1994).

5 CONCLUSIONS

This thesis presents a comparative study on the process of high-order harmonic generation (HHG) by intense few-cycle pulses in single layer graphene (SLG) and single-wall carbon nanotubes (SWNTs). Both are carbon allotropes with effectively reduced dimensions, that react to light in a way different to the most common systems, as atoms, molecules or bulk solids. From our study we can derive the following main conclusions:

1. In both allotropes, the HHG mechanism follows a three step path: (1) Creation of an electron-hole pair; (2) acceleration of the electron (hole) in the conduction (valence) band by the field, and (3) recombination of the pair with the emission of a high-frequency photon. Noticeably, the first step is particular to these kind of systems, as it is not linked to tunneling ionization/excitation, but rather to non-adiabatic excitation, a consequence of the singular geometry of their band structure. In this sense, we have demonstrated the crucial role that Dirac-Weyl points in graphene and van Hove singularities in SWNTs play in the creation of the electron-hole pair. This conclusion is of utmost relevance, since it implies that the generation of higher-order harmonics is not linked to the field amplitude maxima, as occurs in gas systems or bulk solids.

2. As a common feature, the emission spectra of both allotropes present a plateau connected to the non-perturbative character of the HHG process. The cut-off frequency increases with the intensity, but, in contrast to atoms, molecules and bulk solids, we have not found a simple law, linear or quadratic, that describes the scaling of the cut-off frequency with the field amplitude, since it saturates for higher intensities.

3. We have shown that in both systems the main contribution to the high-order spectra comes from interband transitions. We have identified the cut-off saturation frequency with the maximum energy accessible by the electron-hole pair in its quiver motion through the BZ.

4. We have demonstrated that SLG is highly anisotropic, making it possible to emit elliptically polarized harmonics from linear-polarized drivers, and linearly polarized harmonics from elliptically-polarized pulses. The conclusions stemming from our simulations compare well with the experimental results in the literature.

5. For metallic SWNTs, the highest efficiency of the HHG is connected to interband transitions between bands including the first van Hove singularity. On the other hand, semiconducting tubes exhibit a different behavior, since the main contributions come from states at the first and second van Hove singularities. In both cases, the non-perturbative low-order spectra corresponds to both the intraband and interband components of the emission dipole.

6. In metallic SWNTs, it is observed that the spectral efficiency increases with the diameter until it saturates. On the other hand, the spectra of semiconducting tubes does not show a significative correlation with the tube diameter, neither on the efficiency nor in the resolution of the harmonics. For nanotubes of the same diameter, semiconducting species are more efficient targets for HHG than their metallic counterparts.

7. The harmonic spectra is very sensitive to the variation of the chiral angle only if it changes the tube character from semiconducting to metallic and *vice versa*. Otherwise, variation of chirality has little impact on the harmonic response. Therefore, is metallicity rather than chirality what influences the spectral yield.

From the methodological point of view:

1. We have developed a first-principle description of HHG in SLG and SWNTs starting from the tight-binding description of graphene in the nearest neighbors approximation.

2. We have proposed a change of basis to circumvent the numerical instabilities caused by the singularity of the transition matrix element near the Dirac points, which allows to account for the singular non-adiabatic coupling at the Dirac cones without approximation.

3. We have proposed an approximated semiclassical model that explains the main features of HHG in terms of electron-hole trajectories in the reciprocal space.

Our results present a comprehensive description of the HHG process in these low-dimensional carbon allotropes. We have demonstrated that this type of systems posses a very rich non-linear response, that considerably broadens its possible applications compared to bulk solids, atoms and molecules. Although the semiclassical model that we propose is currently limited to linear polarized drivers with the electric field parallel to the main symmetry axis of the samples, our intuition is that it can be extended to drivers with any polarization direction or ellipticity, although not in a straightforward way. Furthermore, we believe that our theoretical approach can be extended to

other low-dimensional materials. In particular, it could be applied to systems with broken inversion and/or time-reversal symmetry [78], where the gap at the Dirac points opens and the anomalous velocity caused by the non-zero Berry curvature will certainly influence the electron dynamics [141]. We find our results encouraging for the development and design of new materials, and methods to control the electron dynamics to tailor the HHG emission [142]. This work paves the way for further investigations in the understanding of the nonlinear optical response of gapless materials and in the manipulation of electron carriers at the petahertz domain.

CONCLUSIONES

Esta tesis presenta un estudio comparativo del proceso de generación de armónicos de orden elevado (HHG) inducido por pulsos láser infrarrojos, ultracortos e intensos, irradiando sobre grafeno monocapa (SLG) y nanotubos de carbono de pared simple (SWNTs). Ambos materiales son alótropos de carbono con dimensiones efectivas reducidas, que interaccionan con la luz de manera diferente a otros sistemas más comunes, como átomos, moléculas o sólidos semiconductores. Las principales conclusiones de nuestro estudio son las siguientes:

1. En ambos sistemas, el mecanismo de HHG sigue una ruta de tres pasos: (1) creación de un par electrón-hueco; (2) aceleración del electrón (hueco) en la banda de conducción (valencia) por el campo, y (3) recombinación del par con la consecuente emisión de un fotón de alta frecuencia. Cabe destacar que el primero de los pasos es especial en estos sistemas, ya que no está ligado a la ionización/excitación por efecto túnel, sino a la excitación no adiabática asociada a la geometría singular de la estructura de bandas. En este sentido, nuestro trabajo demuestra el papel crucial que los puntos de Dirac-Weyl, en el grafeno, y las singularidades de van Hove, en los SWNTs, representan en la creación del par electrón-hueco. Esta conclusión es de suma importancia, ya que implica que la generación de armónicos de orden elevado no se restringe a los instantes de máximo campo, como ocurre en sistemas gaseosos o sólidos semiconductores.

2. Como característica común, los espectros de emisión de ambos alótropos presentan una meseta asociada al carácter no perturbativo del proceso de HHG. La frecuencia de corte aumenta con la intensidad, pero, a diferencia de los sistemas atómicos, moléculares o sólidos semiconductores, no hemos encontrado una ley simple, lineal o cuadrática, que describa el escalado de esta frecuencia con la amplitud del campo, ya que se satura para las intensidades más altas.

3. Hemos demostrado que, en ambos sistemas, la principal contribución a los espectros de armónicos de orden elevado proviene de transiciones interbanda. Hemos identificado además que la saturación de la frecuencia de corte está relacionada con la energía máxima accesible por el par electrón-hueco durante su movimiento oscilatorio en el espacio recíproco.

4. Hemos demostrado que la HHG en SLG es altamente anisotrópica, lo que hace posible la emisión de armónicos polarizados elípticamente a partir de haces incidentes linealmente polarizados, y de armónicos polarizados linealmente generados con pulsos polarizados elípticamente. Las conclusiones derivadas de nuestras simulaciones están alineadas con los resultados experimentales.

5. Para SWNTs metálicos, la mayor eficiencia de la emisión armónica está asociada a transiciones interbanda entre estados localizados en la primera singularidad de van Hove. Los nanotubos semiconductores presentan un comportamiento diferente, ya que las principales contribuciones provienen de estados en localizados en las dos primeras singularidades de van Hove. En ambos casos, los espectros de armónicos de orden bajo corresponden a las componentes intrabanda e interbanda de la emisión dipolar.

6. En los SWNTs metálicos se observa que la eficiencia espectral aumenta con el diámetro, hasta cierto valor de saturación. Por otro lado, los espectros de los nanotubos semiconductores no muestran una correlación significativa con el diámetro del tubo, ni en la eficiencia ni en la resolución de los armónicos. Para nanotubos del mismo diámetro, las especies semiconductoras son blancos más eficientes para la HHG que las especies metálicas.

7. Hemos encontrado que el espectro armónico es muy sensible a la variación del ángulo quiral sólo si ésta se traduce en que el carácter del tubo pase de semiconductor a metálico y viceversa. En caso contrario, la variación de la quiralidad tiene poco impacto en la respuesta armónica. Por lo tanto, es la metalicidad más que la quiralidad lo que influye en el rendimiento espectral.

Desde el punto de vista metodológico:

1. Hemos desarrollado una descripción desde primeros principios de la HHG en SLG y SWNTs a partir del modelo *tight-binding* del grafeno en la aproximación de vecinos más próximos.

2. Hemos propuesto un cambio de base para evitar las inestabilidades numéricas causadas por la singularidad del elemento de

matriz de la transición dipolar en el entorno de los puntos de Dirac, lo que permite dar cuenta del singular acoplamiento no adiabático en los conos de Dirac, sin realizar aproximaciones.

3. Hemos propuesto un modelo semiclásico aproximado que explica las características principales de la HHG en términos de las trayectorias seguidas por electrones y huecos en el espacio recíproco.

En resumen, nuestros resultados presentan una descripción completa del proceso de HHG en estos alótropos de carbono de baja dimensión. Hemos demostrado que este tipo de sistemas posee una respuesta no lineal muy rica, que amplía considerablemente sus posibles aplicaciones en comparación con los sistemas atómicos y moleculares, y los sólidos semiconductores. Aunque la validez del modelo semiclásico que proponemos se limita actualmente a haces incidentes polarizados linealmente y con el campo eléctrico paralelo a los ejes principales de simetría de los blancos, nuestra intuición es que pueda extenderse a haces con cualquier dirección de polarización o elipticidad, si bien no de forma sencilla. Creemos que nuestro enfoque teórico puede extenderse a otros materiales de dimensiones reducidas. En particular, podría aplicarse a sistemas con rotura de las simetrías de inversión temporal y/o espacial [78], donde el *gap* en los puntos de Dirac se abre y en los que la componente anómala de la velocidad causada por la curvatura de Berry ciertamente influirá sobre la dinámica del electrón [141]. Nuestros resultados alientan el desarrollo y diseño de nuevos materiales y métodos para controlar la dinámica de los electrones y modificar la emisión de HHG [142]. Este trabajo allana el camino para futuras investigaciones sobre la respuesta óptica no lineal de materiales sin *gap* y sobre la manipulación de portadores en el dominio del petahercio.

BIBLIOGRAPHY

1. Terrones, M., Botello-Méndez, A. R., Campos-Delgado, J., López-Urías, F., Vega-Cantú, Y. I., Rodríguez-Macías, F. J., Elías, A. L., Muñoz-Sandoval, E., Cano-Márquez, A. G., Charlier, J.-C. & Terrones, H. Graphene and graphite nanoribbons: Morphology, properties, synthesis, defects and applications. *Nano Today* **5,** 351–372 (2010).
2. Wallace, P. R. The Band Theory of Graphite. *Phys. Rev.* 622 (1947).
3. Boehm, H. P., Clauss, A., Fischer, G. O. & Hofmann, U. Das Adsorptionsverhalten sehr dünner Kohlenstoff-Folien. *Zeitschrift für anorganische und allgemeine Chemie* **316,** 119–127 (1962).
4. Novoselov, K. S., Geim, A. K., Morozov, S. V., Jiang, D., Zhang, Y., Dubonos, S. V., Grigorieva, I. V. & Firsov, A. A. Electric Field Effect in Atomically Thin Carbon Films. *Science* **306,** 666–669 (2004).
5. Novoselov, K. S., Jiang, D., Schedin, F., Booth, T. J., Khotkevich, V. V., Morozov, S. V. & Geim, A. K. Two-dimensional atomic crystals. *Proceedings of the National Academy of Sciences* **102,** 10451–10453 (2005).
6. Berger, C., Song, Z., Li, X., Wu, X., Brown, N., Naud, C., Mayou, D., Li, T., Hass, J., Marchenkov, A. N., Conrad, E. H., First, P. N. & de Heer, W. A. Electronic Confinement and Coherence in Patterned Epitaxial Graphene. *Science* **312,** 1191–1196 (2006).
7. Geim, A. K. & Novoselov, K. S. The rise of graphene. *Nature Materials* **6,** 183–191 (2007).
8. Novoselov, K. S., Geim, A. K., Morozov, S. V., Jiang, D., Katsnelson, M. I., Grigorieva, I. V., Dubonos, S. V. & Firsov, A. A. Two-dimensional gas of massless Dirac fermions in graphene. *Nature* **438,** 197–200 (2005).
9. Buna, M. & Borini, S. Optical constants of graphene layers in the visible range. *Appl. Phys. Lett.* 031901 (2009).
10. Mikhailov, S. A. & Ziegler, K. Nonlinear electromagnetic response of graphene: frequency multiplication and the self consistent field effects. *J. Phys.: Condens. Matter,* 384204 (2008).
11. Ishikawa, K. L. Nonlinear Optical Response of Graphene in Time Domain. *Phys. Rev. B,* 201402 (2010).
12. Dean, J. J. & van Driel, H. M. Second harmonic generation from graphene and graphitic films. *Appl. Phys. Lett.* 261910 (2009).

13. Kumar, N., Kumar, J., Gerstenkorn, C., Wang, R., Chiu, H., Smirl, A. & Zhao, H. Third harmonic generation in graphene and few-layer graphite films. *Phys. Rev. B,* 121406 (2013).

14. Hong, S., Dadap, J., Petrone, N., Yeh, P., Hone, J. & Osgood, R. Optical Third-Harmonic Generation in Graphene. *Phys. Rev. X,* 021014 (2013).

15. Baudisch, M., Marini, A., Cox, J. D., Zhu, T., Silva, F., Teichmann, S., Massicotte, M., Koppens, F., Levitov, L. S., de Abajo, F. J. G. & Biegert, J. Petahertz optical response in graphene. *arXiv:1703.10945* (2017).

16. Yoshikawa, N., Tamaya, T. & Tanaka, K. High-harmonic generation in graphene enhanced by elliptically polarized light excitation. *Science,* 736 (2017).

17. Taucer, M., Hammond, T. J., Corkum, P. B., Vampa, G., Couture, C., Thiré, N., Schmidt, B. E., Légaré, F., Selvi, H., Unsuree, N., Hamilton, B., Echtermeyer, T. J. & Denecke, M. A. Nonperturbative harmonic generation in graphene from intense midinfrared pulsed light. *Phys. Rev. B* **96,** 195420 (2017).

18. Balandin, A. A., Ghosh, S., Bao, W., Calizo, I., Teweldebrhan, D., Miao, F. & Lau, C. N. Superior Thermal Conductivity of Single-Layer Graphene. *Nano Letters* **8,** 902–907 (Mar. 2008).

19. Lee, C., Wei, X., Kysar, J. W. & Hone, J. Measurement of the Elastic Properties and Intrinsic Strength of Monolayer Graphene. *Science* **321,** 385–388 (2008).

20. Cao, K., Feng, S., Han, Y., Gao, L., Hue Ly, T., Xu, Z. & Lu, Y. Elastic straining of free-standing monolayer graphene. *Nature Communications* **11,** 284 (2020).

21. Zheng, L. X., O'Connell, M. J., Doorn, S. K., Liao, X. Z., Zhao, Y. H., Akhadov, E. A., Hoffbauer, M. A., Roop, B. J., Jia, Q. X., Dye, R. C., Peterson, D. E., Huang, S. M., Liu, J. & Zhu, Y. T. Ultralong single-wall carbon nanotubes. *Nature Materials* **3,** 673–676 (2004).

22. Iijima, S. Helical microtubules of graphitic carbon. *Nature* **354,** 56–58 (1991).

23. Monthioux, M. & Kuznetsov, V. L. Who should be given the credit for the discovery of carbon nanotubes? *Carbon* **44,** 1621–1623 (2006).

24. Oberlin, A., Endo, M. & Koyama, T. Filamentous growth of carbon through benzene decomposition. *Journal of Crystal Growth* **32,** 335–349 (1976).

25. Abrahamson, J., Wiles, P. G. & Rhoades, B. L. Structure of carbon fibres found on carbon arc anodes. *Carbon* **37,** 1873–1874 (1999).

26. Iijima, S. & Ichihashi, T. Single-shell carbon nanotubes of 1-nm diameter. *Nature* **363,** 603–605 (1993).

27. Bethune, D. S., Kiang, C. H., de Vries, M. S., Gorman, G., Savoy, R., Vazquez, J. & Beyers, R. Cobalt-catalysed growth of carbon nanotubes with single-atomic-layer walls. *Nature* **363,** 605–607 (1993).

28. Saito, R., Dresselhaus, G. & Dresselhaus, M. S. *Physical Properties of Carbon Nanotubes* (Imperial College Press, 1998).

29. Hong, S. & Myung, S. A flexible approach to mobility. *Nature Nanotechnology* **2,** 207–208 (2007).

30. Nishidome, H., Nagai, K., Uchida, K., Ichinose, Y., Yomogida, Y., Miyata, Y., Tanaka, K. & Yanagi, K. Control of High-Harmonic Generation by Tuning the Electronic Structure and Carrier Injection. *Nano Letters* **20,** 6215–6221 (2020).

31. Pop, E., Mann, D., Wang, Q., Goodson, K. & Dai, H. Thermal Conductance of an Individual Single-Wall Carbon Nanotube above Room Temperature. *Nano Letters* **6,** 96–100 (2006).

32. Sinha, S., Barjami, S., Iannacchione, G., Schwab, A. & Muench, G. Off-axis Thermal Properties of Carbon Nanotube Films. *Journal of Nanoparticle Research* **7,** 651–657 (2005).

33. Peng, B., Locascio, M., Zapol, P., Li, S., Mielke, S. L., Schatz, G. C. & Espinosa, H. D. Measurements of near-ultimate strength for multiwalled carbon nanotubes and irradiation induced crosslinking improvements. *Nature Nanotechnology* **3,** 626–631 (2008).

34. Jensen, K., Mickelson, W., Kis, A. & Zettl, A. Buckling and kinking force measurements on individual multiwalled carbon nanotubes. *Phys. Rev. B* **76,** 195436 (2007).

35. Yang, Y. H. & Li, W. Z. Radial elasticity of single-walled carbon nanotube measured by atomic force microscopy. *Applied Physics Letters* **98,** 041901 (2011).

36. Ruoff, R. S., Tersoff, J., Lorents, D. C., Subramoney, S. & Chan, B. Radial deformation of carbon nanotubes by van der Waals forces. *Nature* **364,** 514–516 (1993).

37. *Carbon Nanotubes: Synthesis, Structure, Properties, and Applications* (eds Dresselhaus, M. S., Dresselhaus, G. & Avouris, P.) (Springer-Verlag Berlin Heidelberg, 2001).

38. Maiman, T. H. Stimulated Optical Radiation in Ruby. *Nature* **187,** 493–494 (1960).

39. Krause, J. L., Shafer, K. J. & Kulander, K. C. High-order harmonic generation from atoms and ions in the high intensity regime. *Phys. Rev. Lett.* 3535 (1992).

40. Popmintchev, T., Chen, M. C., Popmintchev, D., Arpin, P., Brown, S., Ališauskas, S., Andriukaitis, G., Balčiunas, T., Mücke, O. D., Pugzlys, A., Baltuška, A., Shim, B., Schrauth, S. E., Gaeta, A., Hernández-García, C., Plaja, L., Becker, A., Jaron-Becker, A., Murnane, M. M. & Kapteyn, H. C. Bright Coherent Ultrahigh Harmonics in the keV X-ray Regime from Mid-Infrared Femtosecond Lasers. *Science* **336,** 1287–1291 (2012).

41. Silva, F., Teichmann, S. M., Cousin, S. L. & Biegert, J. Spatiotemporal isolation of attosecond soft x-ray pulses in the water window. *Nat. Commun.* 6611 (2015).

42. Franken, P. A., Hill, A. E., Peters, C. W. & Weinreich, G. Generation of Optical Harmonics. *Phys. Rev. Lett.* **7,** 118–119 (1961).

43. McPherson, A., Gibson, G., Jara, H., Johann, U., Luk, T. S., McIntyre, I. A., Boyer, K. & Rhode, C. K. Studies of multiphoton production of vacuum-ultraviolet radiation in the rare gases. *J. Opt. Soc. Am. B,* 595–601 (1987).

44. Ferray, M., L'Huillier, A., Li, X., Lompré, L., Mainfray, G. & Manus, C. Multiple harmonic conversion of 1064 nm radiation in rare gases. *J. Phys. B: At. Mol. Opt. Phys.* L31–L35 (1988).

45. L'Huillier, A. & Balcou, P. High-order harmonic generation in rare gases with a 1-ps 1053-nm laser. *Phys. Rev. Lett.* **70,** 774–777 (1993).

46. Mackling, J. J., Kmetec, J. D. & Gordon III, C. L. High-order harmonic generation using intense femptosecond pulses. *Phys. Rev. Lett.* **70,** 766–769 (1993).

47. Schafer, K., Yang, B., DiMauro, L. F. & Kulander, K. C. Above threshold ionization beyond the high harmonic cutoff. *Phys. Rev. Lett.* 1599–1602 (1993).

48. Corkum, P. B. Plasma Perspective on Strong-field Multiphoton Ionization. *Phys. Rev. Lett.* 1994–1997 (1993).

49. Lewenstein, M., Balcou, P., Ivanov, M. Y., L'Huillier, A. & Corkum, P. B. Theory of high-harmonic generation by low frequency laser fields. *Phys. Rev. A* **49,** 2117–2132 (1994).

50. Chang, Z., Rundquist, A., Wang, H., Murnane, M. M. & Kapteyn, H. C. Generation of Coherent Soft X Rays at 2.7 nm Using High Harmonics. *Phys. Rev. Lett.* **79,** 2967–2970 (1997).

51. Schnürer, M., Spielmann, C., Wobrauschek, P., Streli, C., Burnett, N. H., Kan, C., Ferencz, K., Koppitsch, R., Cheng, Z., Brabec, T. & Krausz, F. Coherent 0.5-keV X-Ray Emission from Helium Driven by a Sub-10-fs Laser. *Phys. Rev. Lett.* **80,** 3236–3239 (1998).

52. Ghimire, S., DiChiara, A., Sistrunk, E., Agostini, P., DiMauro, L. & Reis, D. Observation of high-order harmonic generation in a bulk crystal. *Nat. Phys.* 138 (2011).

53. Schubert, O., Hohenleutner, M., Langer, F., Urbanek, B., Lange C. and. Huttner, U., Golde, D., Meier, T., Kira, M., Koch, S. & R., H. Sub-cycle control of terahertz high-harmonic generation by dynamical Bloch oscillations. *Nat. Photon* **8,** 119 (2014).

54. Luu, T., Garg, M., Kruchinin, S., Moulet, A., Hassan, M. & Goulielmakis, E. Extreme ultraviolet high-harmonic spectroscopy of solids. *Nature* **521,** 498 (2015).

55. Hohenleutner, M., Langer, F., Schubert, O., Knorr, M., Huttner, U., Koch, S., Kira, M. & Huber, R. Real-time observation of interfering crystal electrons in high-harmonic generation. *Nature* **523,** 572 (2015).

56. Vampa, G., Hammond, T., Thiré, N., Schmidt, B., Légaré, F., McDonald, C., Brabec, T. & Corkum, P. B. Linking high harmonics from gases and solids. *Nature* **522,** 462 (2015).

57. Ndabashimiye, G., Ghimire, S., Wu, M., Browne, D., Schafer, K., Gaarde, M. & Reis, D. Solid-state harmonics beyond the atomic limit. *Nature* **534,** 520 (2016).

58. Liu, H., Li, Y., You, Y., Ghimire, S., Heinz, T. F. & Reis, D. A. Solid-state harmonics beyond the atomic limit. *Nat. Phys.* **13,** 262 (2017).

59. Vampa, G. & Brabec, T. Merge of high harmonic generation from gases and solids and its implications for attosecond science. *J. Phys. B: At. Mol. Opt. Phys.* 083001 (2017).

60. Teubner, U. & P., G. High-order harmonics from laser-irradiated plasma surfaces. *Rev. Mod. Phys.* **81,** 445 (2009).

61. Plaja, L. & Franco, L. R. High-order harmonic generation in a crystalline solid. *Phys. Rev. B,* 8334 (1992).

62. Picón, A., Roso, L., Mompart, J., Varela, O., Ahufinger, V., Corbalán, R. & Plaja, L. Dipole spectrum structure of nonresonant nonpertubative driven two-level atoms. *Phys. Rev. A,* 033420 (2010).

63. Ghimire, S., DiChiara, A., Sistrunk, E., Ndabashimiye, G., Szafruga, U., Mohammad, A., Agostini, P., DiMauro, L. & Reis, D. Generation and propagation of high-order harmonics in crystals. *Phys. Rev. A,* 043836 (2012).

64. Golde, D., Meier, T. & Koch, S. W. High harmonics generated in semiconductor nanostructures by the coupled dynamics of optical inter- and intraband excitations. *Phys. Rev. B,* 075330 (2008).

65. Vampa, G., McDonald, C., Orlando, G., Klug, D., Corkum, P. & Brabec, T. High harmonics generated in semiconductor nanostructures by the coupled dynamics of optical inter- and intraband excitations. *Phys. Rev. Lett.* 073901 (2014).

66. Wu, M., S. Ghimire, D., Reis, Schafer, K. & Gaarde, M. High harmonics generated in semiconductor nanostructures by the coupled dynamics of optical inter- and intraband excitations. *Phys. Rev. A,* 043839 (2015).

67. Luu, T. & W′orner, H. High-order harmonic generation in solids: A unifying approach. *Phys. Rev. B,* 115164 (2016).

68. Osika, E., Chacón, A., Ortmann, L., Suárez, N., Hernández, J. P., Szafran, B., Ciappina, M., Sols, F., Landsman, A. & Lewenstein, M. Wannier-Bloch Approach to Localization in High-Harmonics Generation in Solids. *Phys. Rev. X,* 021017 (2017).

69. Foa Torres, L. E. F., Roche, S. & Charlier, J.-C. *Introduction to Graphene-Based Nanomaterials: From Electronic Structure to Quantum Transport* (Cambridge University Press, 2014).

70. Kogan, E., Nazarov, V. U., Silkin, V. M. & Krasovskii, E. E. *Space Group Symmetry Classification of Energy Bands in Graphene and Destruction of Dirac Points by Supercell Potential* 2013.

71. Lomer, W. M. The valence bands in two-dimensional graphite. *Proc. Roy. Soc. A* **227,** 330–349 (1955).

72. Kogan, E. & Nazarov, V. U. Symmetry classification of energy bands in graphene. *Phys. Rev. B* **85,** 115418 (2012).

73. Kogan, E. Symmetry Classification of Energy Bands in Graphene and Silicene. *Graphene* **2,** 74–80 (2013).

74. Reich, S., Thornsen, C. & Maultzsch, J. *Carbon Nanotubes: Basic Concepts and Physical Properties* (WILEY-VCH Verlag GmbH and Co. KGaA, 2004).

75. Bloch, F. Über die Quantenmechanik der Elektronen in Kristallgittern. *Zeitschrift für Physik* **52,** 555–600 (1929).

76. Bouckaert, L. P., Smoluchowski, R. & Wigner, E. Theory of Brillouin zones and symmetry properties of wave functions in crystals. *Phys. Rev.* **50,** 58–67 (1936).

77. Reich, S., Maultzsch, J., Thomsen, C. & Ordejón, P. Tight binding description of graphene. *Phys. Rev. B* **66,** 035412 (2002).

78. Yang, S. A. Dirac and Weyl Materials: Fundamental Aspects and Some Spintronics Applications. *SPIN* **06,** 1640003 (2016).

79. Haldane, F. D. M. Model for a Quantum Hall Effect without Landau Levels: Condensed-Matter Realization of the "Parity Anomaly". *Phys. Rev. Lett.* **61,** 2015–2018 (1988).

80. Ando, T., Nakanishi, T. & Saito, R. Berry's phase and absence of back scattering in carbon nanotubes. *J. Phys. Soc. Jpn.* **67,** 2857–2862 (1998).

81. Wang, Q. H., Kalantar-Zadeh, K., Kis, A., Coleman, J. N. & Strano, M. S. Electronics and optoelectronics of two-dimensional transition metal dichalcogenides. *Nature Nanotechnology* **7,** 699–712 (2012).

82. Kane, C. L. & Mele, E. J. Quantum Spin Hall Effect in Graphene. *Phys. Rev. Lett.* **95,** 226801 (2005).

83. Damnjanović, M., Milošević, I., Vuković, T. & Sredanović, R. Symmetry and lattices of single-wall nanotubes. *J. Phys. A,* 4097 (1999).

84. Damnjanović, M., Vuković, T. & Milošević, I. Modified group projectors: Tight binding method. *J. Phys. A: Math. Gen.* 6561 (2000).

85. Vuković, T., Milošević, I. & Damnjanović, M. Carbon nanotubes band assignation, topology, Bloch states, and selection rules. *Phys. Rev. B,* 045418 (2002).

86. Hamada, N., Sawada, S.-I. & Oshiyama, A. New one dimensional conductors: Graphitic microtubules. *Phys. Rev. Lett.* 1579–1581 (1992).

87. Saito, R., Fujita, M., Dresselhaus, G. & Dresselhaus, M. S. Electronic structure of chiral graphene tubules. *Appl. Phys. Lett.* 2204–2206 (1992).

88. White, C. T. & Mintmire, J. W. Density of states reflects diameter in nanotubes. *Nature,* 29–30 (1998).

89. Božović, I., Božović, N. & Damnjanović, M. Optical dichroism in nanotubes. *Phys. Rev. B* **62,** 6971–6974 (2000).

90. Yariv, A. *Quantum electronics (3rd. Ed.)* (Wiley, 1989).

91. Glauber, R. J. Coherent and Incoherent States of the Radiation Field. *Phys. Rev.* **131,** 2766–2788 (1963).

92. Kaiser, W. & Garrett, C. G. B. Two-Photon Excitation in CaF_2: Eu^{2+}. *Phys. Rev. Lett.* **7,** 229–231 (1961).

93. Giordmaine, J. A. & Miller, R. C. Tunable Coherent Parametric Oscillation in $LiNbO_3$ at Optical Frequencies. *Phys. Rev. Lett.* **14,** 973–976 (1965).

94. Colin, S., Contesse, E., Le Boudec, P., Stephan, G. & Sanchez, F. Evidence of a saturable-absorption effect in heavily erbium-doped fibers. *Optics Letters* **21,** 1987–1989 (Dec. 1996).

95. Dong, L., Archambault, J. L., Reekie, L., Russell, P. S. J. & Payne, D. N. Photoinduced absorption change in germanosilicate preforms: evidence for the color-center model of photosensitivity. *Appl. Opt.* **34,** 3436 (June 1995).

96. Paoli, T. L. Saturable absorption effects in the self-pulsing (AlGa) As junction laser. *Applied Physics Letters* **34,** 652 (May 1979).

97. Kazzaz, A., Ruschin, S., Shoshan, I. & Ravnitsky, G. Stimulated Raman scattering in methane-experimental optimization and numerical model. *IEEE Journal of Quantum Electronics* **30,** 3017–3024 (Jan. 1994).

98. Boyd, R. W. *Nonlinear Optics* Third Edition (Academic Press, 2008).

99. Li, X., L'Huillier, A., Ferray, M., Lompré, L. & Mainfray, G. Multiple-harmonic generation in rare gases at high laser intensity. *Phys. Rev. A,* 5751 (1989).

100. Krause, J. L., Schafer, K. J. & Kulander, K. C. Calculation of photoemission from atoms subject to intense laser fields. *Phys. Rev. A,* 4998 (1992).

101. Van Linden van den Heuvell, H. B. & Muller, H. G. *Multiphoton Processes* (eds Smith, S. J. & Knight, P. L.) (Cambridge University Press, 1988).

102. Gallagher, T. F. Above-Threshold Ionization in Low-Frequency Limit. *Phys. Rev. Lett.* 2304 (1988).

103. Popmintchev, T., Chen, M., Arpin, P., Murnane, M. M. & Kapteyn, H. C. The attosecond nonlinear optics of bright coherent X-ray generation. *Nature Photon,* 822 (2010).

104. García, C. H. *Coherent attosecond light sources based on high-order harmonic generation: influence of the propagation effects* PhD thesis (Departamento de Física Aplicada. Universidad de Salamanca, 2013).

105. Pérez-Hernández, J. A., Ramos, J., Roso, L. & Plaja, L. Harmonic generation beyond the strong-field approximation: phase and temporal description. *Laser Phys.* **5,** 1044–1050 (2010).

106. Zurrón, Ó., Picón, A. & Plaja, L. Theory of high-order harmonic generation for gapless graphene. *New Journal of Physics* **20,** 053033 (2018).

107. Óscar Zurrón-Cifuentes, Boyero-García, R., Hernández-García, C., Picón, A. & Plaja, L. Optical anisotropy of non-perturbative high-order harmonic generation in gapless graphene. *Opt. Express* **27,** 7776–7786 (2019).

108. Breusing, M., Ropers, C. & Elsaesser, T. Ultrafast carrier dynamics in graphite. *Phys. Rev. Lett.* 086809 (2009).

109. Brida, D., Tomadin, A., Manzoni, C., Kim, Y. J., Lombardo, A., Milana, S., Nair, R. R., Novoselov, K. S., Ferrari, A. C., Cerullo, G. & Polini, M. Ultrafast collinear scattering and carrier multiplication in graphene. *Nat. Commun.* 611 (2013).

110. Iglesias, J. M., Martín, M. J., Pascual, E. & Rengel, R. Carrier-carrier and carrier-phonon interactions in the dynamics of photoexcited electrons in graphene. *J. Phys.: Conf. Ser.* 012003 (2015).

111. Meystre, P. & Sargent, M. *Elements of Quantum Optics* 4th ed. (Springer-Verlag Berlin Heidelberg, 2007).

112. Kelardeh, H. K., Apalkov, V. & Stockman, M. I. Wannier-Stark states of graphene in strong electric field. *Phys. Rev. B* **90,** 085313 (2014).

113. Kelardeh, H. K., Apalkov, V. & Stockman, M. I. Graphene in ultrafast and superstrong laser fields. *Phys. Rev. B* **91,** 045439 (2015).

114. Zak, J. Dynamics of Electrons in Solids in External Fields. *Phys. Rev.* **168,** 686–695 (1968).

115. Houston, W. V. Acceleration of electrons in a crystal lattice. *Phys. Rev.* 184–186 (1940).

116. Wolkow, D. M. Über eine Klasse von Lösungen der Diracschen Gleichung. *Zeitschrift für Physik* **94,** 250–260 (1935).

117. Jackson, J. D. *Classical Electrodynamics* 3rd Edition (Wiley, 1998).

118. Landau, L. D. & Lifshitz, E. M. *The Classical Theory of Fields* 4th Edition (Pergamon, 1975).

119. Boyero-García, R., Zurrón-Cifuentes, O., Plaja, L. & Hernández-García, C. Transverse phase matching of high-order harmonic generation in single-layer graphene. *Opt. Express* **29,** 2488–2500 (2021).

120. Wikmark, H., Guo, C., Vogelsang, J., Smorenburg, P. W., Coudert-Alteirac, H., Lahl, J., Peschel, J., Rudawski, P., Dacasa, H., Carlstrom, S., Macloa, S., Gaarde, M. B., Johnsson, P., Arnold, C. L. & L'Huillier, A. Spatiotemporal coupling of attosecond pulses. *PNAS,* 4779–4787 (2019).

121. García, C. H., Román, J. S., Plaja, L. & Picón, A. Quantum-path signatures in attosecond helical beams driven by optical vortices. *New J. Phys.* 093029 (2015).

122. L'Huillier, A., Balcou, P., Candel, S., Schafer, K. J. & Kulander, K. C. Calculations of high-order harmonic generation processes in xenon at 1064 nm. *Phys. Rev. A,* 2778 (1992).

123. Rego, L., Román, J. S., Picón, A., Plaja, L. & García, C. H. Nonperturbative twist in the generation of extreme-ultraviolet vortex beams. *Phys. Rev. Lett.* 163202 (2016).

124. Roberts, A., Cormode, D., Reynolds, C., Newhouse-Illige, T., LeRoy, B. J. & Sandhu, A. S. Response of graphene to femtosecond high-intensity laser irradiation. *Appl. Phys. Lett.* 051912 (2011).

125. Pérez, J. M. I. *Out-of-equilibrium carrier dynamics in graphene and graphene-based devices for high-performance electronics* PhD thesis (Departamento de Física Aplicada. Universidad de Salamanca, 2019).

126. Huang, P. C., Hernández-García, C., Huang, J. T., Huang, P. Y., Lu, C. H., Rego, L., Hickstein, D. D., Ellis, J. L., Jaron-Becker, A., Becker, A., Yang, S. D., Durfee, C. G., Plaja, L., Kapteyn, H. C., Murnane, M. M., Kung, A. H. & Chen, M. C. Polarization control of isolated high-harmonic pulses. *Nat. Photonics* **12,** 349–354 (2018).

127. Dorney, K. M., Rego, L., Brooks, N. J., San Román, J., Liao, C.-T., Ellis, J. L., Zusin, D., Gentry, C., Nguyen, Q. L., Shaw, J. M., Picón, A., Plaja, L., Kapteyn, H. C., Murnane, M. M. & Hernández-García, C. Controlling the polarization and vortex charge of attosecond high-harmonic beams via simultaneous spin–orbit momentum conservation. *Nature Photonics* **13,** 123–130 (2019).

128. You, Y. S., Lu, J., Cunningham, E. F., Roedel, C. & Ghimire, S. Crystal orientation-dependent polarization state of high-order harmonics. *Opt. Lett.* **44,** 530–533 (2019).

129. Budil, K. S., Salières, P., L'Huillier, A., Ditmire, T. & Perry, M. D. Influence of ellipticity on harmonic generation. *Phys. Rev. A* **48,** R3437–R3440 (1993).

130. Chen, Z.-Y. & Qin, R. Circularly polarized extreme ultraviolet high harmonic generation in graphene. *Opt. Express* **27,** 3761–3770 (2019).

131. Milošević, D. B., Becker, W. & Kopold, R. Generation of circularly polarized high-order harmonics by two-color coplanar field mixing. *Phys. Rev. A* **61,** 063403 (2000).

132. Fleischer, A., Kfir, O., Diskin, T., Sidorenko, P. & Cohen, O. Spin angular momentum and tunable polarization in high-harmonic generation. *Nature Photonics* **8,** 543–549 (2014).

133. Chen, C., Tao, Z., Hernández-García, C., Matyba, P., Carr, A., Knut, R., Kfir, O., Zusin, D., Gentry, C., Grychtol, P., Cohen, O., Plaja, L., Becker, A., Jaron-Becker, A., Kapteyn, H. & Murnane, M. Tomographic reconstruction of circularly polarized high-harmonic fields: 3D attosecond metrology. *Science Advances* **2** (2016).

134. Barreau, L., Veyrinas, K., Gruson, V., Weber, S. J., Auguste, T., Hergott, J. F., Lepetit, F., Carré, B., Houver, J. C., Dowek, D. & Salières, P. Evidence of depolarization and ellipticity of high harmonics driven by ultrashort bichromatic circularly polarized fields. *Nat. Commun.* **9,** 4727 (2018).

135. Óscar Zurrón-Cifuentes, Boyero-García, R., Hernández-García, C. & Plaja, L. High harmonic generation in armchair carbon nanotubes. *Opt. Express* **28,** 19760–19771 (2020).

136. Damnjanović, M. Standard components of polar and axial vectors for quasi one-dimensional systems. *Physics Letters A* **94,** 337–339 (1983).

137. Bozovic, N, Bozovic, I & Damnjanovic, M. Selection rules for polymers and quasi-one-dimensional crystals. IV. Kronecker products for the line groups isogonal to Dnh. *Journal of Physics A: Mathematical and General* **18,** 923–937 (1985).

138. Goupalov, S. V. Optical transitions in carbon nanotubes. *Phys. Rev. B* **72,** 195403 (2005).

139. Goupalov, S. V., Zarifi, A. & Pedersen, T. G. Calculation of optical matrix elements in carbon nanotubes. *Phys. Rev. B* **81,** 153402 (2010).

140. Nayak, A., Dumergue, M., Kühn, S., Mondal, S., Csizmadia, T., Harshitha, N., Füle, M., Upadhyay-Kahaly, M., Farkas, B., Major, B., Szaszkó-Bogá, V., Földi, P., Majorosi, S., Tsatrafyllis, N., Skantzakis, E, Neoričić, L., Shirozhan, M., Vampa, G., Varjú, K., Tzallas, P., Sansone, G., Charalambidis, D. & Kahaly, S. Saddle point approaches in strong field physics and generation of attosecond pulses. *Physics Reports* **833,** 1–52 (2019).

141. Xiao, D., Chang, M. C. & Niu, Q. Berry phase effects on electronic properties. *Rev. Mod. Phys.* **82,** 1959–2007 (2010).

142. Sivis, M., Taucer, M., Vampa, G., Johnston, K., Staudte, A., Naumov, A. Y., Villeneuve, D. M., Ropers, C. & Corkum, P. B. Tailored semiconductors for high-harmonic optoelectronics. *Science* **357,** 303–306 (2017).

COLOPHON

This document was typeset using the typographical look-and-feel `classicthesis` developed by André Miede. The style was inspired by Robert Bringhurst's seminal book on typography "*The Elements of Typographic Style*". `classicthesis` is available for both LaTeX and LyX:

https://bitbucket.org/amiede/classicthesis/

Final Version as of March 28, 2021.

This thesis presents a comprehensive theoretical study of the process of high-order harmonic generation induced by intense few-cycle infrared laser pulses in two different types of low dimensional carbon allotropes: 2D single layer graphene and 1D single-wall carbon nanotubes. Our results show the emergence of the typical non-perturbative spectral characteristics but, unlike other more common systems, there is no simple law governing the scaling of the cut-off frequency. Interpreting this particular behavior allows us to unveil the fundamental mechanism for HHG in those low dimensional carbon allotropic structures. We show that the first step for HHG is radically different from the tunneling ionization/excitation process found in gas systems and finite gap solids, and that is closely related to the singular geometry of their band structure.

ALF USAL